Karlsruher Institut für Technologie

Schriftenreihe
Kontinuumsmechanik im Maschinenbau

33

Celine Lauff

Multiscale simulation of fiber-reinforced thermoplastics accounting for damage

KIT Scientific Publishing

Celine Lauff

Multiscale simulation of fiber-reinforced thermoplastics accounting for damage

Schriftenreihe
Kontinuumsmechanik im Maschinenbau
Band 33

Karlsruher Institut für Technologie (KIT)
Institut für Technische Mechanik
Bereich Kontinuumsmechanik

Hrsg. Prof. Dr.-Ing. habil. Thomas Böhlke

Eine Übersicht aller bisher in dieser Schriftenreihe erschienenen Bände finden Sie am Ende des Buchs.

Multiscale simulation of fiber-reinforced thermoplastics accounting for damage

by
Celine Lauff

KIT Scientific Publishing

Karlsruher Institut für Technologie
Institut für Technische Mechanik
Bereich Kontinuumsmechanik

Multiscale simulation of fiber-reinforced
thermoplastics accounting for damage

Zur Erlangung des akademischen Grades Doktor der Ingenieurwissenschaften von der KIT-Fakultät für Maschinenbau des Karlsruher Instituts für Technologie (KIT) genehmigte Dissertation

von Celine Lauff, M.Sc.

Tag der mündlichen Prüfung: 27. April 2026
Hauptreferent: Prof. Dr.-Ing. Thomas Böhlke
Korreferent: Prof. Dr. Matti Schneider
Korreferent: Prof. Dr.-Ing. Philipp Junker

Impressum

KIT Scientific Publishing

Karlsruher Institut für Technologie (KIT)
KIT Scientific Publishing
Straße am Forum 2
D-76131 Karlsruhe

KIT Scientific Publishing is a registered trademark
of Karlsruhe Institute of Technology.
Reprint using the book cover is not allowed.

www.bibliothek.kit.edu/ksp.php | E-Mail: info@ksp.kit.edu | Shop: www.ksp.kit.edu



This document – excluding parts marked otherwise, the cover, pictures and graphs – is licensed under a Creative Commons Attribution-Share Alike 4.0 International License (CC BY-SA 4.0): https://creativecommons.org/licenses/by-sa/4.0/deed.en



The cover page is licensed under a Creative Commons Attribution-No Derivatives 4.0 International License (CC BY-ND 4.0): https://creativecommons.org/licenses/by-nd/4.0/deed.en

Print on Demand 2026 – Gedruckt auf FSC-zertifiziertem Papier

ISSN 2192-693X
ISBN 978-3-7315-1486-2
DOI 10.5445/KSP/1000193409

Publications and citations

This thesis is based on five scientific publications in accordance with §12(3) of the doctoral regulations for mechanical engineering at the Karlsruhe Institute of Technology (KIT) issued in 2017, see Chapters 3-7. For the contextualization of these publications, the thesis additionally contains a general introduction in Chapter 1, the fundamentals of small-strain continuum mechanics in Chapter 2 and a conclusion in Chapter 8.

Copyrighted content has been reproduced with permission of the respective rights holders for those publications for which the copyright licenses required permission. Whenever text sections from existing publications are used, this is indicated by a footnote in the corresponding chapter or section heading. To specify the manner in which text sections from publications is utilized, we define and use the clause *based on* as follows:

- Chapters or sections based on one or multiple publications include, but are not restricted to, selected content from the referenced publications. The sections from which the publication content was taken are given in the footnotes.
- Notation, spelling, grammar, and citation style of the publication content were adjusted to the requirements to this thesis, and references to other chapters of this thesis were introduced.
- Repeated content was omitted and replaced with references to other sections of this thesis as appropriate.
- The numbering of equations, figures, tables and algorithms was adapted.

Additionally, the captions of figures, tables and algorithms taken from existing publications are furnished with the clause *adapted from*. The

formatting of figures, tables and algorithms *adapted from* publications may have been changed. The respective reference publication and the respective figure, table or algorithm number are provided in the captions.

List of publications

This thesis incorporates content from the following scientific publications, licensed under the terms of the Creative Commons CC-BY 4.0 license[1]:

- **Lauff, C.**, Schneider, M., Montesano, J. and Böhlke, T., 2023. An orientation corrected shaking method for the microstructure generation of short fiber-reinforced composites with almost planar fiber orientation. Composite Structures 322, 117352.
- **Lauff, C.**, Schneider, M., Montesano, J. and Böhlke, T., 2024. Generating microstructures of long fiber reinforced composites by the fused sequential addition and migration method. International Journal for Numerical Methods in Engineering 125(22), e7573.
- **Lauff, C.**, Schneider, M. and Böhlke, T., 2025. Microstructure generation of long fiber reinforced hybrid composites using the fused sequential addition and migration method. Journal of Thermoplastic Composite Materials 38(8), 2855–2893.
- **Lauff, C.**, Krause, M., Schneider, M. and Böhlke, T., 2025. On the influence of the fiber curvature on the stiffness of long fiber reinforced composites. International Journal for Numerical Methods in Engineering 126(15), e70094.
- **Lauff, C.**, Schneider, M. and Böhlke, T., 2026. Numerically robust local continuum damage models with softening response via convex re-

[1] https://creativecommons.org/licenses/by/4.0/

laxation. Computer Methods in Applied Mechanics and Engineering 452, 118759.

In accordance with §12(1) of the doctoral regulations for mechanical engineering at the Karlsruhe Institute of Technology (KIT) issued in 2017, other published articles, which are not included in this thesis, are listed as follows:

- Faes, M.G.R., Fina, M., Valdebenito, M.A., **Lauff, C.**, Wagner, W. and Freitag, S., 2022. Bounding Failure Probabilities in Imprecise Stochastic FE models. In: Proceedings of the 8th International Symposium on Reliability Engineering and Risk Management.
- Fina, M., **Lauff, C.** and Wagner, W., 2022. Optimal shell design with polymorphic uncertain parameters. In: Proceedings of the 8th International Symposium on Reliability Engineering and Risk Management.
- Faes, M.G.R., Fina, M., **Lauff, C.**, Valdebenito, M.A., Wagner, W. and Freitag, S., 2022. Bounding the first excursion probability of stochastic oscillators under randomness and imprecision. In: Proceedings of the 30th International Conference on Noise and Vibration Engineering and the 9th International Conference on Uncertainty in Structural Dynamics.
- Fina, M., **Lauff, C.**, Faes, M.G.R., Valdebenito, M.A., Wagner, W. and Freitag, S., 2023. Bounding imprecise failure probabilities in structural mechanics based on maximum standard deviation. Structural Safety 101, 102293.
- **Lauff, C.**, Schneider, M. and Böhlke, T., 2023. Generation and analysis of digital twins for CoDiCoFRP accounting for fiber length and orientation distribution. In: Proceedings of the 23rd International Conference on Composite Materials.

Zusammenfassung

Aufgrund ihrer hohen spezifischen Steifigkeit, der Möglichkeit zur Massenproduktion und der Gestaltungsfreiheit werden diskontinuierlich faserverstärkte Polymere häufig für Leichtbauanwendungen eingesetzt. Infolge der Herstellungsverfahren, z. B. Spritzgießen, sind ihre Mikrostrukturen heterogen, zufällig und anisotrop. Für solche Materialien sind rechnergestützte Multiskalenmethoden, die die mikrostrukturellen Eigenschaften berücksichtigen, geeignete Werkzeuge, um das mechanische Verhalten auf Bauteilebene zuverlässig vorherzusagen.

Um ein Framework für die rechnergestützte Multiskalenmodellierung faserverstärkter Polymere zu entwickeln, ergeben sich drei wesentliche Forschungsaufgaben. Erstens sind repräsentative Mikrostrukturen erforderlich, wobei die Mikrostrukturgenerierung zeit- und ressourcenintensive Experimente auf effiziente Weise ergänzt. Zweitens müssen geeignete Materialmodelle entwickelt werden, die das nichtlineare Materialverhalten, z. B. aufgrund von Schadensdegradation, berücksichtigen. Nicht zuletzt sind effiziente Löser von zentraler Bedeutung, um das mechanische Verhalten von Verbundwerkstoffen mit nichtlinearen Materialmodellen und komplexen Mikrostrukturen zu berechnen.

Diese Arbeit leistet einen Beitrag zur rechnergestützten Homogenisierung faserverstärkter Polymere, indem sie die Erzeugung repräsentativer Volumenelemente behandelt und ein Schadensmodell vorstellt, das ein für industrielle Polymere charakteristisches Entfestigungsverhalten abbildet. Auf der Grundlage der erzeugten Mikrostrukturen und des vorgestellten Schadensmodells werden die mechanischen Eigenschaften

faserverstärkter Polymere unter Verwendung moderner FFT-basierter Homogenisierungstechniken als mikromechanische Löser untersucht.

Im Konkreten werden effiziente Algorithmen zur Erzeugung periodischer Mikrostrukturen für kurz- und langfaserverstärkte Polymere sowie hybride Materialsysteme vorgestellt. Um die Repräsentativität der synthetischen Mikrostrukturen sicherzustellen, werden die wichtigsten Deskriptoren der Mikrostruktur berücksichtigt, d. h. der Faservolumenanteil, die Faserlängen und -orientierungsverteilungen sowie die Faserkrümmung. Die Algorithmen werden auf industrielle Materialsysteme angewandt und die Repräsentativität der generierten Mikrostrukturen durch Vergleich des linear-elastischen Materialverhaltens mit experimentellen Daten geprüft. Durch die präzise Realisierung der mikrostrukturellen Deskriptoren und die Periodizität der Geometrien wird die für die Repräsentativität erforderliche Einheitszellengröße minimiert und damit der Aufwand für die numerische Homogenisierung verringert.

Darüber hinaus wird eine neue Klasse linear-elastischer isotroper Schadensmodelle mit Entfestigung entwickelt. Dazu wird konvexe Regularisierung auf ein klassisches isotropes Schadensmodell mit Schadensratenbegrenzung angewandt. Die daraus resultierende Modellformulierung umfasst eindimensionale Schadensverteilungen zur Charakterisierung des internen Schadenszustands, wobei die zeitliche Entwicklung der Schadensverteilungen durch optimalen Transport bestimmt wird. Zudem gewährleistet die Konvexität der kondensierten inkrementellen Energie auch bei Entfestigung netzunabhängige Ergebnisse, d. h. verhindert Lokalisierungseffekte. In numerischen Studien wird die Leistungsfähigkeit des entwickelten Algorithmus sowie die mechanischen Auswirkungen der neuen Klasse von Schadensmodellen untersucht. Durch die Anwendung auf das Matrixmaterial faserverstärkter Polymere wird gezeigt, dass aufgrund der netzunabhängigen Ergebnisse repräsentative Volumenelemente existieren, was eine grundlegende Voraussetzung für die numerische Homogenisierung darstellt.

Summary

Due to their high specific stiffness, the feasibility of mass production and the design freedom, discontinuous fiber-reinforced polymers are frequently used for lightweight applications. As a result of the manufacturing processes, e.g., injection molding, their microstructures are heterogeneous, random and anisotropic. For such materials, computational multiscale methods accounting for the microstructural characteristics are suitable tools to predict the mechanical behavior on the component scale reliably.

To develop a framework of computational homogenization for fiber-reinforced polymers, three main research tasks arise. First, representative microstructures are required, where microstructure generation tools complement time- and resource-intensive experimental methods in an efficient manner. Secondly, adequate material models need to be derived which account for the non-linear material behavior, e.g., due to damage degradation. Last but not least, efficient solvers are mandatory to compute the mechanical behavior of composite materials with non-linear material models and complex microstructures.

This thesis contributes to the field of computational multiscale modeling for fiber-reinforced polymers by addressing the generation of representative volume elements and by introducing a damage model with damage softening behavior, typical for industrial polymers. Based on the generated microstructures and the presented damage model, the mechanical properties of fiber-reinforced polymers are studied, using modern FFT-based homogenization techniques as the micromechanical solvers.

More specifically, efficient algorithms for the generation of periodic microstructures for short and long fiber reinforced polymers as well as hybrid material systems are presented. To ensure the representativity of the synthetic microstructures, the main descriptors of the microstructure are taken into account, i.e., the fiber volume fraction, the fiber length and orientation distributions as well as the fiber curvature. The generation tools are applied to industrial material systems and the representativity of the generated microstructures is demonstrated by comparing the linear-elastic material behavior with experimental data. Due to the precise realization of the microstructural descriptors and the periodicity of the geometries, the necessary unit cell size for representativity is minimized, decreasing the effort for the computational homogenization.

In addition, a novel class of linear-elastic isotropic damage models with damage softening behavior is developed. To do so, convex regularization techniques are applied to a classical isotropic damage model with damage rate limitation. The emerging damage model formulation includes one-dimensional damage-distributions to characterize the internal damage state, and the time evolution of the damage-distributions is governed by optimal transport. Furthermore, the convexity of the resulting condensed incremental energy ensures mesh-independent results even for damage softening, i.e., prevents localization. In computational studies, the performance of the developed algorithm and the mechanical implications of the novel class of damage models are studied. By applying the damage models to the matrix material of fiber-reinforced polymers, the existence of representative volume elements due to the mesh-independent results is demonstrated - indispensable for computational homogenization.

Acknowledgments

First and foremost, I would like to thank my supervisors Prof. Dr.-Ing. Thomas Böhlke and Prof. Dr. rer. nat. Matti Schneider for their profound guidance and support. Building my scientific journey on the intersection of continuum mechanics and mathematics has been incredibly rewarding. This path was enriched by invaluable insights provided by my supervisors and countless fruitful discussions for which I am truly grateful. In addition, I thank Prof. Dr.-Ing. Philipp Junker for reviewing my thesis and for the interest in my research. I would also like to thank Prof. Dr. Sc. Eng. Kaline Furlan for chairing my doctoral exam.

I am very grateful for the supportive and collegial environment at the ITM. The coffee breaks, diverse discussions, work-related as well as private activities and especially the shared experiences formed a surrounding where challenging periods got a lot easier and cheerful events were celebrated together. I also want to thank the administration for managing the operational tasks, allowing me to focus on my research. Such an inspiring environment made it a joy to start work with a smile every single day.

Being part of the international research training group IRTG 2078 was an encouraging enrichment of my research journey. The collaborative work on the topic of continuous-discontinuous fiber-reinforced polymers was essential in placing my research topic into a wider perspective. Especially, the interdisciplinary exchange in joint regular meetings, conferences and workshops formed a valuable opportunity to gain insight into research problems surrounding the individual scope of my

own research. In particular, I would like to thank Prof. John Montesano for his interest in my research, the collaborative work and the excellent research stay at the University of Waterloo. I am deeply grateful for the experiences gained during my research stay and the inspiring exchange with new colleagues, which enriched my doctoral thesis.

I am very grateful for all members of my family and for all my friends for their unwavering support and for always believing in me. By doing so, you are the ones who made my doctoral journey possible in the first place. Heartfelt gratitude is devoted to my brother Marius for sharing the same sense of humor and being the best brother I could imagine. Furthermore, I am sincerely grateful for the support and the love of my partner Dani, always standing by my side. You helped me to keep a healthy balance between work and private life even during the most stressful times. My deepest honor goes to my parents Ines and Markus for creating the best family environment, for their love, for their trust and the encouraging guidance throughout my entire life. You empowered me to follow my dreams.

The research documented in this doctoral thesis has been funded by the German Research Foundation (DFG) within the International Research Training Group "Integrated engineering of continuous-discontinuous long fiber reinforced polymer" (GRK 2078). The support by the German Research Foundation (DFG) is gratefully acknowledged.

Karlsruhe, June 2026 Celine Lauff

Contents

Publications and citations i

Zusammenfassung v

Summary vii

Acknowledgments ix

1 Introduction 1
1.1 Motivation and objectives 1
1.2 State of the art 5
1.2.1 Microstructure generation 5
1.2.2 Damage modeling 9
1.3 Outline and original contributions 15
1.4 Notation, frequently used acronyms, symbols and operators 18

2 Fundamentals of geometrically linear continuum mechanics 25
2.1 Kinematics 25
2.2 Balance equations 29
2.3 Generalized standard materials 33

3 Microstructure generation of short fiber reinforced composites 37
3.1 Introduction 37
3.2 Microstructure generation for short fiber reinforced composites 39
3.2.1 Description of short fiber reinforced composites . 39
3.2.2 Prescribing the fiber length distribution 41

3.2.3 Inter-fiber collision checks for periodic boundary conditions . . . 42
3.3 The orientation corrected shaking method . . . 44
3.3.1 The initial step . . . 44
3.3.2 The shaking step . . . 47
3.3.3 Control of the second-order fiber orientation tensor 50
3.3.4 Single and multiple orientation shaking . . . 55
3.4 Computational investigations . . . 59
3.4.1 Setup . . . 59
3.4.2 On using the semi-analytic shaking parameter estimation . . . 61
3.4.3 On the difference between single and multiple orientation shaking . . . 65
3.4.4 Study on the resolution and the RVE size . . . 67
3.4.5 Effective stiffness compared to the SAM algorithm 73
3.4.6 Application to a PA66GF35 material . . . 77
3.5 Summary and conclusion . . . 80

4 Microstructures generation of long fiber reinforced composites 85
4.1 Introduction . . . 85
4.2 Optimization on the configuration space of curved fibers 89
4.2.1 Riemannian manifolds and submanifolds . . . 89
4.2.2 Description and discretization of curved fibers . . 91
4.2.3 Adapted gradient descent approach on the configuration space of curved fibers . . . 96
4.2.4 D'Alembert type constrained mechanical system governing the geodesics . . . 98
4.2.5 Numerical integration of the d'Alembert type constrained mechanical system . . . 100
4.3 Microstructure generation for long fiber reinforced composites . . . 102
4.3.1 Description of long fiber reinforced composites . 102

4.3.2 Fused sequential addition and migration (fSAM) algorithm . . . 103
4.3.3 Gamma distribution as fiber length distribution . 109
4.3.4 Handling of extremely long fibers . . . 112
4.4 Computational investigations . . . 115
4.4.1 Setup . . . 115
4.4.2 On the difference between the SAM and the fSAM algorithm . . . 117
4.4.3 Resolution study . . . 120
4.4.4 On the size of the representative volume element 123
4.4.5 Study on the maximum segment length . . . 126
4.4.6 Generation of microstructures with high fiber volume fractions . . . 130
4.4.7 Application to a PPGF30 material accounting for the fiber length distribution . . . 132
4.5 Summary and conclusion . . . 135

5 Microstructure generation of long fiber reinforced hybrid composites . . . 139
5.1 Introduction . . . 139
5.2 Optimization on the configuration space of curved and constrained fibers . . . 142
5.2.1 Parametrization of curved and constrained fibers 142
5.2.2 Adapted gradient descent approach on the configuration space of curved and constrained fibers . . 146
5.2.3 Exponential mapping on the configuration space of curved and constrained fibers . . . 148
5.3 Microstructure generation of long fiber reinforced hybrid composites . . . 152
5.3.1 Description of long fiber reinforced hybrid composites . . . 152

5.3.2 Extension of the fused sequential addition and migration (fSAM) algorithm . . . 154
5.4 Computational investigations . . . 160
5.4.1 Setup . . . 160
5.4.2 On the algorithmic handling of the box constraints 161
5.4.3 Resolution study . . . 164
5.4.4 RVE study . . . 166
5.4.5 On the difference between soft and hard box constraints . . . 168
5.4.6 Comparison to experimental data . . . 171
5.5 Summary and conclusion . . . 178

6 On the influence of the fiber curvature on the stiffness . . . 183
6.1 Introduction . . . 183
6.2 Description and discretization of curved fibers . . . 185
6.2.1 Quantifying the orientation and the curvature of a single fiber . . . 185
6.2.2 Discretization of the curved fibers . . . 190
6.3 Generating microstructures filled with curved fibers . . . 193
6.3.1 Description of fiber-reinforced composites with long and curved fibers . . . 193
6.3.2 Objective function with extended curvature control 195
6.3.3 Pre-optimization step . . . 198
6.4 Computational investigations . . . 200
6.4.1 Setup . . . 200
6.4.2 Resolution study . . . 202
6.4.3 RVE study . . . 205
6.4.4 On the realized fiber curvatures and their effect on the mechanical properties . . . 209
6.4.5 Study on the maximum segment length for varying degrees of curvature . . . 213
6.5 Summary and conclusion . . . 216

7 Numerically robust local continuum damage models via convex relaxation 219
7.1 Introduction 219
7.2 Convex relaxation of a class of damage models 223
7.2.1 A rate-dependent damage model to be convexified 223
7.2.2 The convex envelope 229
7.2.3 Computing the convex envelope explicitly 233
7.2.4 The optimal transport point-of-view 237
7.3 Computational mechanics of the damage model 244
7.3.1 Discussion of the model 244
7.3.2 Computational aspects on material-point level . . 247
7.3.3 Convexity properties of the condensed incremental energy 252
7.4 Computational investigations 254
7.4.1 Setup 254
7.4.2 Studies on material point level 256
7.4.3 Implications of the OT damage model for boundary value problems 264
7.4.4 Validation of the representativity for stochastic homogenization 271
7.4.5 Matrix-failure mechanisms of unidirectional fiber reinforced composites 279
7.5 Conclusion 281

8 Summary and conclusions 287
8.1 Summary 287
8.2 Conclusions 290

A Separating the first eigenvalue of the computed fiber orientation tensor of second order into two terms 295

B Metric of the Riemannian manifold describing a curved fiber 299

C Geodesics on the Riemannian manifold of curved fibers . . . 303

D Properties of the deviation from straight curve (DSC) 307
D.1 A simple representation formula for the DSC 307
D.2 Upper and lower bounds of the DSC 308
D.3 Vanishing DSC implies a straight fiber 308
D.4 Lower bound for the average curvature 309

E The emergence of the harmonic mean 313

F Mathematical details for the mixing formula (7.41) 315

G Arguments for the convexity properties of the condensed incremental energy 321
G.1 Two-sided quadratic bounds 321
G.2 Convexity of the condensed incremental energy 323
G.3 Lack of strict convexity of the condensed incremental energy 325
G.4 Existence of minimizers to mechanical mixed boundary-value problems 329

Bibliography 331

Chapter 1

Introduction

1.1 Motivation and objectives

Facing the global climate change and its drastic impacts on the environment and the lives on earth, the development of innovative strategies to reduce greenhouse gas emissions is a demanding task. With respect to the transport sector, an important factor to improve on the climate-neutrality is weight-saving component construction, decreasing the required fuel consumption (Friedrich, 2017). Thus, research on lightweight materials is crucial when thinking of future-oriented material development.

Due to their high specific stiffness and the existing technologies for mass-production, *fiber-reinforced polymers* play a key role for lightweight technologies (Fuchs et al., 2008; Böhlke et al., 2019). In general, these materials consist of a polymeric matrix and fibers as the filler. For the matrix material, typically either thermosets, e.g., epoxy resin, or thermoplastics, e.g., polyamide, are used. In this thesis, we consider thermoplastic matrix materials. The most common fiber type is glass, complemented by other types as, e.g., carbon, wood or cotton (Kehrer et al., 2023). Fiber-reinforced polymers may be classified into *continuous* fiber-reinforced polymers (CoFRPs) and *discontinuous* fiber-reinforced polymers (DicoFRPs), depending on the fiber length. Whereas CoFRPs feature a higher stiffness, DicoFRPs offer an improved design freedom as well as

a cheaper and faster production. As the combination of both classes, the *continuous-discontinuous* fiber-reinforced polymers (CoDicoFRPs) exhibit the favorable properties of CoFRPs and DicoFRPs. The establishment of an integrated engineering approach for the physical and virtual process chain of CoDicoFRPs (Böhlke et al., 2019; Görthofer et al., 2019; Meyer et al., 2023) is the main objective of the International Research Training Group "Integrated engineering of continuous-discontinuous long fiber reinforced polymer structures" (GRK 2078), funded by the German Research Foundation (DFG).

As a result of the manufacturing processes, the microstructure of DicoFRPs is highly anisotropic, random and heterogeneous, and mainly described by the fiber volume fraction, the fiber length and orientation distributions as well as the fiber curvature (Fliegener et al., 2014; Hessman et al., 2019). To predict the effective macroscopic behavior of such heterogeneous materials, computational multiscale methods (Matouš et al., 2017; Fish et al., 2021; Elmasry et al., 2023) based on homogenization theory (Kozlov, 1979; Papanicolaou and Varadhan, 1981) may be used. However, therefore suitable material models, including, e.g., viscoelasticity (Kehrer et al., 2023), damage (Görthofer et al., 2022) or fatigue (Magino et al., 2022b; 2023), as well as representative descriptions of the microstructure are necessary.

For the required microstructures, typically real image data obtained from μCT-scans (De Paiva et al., 1996; Shen et al., 2004) or synthetic, i.e., generated, microstructures are used. In this context, microstructure generation has several advantages compared to real image data, which motivates the development of microstructure generation tools. First, μCT imaging is expensive in time and resources for each realization, limiting the amount of affordable geometries, whereas synthetic geometries may be generated in an efficient and purely computational manner. Furthermore, image data obtained from μCT-scans is restricted to the descriptors realized within the manufactured parts. In contrast, gener-

ated microstructures may be available for a wide span of descriptors, and we may select a specific combination of descriptors as input for the microstructure generation. The last advantage concerns the periodicity of the geometries, which is favorable to reduce the representative element size (Kanit et al., 2003; Sab and Nedjar, 2005; Schneider et al., 2022). Whereas periodization of microstructure generation tools is quite simple, the direct extraction of periodic geometric from image data is impossible, in general.

This thesis addresses the field of computational multiscale modeling for discontinuous fiber-reinforced composites, taking the damage degradation of the material into account. As representative microstructures are crucial to establish a framework for the prediction of the micromechanical behavior via full-field simulations, we aim to develop microstructure generation tools for fiber-reinforced composites, concerning the following objectives:

- First of all, we are interested in computationally efficient and robust microstructure generation tools to save time and resources.
- To ensure the representativity of the generated microstructures, we seek to realize the desired microstructural properties, i.e., the fiber volume fraction, the fiber length and orientation distribution as well as the fiber curvature, with high fidelity. To do so, we discuss suitable descriptors to assess the properties, and include these descriptors as the input for the microstructure generation.
- We aim to generate periodic microstructures to reduce the boundary artifacts due to the finite cell size, leading to minimal unit cell sizes for representativity (Kanit et al., 2003; Sab and Nedjar, 2005; Schneider et al., 2022).
- One of the most challenging tasks in the field of microstructure generation concerns the generation of packings with long fibers in combination with high fiber volume fractions. Thus, we are interested

in enhancing the packing limits to enable the application of the microstructure generation tools to industrial fiber-reinforced composites.

- Whereas for short fiber reinforced composites the fiber bending is negligible, long fibers should be modeled with a curved fiber description to improve the achievable fiber volume fraction and to account for the influence of the fiber bending on the mechanical behavior.
- Based on the generated microstructures, we aim to study the sensitivity of the mechanical behavior with respect to the desired descriptors. Therefore, we compute the effective stiffness tensor with FFT-based homogenization methods, assuming linear-elastic material behavior for the matrix and the fibers.

Besides the microstructure generation, we seek to introduce a class of suitable damage models which include damage softening, often observed in polymers. To do so, we address the following tasks:

- We aim to formulate the damage models in the framework of generalized standard materials (GSMs), intrinsically ensuring the thermodynamical consistency.
- When accounting for damage softening, classical modeling approaches require non-local regularization techniques (Forest and Lorentz, 2004) to prevent mesh-dependent results caused by localization effects, which significantly increase the computational effort. In contrast, we intend to avoid damage localization by applying regularization techniques on material point level, i.e., without further neighborhood information.
- Last but not least, we aim to apply the derived class of damage models to fiber-reinforced polymers to study the damage progression on the microscale, and to predict the material response on component scale level with FFT-based homogenization. Due to the regularization of the damage model, the emergence of a representative volume element is guaranteed, which is fundamental to apply computational homogenization.

1.2 State of the art

1.2.1 Microstructure generation[1]

In general, methods for generating particle composites may be roughly classified into two categories: sequential insertion algorithms and collective rearrangement algorithms. For sequential insertion algorithms, the particles are placed one by one, keeping the positions and orientations of the previously placed inclusions fixed. The prime representative of this class is the random sequential addition (RSA) algorithm initially introduced for spheres (Widom, 1966) and subsequently extended to more general inclusion shapes (Feder, 1980). Until the desired fiber volume fraction is reached, particles are placed successively under the condition of mutual non-intersection. More precisely, for each fiber, its direction, length and midpoint are sampled randomly from suitable distribution functions until an admissible, i.e., non-overlapping, configuration is found. In case a generated fiber is not placed in a non-overlapping position, there are two typical strategies for re-sampling. Either only the midpoint is sampled anew or the direction and length as well. The latter strategy permits to reach higher fiber volume fractions than the former. This increase, however, comes at a cost - systematic deviations of the desired orientation and length distribution functions may be unavoidable then.

For sequential insertion algorithms, the particle characteristics are permanent after its placement, i.e., it will never be moved thereafter. Hence, the achievable fiber volume fraction is comparatively low. Moreover, with increasing fiber aspect ratio r_a, i.e., the ratio between fiber length and diameter, the achievable fiber volume fraction decreases as well (Evans

[1] This section is based on Section 1.1 of the publication "Generating microstructures of long fiber reinforced composites by the fused sequential addition and migration method" (Lauff et al., 2024).

and Gibson, 1986; Toll, 1998). In fact, RSA-type methods permit to realize high volume fraction for unidirectional fiber arrangement only. Nevertheless, the RSA algorithm is the most common microstructure generator and a number of extensions are available (Tian et al., 2015; Chen et al., 2019; Bahmani et al., 2019; Tian et al., 2021; Bahmani et al., 2023). For almost planar fiber arrangements, the two-step shaking algorithm introduced by Li et al. (2022) generates fiber packings with high fiber volume fractions and rather long fibers. In a first step, the fibers are arranged in a planar setting without inter-fiber penetration using a deterministic procedure. Then, in a second step, a shaking procedure is applied to introduce randomness and to account for out-of-plane fiber directions.

The second category of microstructure-generation algorithms for matrix-inclusion composites comprises methods which position all particles in the cell first and then change their positions simultaneously. The mechanical contraction method (MCM) introduced by Williams and Philipse (2003) permits to generate microstructures of spherocylinders, i.e., cylinders with half-caps at their ends, are generated. In the first step of the MCM, RSA is used to generate a microstructure with small volume fraction and non-overlapping fiber configuration. Then, the unit cell is shrunk while retaining the size of the inclusions to increase the volume fraction. The resulting fiber overlap is removed by an iterative procedure. In its original form, the MCM is restricted to isotropic orientation states and fails to generate microstructures with industrial fiber volume fractions for long fibers. For more general fiber orientation distributions, the sequential addition and migration (SAM) algorithm may be used, first presented for short straight fibers with uniform length (Schneider, 2017). As starting point, a fiber arrangement is sampled according the descriptive components, e.g., the fiber volume fraction or the fiber orientation distribution. In contrast to the MCM, in the starting configuration overlap between the fibers is allowed. Then, an

optimization framework is used to find a configuration which satisfies the non-overlap condition and further desired criteria. Therefore, a non-negative objective function is introduced where every configuration corresponding to a root of the objective function is admissible.

Besides the SAM algorithm for short straight fibers with constant lengths (Schneider, 2017), also extensions for short fibers with fiber length distributions (Mehta and Schneider, 2022) and for coupled fiber length-orientation distributions (Mehta and Schneider, 2024) are available. Using the extension for the fiber length distribution (Mehta and Schneider, 2022), the SAM algorithm accounts for variability in the fiber lengths, which is typical for industrial discontinuous fiber-reinforced composites. Additionally, considering fiber length distributions instead of uniform fiber lengths increases the volume-weighted mean fiber length which can be realized by the algorithm. Thus, the SAM algorithm which accounts for a fiber length distribution is capable of generating long fiber reinforced composites as PPGF30 (13.22% fiber volume fraction), when restricting the volume-weighted mean fiber length to about $2 - 3\mathrm{mm}$. However, there are two apparent shortcomings of the original SAM algorithm. For a start, the generated unit cells can become quite large. In fact, due to the straight fibers, the side length of the unit cells need to be as long as the imposed mean fiber length, at least. This constraint may be rather restrictive for long fibers. Secondly, the straight-fiber model of the original SAM algorithm leads automatically to the formation of bundles of more or less aligned straight fibers. As such bundles of straight fibers are seldomly found in real composites, the effective properties of the composite may be overestimated by computations based on such unit cells.

To enable microstructure generation for industrial long fiber reinforced thermoplastics (LFTs), the packing limit with increasing fiber aspect ratio needs to be overcome. However, to deal with this challenge, the reason for the packing limit should be understood first. In terms of general

packing mechanics of straight fibers, Toll (1998) reveals that the fiber volume fraction may be increased until a maximum number of contacts per fiber is reached. By modeling the fibers with straight cylinders, this maximum number of contacts turns out to be independent of the fiber aspect ratio r_a. However, the apparent number of contacts during the microstructure generation is higher for increasing fiber aspect ratios. Hence, besides unidirectional fiber arrangement less fiber volume fraction is achieved for increasing fiber aspect ratios. With this insight at hand, we conclude that modeling the fibers with straight cylinders restricts the achievable fiber volume fraction due to their low maximum number of contacts. To overcome this limitation, modeling not necessarily straight fibers may enable packings with higher volume fractions for longer fibers (Toll, 1998). Moreover, this appears to be the more natural way of describing real fibers in long fiber reinforced composites as they exhibit significant fiber bending due to the manufacturing processes (Fliegener et al., 2014; Kuhn et al., 2017; Blarr et al., 2023).

For typical manufacturing processes, long fiber reinforced composites feature almost planar fiber orientation states (Advani and Tucker III, 1990; Dray et al., 2007; Bernasconi et al., 2012; Görthofer et al., 2019) as the fiber lengths exceed the plate thickness. For these cases, Fliegener et al. (2014) present an algorithm for microstructure generation with curved fibers, achieving high fiber volume fractions. First, a planar microstructure with low fiber volume fraction is generated by RSA. Then, the structure is compressed in thickness direction using a full finite element analysis until the required volume fraction is reached. Due to the finite element analysis, the method is computationally complex and time-consuming, as many elements are necessary to resolve the microstructure adequately. Additionally, changing the resolution after the microstructure generation, e.g., for the homogenization, is a challenging topic as the fibers are modeled with hexahedral elements and not with an underlying analytical formulation.

An alternative approach accounting for fiber bending, is the extension of the SAM algorithm for long curved fibers (Schneider, 2022). For this algorithm, a curved fiber is discretized by a polygonal chain with spherocylinders as segments. Thus, the optimization problem incorporates the additional condition that adjacent segments need to be connected. In general, such a constraint may be considered in the optimization process in two ways. On one hand, the constraint may only be satisfied at convergence and may be violated for previous iterative steps. For the previous SAM approach, this is realized by adding a penalty term to the objective function. To make this strategy work, the penalty parameter needs to be selected in a clever way and may influence the convergence behavior negatively. The alternative strategy satisfies the constraint in every step, resulting in a more complex iteration rule. Within the optimization procedure of the SAM algorithm for long curved fibers (Schneider, 2022), the first strategy is used. Hence, the segments move separately during the optimization process. However, the penalty term leads to convergence problems for complex microstructures. Thus, microstructures with high fiber volume fractions are barely achieved.

1.2.2 Damage modeling [2]

Damage models are essential in various fields, such as engineering, materials science, and structural analysis, to predict and understand how materials or systems degrade over time under different loading conditions. These models allow simulating the progression of damage, e.g., caused by erosion, material aging, fatigue, or fracture, and help engineers design safer, more durable structures and products. By accurately forecasting the behavior of materials under stress, damage

[2] This section is based on Section 1.1 of the publication "Numerically robust local continuum damage models with softening response via convex relaxation" (Lauff et al., 2026).

models enable identifying potential weak spots, improving the efficiency of maintenance as well as repair strategies and reducing the risk of catastrophic failures.

To model the loss of stiffness caused by the damage progression, continuum damage mechanics (Murakami, 2012; Menzel, 2020) provides suitable tools based on the fundamental concepts introduced by Kachanov (1999) and Rabotnov (1963). As the main assumptions, the materials are modeled as continuous and homogeneous media on the macroscale, and the damage evolution is given as an irreversible evolutionary process.

Typically, the damage degradation starts as cracks or voids on lower length scales first, then grows to defects on the macroscale and eventually leads to failure of the structure (Lemaitre, 1996; Li and Tang, 2015). Depending on the underlying approach, continuum-damage models may be roughly divided into two main categories (Krajcinovic, 1989; Liu et al., 2025). Micromechanics based models (Krajcinovic, 1989; Fitoussi et al., 1996; Guo et al., 1997; Weigel et al., 2001) account for the multiscale progression of the defects, and work on two scales: the continuous and homogeneous macroscale and the heterogeneous and locally discontinuous lower length scale. These models proceed as follows. First, the damage mechanisms on the lower length scale are determined. Subsequently, basic mechanics principles are employed to quantify the nonlinear response at the lower length scale accounting for the defects. Last but not least, the obtained fields are homogenized to predict the behavior on the macroscale. Due to their physical foundation, micromechanics based models are still subject to recent research and find application to several material systems and loading cases (Ju and Wu, 2016; Wu and Ju, 2017; Li et al., 2020; Tojaga et al., 2023).

The second category of continuum-damage models comprises phenomenological approaches (Krajcinovic, 1989; Liu et al., 2025). In contrast to micromechanics-based strategies, these models are not informed on the actual damage origin and propagation on the lower length scales, but

rather provide a rational prediction based on macroscopic experiments. For the phenomenological approaches, a (set of) damage variable is selected first. Then, a thermodynamical model is postulated, linking the damage progression to an irreversible internal energy dissipation (Lemaitre, 1985; Simo and Ju, 1987; Chaboche, 1988; Hansen and Schreyer, 1994; Brünig and Michalski, 2017). By construction, phenomenological approaches are strategies to describe the damage behavior directly at the macroscale. Thus, for heterogeneous materials, the stochastics at lower length scales are not taken into consideration. However, this limitation may be overcome by starting at the lower length scale and assigning to each component a phenomenological material model individually, and then homogenizing (Wriggers and Moftah, 2006; Görthofer et al., 2022). For such a phenomenological multiscale strategy, the medium at the lower length scale is still continuous, whereas micromechanics based approaches may include local discontinuities due to the actual defects.

Selecting the appropriate damage variable(s) plays a key role within the framework of phenomenological continuum-damage models. Scalar damage variables are used to model isotropic, i.e., direction-independent, damaging behavior (Lemaitre, 1985; Zhu and Tang, 2004; Voyiadjis and Kattan, 2009) and may be interpreted as the ratio of the effective load-bearing area to the total area. Due to its simplicity, scalar damage models are used frequently, also in recent publications (Li and Wu, 2018; Liu et al., 2018; Yan et al., 2020; Abu-Farsakh and Asfa, 2020; Song et al., 2024). To incorporate anisotropic damage into the continuum damage formulation, damage variables with higher tensor orders may be used, such as second-order damage variables (Chow and Wang, 1987; Murakami, 1988; Chaboche, 1993; Onodera and Okabe, 2020) or fourth-order damage tensors (Chaboche, 1981; 1993; Olsen-Kettle, 2018b;a; Voyiadjis and Kattan, 2006; Görthofer et al., 2022).

In continuum damage mechanics, selecting the damage variables is only half of the story: Care has to be taken when dealing with damage models that capture softening behavior of the material, as the material then favors localization (Lemaitre, 1986) which cannot be captured on a volumetric mesh by standard local models. Rather, finite element computations lead to mesh-dependent predictions (De Borst et al., 1993). These observed "mesh dependencies" are actually just the ramifications of the underlying lack of mathematical sensibility of the softening damage model.

Different countermeasures were reported in the literature (Forest and Lorentz, 2004). The simplest approach is based on viscous regularization (Needleman, 1988; Sluys and De Borst, 1992; Dubé et al., 1996), which implicitly enforces an upper bound on the damage increment for each mesh-element, thus limiting the dissipation and excluding the localization. Such strategies typically lead to reasonable models in practice, but lack a sound mathematical foundation.

Integral based approaches (Pijaudier-Cabot and Bažant, 1987; Liu et al., 1999; Bažant and Jirásek, 2002; Lorentz and Andrieux, 2003) incorporate long-range interactions by computing a filtered response of either the damage or the evaluated degradation function on a neighborhood of the material point. This averaging process smears out the intended localization and effectively excludes strong localization effects.

It is also possible to consider gradient-enhanced formulations (Peerlings et al., 1996; Brünig and Ricci, 2005; Abu Al-Rub and Voyiadjis, 2009; Dimitrijevic and Hackl, 2011), which add a gradient term of the damage variable within the damage evolution equation. From a physical point of view, the emergence of the damage gradient may be interpreted as quantifying the "average crack area", and the additional gradient term permits to limit the energy dissipated when forming crack surfaces – the physical phenomenon responsible for the localization. Such approaches penalize strong fluctuations of damage in the same way

as those strategies based on integral averages. In fact, most gradient-extended damage models may be equivalently expressed a non-local approaches by rewriting the evolution equation for the damage variable with a suitable Green's function.

Despite their success, these reported ameliorations come with a number of shortcomings:

- Incorporating non-local or gradient-enhanced damage models into existing software codes is often challenging. In particular, for commercial codes specific tricks are required. For instance, Navidtehrani et al. (2021) report on an implementation of a phase field fracture model into the commercial software Abaqus hijacking the thermomechanical solver, i.e., the temperature is treated as the damage variable.
- Both non-local and gradient-extended damage models require a length-scale parameter to be chosen. More often than not, the physical significance of this parameter is unclear and its identification based on experimental results is challenging. Also this length-scale parameter effectively excludes homogenization to apply (Ernesti and Schneider, 2021): If the length scale is proportional to the unit-cell size, it will become infinitesimal upon homogenization, removing the required regularization of the effective model to be sensible. In particular, no representative volume elements (Drugan and Willis, 1996; Kanit et al., 2003; Gitman et al., 2007) emerge.

For these and other reasons, methods based on *convex relaxation* (Balzani and Ortiz, 2012; Schmidt and Balzani, 2016; Schwarz et al., 2021; Balzani et al., 2024) were investigated recently. These works take a closer look at the mathematical underpinnings of the localization phenomena: In a variational setting, the considered damage models lack *quasi-convexity*. Morrey (1952) identified the property of quasi-convexity as a necessary and sufficient condition for the existence of minimizers in the calculus of variations, provided certain necessary growth conditions on the integrands hold. Physically speaking, quasi-convexity of an integrand

means that a homogeneous variational problem with uniform boundary conditions admits a homogeneous solution. Interestingly, neither the shape of the considered body nor whether Dirichlet-, Neumann- or periodic boundary conditions are used plays a role to decide whether a specific integrand is quasi-convex or not, see Dacorogna (1982). For damage mechanics with softening, quasi-convexity of the integrands is not expected by physical considerations - cracks are supposed to form at a lower scale, leading to a non-homogeneous response. As quasi-convexity is a necessary condition for the existence of minimizers, it does not come as a surprise that softening behavior does in fact lead to ill-posed mathematical problems.

Methods based on convex relaxation intend to restore the quasi-convexity of the integrand by computing the (quasi-)convex envelope explicitly and to consider the obtained relaxed integrand as the ground truth. Such a strategy might be considered as adding "microstructural information", i.e., the heterogeneities obstructing quasi-convexity, into the picture. Thus, relaxation approaches operate in two stages: First, the model is selected. Secondly, the convex envelope is computed. Both stages involve *choices*. The real problem for the relaxation approach is actually *computing the envelope*, which amounts to solving a non-convex variational problem more or less explicitly. In this way, this difficulty of non-quasi-convexity is handled by an *analytical method*. Unfortunately, achieving this task is only possible in rare cases, and the choice of the original model and the type of convex envelope is driven by whether it can be handled analytically and explicitly or not. For instance, computing the quasi-convex envelope explicitly is notoriously difficult. Computing the convex envelope is typically simpler, and every convex function is also quasi-convex. Thus, the convex envelope is regularly considered although it is less physical than the quasi-convex envelope. Due to the convexification process, relaxation-based models are *local*, i.e., do not require non-local terms or damage-gradient terms

for regularization. We wish to clarify that the term local model is used to distinguish such approaches from non-local damage models or gradient-enhanced formulations, which include neighborhood information to compute the material response at a single material point.

The described program was set up by Schwarz et al. (2021) who considered an isotropic damage model without tension-compression asymmetry. To ensure coercivity of the functionals, a damage-rate limitation (Allix, 2013) was enforced. Then, the incremental condensed free energy was selected as the function to be convexified. Schwarz et al. (2021) managed to solve the minimization problem with respect to the strain, but did not arrive at an explicit formula for the damage-minimization process. Rather, an approximation based on physical considerations - termed *emulated RVE* - was introduced and investigated.

1.3 Outline and original contributions

In this thesis, we contribute to the field of computational multiscale methods for short and long fiber reinforced polymers by addressing the research questions in Section 1.1. In particular, we present suitable microstructure generation tools for short and long fiber reinforced polymers, accounting for the important descriptors, i.e., the fiber volume fraction, the fiber length and orientation distributions as well as the fiber curvature. In addition, we introduce a novel class of phenomenological damage models reproducing damage softening behavior, to predict the damage evolution within fiber-reinforced composites.

The thesis is organized into the following chapters:

- **Chapter 2** gives a brief summary of the fundamentals of small-strain continuum mechanics, including kinematics, balance equations and generalized standard materials.

- In **Chapter 3**, we present the orientation corrected shaking (OCS) method for short fiber reinforced composites with almost planar fiber orientations. Therefore, we extend a two-step shaking algorithm by Li et al. (2022) to generate microstructures with periodic geometries and user-selected cell sizes. In addition, we provide information on the hidden orientation closure structure and present a shaking scheme to realize the desired fiber orientation tensor precisely. We apply the OCS method to an industrial PA66GF35 material with sandwich structure and compare the computed effective linear-elastic stiffness with experimental data, showing good agreement.
- To generate microstructures for long fiber reinforced polymers with high fiber volume fractions, we introduce the fused sequential addition and migration (fSAM) algorithm in **Chapter 4**. The flexibility of long fibers is taking into account by modeling the fibers as polygonal chains with straight cylindrical segments. As an alternative approach to the SAM algorithm for long fibers (Schneider, 2022), we present an iterative procedure where the connectivity constraint between adjacent segments is always satisfied. To do so, we discuss the equations governing the motion of a flexible fiber, and elaborate on an adapted gradient scheme to restrict the optimization iterates on the admissible configuration space of flexible fibers. The fSAM algorithm leads to an improved convergence behavior, increasing the efficiency of the microstructure generations as well as the packing limit with respect to the fiber volume fraction and the fiber aspect ratio.
- In **Chapter 5**, we extend the fSAM algorithm for hybrid materials, consisting of materials with different descriptors, e.g., varying fiber volume fractions. Therefore, we adjust the objective function to account for multiple subcells with individual desired descriptors. To assign and restrict each fiber to a single subcell, we extend the objective function with respect to box constraints. Depending on the manufacturing processes and materials, the interface between

different materials shows either strict layer separation or layer connection by interlocking fibers. For a user-selected interface, we provide different box constraint types, i.e., hard box constraint, where an entire fiber is restricted to its subcell, as well as soft box constraints, where only the midpoints of specific segments are enforced to be within their subcell. The fSAM algorithm for hybrid materials shows its capabilities to generate representative hybrid microstructures by comparing the mechanical behavior of generated CoDicoFRPs with experiments.

- The original fSAM algorithm accounts for fiber bending with a flexible description of the fibers. However, the extent of fiber curvature is neither assessed nor controlled, and thus may not be prescribed. To study the influence of the fiber curvature on the mechanical behavior of fiber-reinforced polymers, **Chapter 6** concerns the introduction of the deviation from straight curve (DSC) as suitable descriptor for the fiber curvature, as well as the integration of the novel measure within the fSAM algorithm. Due to the extension for the direct curvature control, the fSAM algorithm is capable of generating microstructures for wide ranges of degrees of fiber curvature. With these microstructures at hand, we investigate the differences in the linear-elastic material response, observing significant influence of the fiber curvature.
- To predict the damage behavior of fiber-reinforced polymers, we introduce a novel class of phenomenological isotropic damage models with softening behavior in **Chapter 7**. Starting with an isotropic damage model with rate limitation, we derive the convex envelope of the incremental condensed energy in a time-discretized setting explicitly. As a result, the damage state is characterized by a one-dimensional damage-distribution and the damage evolution follows the principals of optimal transport, which is the reason for the name *optimal transport* (OT) damage model. Due to the convexification process, the existence of a minimizer to mechanical boundary value

problems is ensured, even without non-local regularization techniques. Thus, the application of the OT damage model to the matrix material of fiber-reinforced polymers leads to mesh-independent results, making the novel damage class a suitable material model for multiscale damage prediction.

1.4 Notation, frequently used acronyms, symbols and operators

Notation

In this thesis, we use a direct tensor notation or matrix-vector notation with orthonormal basis $\{\boldsymbol{e}_1, \ldots, \boldsymbol{e}_{n_{\text{dim}}}\}$ with $n_{\text{dim}} \in \mathbb{N}$. We denote scalars by non-bold letters, e.g., a. In matrix-vector notation, vectors are represented with non-cursive bold lowercase letters, e.g., $\mathbf{a}$, and matrices with non-cursive uppercase letters, e.g., $\mathbf{A}$. In direct tensor notation, we denote the vectors with cursive bold lowercase letters, e.g., $\boldsymbol{a}$, tensors of second order with bold cursive uppercase letters, e.g., $\boldsymbol{A}$, and tensors of fourth order with blackboard bold uppercase letters, e.g., $\mathbb{A}$.

Acronyms

μCT	Micro computed tomography
ACG	Angular central Gaussian
CDI	Clausius-Duhem inequality
CoDicoFRP	Continuous-discontinuous fiber-reinforced polymer
CoFRP	Continuous fiber-reinforced polymer
DFG	German research foundation
DicoFRP	Discontinuous fiber-reinforced polymer

DSC	Deviation from straight curve
FFT	Fast Fourier transform
fSAM	Fused sequential addition and migration
GF	Glass fiber
GSM	Generalized standard material
KKT	Karush-Kuhn-Tucker
LFT	Long fiber reinforced thermoplastic
LFT-D	Long fiber reinforced thermoplastic direct process
MCM	Mechanical contraction method
MEC	Maximum entropy closure
OCS	Orientation corrected shaking
OT	Optimal transport
PA	Polyamide
PP	Polypropylene
RSA	Random sequential addition
RVE	Representative volume element
SAM	Sequential addition and migration

Sets

$\mathcal{B}, \mathcal{F}, \mathcal{M}, \mathcal{R}$	Riemannian manifolds
C, Q	Periodic rectangular unit cells
$\mathbb{N}$	Natural numbers
$\operatorname{null}(\mathbf{A})$	Null space of the matrix $\mathbf{A}$
$\mathbb{R}$	Real numbers
S^2	Unit sphere in $\mathbb{R}^3$
Sym	Symmetric second-order tensors
$T_{\boldsymbol{x}}\mathcal{M}$	Tangent space of the manifold $\mathcal{M}$ at the point $\boldsymbol{x}$
$\mathcal{Z}, \mathcal{Z}^*$	Banach space $\mathcal{Z}$ and its dual space $\mathcal{Z}^*$

Digits

$\mathbf{0}_{m_{\text{dim}} \times n_{\text{dim}}}$	Zero matrix with dimension $m_{\text{dim}} \times n_{\text{dim}}$
$\mathbf{1}_{n_{\text{dim}} \times n_{\text{dim}}}$	Identity matrix of size n_{dim}

Latin letters

a_1, a_2, a_3	Eigenvalues of the fiber orientation tensor of second order
$\boldsymbol{A}$	Volume-averaged fiber orientation tensor of second order
$\boldsymbol{A}_f$	Fiber orientation tensor of second order of a single fiber
$\mathbb{A}_{\langle l \rangle}$	Volume-averaged fiber orientation tensors of order l
$\mathbb{A}$	Volume-averaged fiber orientation tensor of fourth order
$\boldsymbol{c}$	Twice continuously differentiable curve
$\mathbb{C}$	Stiffness tensor
d	Damage variable
$d_{\min}$	Minimum distance between the fibers
D	Fiber diameter
$\mathcal{D}$	Dissipation distance
$\{\boldsymbol{e}_i\}_{i=1}^{n}$	Euclidean base vectors
E	Young's modulus
f	Damage degradation
$\mathbf{f}, \mathbf{q}$	Fiber coordinate vectors
G	Shear modulus
$\mathbf{G}$	Symmetric positive-definite metric matrix

h	Voxel-edge length
$\boldsymbol{I}$	Second-order identity tensor
$\mathbf{J}$	Jacobian matrix of the constraint function
$\bar{K}$	Volume-averaged deviation from straight curve
K_f	Deviation from straight curve of a single fiber
ℓ	Fiber segment length
L	Fiber length
L_{mean}	Mean fiber length
L_{total}	Total fiber length
m_{dim}, n_{dim}	Dimensions
n	Fiber segment number
N	Total number of fibers
$\boldsymbol{p}$	Fiber direction vector
$\mathbf{P}$	Null space matrix
$\hat{\mathbf{Q}}$	Normalization matrix for the starting point of a fiber
r_a	Fiber aspect ratio
$\mathbb{S}$	Compliance tensor
$\boldsymbol{u}$	Displacement vector
V	Volume
w	Optimization weight
$\boldsymbol{x}$, $\boldsymbol{X}$	Material points

Greek letters

ϵ	Termination criterion for the optimization procedure
$\boldsymbol{\epsilon}$	Permutation symbol

ε	Volume-specific moment of inertia of a spherocylinder
$\boldsymbol{\varepsilon}$	Infinitesimal strain tensor
κ	Local curvature vector
$\boldsymbol{\lambda}$	Vector of the Lagrangian multipliers
μ	Probability measure
ν	Poisson's ratio
ρ	Fiber length distribution
$\boldsymbol{\rho}$	Vector of the damage fractions
$\boldsymbol{\sigma}$	Cauchy stress tensor
φ, θ	Fiber angles
$\boldsymbol{\Phi}$	Vectorial constraint function
ϕ	Fiber volume fraction
$\boldsymbol{\phi}^{\text{mix}}$	Vector of the damage transition fractions
ψ	Helmholtz free energy density
ψ_{cond}	Condensed incremental energy density
Ψ	Dissipation potential

Operators

$\boldsymbol{a} \cdot \boldsymbol{b}$	$= a_i b_i$	Inner product of two vectors
$\boldsymbol{a} \times \boldsymbol{b}$	$\hat{=} \varepsilon_{ijk} a_j b_k$	Cross product of two vectors
$\boldsymbol{a} \odot \boldsymbol{b}$	$\hat{=} \operatorname{diag}(\boldsymbol{a})\, \boldsymbol{b}$	Elementary multiplication of two vectors
$\boldsymbol{a} \otimes \boldsymbol{b}$	$\hat{=} a_i b_j$	Dyadic product of two vectors
$\boldsymbol{a}^{\otimes n}$	$= \boldsymbol{a} \otimes \boldsymbol{a} \cdots \otimes \boldsymbol{a}$	Dyadic product n-times repeated
$[\boldsymbol{a}]_\times$	$\hat{=} \epsilon_{ikj} a_k$	Second-order skew-symmetric tensor with axial vector $\boldsymbol{a}$
$\|\boldsymbol{a}\|$	$= \sqrt{a_i a_i}$	Norm of vector

$\boldsymbol{A} \cdot \boldsymbol{B}$	$= A_{ij} B_{ij}$	Frobenius inner product of two second-order tensors
$\boldsymbol{A}\boldsymbol{b}$	$\hat{=} A_{ij} b_j$	Linear mapping of a vector by a second-order tensor
$\mathbb{A}[\boldsymbol{B}]$	$\hat{=} A_{ijkl} B_{kl}$	Linear mapping of a second-order tensor by a fourth-order tensor
$\mathbb{A}\left[\boldsymbol{B}_{\langle 3 \rangle}\right]$	$\hat{=} A_{ijkl} B_{jkl}$	Linear mapping of a third-order tensor by a fourth-order tensor
$\|\mathbb{A}\|$	$= \sqrt{A_{ijkl} A_{ijkl}}$	Norm of a fourth-order tensor
$\mathrm{tr}\,(\mathbb{A})$	$= A_{ijij}$	Trace of a fourth-order tensor
$\langle \blacksquare, \blacksquare \rangle_{\mathbb{R}^n}$		Scalar product on the Euclidean space $\mathbb{R}^n$
$\blacksquare^{\mathsf{T}}$		Transposition of a vector or a second-order tensor
$\blacksquare^{-1}$		Inverse of a second-order tensor
$\lfloor \blacksquare \rfloor$		Floor function
$\lceil \blacksquare \rceil$		Ceil function
$\langle \blacksquare \rangle$		Expectation of a random variable
$\langle \blacksquare \rangle_{[0,1]}$	$= \int_0^1 \blacksquare \, \mathrm{d}s$	Mean of a function on the unit interval
$\langle \blacksquare \rangle_+$	$= \max(0, \blacksquare)$	Macaulay bracket
$\dot{\blacksquare}$		Material time derivative
$\frac{\partial \blacksquare}{\partial \blacksquare}$		Partial differentiation
$\nabla_{\blacksquare} \blacksquare$		Gradient with respect to a given quantity
$\partial \blacksquare$		Subdifferential
$\mathrm{diag}(\blacksquare)$		Diagonal matrix
$\mathrm{epi}(\blacksquare)$		Epigraph of a function
$\exp_{\blacksquare}(\blacksquare)$		Exponential mapping

Chapter 2

Fundamentals of geometrically linear continuum mechanics

In this chapter, we briefly present the fundamentals of small-deformation continuum mechanics as the framework for the modeling approaches considered in this manuscript. We introduce the concept of a Cauchy-Boltzmann continuum and give an overview to the description of the kinematics. Additionally, we discuss the balance equations and present the fundamentals of generalized standard materials, representing a suitable modeling framework for materials with dissipative behavior. For more details, we refer to Liu (2002); Haupt (2002); Marsden and Hughes (2012); Bertram (2021).

2.1 Kinematics

Motion and placements The field of continuum mechanics studies the deformation of a *continuous* body $\mathcal{B}$ in $n_{\text{dim}} \in \{2, 3\}$ spatial dimensions, where each point of the (material) body $\mathcal{B}$ is called a material point. By describing the body $\mathcal{B}$ as Cauchy-Boltzmann continuum, a material point is modeled with n_{dim} translational degrees of freedom. For a given reference placement of the material body into the Euclidean space $\Omega_0 \subseteq \mathbb{R}^{n_{\text{dim}}}$ at the time $t = 0$, the current position of a material point at time $t \in [0, T]$ is

$$\boldsymbol{x} = \boldsymbol{\chi}(\boldsymbol{X}, t) \tag{2.1}$$

with the reference position of a material point $\boldsymbol{X} \in \Omega_0$. The function $\boldsymbol{\chi}$ is called *motion of a material body* (Marsden and Hughes, 2012), and is bijective, continuous, continuous differentiable and invertible (Bertram, 2021) for smooth material bodies without cracks. Its inverse

$$\boldsymbol{X} = \boldsymbol{\chi}^{-1}(\boldsymbol{x}, t) \tag{2.2}$$

maps from the current placement

$$\Omega_t = \{\boldsymbol{x} = \boldsymbol{\chi}(\boldsymbol{x}, t) \in \mathbb{R}^{n_{\text{dim}}} | \boldsymbol{X} \in \Omega_0\} \tag{2.3}$$

into the reference placement Ω_0. A tensorial property of a material point $\boldsymbol{\Lambda}$ may either be parametrized with the position of the material point in the reference placement $\boldsymbol{\Lambda}_L(\boldsymbol{X}, t)$ (*Lagrangian description*) or with its current position $\boldsymbol{\Lambda}_E(\boldsymbol{x}, t)$ (*Eulerian description*).

The material time derivative of a tensorial field $\boldsymbol{\Lambda}$ is defined as the partial time derivative for a fixed material point and designated by dot

$$\dot{\boldsymbol{\Lambda}} = \frac{\partial \boldsymbol{\Lambda}_L(\boldsymbol{X}, t)}{\partial t}. \tag{2.4}$$

With the definition of the material time derivative (2.4) at hand, we introduce the velocity of a material point

$$\boldsymbol{v} = \dot{\boldsymbol{x}} = \frac{\partial \boldsymbol{\chi}(\boldsymbol{X}, t)}{\partial t} \tag{2.5}$$

as well as its acceleration

$$\boldsymbol{a} = \ddot{\boldsymbol{x}} = \frac{\partial^2 \boldsymbol{\chi}(\boldsymbol{X}, t)}{\partial t^2} = \frac{\partial \boldsymbol{v}(\boldsymbol{X}, t)}{\partial t}. \tag{2.6}$$

If a tensorial field $\boldsymbol{\Lambda}$ is given in Eulerian description, the material derivative can be determined as

$$\dot{\boldsymbol{\Lambda}} = \frac{\partial \boldsymbol{\Lambda}_E(\boldsymbol{x}, t)}{\partial t} + \frac{\partial \boldsymbol{\Lambda}_E(\boldsymbol{x}, t)}{\partial \boldsymbol{x}} \boldsymbol{v}. \tag{2.7}$$

Deformation The deformation gradient

$$\boldsymbol{F}(\boldsymbol{X}, t) = \frac{\partial \boldsymbol{\chi}(\boldsymbol{X}, t)}{\partial \boldsymbol{X}} \tag{2.8}$$

maps infinitesimal line elements from the reference placement into the current placement

$$\mathrm{d}\boldsymbol{x} = \boldsymbol{F}(\boldsymbol{X}, t)\ \mathrm{d}\boldsymbol{X}. \tag{2.9}$$

To decompose the deformation gradient into a rotation-dependent and a rotation-independent term, we may apply the polar decomposition

$$\boldsymbol{F} = \boldsymbol{R}\boldsymbol{U} = \boldsymbol{V}\boldsymbol{R}, \tag{2.10}$$

where the orthogonal tensor $\boldsymbol{R}$ specifies the average rotation of a material point and the positive-definite tensors $\boldsymbol{U}$ and $\boldsymbol{V}$ describe the stretching of a material point. Thus, the *right Cauchy-Green tensor*

$$\boldsymbol{C} = \boldsymbol{F}^{\mathsf{T}}\boldsymbol{F} = \boldsymbol{U}^{\mathsf{T}}\boldsymbol{U} \tag{2.11}$$

turns out to be rotation-independent. By means of the right Cauchy-Green tensor $\boldsymbol{C}$, the generalized strain tensors (Seth, 1961; Hill, 1968) may be introduced, which are zero with respect to the reference placement. A commonly used representative of the generalized strain tensor is the Green–St-Venant strain tensor

$$\boldsymbol{E} = \frac{1}{2}(\boldsymbol{C} - \boldsymbol{I}). \tag{2.12}$$

Simplification for small deformations To assess the magnitude of the deformation, we first introduce the displacement field in a Lagrangian setting

$$\boldsymbol{u}(\boldsymbol{X},t) = \boldsymbol{\chi}(\boldsymbol{X},t) - \boldsymbol{X}, \tag{2.13}$$

measuring the difference between the reference placement and the current placement. Based on the displacement field (2.13), the (material) displacement gradient $\boldsymbol{H}$ is defined via

$$\boldsymbol{H}(\boldsymbol{X},t) = \frac{\partial \boldsymbol{u}(\boldsymbol{X},t)}{\partial \boldsymbol{X}} = \boldsymbol{F}(\boldsymbol{X},t) - \boldsymbol{I}. \tag{2.14}$$

Then, we use the norm of the displacement gradient to define the range of a geometrically linear theory (Bertram, 2021)

$$\|\boldsymbol{H}(\boldsymbol{X},t)\| \ll 1. \tag{2.15}$$

In case of small deformations, the deformation gradient is approximated by the relation

$$\boldsymbol{F}(\boldsymbol{X},t) \approx \boldsymbol{I}, \tag{2.16}$$

i.e., the line elements $\mathrm{d}\boldsymbol{x}$ and $\mathrm{d}\boldsymbol{X}$ are approximately equal. If the displacement field $\boldsymbol{u}$ is also small, the distinction between the Lagrangian and the Eulerian description becomes negligible. For the theory of small deformations, all generalized strain tensors coincide and are given by the infinitesimal strain tensor

$$\boldsymbol{\varepsilon}(\boldsymbol{X},t) = \frac{1}{2}\left(\boldsymbol{H}(\boldsymbol{X},t) + \boldsymbol{H}(\boldsymbol{X},t)^{\mathsf{T}}\right), \tag{2.17}$$

i.e., the symmetric part of the displacement gradient $\boldsymbol{H}(\boldsymbol{X},t)$.

2.2 Balance equations

General balance equation The thermomechanical behavior of a body $\mathcal{B}$ is governed by physical laws, which are typically formulated as *balance equations* (Liu, 2002; Papenfuß, 2020). For a placement Ω_t, the volume-integral of the tensorial field quantity $\boldsymbol{\Lambda}$ over any bounded regular subregion of the material body $P_t \subset \Omega_t$ is given as

$$\int_{P_t} \boldsymbol{\Lambda}\left(\boldsymbol{x}, t\right) \,\mathrm{d}V. \tag{2.18}$$

The general balance equation postulates that the change of the volume-integral of the field quantity $\boldsymbol{\Lambda}$ is composed of the internal production $\boldsymbol{p}_{\boldsymbol{\Lambda}}$ and the external supply $\boldsymbol{s}_{\boldsymbol{\Lambda}}$ of the field quantity over the volume P_t, as well as of the non-convective flux $\boldsymbol{q}_{\boldsymbol{\Lambda}}$ of the field quantity over the boundary ∂P_t. Thus, the general balance equation may be formulated mathematically in the integral form

$$\frac{\mathrm{d}}{\mathrm{d}t}\int_{P_t} \boldsymbol{\Lambda}\left(\boldsymbol{x}, t\right) \,\mathrm{d}V = \int_{P_t} \boldsymbol{p}_{\boldsymbol{\Lambda}}\left(\boldsymbol{x}, t\right) + \boldsymbol{s}_{\boldsymbol{\Lambda}}\left(\boldsymbol{x}, t\right) \,\mathrm{d}V + \int_{\partial P_t} \boldsymbol{q}_{\boldsymbol{\Lambda}}\left(\boldsymbol{x}, t\right) \cdot \boldsymbol{n} \,\mathrm{d}A, \tag{2.19}$$

where $\mathrm{d}A$ denotes an infinitesimal area element of the boundary ∂P_t and $\boldsymbol{n}$ is the normal vector corresponding to the infinitesimal area element $\mathrm{d}A$. The tensors $\boldsymbol{p}_{\boldsymbol{\Lambda}}$ and $\boldsymbol{s}_{\boldsymbol{\Lambda}}$ have the same tensor order as the field quantity $\boldsymbol{\Lambda}$, whereas the non-convective flux $\boldsymbol{q}_{\boldsymbol{\Lambda}}$ is one tensor order higher.

For regular points, i.e., where the field quantity $\boldsymbol{\Lambda}$ is smooth, the integral form (2.19) may be transformed in a local form by applying Reynold's transport theorem and the divergence theorem (Liu, 2002)

$$\frac{\partial \boldsymbol{\Lambda}\left(\boldsymbol{x}, t\right)}{\partial t} + \mathrm{div}\left(\boldsymbol{\Lambda}\left(\boldsymbol{x}, t\right) \otimes \boldsymbol{v}\left(\boldsymbol{x}, t\right)\right) = \boldsymbol{p}_{\boldsymbol{\Lambda}}\left(\boldsymbol{x}, t\right) + \boldsymbol{s}_{\boldsymbol{\Lambda}}\left(\boldsymbol{x}, t\right) + \mathrm{div}\left(\boldsymbol{q}_{\boldsymbol{\Lambda}}\left(\boldsymbol{x}, t\right)\right). \tag{2.20}$$

For the sake of clarity, we will omit explicit variable dependencies for the following specific balance equations. All quantities refer to the Eulerian description.

Balance of mass For the mass balance, the field quantity corresponds to the mass density $\boldsymbol{\Lambda} \hat{=} \varrho$, and we obtain the local form of the balance equation

$$\frac{\partial \varrho}{\partial t} + \operatorname{div}(\varrho \boldsymbol{v}) = 0, \tag{2.21}$$

where the production p_ϱ, the supply s_ϱ and the flux $\boldsymbol{q}_\varrho$ are zero. For a given deformation gradient $\boldsymbol{F}$, the mass density with respect to the current placement is computed as $\varrho = \det(\boldsymbol{F})^{-1}\varrho_0$ (Liu, 2002), where ϱ_0 denotes the mass density of the reference placement. Thus, the mass density is approximately constant in time $\varrho = (1 - \operatorname{tr}(\boldsymbol{\varepsilon}))\varrho_0 \approx \varrho_0$ for small deformations.

Balance of linear momentum The balanced field quantity is given by the linear momentum density $\boldsymbol{\Lambda} = \varrho \boldsymbol{v}$. As the linear momentum is a conserved quantity, the production term is zero. Furthermore, the supply corresponds to the volume force density $\varrho \boldsymbol{b}$ and the flux is characterized by the Cauchy stress tensor $\boldsymbol{\sigma}$. Inserting these quantities into the general balance equation (2.20) yields the balance of linear momentum

$$\frac{\partial \varrho \boldsymbol{v}}{\partial t} + \operatorname{div}(\varrho \boldsymbol{v} \otimes \boldsymbol{v}) = \varrho \boldsymbol{b} + \operatorname{div}(\boldsymbol{\sigma}), \tag{2.22}$$

which simplifies to

$$\varrho \dot{\boldsymbol{v}} = \varrho \boldsymbol{b} + \operatorname{div}(\boldsymbol{\sigma}), \tag{2.23}$$

taking the balance of mass (2.21) into account.

Balance of angular momentum For a Cauchy-Boltzmann continuum, i.e., a non-polar material without rotational degrees of freedom at the material points, the local formulation of the balance of angular momentum

is given as

$$\boldsymbol{\sigma} = \boldsymbol{\sigma}^{\mathsf{T}}, \tag{2.24}$$

requiring the symmetry of the Cauchy stress tensor.

Balance of energy The balance of total energy (first law of thermodynamics) describes the change of the volume-integral of the volume-specific total energy $\boldsymbol{\Lambda} \hat{=} \varrho \boldsymbol{v} \cdot \boldsymbol{v}/2 + \varrho e$, which is comprised by the sum of the kinetic energy and the internal energy. Due to the conservation of the total energy, the production term is zero. The supply consists of the volume-specific heat source ϱw and the power of the volume forces $\varrho \boldsymbol{b} \cdot \boldsymbol{v}$. As the flux term is the sum of the negative heat flux $-\boldsymbol{q}$ and the power of the surface forces $\boldsymbol{\sigma}^{\mathsf{T}} \boldsymbol{v}$, the local form of the balance of total energy reads

$$\varrho \dot{e} + \frac{\varrho}{2} \left(\boldsymbol{v} \cdot \boldsymbol{v} \right)^{\cdot} = \varrho w + \varrho \boldsymbol{b} \cdot \boldsymbol{v} - \operatorname{div} \left(\boldsymbol{q} \right) + \operatorname{div} \left(\boldsymbol{\sigma}^{\mathsf{T}} \boldsymbol{v} \right) \tag{2.25}$$

under the assumption of the local balance of mass.

To condense the balance of total energy (2.25) to the balance of internal energy, we subtract the scalar product of the velocity vector and the balance of linear momentum (2.23) from the balance of total energy (2.25)

$$\varrho \dot{e} = \varrho w - \operatorname{div} \left(\boldsymbol{q} \right) + \boldsymbol{\sigma} \cdot \boldsymbol{D}. \tag{2.26}$$

The tensor $\boldsymbol{D}$ denotes the strain-rate tensor

$$\boldsymbol{D} = \frac{1}{2} \left(\boldsymbol{L} + \boldsymbol{L}^{\mathsf{T}} \right) \quad \text{with} \quad \boldsymbol{L} = \dot{\boldsymbol{F}} \boldsymbol{F}^{-1}, \tag{2.27}$$

i.e., the symmetric part of the velocity gradient $\boldsymbol{L}$. For small deformations, the relation

$$\boldsymbol{\sigma} \cdot \boldsymbol{D} \approx \boldsymbol{\sigma} \cdot \dot{\boldsymbol{\varepsilon}} \tag{2.28}$$

holds.

Balance of entropy The local form of the balance of entropy reads (Coleman and Noll, 1963)

$$\varrho\dot{\eta} = \frac{\varrho w}{\theta} - \operatorname{div}\left(\frac{\boldsymbol{q}}{\theta}\right) + \varrho p_\eta \tag{2.29}$$

with the volume-specific entropy density $\boldsymbol{\Lambda}\hat{=}\varrho\eta$ as the balanced field quantity, the supply $\varrho w/\theta$, the flux $-\boldsymbol{q}/\theta$ and the entropy production ϱp_η. According to the second law of thermodynamics, the entropy production density has to be non-negative

$$p_\eta \geq 0 \tag{2.30}$$

for all thermomechanical processes.

Starting with the balance of entropy (2.29), we eliminate the heat source w with the balance of internal energy (2.26) and take the second law of thermodynamics (2.30) into account to derive the Clausius-Duhem inequality (CDI), or dissipation inequality, for small deformations

$$\frac{1}{\varrho}\boldsymbol{\sigma}\cdot\dot{\boldsymbol{\varepsilon}} + \theta\dot{\eta} - \dot{e} - \frac{\nabla\theta\cdot\boldsymbol{q}}{\varrho\,\theta} \geq 0. \tag{2.31}$$

Using the Legendre-Transformation $e = \eta\,\theta + \psi/\varrho$ with the volume-specific Helmholtz free energy ψ, yields the reformulated small-deformation CDI

$$\frac{1}{\varrho}\boldsymbol{\sigma}\cdot\dot{\boldsymbol{\varepsilon}} - \eta\dot{\theta} - \frac{1}{\varrho}\dot{\psi} - \frac{\nabla\theta\cdot\boldsymbol{q}}{\varrho\,\theta} \geq 0. \tag{2.32}$$

For an isothermal setting, the small-deformation CDI shortens to

$$\boldsymbol{\sigma}\cdot\dot{\boldsymbol{\varepsilon}} - \dot{\psi} \geq 0. \tag{2.33}$$

2.3 Generalized standard materials

Generalized standard materials (GSMs) (Halphen and Nguyen, 1975; Germain et al., 1983; Lahellec and Suquet, 2007) are a widely used framework for thermodynamically consistent material modeling with dissipative behavior. In a small-deformation and isothermal setting, besides the infinitesimal strain tensor $\boldsymbol{\varepsilon} \in \mathrm{Sym}\,(n_{\mathrm{dim}})$ with the dimension $n_{\mathrm{dim}} = 2, 3$ four more building blocks are elementary:

1. The *internal variables* $\boldsymbol{z} \in \mathcal{Z}$, defined on the Banach space $\mathcal{Z}$, i.e., a completely normed vector space, complementing the strain tensor $\boldsymbol{\varepsilon}$ to determine the material state.
2. The initial condition of the internal variables denoted with $\boldsymbol{z}_0 \in \mathcal{Z}$.
3. The volume-specific *Helmholtz free energy*

$$\psi : \mathrm{Sym}\,(n_{\mathrm{dim}}) \times \mathcal{Z} \to \mathbb{R}_{\geq 0}, \quad (\boldsymbol{\varepsilon}, \boldsymbol{z}) \to \psi\,(\boldsymbol{\varepsilon}, \boldsymbol{z})\,, \tag{2.34}$$

   continuously differentiable with respect to its arguments.
4. The non-negative, lower semicontinuous and convex *dissipation potential*

$$\Psi : \mathcal{Z} \to \mathbb{R}_{\geq 0} \cup \{+\infty\}, \quad \dot{\boldsymbol{z}} \to \Psi\,(\dot{\boldsymbol{z}}) \tag{2.35}$$

   with the material time derivative of the internal variables $\dot{\boldsymbol{z}}$ as its argument. Furthermore, the dissipation potential is required to satisfy the condition $\Psi(\mathbf{0}) = 0$. A GSM is rate-independent only if the dissipation potential is positively homogeneous of degree one (Carstensen et al., 2002; Mielke and Roubíček, 2015).

To investigate the implications of the CDI on the formulation of GSMs, we insert the material time derivative of the free energy

$$\dot{\psi}\,(\boldsymbol{\varepsilon}, \boldsymbol{z}) = \frac{\partial \psi\,(\boldsymbol{\varepsilon}, \boldsymbol{z})}{\partial \boldsymbol{\varepsilon}} \cdot \dot{\boldsymbol{\varepsilon}} + \frac{\partial \psi\,(\boldsymbol{\varepsilon}, \boldsymbol{z})}{\partial \boldsymbol{z}}\,[\dot{\boldsymbol{z}}] \tag{2.36}$$

into the isothermal CDI for small strains (2.33) and obtain the relation

$$\left[\boldsymbol{\sigma} - \frac{\partial \psi\left(\boldsymbol{\varepsilon}, \boldsymbol{z}\right)}{\partial \boldsymbol{\varepsilon}}\right] \cdot \dot{\boldsymbol{\varepsilon}} - \frac{\partial \psi\left(\boldsymbol{\varepsilon}, \boldsymbol{z}\right)}{\partial \boldsymbol{z}}\left[\dot{\boldsymbol{z}}\right] \geq 0. \tag{2.37}$$

In Equations (2.36) and (2.37), the derivative $\partial \psi\left(\boldsymbol{\varepsilon}, \boldsymbol{z}\right) / \partial \boldsymbol{z} \in \mathcal{Z}^*$ is an element of the continuous dual space $\mathcal{Z}^*$ of the Banach space $\mathcal{Z}$, and the linear functional

$$\frac{\partial \psi\left(\boldsymbol{\varepsilon}, \boldsymbol{z}\right)}{\partial \boldsymbol{z}} : \mathcal{Z} \to \mathbb{R}, \quad \dot{\boldsymbol{z}} \to \frac{\partial \psi\left(\boldsymbol{\varepsilon}, \boldsymbol{z}\right)}{\partial \boldsymbol{z}}\left[\dot{\boldsymbol{z}}\right], \tag{2.38}$$

assigns a real number to any element $\dot{z} \in \mathcal{Z}$.

By requiring that the CDI (2.37) is satisfied, we arrive at the potential relation for the stress

$$\boldsymbol{\sigma} = \frac{\partial \psi\left(\boldsymbol{\varepsilon}, \boldsymbol{z}\right)}{\partial \boldsymbol{\varepsilon}} \tag{2.39}$$

and the residual inequality

$$-\frac{\partial \psi\left(\boldsymbol{\varepsilon}, \boldsymbol{z}\right)}{\partial \boldsymbol{z}}\left[\dot{\boldsymbol{z}}\right] \geq 0 \quad \forall \dot{\boldsymbol{z}} \tag{2.40}$$

which states that the mechanical dissipation

$$D_{\text{mech}} \equiv -\frac{\partial \psi\left(\boldsymbol{\varepsilon}, \boldsymbol{z}\right)}{\partial \boldsymbol{z}}\left[\dot{\boldsymbol{z}}\right], \tag{2.41}$$

is non-negative. Thus, the *thermodynamical driving force*

$$\boldsymbol{\beta} = -\frac{\partial \psi\left(\boldsymbol{\varepsilon}, \boldsymbol{z}\right)}{\partial \boldsymbol{z}} \in \mathcal{Z}^* \tag{2.42}$$

is governed by Biot's equation (Biot, 1965)

$$-\frac{\partial \psi\left(\boldsymbol{\varepsilon}, \boldsymbol{z}\right)}{\partial \boldsymbol{z}} \in \partial \Psi\left(\dot{\boldsymbol{z}}\right). \tag{2.43}$$

The subdifferential of the convex dissipation potential $\partial\Psi$ is defined via

$$\partial\Psi(\boldsymbol{\gamma}) = \{\boldsymbol{\beta} \in \mathcal{Z}^* \mid \Psi(\tilde{\boldsymbol{\gamma}}) - \Psi(\boldsymbol{\gamma}) \geq \boldsymbol{\beta}[\tilde{\boldsymbol{\gamma}} - \boldsymbol{\gamma}] \quad \forall \tilde{\boldsymbol{\gamma}} \in \mathcal{Z}\}, \tag{2.44}$$

see Rockafellar (1970). By evaluating Equation (2.44) for $\boldsymbol{\gamma} = \dot{\boldsymbol{z}}, \tilde{\boldsymbol{\gamma}} = \mathbf{0}$ and using the constraints on the dissipation potential $\Psi(\mathbf{0}) = 0$ and $\Psi \geq 0$, we obtain

$$D_{\text{mech}} = \boldsymbol{\beta}[\dot{\boldsymbol{z}}] = -\frac{\partial\psi(\boldsymbol{\varepsilon}, \boldsymbol{z})}{\partial \boldsymbol{z}}[\dot{\boldsymbol{z}}] \geq \Psi(\dot{\boldsymbol{z}}) \geq 0, \quad \forall \dot{\boldsymbol{z}}, \tag{2.45}$$

demonstrating that the residual inequality (2.40) holds. As the formulation of GSMs inherently satisfies the CDI, the modeling approach guarantees thermodynamical consistency provided the previously defined properties of the building blocks hold, regardless of the specific selection for the internal variables, the Helmholtz free energy and the dissipation potential.

Chapter 3

Microstructure generation of short fiber reinforced composites[1]

3.1 Introduction

In this chapter, we introduce the Orientation Corrected Shaking (OCS) method based on the two-step shaking algorithm for almost planar fiber orientation states by Li et al. (2022). We address two main objectives for the generated microstructures. First, we aim to minimize the necessary representative volume element size to reduce the time effort for the microstructure generation and computational homogenization. Secondly, we require an accurate realization of the fiber volume fraction, as well as the fiber length and orientation distributions.

For this purpose, we concern three restrictions of the algorithm provided by Li et al. (2022). First of all, the generated microstructures are fixed to an intrinsically calculated size of the rectangular unit cell. In particular only thin plate shapes are obtained. However, to investigate the representativity of different unit cell sizes, the size of the rectangular volume elements has to be chosen in an arbitrary way. Hence, we adapt the

[1] This chapter is based on the Sections 1.2 and 2 to 5 of the publication "An orientation corrected shaking method for the microstructure generation of short fiber-reinforced composites with almost planar fiber orientation" (Lauff et al., 2023).

initial deterministic fiber placement to a modular procedure accounting for the user-selected dimensions of the unit cell.

The second restriction concerns the non-periodicity of the generated microstructures. In previous studies (Kanit et al., 2003; Sab and Nedjar, 2005; Schneider, 2022) it turns out that non-periodic geometries may adversely influence the representativity of a unit cell due to increased boundary condition artifacts. To reduce the necessary RVE size, we extend the algorithmic implementation, e.g., the inter-fiber overlap detection, to a periodic description of the geometry.

Last but not least, the fiber orientation state is not represented sufficiently by the original algorithm. Actually, the source of this restriction is twofold. First, Li et al. (2022) control the fiber orientation state via fiber orientation tensors of second order. However, for computing the effective elastic properties accurately the fiber orientation tensor of fourth order is mandatory, see Müller and Böhlke (2016). The second cause concerns the shaking procedure of the fibers. Especially for increasing fiber alignment and volume fraction, deviations in the realized fiber orientation tensor of second order are obtained. To handle the latter two limitations, we provide an appropriate shaking strategy. More precisely, we uncover the hidden closure approximation of the shaking procedure. With this insight at hand, a semi-analytic estimation of the shaking parameters is identified and implemented. Moreover, we introduce the procedure of single orientation shaking to realize the fiber orientation tensor of fourth order accurately.

This chapter is organized as follows. Section 3.2 provides the terminology for short fiber reinforced composites and details on the implementation of the fiber length distribution, as well as the inter-fiber overlap detection. In Section 3.3, we introduce the OCS method and describe the required extensions of the original two-step shaking algorithm (Li et al., 2022). Computational investigations on the implemented OCS method are conducted in Section 3.4. After studying the effect of the

semi-analytic parameter estimation and the procedure of single orientation shaking, we discuss the necessary resolution and RVE size. Subsequently, the computed effective stiffness is compared to microstructures generated by the SAM algorithm based on the exact and the maximum entropy closure. Moreover, we apply the OCS method to an industrial PA66GF35 material and compare the results to experimental data, as well as to microstructures generated by the SAM algorithm. The Appendix A provides details for the semi-analytic estimation of the shaking parameters.

3.2 Microstructure generation for short fiber reinforced composites

3.2.1 Description of short fiber reinforced composites

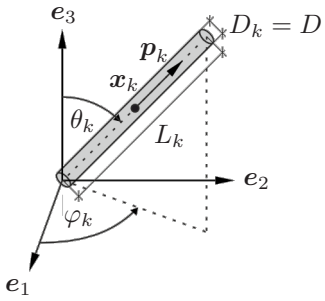


Figure 3.1: Description of a short fiber. Figure adapted from Figure 1 of Lauff et al. (2023).

We consider a rectangular cell $Q = [0, Q_1] \times [0, Q_2] \times [0, Q_3]$ including N right circular cylindrical fibers in a non-penetrating fiber arrangement.

The k^{th}-fiber is characterized by the length L_k, the diameter D_k, the midpoint $\boldsymbol{x}_k \in Q$ and the direction $\boldsymbol{p}_k \in S^2$, see Figure 3.1. We assume uniform fiber diameters $D = D_k$, but varying fiber lengths following a given fiber length distribution $\rho(L_k)$. For short fiber reinforced composites, the Weibull distribution (Weibull, 1951) is often used (Bernasconi et al., 2008; Hessman et al., 2021; Fu et al., 1999). Alternatively, the unit vector $\boldsymbol{p}_k$ may be represented by the angles θ_k and φ_k:

$$\boldsymbol{p}_k \mathrel{\hat{=}} \begin{bmatrix} \sin(\theta_k)\cos(\varphi_k) \\ \sin(\theta_k)\sin(\varphi_k) \\ \cos(\theta_k) \end{bmatrix}, \quad \theta_k, \varphi_k \in \mathbb{R}. \tag{3.1}$$

Notice that the angles θ_k and φ_k may be parameterized on the domain $[0, 2\pi)$ equivalently by accounting for the periodic characteristics of the trigonometrical functions throughout the article.
In a non-overlapping configuration, the fiber volume fraction ϕ computes as

$$\phi = \frac{\pi D^2}{4 Q_1 Q_2 Q_3} L_{\text{total}} \tag{3.2}$$

with the total length

$$L_{\text{total}} = \sum_{k=1}^{N} L_k. \tag{3.3}$$

In this work, fiber orientation tensors are used as a compact characteristic of the fiber orientation distribution, see Kanatani (1984); Advani and Tucker III (1987). Due to the finite number of fibers in a generated microstructure and the varying fiber lengths, the volume-weighted fiber orientation tensors of order l compute as

$$\mathbb{A}_{\langle l \rangle} = \frac{1}{L_{\text{total}}} \sum_{k=1}^{N} L_k \, \boldsymbol{p}_k^{\otimes l}. \tag{3.4}$$

For fiber-reinforced composites, micro-computed tomography is a convenient tool to estimate the fiber orientation tensors (Hessman et al., 2019; Krause et al., 2010; Wirjadi et al., 2016). By applying mean field homogenization methods (Dray et al., 2007; Müller and Böhlke, 2016; Bauer and Böhlke, 2022a), it turns out that the effective properties can be approximated by functions of the first two moment tensors. For this reason, typically the second- and fourth-order tensors $\boldsymbol{A}$ and $\mathbb{A}$ are considered.

3.2.2 Prescribing the fiber length distribution

In this work, we use the Weibull distribution to describe the fiber lengths within the generated microstructures. It is defined via the density function (Papoulis and Pillai, 2002, Equations (4-43))

$$\rho_{\lambda,\beta}(L) = \frac{\beta}{\lambda}\left(\frac{L}{\lambda}\right)^{\beta-1} e^{-(L/\lambda)^{\beta}}, \quad L, \lambda, \beta > 0, \tag{3.5}$$

with the scale parameter λ and the shape parameter β. According to Mehta and Schneider (2022) the Weibull parameters λ and β may be computed from given values for the volume-weighted mean m and standard deviation s. With this notation at hand, we assume the length L_k of the k^{th}-fiber to follow the corresponding Weibull distribution, i.e.,

$$L_k \sim \text{Weibull}(m, s). \tag{3.6}$$

When generating microstructures, it is necessary to *sample* the fiber lengths with a specific sampling scheme. As result of the finite number of fibers, the selected sampling scheme may lead to an inaccurate fiber length distribution, e.g., characterized by a large deviation of the realized statistical moments compared to the moments of the distribution. Mehta and Schneider (2022) study the introduced error of sampling with the classical Monte Carlo approach (Hammersley and Handscomb, 1964)

and with scrambled or non-scrambled Sobol sequences (Sobol, 1967; 1976). Due to the smallest error for scrambled Sobol sequences, we use this scheme for the following investigations.

We terminate the sampling of fiber lengths whenever the prescribed volume fraction ϕ is exceeded. To match the targeted fiber volume fraction exactly, we rescale each fiber length individually with

$$L_k \leftarrow L_k \frac{4Q_1Q_2Q_3\phi}{\pi D^2 L_{\text{total}}}. \tag{3.7}$$

3.2.3 Inter-fiber collision checks for periodic boundary conditions

To realize a non-penetrating fiber arrangement, it is necessary to compute the inter-fiber distances repeatedly, leading to a significant influence on the computational effort. To decrease the runtime, during the computation of the inter-fiber distances we model each fiber as a spherocylinder (Williams and Philipse, 2003), i.e., a half sphere is attached to each end of the cylinder. Two spherocylinders intersect precisely if the smallest distance between the center lines of the fibers is smaller than the diameter D. For the numerical computation of the effective elastic properties with voxel-based grids, usually a minimum distance d_{min} between the fibers is enforced to avoid excessively high stresses when fibers are too close (Pan et al., 2008; Böhm et al., 2002). To realize the minimum distance, the diameter of the fibers is increased only for the collision detection

$$D \leftarrow D + d_{\text{min}}. \tag{3.8}$$

Notice that a minimum distance between the fibers leads to an increased runtime due to the artificially higher volume fraction during the collision checks. For instance, the volume fraction increases by 44% for a minimum distance of 20% of the fiber diameter.

For computing the smallest distance between the center lines of two fibers, we rely on the modification of the Vega-Lago algorithm (Vega and Lago, 1994) introduced by Pournin et al. (2005). For an efficient implementation of periodic boundary conditions, we use the minimum image convention strategy, commonly employed in molecular dynamics simulations, see, e.g., Deiters (2013). More precisely, for two particles only the distance between their closest periodic realizations is computed. For cylindrical fibers, an adaption of the scheme is presented, e.g., by Schneider (2022), in case the fiber lengths are shorter than half of the smallest edge length. Considering the k^{th}- and the j^{th}-fiber, the three components $(i = 1, 2, 3)$ of one of the fibers' midpoints are corrected only for the collision detection with

$$x_k^i \leftarrow \left\{ \begin{array}{ll} x_k^i - Q_i, & \text{if } x_k^i - x_j^i > Q_i/2 \\ x_k^i + Q_i, & \text{if } x_k^i - x_j^i < Q_i/2 \\ x_k^i, & \text{else} \end{array} \right\} \qquad \text{provided} \quad L_j, L_k < \min\left(Q_1, Q_2, Q_3\right)/2. \tag{3.9}$$

In case of a fiber length distribution with a high variance for strongly anisotropic cells, condition (3.9) may not be satisfied, as the fibers are too long. A simple workaround to treat longer fibers, introduced by Mehta and Schneider (2022), proceeds by a divide and conquer strategy with respect to the fiber length.

Moreover, whenever a fiber exceeds a complete edge length, it is necessary to check self-intersection to ensure a non-overlapping configuration. We use the self-intersection scheme provided by Mehta and Schneider (2022), which is activated for the k^{th}-fiber if the condition

$$L_k p_k^i > Q_i - D \quad \text{with} \quad i = 1, 2, 3 \tag{3.10}$$

is fulfilled for at least one of the three components.

3.3 The orientation corrected shaking method

3.3.1 The initial step

We assume the second-order fiber orientation tensor $\boldsymbol{A}$ to be given in diagonal and ordered form

$$\boldsymbol{A} \hat{=} \operatorname{diag}(a_1, a_2, a_3) \quad \text{with} \quad a_1 \geq a_2 \geq a_3. \tag{3.11}$$

A symmetric second order fiber orientation tensor may be brought into the form of Equation (3.11) by an eigendecomposition and a rotation into the eigenbasis.

The two-step shaking method (Li et al., 2022) assumes the third eigenvalue a_3 to be small. Therefore, an initial fiber orientation tensor $\widetilde{\boldsymbol{A}}$ is introduced which attains the form

$$\widetilde{\boldsymbol{A}} \hat{=} \operatorname{diag}(\widetilde{a}_1, \widetilde{a}_2, 0) \quad \text{with} \quad \widetilde{a}_i = \frac{a_i}{a_1 + a_2}, \quad i = 1, 2. \tag{3.12}$$

The presence of non-zero third component a_3 in the original fiber orientation tensor $\boldsymbol{A}$ (3.11) will be accounted for in the shaking step.

In the initial step, the initial fiber orientation tensor $\widetilde{a}_1$ is realized by a deterministic arrangement of the fibers. According to Li et al. (2022), the microstructure is divided into sublayers with aligned fibers. If the condition $\widetilde{a}_1 < 0.6$ holds, a division into two sublayers will be used, where the standard unit vectors $\boldsymbol{e}_1$ and $\boldsymbol{e}_2$ represent the fiber directions of the sublayers. Alternatively, the directions are represented with the angles

$$\widetilde{\theta}_1 = \frac{\pi}{2}, \widetilde{\varphi}_1 = 0 \quad \text{and} \quad \widetilde{\theta}_2 = \frac{\pi}{2}, \widetilde{\varphi}_2 = \frac{\pi}{2}. \tag{3.13}$$

To fulfill the initial fiber orientation tensor $\widetilde{\boldsymbol{A}}$, the sublayers with fibers in $\boldsymbol{e}_1$- or $\boldsymbol{e}_2$-direction are filled with fibers up to a volume fraction

$$\widetilde{\phi}_1 = 2\,\widetilde{a}_1\phi \quad \text{or} \quad \widetilde{\phi}_2 = 2\,(1-\widetilde{a}_1)\phi. \tag{3.14}$$

For stronger alignment, i.e., under the condition $\widetilde{a}_1 \geq 0.6$, the unit cell is divided into three sublayers to reduce the difference of the volume-fraction between the sublayers. Therefore, the fibers are placed in two sublayers with direction $\boldsymbol{e}_1$ and in one sublayer with direction $\boldsymbol{e}_2$. The fiber volume fractions of the sublayers compute as

$$\widetilde{\phi}_1 = 1.5\,\widetilde{a}_1\phi, \quad \widetilde{\phi}_2 = 3\,(1-\widetilde{a}_1)\phi. \tag{3.15}$$

In the algorithm introduced by Li et al. (2022), the size of the initial filling space depends on the mean length of the fibers $L_{\text{mean}} = L_{\text{total}}/N$, the first eigenvalue of the fiber orientation tensor in the initial arrangement $\widetilde{a}_1$, the fiber volume fraction ϕ and the diameter of the fibers D. Furthermore, hard boundary conditions are considered leading to a low fiber content close to the boundaries. To overcome this problem, Li et al. (2022) choose larger dimensions $Q_{1,2}$ for the initial space than for the shaking step. Computational evidence suggests (Kanit et al., 2003; Sab and Nedjar, 2005; Schneider, 2022) that using periodic microstructures and periodic boundary conditions for computational homogenization minimizes boundary condition artifacts. For this reason, we consider an extension of the original algorithm to generate periodic unit cells. Additionally, as fibers can pass the boundaries without restriction, we use the same cell dimensions for the initial step and for the shaking step.

A second extension concerns the use of more than two or three sublayers, respectively. Indeed, we consider a repetition of the construction, compare Equations (3.14) and (3.15). In this way, we may investigate representativity of the structures in direction $\boldsymbol{e}_3$, as well. Therefore, the structure of $n_{\text{sub}} = 2$ (or $n_{\text{sub}} = 3$) layers is repeated n_{layer}-times until the

prescribed height is achieved. The height of the single sublayers h_{sub} is calculated with

$$c = \sqrt{\frac{\pi D^2}{2\,\widetilde{\phi}_1}}, \quad n_{\text{layer}} = \left\lfloor \max\left(\frac{Q_3}{n_{\text{sub}} c}, 1\right)\right\rfloor \quad \text{and} \quad h_{\text{sub}} = \frac{Q_3}{n_{\text{sub}} n_{\text{layer}}}, \tag{3.16}$$

where the bracket type $\lfloor\cdot\rfloor$ denotes the floor function.

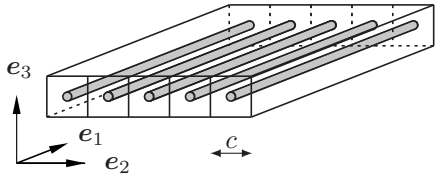


Figure 3.2: Sublayer with a single continuous fiber per cell, compare (Li et al., 2022, Fig. 4(a)). Figure adapted from Figure 2 of Lauff et al. (2023).

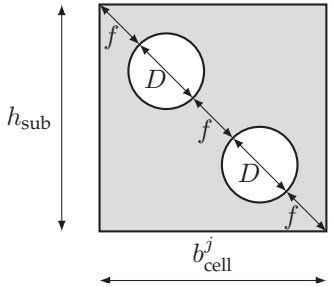


Figure 3.3: Cross-section of a cell with two fibers. Figure adapted from Figure 3 of Lauff et al. (2023).

According to Li et al. (2022), we decompose each sublayer into a row of smaller cells. In Figure 3.2, schematically a single sublayer with continuous fibers in direction e_1 is shown consisting of five cells. The parameter c in Equation (3.16) refers to the quadratic edge length of the cells and is computed under the assumption of continuous, i.e., infinitely long, fibers. For increasing the possible density of the initial packing, two fibers per cell are assumed (Z. Li, personal communication, January 17, 2022), see Figure 3.3. Therefore, an additional factor $\sqrt{2}$ in Equation (3.16) for the parameter c arises.

To fill the j^{th}-sublayer, fiber lengths are sampled according to the fiber length distribution in a successive fashion and assigned to the first cell. If a fiber cannot be arranged without fiber intersection, a new cell will be filled. This procedure is terminated provided the target volume fraction is reached. In case its length exceeds the edge lengths, a fiber is exclusively assigned to a cell and fiber self-intersection in the initial step is accepted. We denote the number of cells considered in the j^{th}-sublayer with n^j_{cell}.

The width of the cells b^j_{cell}, see Figure 3.3, computes for each sublayer $(j = 1, ..., n_{\text{sub}} n_{\text{layer}})$ as

$$b^j_{\text{cell}} = \frac{b^j_{\text{sub}}}{n^j_{\text{cell}}}, \tag{3.17}$$

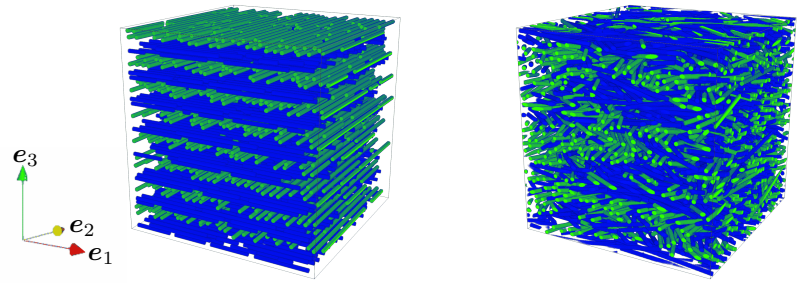
accounting for the number of cells n^j_{cell} considered in the sublayer and its total width b^j_{sub} – either Q_1 or Q_2. As a consequence of the extension of the initial step proposed in the article at hand, the dimensions of a rectangular unit cell may be chosen in an arbitrary way. This contrasts with Li et al. (2022), where the size of the unit cell is fixed.

In Figure 3.4(a), an initial microstructure with edge length $Q_i = 500\mu\text{m}$, volume fraction $\phi = 20\%$, uniform diameter $D = 10\mu\text{m}$, lengths distributed according to $L_k \sim \text{Weibull}(m = 200\mu\text{m}, s = 80\mu\text{m})$ and second-order fiber orientation tensor $\boldsymbol{A} \mathrel{\hat{=}} \text{diag}\,(0.49, 0.49, 0.02)$ is shown.

3.3.2 The shaking step

After the initial placement the fibers are shaken to introduce randomness. Li et al. (2022) present a procedure where the fibers are shaken consecutively, using the initial arrangement as starting point. For every fiber, first intense shaking (*global shaking*) is applied. To ensure non-interpenetration of the fibers, a shaken fiber will be accepted if there is no collision with any fiber that has already been accepted. If within a maximum number of attempts m_{max} no admissible setting was found,

smaller shaking steps will be applied (*local shaking*). In case the fiber placement fails again, it will be broken into two smaller parts and they are shaken individually (*breaking and shaking*). Fibers which can not be updated in one of these three steps are deleted. Broken or deleted fibers lead to errors in the fiber length distribution ρ and the fiber orientation tensor $\boldsymbol{A}$. The shaking procedure of the entire microstructure is repeated N_{max}-times. With increasing N_{max}, the intensity of shaking in a single iteration decreases (Li et al., 2022, Equation (14)).



(a) Initial microstructure **(b)** Shaken microstructure

Figure 3.4: Initial and shaken microstructure with edge length $Q_i = 500\mu\text{m}$, volume fraction $\phi = 20\%$, lengths distributed according to $L_k \sim \text{Weibull}(m = 200\mu\text{m}, s = 80\mu\text{m})$, uniform diameter $D = 10\mu\text{m}$ and second-order fiber orientation tensor $\boldsymbol{A} \mathrel{\hat{=}} \text{diag}\,(0.49, 0.49, 0.02)$. Figure adapted from Figure 4 of Lauff et al. (2023).

In contrast to Li et al. (2022), we only shake the entire microstructure once ($N_{\text{max}} = 1$) and use the procedure of *global shaking*, as this turns out to be sufficient for obtaining good results. Furthermore, we require that all fibers can be updated successfully to preserve the fiber length distribution ρ and the fiber orientation tensor $\boldsymbol{A}$.

Let us focus on the update of the midpoint and the direction of a single fiber during the shaking step. For every attempt $1 \leq m \leq m_{\text{max}}$, the midpoint of the k^{th}-fiber is computed by adding a shaking step to the

midpoint of the previous attempt:

$$\boldsymbol{x}_k^m \leftarrow \boldsymbol{x}_k^{m-1} + \Delta\boldsymbol{x}, \quad \Delta\boldsymbol{x} \hat{=} c\begin{bmatrix}\alpha\,\xi_1 & \alpha\,\xi_2 & \beta\,\xi_3\end{bmatrix}^{\mathsf{T}}. \tag{3.18}$$

Randomness is introduced by the realizations ξ_1, ξ_2 and ξ_3 of the normal distribution $\mathcal{N}\left(\mu = 0, \sigma^2 = 1/3\right)$ with mean $\mu = 0$ and variance $\sigma^2 = 1/3$. The parameter c follows Equation (3.16). To control the intensity of the shaking, the parameters α and β are selected by trial and error. The location of the midpoint in the initial arrangement $\widetilde{\boldsymbol{x}}_k$ is used as starting point for computing the midpoint of the first attempt.

The angles of the fibers with initial direction $\boldsymbol{e}_i$ $(i = 1, 2)$ are computed according to the sampling procedure

$$\theta_i \leftarrow \widetilde{\theta}_i + \Delta\theta\,\xi_\theta = \frac{\pi}{2} + \Delta\theta\,\xi_\theta \quad \text{and} \quad \varphi_i \leftarrow \widetilde{\varphi}_i + \Delta\varphi\,\xi_\varphi. \tag{3.19}$$

Notice that Equation (3.19) depends on the initial direction $\boldsymbol{e}_i$ but not on the specific fiber k or number of attempt m. The parameters $\Delta\theta$ and $\Delta\varphi$ control the intensity of the directional shaking and are set to

$$\Delta\theta = \gamma_1 \arcsin\left(\frac{Q_3}{L_f}\right) \quad \text{and} \quad \Delta\varphi = \gamma_2\frac{\pi}{4}. \tag{3.20}$$

Similar to α and β, the shaking parameters γ_1 and γ_2 are selected by trial and error. Randomness is introduced by realizations ξ_θ and ξ_φ of the normal distribution $\mathcal{N}(0, 1/3)$. A pseudo-code for the OCS method is provided in Algorithm 1 and a result of the shaking step visualized in Figure 3.4(b).

Algorithm 1: OCS method with multiple orientation shaking. Algorithm adapted from Algorithm 1 of Lauff et al. (2023).

Initial Step
Arrange fibers in orthogonal layers according to ϕ, $\rho_{\lambda,\beta}$, $\widetilde{\boldsymbol{A}}$ and Q
Shaking Step
Sort fibers by length (long to short)
for $k \leftarrow 1$ **to** N **do**
    for $m \leftarrow 1$ **to** $m_{\max}$ **do**
        Update the fiber state
                ▷ Equations (3.18) and (3.19)
        Check the inter-fiber distances with the already accepted fibers
        if no collision is detected **then**
            Accept updated fiber
            Exit loop
        else if $m = m_{\max}$ **then**
            Exit program (microstructure generation failed)

3.3.3 Control of the second-order fiber orientation tensor

We are interested in the effect of the shaking procedure (3.19) on the fiber orientation tensors of order l. Recall that the volume-weighted fiber orientation tensors of l^{th}-order for a finite number of fibers are defined via Equation (3.4). Suppose the fibers follow the shaking procedure (3.19) and ignore the non-interpenetration condition. Then, the empirical fiber orientation tensors compute as

$$\mathbb{A}_{\langle l \rangle} = \frac{1}{L_{\text{total}}} \sum_{k=1}^{N} L_k \, \boldsymbol{p}_k \left(\theta_i(\xi_\theta), \varphi_i(\xi_\varphi)\right)^{\otimes l} \tag{3.21}$$

with the additional information on the initial direction $\boldsymbol{e}_i$ of each fiber. To understand this formula more thoroughly, we consider the continuum limit as the number of fibers N goes to infinity. A specific direction

$\boldsymbol{p}\left(\theta_i(\xi_\theta), \varphi_i(\xi_\varphi)\right)$ depends on the realizations ξ_θ and ξ_φ of the normal distribution $\mathcal{N}\left(0, 1/3\right)$. Hence, an integration over the realizations ξ_θ and ξ_φ is necessary to include all directions on the unit sphere in the computation of $\mathbb{A}^{\mathrm{c}}_{\langle l \rangle}$. We are led to the result

$$\begin{aligned}\mathbb{A}^{\mathrm{c}}_{\langle l \rangle} = &\int_{-\infty}^{\infty}\int_{-\infty}^{\infty} \Big[\widetilde{a}_1^{\mathrm{r}}\, \boldsymbol{p}\left(\theta_1(\xi_\theta), \varphi_1(\xi_\varphi)\right)^{\otimes l} \\ &+\widetilde{a}_2^{\mathrm{r}}\, \boldsymbol{p}\left(\theta_2(\xi_\theta), \varphi_2(\xi_\varphi)\right)^{\otimes l}\Big]\ \psi(\xi_\theta)\, \psi(\xi_\varphi)\ \mathrm{d}\xi_\theta\, \mathrm{d}\xi_\varphi, \\ \psi(\xi) = &\sqrt{\frac{3}{2\pi}} e^{-3/2\xi^2}, \quad \xi \in \mathbb{R}.\end{aligned} \tag{3.22}$$

The two additive terms in the brackets account for the shaken directions of the two initial directions. As their influence on the computed fiber orientation tensor depends on their volume fractions, the two terms are weighted by the parameters $\widetilde{a}_1^{\mathrm{r}}$ and $\widetilde{a}_2^{\mathrm{r}}$, which denote the realized eigenvalues of the initial step. The latter may feature deviations in respect to the prescribed initial eigenvalues due to sampling of the fiber lengths. Independently of its initial direction, the probability of a shaken direction is computed by multiplying the probability of the realizations ξ_θ and ξ_φ. Therefore, the function $\psi(\xi)$ is used representing the probability density function for the normal distribution $\mathcal{N}\left(0, 1/3\right)$. Notice that for the probability of the realizations ξ_θ and ξ_φ is accounted in an uncoupled way as Li et al. (2022) assume independent shaking procedures for the angles θ_i and φ_i, see Equation (3.19).

Li et al. (2022) select the shaking parameters $\Delta\theta$ and $\Delta\varphi$ by trial and error. However, the computed fiber orientation tensor of second order $\boldsymbol{A}^{\mathrm{c}}$ only equals the prescribed tensor $\boldsymbol{A}$ for a special parameter selection. Hence, for general fiber orientation the selection by trial and error leads to errors in the fiber orientation state of the generated microstructures. With the insight of the computed fiber orientation tensors at hand (3.22), we require that the computed tensor $\boldsymbol{A}^{\mathrm{c}}$ equals the prescribed tensor $\boldsymbol{A}$.

Therefore, the shaking parameters $\Delta\theta$ and $\Delta\varphi$ are computed instead of selecting them by trial and error.

Computing the shaking parameter $\Delta\theta$

To match the third eigenvalue of the computed second-order fiber orientation tensor $\boldsymbol{A}^{\mathrm{c}}$ with the prescribed tensor $\boldsymbol{A}$, the condition

$$\begin{aligned} a_3 &\stackrel{!}{=} \int_{-\infty}^{\infty} \left[\widetilde{a}_1^{\mathrm{r}}\, p_3\left(\theta_1(\xi_\theta)\right)^2 + \widetilde{a}_2^{\mathrm{r}}\, p_3\left(\theta_2(\xi_\theta)\right)^2 \right] \psi(\xi_\theta)\, \mathrm{d}\xi_\theta \\ &= \int_{-\infty}^{\infty} \cos\left(\frac{\pi}{2} + \Delta\theta\, \xi_\theta\right)^2 \psi(\xi_\theta)\, \mathrm{d}\xi_\theta \end{aligned} \tag{3.23}$$

must hold. The latter Equation (3.23) involves only the single unknown $\Delta\theta$. As all fibers start in a planar setup with $\widetilde{\theta}_i = \pi/2$, the two orthogonal layers are considered in a single term. We use the relationship between the trigonometrical functions to shorten the expression to

$$a_3 \stackrel{!}{=} \int_{-\infty}^{\infty} \sin\left(\Delta\theta\, \xi_\theta\right)^2 \psi(\xi_\theta)\, \mathrm{d}\xi_\theta. \tag{3.24}$$

Recasting Equation (3.24) as optimization problem

$$\min_{\Delta\theta\in\mathbb{R}} \quad \mathrm{abs}\left(\int_{-\infty}^{\infty} \sin\left(\Delta\theta\, \xi_\theta\right)^2 \psi(\xi_\theta)\, \mathrm{d}\xi_\theta - a_3 \right), \tag{3.25}$$

we obtain the shaking parameter $\Delta\theta$ through a one-dimensional optimization procedure.

Computing the shaking parameter $\Delta\varphi$

The first and the second eigenvalue of the prescribed second order fiber orientation tensor are obtained by scaling the eigenvalues of the initial microstructure to consider that the third eigenvalue is set to zero:

$$a_1 = (1 - a_3)\,\widetilde{a}_1 \quad \text{and} \quad a_2 = (1 - a_3)\,\widetilde{a}_2. \tag{3.26}$$

As in Equation (3.26), we split up the first eigenvalue of the tensor $\boldsymbol{A}^{\mathrm{c}}$ into two parts:

$$a_1 \stackrel{!}{=} (1 - a_3) \int_{-\infty}^{\infty} \left[\widetilde{a}_1^{\mathrm{r}} \cos\left(\Delta\varphi\,\xi_\varphi\right)^2 + \widetilde{a}_2^{\mathrm{r}} \sin\left(\Delta\varphi\,\xi_\varphi\right)^2 \right] \psi(\xi_\varphi)\ \mathrm{d}\xi_\varphi. \tag{3.27}$$

A derivation of Equation (3.27) is given in Appendix A.

Let us compare Equation (3.26) and (3.27), then we observe that the integral in Equation (3.27) must equal the initial orientation tensor component $\widetilde{a}_1$ to obtain the prescribed eigenvalue a_1:

$$\widetilde{a}_1 \stackrel{!}{=} \int_{-\infty}^{\infty} \left[\widetilde{a}_1^{\mathrm{r}} \cos\left(\Delta\varphi\,\xi_\varphi\right)^2 + \widetilde{a}_2^{\mathrm{r}} \sin\left(\Delta\varphi\,\xi_\varphi\right)^2 \right] \psi(\xi_\varphi)\ \mathrm{d}\xi_\varphi. \tag{3.28}$$

This condition always holds, for the special case with equal eigenvalues $\widetilde{a}_1 = \widetilde{a}_2$ and an exactly realized initial fiber orientation tensor $\widetilde{a}_1^{\mathrm{r}} = \widetilde{a}_1$:

$$\widetilde{a}_1 \stackrel{!}{=} \widetilde{a}_1 \int_{-\infty}^{\infty} \left[\cos\left(\Delta\varphi\,\xi_\varphi\right)^2 + \sin\left(\Delta\varphi\,\xi_\varphi\right)^2 \right] \psi(\xi_\varphi)\ \mathrm{d}\xi_\varphi = \widetilde{a}_1. \tag{3.29}$$

Indeed, the parameter $\Delta\varphi$ may be selected freely without changing the computed fiber orientation tensors. Besides this special case, the condition as defined in Equation (3.27) can not hold. To handle this problem, two varying shaking parameters $\Delta\varphi_{1,2}$ for the initial directions

have to be defined, i.e., the fibers shake with different intensity. Then, the Equation

$$\widetilde{a}_1 \stackrel{!}{=} \int_{-\infty}^{\infty} \left[\widetilde{a}_1^{\mathsf{r}} \cos\left(\Delta\varphi_1\, \xi_\varphi\right)^2 + \widetilde{a}_2^{\mathsf{r}} \sin\left(\Delta\varphi_2\, \xi_\varphi\right)^2 \right] \psi(\xi_\varphi)\, \mathrm{d}\xi_\varphi. \tag{3.30}$$

may be solved. Therefore, one parameter is set as shaking parameter – we choose $\Delta\varphi_2$ – which is selected by trial and error. The second parameter – we choose $\Delta\varphi_1$ – is identified via the optimization problem

$$\begin{aligned} \min_{\Delta\varphi_1 \in \mathbb{R}} \quad \mathrm{abs} \Bigg(& \int_{-\infty}^{\infty} \left[\widetilde{a}_1^{\mathsf{r}} \cos\left(\Delta\varphi_1\, \xi_\varphi\right)^2 + \widetilde{a}_2^{\mathsf{r}} \sin\left(\Delta\varphi_2\, \xi_\varphi\right)^2 \right] \\ & \psi(\xi_\varphi)\, \mathrm{d}\xi_\varphi - \widetilde{a}_1 \Bigg). \end{aligned} \tag{3.31}$$

Notice that the optimization problem (3.31) is applicable for all cases. For the special case with equal eigenvalues and an exactly realized initial fiber orientation tensor, the parameter $\Delta\varphi_1$ equals the chosen parameter $\Delta\varphi_2$.

Implementation and workflow to determine the shaking parameters

Let us focus on the workflow for computing the shaking parameters $\Delta\theta$ and $\Delta\varphi_1$ which derive from the optimization problems (3.25) and (3.31). For solving these problems, we need the shaking parameter $\Delta\varphi_2$, as well as the orientation tensors $\boldsymbol{A}$, $\widetilde{\boldsymbol{A}}$ and $\widetilde{\boldsymbol{A}}^{\mathsf{r}}$ as input. As the orientation tensor $\widetilde{\boldsymbol{A}}^{\mathsf{r}}$ is only available after the initial placement, we compute the shaking parameters $\Delta\theta$ and $\Delta\varphi_1$ as part of the preprocessing of the shaking step – subsequent to the initial step.

For the numerical implementation of the optimization problems (3.25) and (3.31), we use Python-integrated numerical integration and opti-

mization tools. As limits for the corresponding integrals, we select the 99.99994%-confidence interval of the normal distribution $\mathcal{N}(0, 1/3)$:

$$\xi_{\text{min}} = -5\,\sigma = -5\,\frac{\sqrt{3}}{3} \quad \text{and} \quad \xi_{\text{max}} = 5\,\sigma = 5\,\frac{\sqrt{3}}{3}. \tag{3.32}$$

3.3.4 Single and multiple orientation shaking

The procedure of changing the fiber direction impacts the time efficiency, the achievable volume fraction as well as the realized fiber orientation tensors. We investigate two types of shaking to study the differences. For the first protocol, which we call *multiple orientation shaking*, the fiber direction is updated recursively for every attempt. More precisely, the new shaking step is added to the initial angles of the fiber, see Equation (3.19). By repeatingly changing the fiber direction, a faster microstructure generation is possible and higher volume fractions can be achieved. However, the prescribed fiber orientation state is not accurately realized.

Algorithm 2: Orientation correction (Mehta and Schneider, 2022). Algorithm adapted from Algorithm 2 of Lauff et al. (2023).

while $\|\mathbb{A}^{\text{c}} - \mathbb{A}^{\text{r}}\| > \|\mathbb{A}^{\text{c}}\| \cdot \text{error}$ **do**
  $\mathbb{A}^{\text{r}} = \dfrac{1}{L_{\text{total}}} \left[\sum_{i=1}^{N} L_i\, \boldsymbol{p}_i \otimes \boldsymbol{p}_i \otimes \boldsymbol{p}_i \otimes \boldsymbol{p}_i \right]$
  $t \leftarrow 1/L_{\text{mean}}$
  for $i \leftarrow 1$ **to** N **do**
    $\nabla_{\boldsymbol{p}_i} f = (\mathbf{1} - \boldsymbol{p}_i \otimes \boldsymbol{p}_i)\left((\mathbb{A}^{\text{c}} - \mathbb{A}^{\text{r}})\,[\boldsymbol{p}_i \otimes \boldsymbol{p}_i \otimes \boldsymbol{p}_i]\right)$
    $\boldsymbol{p}_i \leftarrow \dfrac{\boldsymbol{p}_i + L_i\, t\, \nabla_{\boldsymbol{p}_i} f}{\|\boldsymbol{p}_i + L_i\, t\, \nabla_{\boldsymbol{p}_i} f\|}$

In previous studies (Naghipour et al., 2010; Breuer and Stommel, 2019) it turns out that the fiber orientation influences the mechanical properties significantly. Hence, with more accurate fiber orientations in mind, we consider *single orientation shaking* as our second protocol. In this scenario, the angles are computed only once for every fiber before the first shaking attempt starts. After shaking the angles, the sampled direction $\boldsymbol{p}_k$ of every fiber is corrected to fulfill the fiber-orientation tensor of fourth order $\mathbb{A}^{\mathrm{c}}$ obtained by Equation (3.22). To be more precise, we apply the iteration scheme introduced by Mehta and Schneider (2022), see Algorithm 2. The prefactor t is used to account for the influence of the fiber lengths on the volume-weighted fiber orientation tensor.

Although the procedure leads to a higher fidelity, it also increases the runtime and decreases the achievable volume fraction as it is not possible to change the direction during the shaking procedure. To compensate for this effect, we introduce the following idea. Suppose there is a fiber which could not be placed after a critical number m_{crit}. Then, we allow the k^{th}-fiber to change its fiber direction in every attempt – similar to multiple orientation shaking. The critical number of attempts is chosen to depend on the maximum number of attempts m_{max} and the mean number of attempts of the previous ten percent of the fibers $\bar{m}_{10\%}$. As we update the fibers in order of descending fiber length, the volume-weighted fiber orientation tensor is mostly affected by the first fibers. To ensure a stable control of the fiber orientation state, we choose a higher critical number of attempts for the first thirty and last two percent of the N fibers:

$$m_{\mathrm{crit}}(k) = \begin{cases} 0.1\, m_{\mathrm{max}}, & \text{if } k < 0.30\, N, \\ m_{\mathrm{max}}, & \text{if } k > 0.98\, N, \\ \min\left(\max\left(1.5\, \bar{m}_{10\%}, 1000\right), \right. & \\ \qquad \left. 0.1\, m_{\mathrm{max}}\right) & \text{else .} \end{cases} \tag{3.33}$$

By changing the presampled direction of the fiber, we influence the fiber orientation state. To compensate for this error, the presampled directions of the remaining (not updated) fibers are corrected again. For this reason, we adapt the factor t to take into account that the directions of the already updated fibers do not change:

$$t = (N-k)\left(\sum_{i=1}^{k} L_i\right)\left(\sum_{i=k+1}^{N} L_i\right)^{-2}. \tag{3.34}$$

If a correction is not possible, the k^{th}-fiber will be shaken again starting from its last corrected direction with

$$\boldsymbol{p}_k \leftarrow \frac{\boldsymbol{p}_k + \Delta\boldsymbol{p}}{\|\boldsymbol{p}_k + \Delta\boldsymbol{p}\|}, \quad \Delta\boldsymbol{p} \hat{=} \begin{bmatrix} \xi_{\Delta p_1} & \xi_{\Delta p_2} & \xi_{\Delta p_3} \end{bmatrix}^{\mathsf{T}}. \tag{3.35}$$

The parameters $\xi_{\Delta p_1}$, $\xi_{\Delta p_2}$ and $\xi_{\Delta p_3}$ are realizations of the normal distribution $\mathcal{N}(0, g)$ using the parameter g to control the intensity of changing the direction. We choose an initial value of $g = 1/3$ for every fiber. If a correction is not accepted repeatedly, we will decrease the parameter with $g \leftarrow \max(g/1.5, 0.001)$.

In Algorithm 3, a pseudo-code for the OCS method with single orientation shaking is provided.

Algorithm 3: OCS method with single orientation shaking. Algorithm adapted from Algorithm 3 of Lauff et al. (2023).

Initial Step

Arrange fibers in orthogonal layers according to ϕ, $\rho_{\lambda,\beta}$, $\widetilde{\boldsymbol{A}}$ and Q

Shaking Step

Sort fibers by length (long to short)
Update the directions of all fibers ▷ `Equation (3.19)`
Correct the directions of all fibers ▷ `Algorithm 2`
for $k \leftarrow 1$ **to** N **do**
    for $m \leftarrow 1$ **to** m_{max} **do**
        Update the fiber midpoint ▷ `Equation (3.18)`
        if $m > m_{\text{crit}}(k)$ **then**
            if correction failed in the previous attempt **then**
                Update the fiber direction ▷ `Equation (3.35)`
            else
                Update the fiber direction ▷ `Equation (3.19)`
        Check the inter-fiber distances with the already accepted fibers
        if no collision is detected **then**
            if $m > m_{\text{crit}}(k)$ **then**
                Correct the directions of the unshaken fibers ▷ `Algorithm 2 with Equation (3.34)`
                if correction is successful **then**
                    Accept updated fiber
                    Exit loop
            else
                Accept updated fiber
                Exit loop
        else if $m = m_{\text{max}}$ **then**
            Exit program (microstructure generation failed)

3.4 Computational investigations

3.4.1 Setup

The presented algorithm is implemented in Python with Cython extensions. The collision checks between the fibers are parallelized with OpenMP. The runtimes for the microstructure generation are recorded on a desktop computer with a 8-core Intel i7 CPU and 64GB RAM.

For computing the effective elastic properties, we use FFT-based computational homogenization software (Moulinec and Suquet, 1994; 1998) with discretization on a staggered grid (Schneider et al., 2016) and a conjugate gradient solver (Zeman et al., 2010; Brisard and Dormieux, 2012) terminated at a relative tolerance of 10^{-5}. For more details, we refer to the review article (Schneider, 2021). The effective elasticity tensor is computed based on six independent load cases. As the microstructures are orthotropic on average, we report on the effective orthotropic engineering constants. These are computed from the full effective elastic tensor in a postprocessing step (Görthofer et al., 2020; Cowin, 1985).

E-glass fibers			PA66 matrix		
E	$=$	72.0 GPa	E	$=$	3.0 GPa
ν	$=$	0.22	ν	$=$	0.40

Table 3.1: Material properties for the PA66 matrix and the E-glass fibers (Hessman et al., 2021). Table adapted from Table 1 of Lauff et al. (2023).

We consider a polyamide 6.6 matrix, reinforced by E-glass fibers with the isotropic elastic parameters listed in Table 3.1, obtained by Hessman et al. (2021). For our studies, we select as our reference setup fibers with a diameter of $D = 10\mu\mathrm{m}$ and Weibull-distributed lengths with (volume-weighted) mean $m = 200\mu\mathrm{m}$ and standard deviation $s = 80\mu\mathrm{m}$.

We quantify the anisotropy of the microstructure in a unified way using the fiber orientation tensor of second order $\boldsymbol{A}$. A material with an isotropic fiber orientation is represented by the fiber orientation tensor $\boldsymbol{A} \hat{=} \operatorname{diag}(1/3, 1/3, 1/3)$. Thus, the deviation of the fiber orientation tensor from this diagonal state represents a convenient measure of anisotropy. Moreover, the class of anisotropy may be read off the fiber orientation tensor. For instance, the fiber orientation tensors representing the class of transversely isotropic materials with polar direction $\boldsymbol{e}_1$ read as

$$\boldsymbol{A} \hat{=} \operatorname{diag}(a, b, b) \quad \text{with} \quad b = \frac{1-a}{2} \quad \text{and} \quad a \in [0, 1], \tag{3.36}$$

where we drop the sorting of the eigenvalues in the diagonal matrix $\boldsymbol{A}$ for notational clarity.

We correct the fiber directions in the procedure with single orientation shaking until the relative error of the fiber-orientation tensor of fourth order is lower than 10^{-5}. To avoid excessively high stresses between close fibers, we choose 20% of the fiber diameter, i.e., $2\mu\mathrm{m}$, as the minimum inter-fiber distance. The selected shaking parameters and the maximum number of attempts are listed in Table 3.2.

α	β	$\Delta\varphi_2$	$m_{\max}$
4	2	$3\pi/8$	10^7

Table 3.2: Used algorithmic parameters. Table adapted from Table 2 of Lauff et al. (2023).

Previous studies showed (Kanit et al., 2003; Schneider, 2022) that periodization of non-periodic media in combination with periodic boundary conditions leads to the lowest errors between the computed apparent stiffness and the desired effective stiffness for a given unit-cell size. According to these results, we generate periodic microstructures and

use periodic boundary conditions for the displacement fluctuation to decrease the size of the RVEs.

3.4.2 On using the semi-analytic shaking parameter estimation

In this section, we investigate the difference in the computed and realized fiber orientation tensors by using identical parameter $\Delta\varphi_1 = \Delta\varphi_2$ for both orthogonal layers and computing the parameter $\Delta\varphi_1$ separately (3.31). For the study, we restrict to four volume fractions ϕ_i and five different fiber orientation tensors $\boldsymbol{A}_j \mathrel{\hat{=}} \mathrm{diag}(t_j, 0.98 - t_j, 0.02)$, see Table 3.3.

ϕ_1	ϕ_2	ϕ_3	ϕ_4	t_1	t_2	t_3	t_4	t_5
5%	10%	15%	20%	0.49	0.59	0.69	0.79	0.89

Table 3.3: Considered volume fractions ϕ_i and parameters t_j. Table adapted from Table 3 of Lauff et al. (2023).

Let us start by comparing the computed fiber orientation tensors obtained via evaluating Equation (3.22). Using the computation of parameter $\Delta\varphi_1$ leads to coinciding tensors $\boldsymbol{A}^{\mathsf{c}}$ and $\boldsymbol{A}$ by construction (3.31). Hence, no error in the fiber orientation state is induced by the semi-analytic parameter estimation. In contrast, a difference between the tensors occurs for a parameter selection $\Delta\varphi_1 = \Delta\varphi_2$, see Table 3.4, in general. Notice that the prediction only depends on the shaking parameter $\Delta\varphi_2$ and is independent of the volume fraction.

We observe that for mainly-planar isotropic microstructures the absolute error is zero. In this special case, the assumption of equal shaking parameters $\Delta\varphi_1 = \Delta\varphi_2$ does not infer an additional error, in agreement with the theoretical prediction (3.29). With increasing alignment of

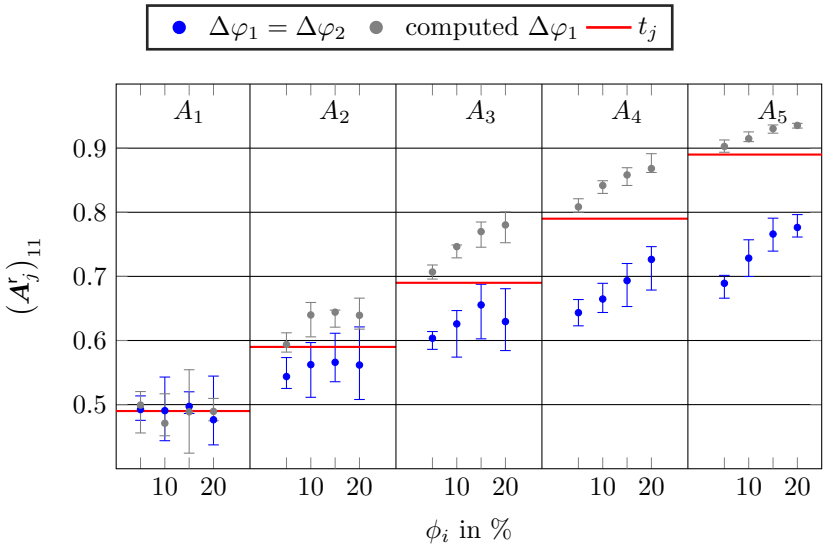
the fibers, the error intensifies and the maximum error is realized for the orientation state $\boldsymbol{A}_5$ with an absolute deviation of 0.341. Hence, it turns out that selecting equal shaking parameters $\Delta\varphi_i$ for both initial directions leads to a significant error in the computed fiber orientation tensors.

	$\left(\boldsymbol{A}_j^{\mathsf{c}}\right)_{11}$	$\left(\boldsymbol{A}_j^{\mathsf{c}}\right)_{22}$	$\left(\boldsymbol{A}_j^{\mathsf{c}}\right)_{33}$	$\|\boldsymbol{A}_j^{\mathsf{c}} - \boldsymbol{A}_j\|$
$\boldsymbol{A}_1$	0.490	0.490	0.020	0.000
$\boldsymbol{A}_2$	0.530	0.450	0.020	0.085
$\boldsymbol{A}_3$	0.569	0.411	0.020	0.171
$\boldsymbol{A}_4$	0.609	0.371	0.020	0.256
$\boldsymbol{A}_5$	0.649	0.331	0.020	0.341

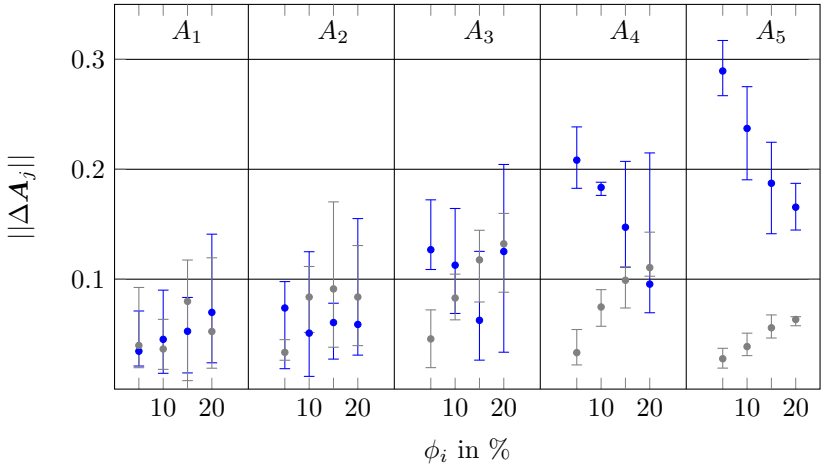
Table 3.4: Computed fiber orientation tensor $\boldsymbol{A}_j^{\mathsf{c}}$ with $\Delta\varphi_1 = \Delta\varphi_2$. Table adapted from Table 4 of Lauff et al. (2023).

To compare this results with the realized fiber orientation tensors, we generated ten microstructures for every case of the study. For the process of changing the direction, we use the multiple orientation shaking protocol resulting in a new direction in every attempt. We choose a cubic cell-size with dimension $Q_i = 500\mu\mathrm{m}$ representing the 99.98%-quantile of the prescribed fiber length distribution. Hence, most of the fibers are smaller than an edge length.

For the lowest volume fraction of 5%, the observed errors transfer to the mean of the realized fiber orientation states with low discrepancy, see Figure 3.5(a) for the component $\left(\boldsymbol{A}_j^{\mathsf{c}}\right)_{11}$. The discrepancy is caused by sampling the direction of a fiber multiple times as result of detected inter-fiber collisions. Hence, the prescribed fiber orientation distribution is not realized exactly. For higher volume fractions, the deviation is increasing, as inter-fiber collisions are detected more frequently.



(a) Component $\left(\boldsymbol{A}^{\mathrm{r}}_j\right)_{11}$



(b) Absolute error $\|\Delta \boldsymbol{A}_j\|$

Figure 3.5: Comparison of the realized fiber orientation tensor $\boldsymbol{A}^{\mathrm{r}}_j$ between using $\Delta\varphi_1 = \Delta\varphi_2$ and computing $\Delta\varphi_1$ with Equation (3.31) for five different prescribed fiber orientation tensors $\boldsymbol{A}_j$. Figure adapted from Figure 5 of Lauff et al. (2023).

We notice that the deviation leads to an increasing mean of the component $\left(\boldsymbol{A}_j^{\mathsf{c}}\right)_{11}$ for the orientation tensors $\boldsymbol{A}_2$ to $\boldsymbol{A}_5$. This tendency is caused by the preference of the fibers to arrange in more aligned states with increasing fiber volume fraction, also observed in previous studies (Duschlbauer et al., 2006; Iorga et al., 2008). For the mainly-planar isotropic orientation tensor $\boldsymbol{A}_1$, the fiber orientation state does not feature a preferred direction. Hence, the mean value of the component $(\boldsymbol{A}_1^{\mathsf{c}})_{11}$ does not change systematically. As a result of the tendency to arrange in more aligned states, the absolute error $\|\Delta \boldsymbol{A}_j\| = ||\boldsymbol{A}_j^{\mathsf{r}} - \boldsymbol{A}_j||$ $(j = 2, \ldots, 5)$ increases for higher volume fractions with computation of the parameter $\Delta\varphi_1$, see Figure 3.5(b). In contrast, the error decreases for equal parameters $\Delta\varphi_{1,2}$ as the underestimation of the component $\left(\boldsymbol{A}_j^{\mathsf{c}}\right)_{11}$ $(j = 2, \ldots, 5)$ is compensated. However, for the orientation state $\boldsymbol{A}_5$, even for the highest volume fraction of 20%, the absolute error is 0.16 with equal shaking parameters, whereas, with computing the parameter $\Delta\varphi_1$, it is 0.06. Due to the lower errors resulting for the fiber orientation states $\boldsymbol{A}_j$ $(j = 2, \ldots, 5)$, we conclude that computing the parameter $\Delta\varphi_1$ is an essential factor for achieving reliable results.

Last but not least, we focus on the differences in the runtime. Solving the problem (3.31) is conducted as part of the preprocessing of the shaking step and has no significant influence on the runtime. During the shaking step the runtime slightly increases for equal parameters $\Delta\varphi_1 = \Delta\varphi_2$ as it is computationally more expensive to generate microstructures which are closer to the mainly-planar isotropic state.

As a result of the smaller errors in the fiber orientation state, the subsequent investigations use a computed parameter $\Delta\varphi_1$.

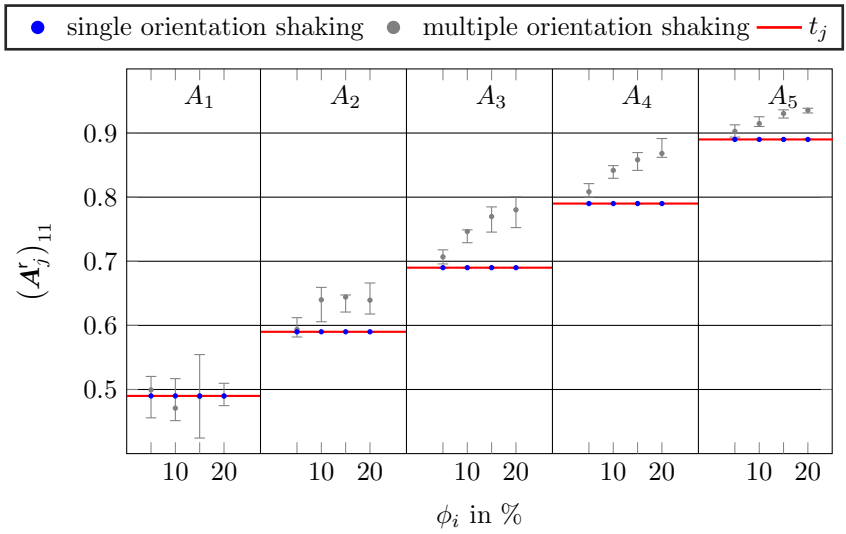
3.4.3 On the difference between single and multiple orientation shaking

In the previous section, significant errors in the fiber orientation states, even with computed $\Delta\varphi_1$, are observed due to the multiple orientation shaking in case of inter-fiber collisions. As the effective mechanical properties of a composite strongly depend on the orientation state of the reinforcing fibers, it is essential to match the prescribed fiber orientation tensors accurately. To focus on this objective, we additionally investigate the procedure of single orientation shaking, which leads to matching fiber orientation tensors:

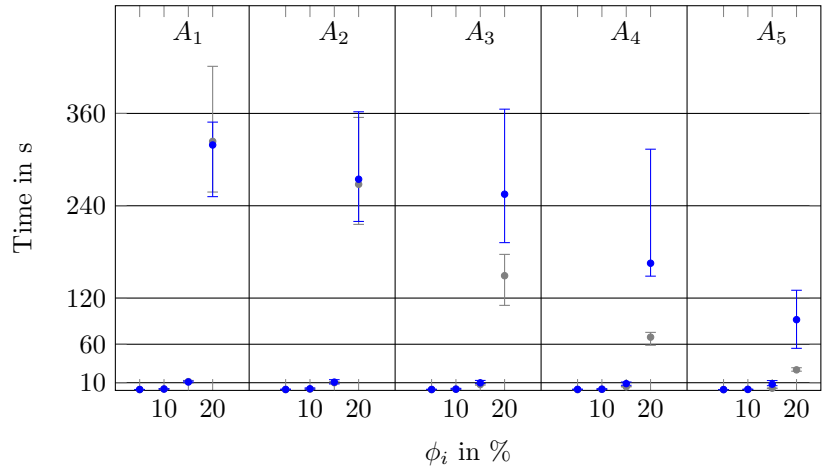
$$\boldsymbol{A} = \boldsymbol{A}^{\mathrm{c}} = \boldsymbol{A}^{\mathrm{r}} \quad \text{and} \quad \mathbb{A}^{\mathrm{c}} = \mathbb{A}^{\mathrm{r}}. \tag{3.37}$$

We repeat the study from Section 3.4.2 for single orientation shaking and compare the results to multiple orientation shaking. Figure 3.6(a) shows that the component $\left(\boldsymbol{A}_j^{\mathrm{r}}\right)_{11}$ equals the component t_j for all cases.
The price to pay for this increase in accuracy is an increase in runtime, see Figure 3.6(b).

For the mainly-planar isotropic case, the mean of the runtime is similar for both procedures and only the high whisker is larger for multiple orientation shaking. For the fiber orientation states $\boldsymbol{A}_j$ $(j = 2, \ldots, 5)$, the procedure of multiple orientation shaking leads to smaller runtimes as it permits the fibers to follow their natural, and computationally less expensive, tendency to more aligned orientation states. In contrast, single orientation shaking enforces the prescribed fiber orientation state which leads to a higher computational expense, in general. By taking the fiber orientation tensor $\boldsymbol{A}_3$ and a volume fraction of 20% as example, the runtime is $149\mathrm{s}$ for multiple orientation shaking and $255\mathrm{s}$ for single orientation shaking, i.e., an increase by 71%.



(a) Component $\left(A_j^r\right)_{11}$



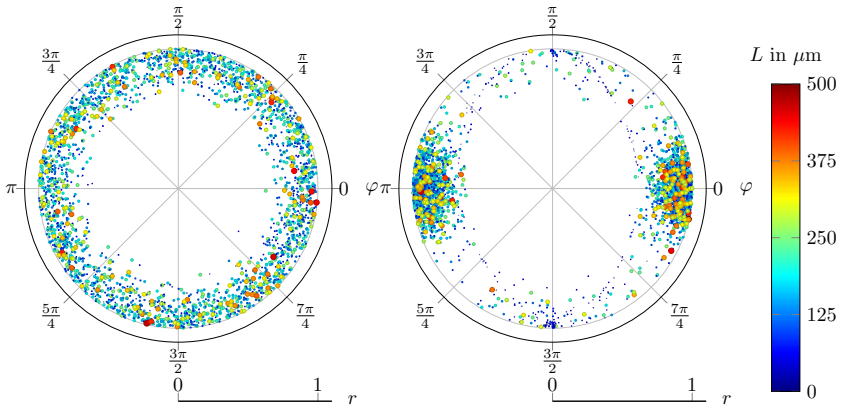
(b) Runtime

Figure 3.6: Comparison of the realized fiber orientation tensor $\left(A_j^r\right)_{11}$ and the runtime between single and multiple orientation shaking for five different prescribed fiber orientation tensors A_j. Figure adapted from Figure 6 of Lauff et al. (2023).

Despite the increase in runtime, the microstructures are still generated in acceptable time. Hence, we use single orientation shaking throughout the next investigations to ensure reliable microstructures.

3.4.4 Study on the resolution and the RVE size

To compute precise effective properties, we need to investigate the necessary resolution and the RVE size leading to accurate results. For this purpose, we consider the fiber setup from the study in the Section 3.4.2 and the material parameters of Table 3.1. We examine the extreme fiber orientation states $\boldsymbol{A}_{1,5}$ and choose $\phi = 20\%$ as volume fraction.



(a) $\boldsymbol{A}_1 \mathrel{\hat{=}} \mathrm{diag}(0.49, 0.49, 0.02)$ **(b)** $\boldsymbol{A}_5 \mathrel{\hat{=}} \mathrm{diag}(0.89, 0.09, 0.02)$

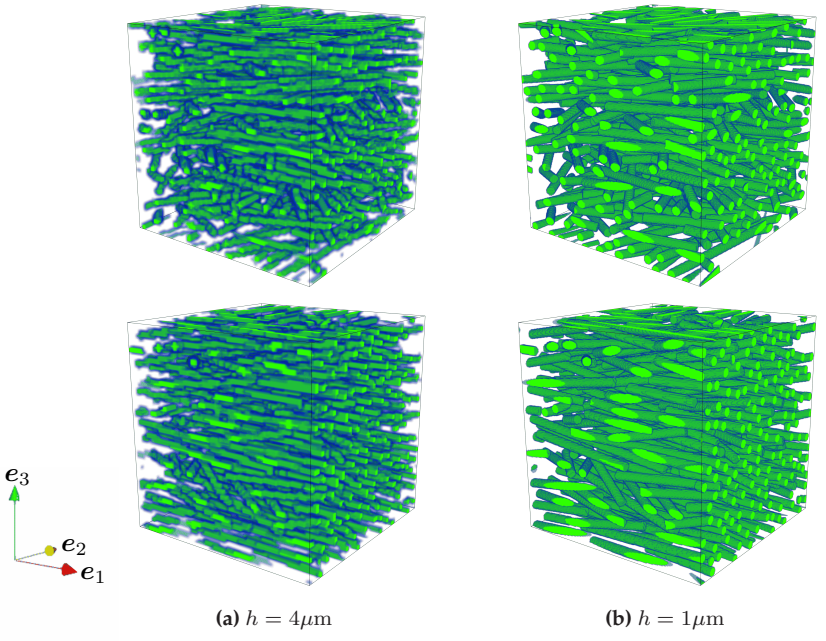
Figure 3.7: Stereographic projection of the fiber directions of two realized microstructures for varying fiber orientation tensors. Figure adapted from Figure 7 of Lauff et al. (2023).

In Figure 3.7, the realized directions of two corresponding microstructures are represented by a pole figure. For a two-dimensional representation, a stereographic projection of the fiber directions into the plane with normal direction $\boldsymbol{e}_3$ is used. Then, the angle θ of each fiber is

represented by the parameter $r = \tan(\theta/2)$, see Böhlke and Brüggemann (2001). Notice that for this representation the angle φ is parameterized on the domain $[0, 2\pi)$ and θ on the domain $[0, \pi/2]$ using the periodic characteristic of the angles and the equivalent description of a fiber with direction $\boldsymbol{p}$ or $-\boldsymbol{p}$. To represent the influence of a single fiber on the volume-weighted fiber orientation tensor, the color and size of the marks accounts for the fiber lengths. We observe that in Figure 3.7(a) the fiber directions are equally distributed in respect to the angle φ, but tend to the outer parts for the parameter r, which represent more planar orientation states. This corresponds to the mainly-planar isotropic characteristic of the fiber orientation tensor $\boldsymbol{A}_1$. In contrast, in Figure 3.7(b) most directions are located near the horizontal line at $\varphi = 0$, representing the almost unidirectional fiber orientation tensor $\boldsymbol{A}_5$.

To compute the effective properties accurately, the resolution has to be sufficiently fine Schneider (2015); Brisard and Dormieux (2012). However, with smaller mesh size, the runtime for the computation of the effective properties is increasing. To balance these conflicting objectives, it is necessary to select a resolution leading to reasonable computational effort and sufficient accuracy. We select one of the ten microstructures generated in Section 3.4.3 for both fiber orientation tensors. We consider the voxel edge-lengths $4\mu\mathrm{m}$, $2\mu\mathrm{m}$ and $1\mu\mathrm{m}$ resolving a fiber with 2.5, 5 and 10 voxels per diameter, respectively. In Figure 3.8, $(240\mu\mathrm{m})^3$-extractions of the microstructures for varying mesh sizes are shown.

For the mainly-planar isotropic fiber orientation tensor $\boldsymbol{A}_1$, the fibers' directions feature no preference in the $\boldsymbol{e}_1$-$\boldsymbol{e}_2$-plane. Hence, the Young's moduli in $\boldsymbol{e}_1$- and $\boldsymbol{e}_2$-direction almost coincide for all three resolutions, see Table 3.5.



(a) $h = 4\mu\mathrm{m}$ **(b)** $h = 1\mu\mathrm{m}$

Figure 3.8: $(240\mu\mathrm{m})^3$-extractions of microstructures with two different voxel-edge lengths and fiber orientation tensors $\boldsymbol{A}_1 \mathrel{\hat{=}} \mathrm{diag}(0.49, 0.49, 0.02)$ (top) and $\boldsymbol{A}_5 \mathrel{\hat{=}} \mathrm{diag}(0.89, 0.09, 0.02)$ (bottom). Figure adapted from Figure 8 of Lauff et al. (2023).

Due to the dominant fiber arrangement in the $\boldsymbol{e}_1$-$\boldsymbol{e}_2$-plane, the Young's modulus in $\boldsymbol{e}_3$-direction is smaller. The same reason leads to a higher shear modulus G_{12} compared to the other two shear moduli. For a voxel edge-length $h = 4\mu\mathrm{m}$, the largest relative error – relative to the highest resolution – is obtained for the shear modulus G_{12} with 5.95%, decreasing to 2.38% for $h = 2\mu\mathrm{m}$. As we report on the approximated orthotropic engineering constants instead of the full effective elastic tensor, the orthotropic approximation error $\mathrm{err}_{\mathrm{orth}}$ must be assessed to control the quality of the results. We observe that even for the coarsest resolution, the error is lower than two percent and decreases to a quarter percent for the finest resolution.

	h μm	E_1 GPa	E_2 GPa	E_3 GPa	G_{23} GPa	G_{13} GPa	G_{12} GPa	err_{orth} %
$\boldsymbol{A}_1$	4	6.59	6.61	5.16	1.78	1.78	2.46	1.91
	2	6.79	6.82	5.19	1.72	1.72	2.51	0.74
	1	6.86	6.89	5.18	1.68	1.68	2.52	0.25
$\boldsymbol{A}_5$	4	10.25	5.07	4.90	1.69	1.86	1.98	1.48
	2	10.81	5.09	4.90	1.63	1.80	1.94	0.63
	1	11.02	5.08	4.89	1.59	1.77	1.91	0.30

Table 3.5: Approximated effective orthotropic engineering constants for three different resolutions and fiber orientation tensors $\boldsymbol{A}_1 \mathrel{\hat{=}} \text{diag}(0.49, 0.49, 0.02)$ and $\boldsymbol{A}_5 \mathrel{\hat{=}} \text{diag}(0.89, 0.09, 0.02)$. Table adapted from Table 5 of Lauff et al. (2023).

For the almost aligned case, the Young's modulus E_1 exceeds the other moduli by at least a factor of two. Also it is affected the most by increasing the resolution. For the coarsest resolution, the relative error is 6.99% decreasing to 1.91% for $h = 2\mu\text{m}$. Similar to the mainly-planar isotropic case, the approximation error is rather low and decreases to under one percent with $h = 2\mu\text{m}$.

As an outcome of the resolution study, we choose a voxel edge-length of five voxels per diameter leading to a relative error below three percent and an orthotropic error below one percent. This selection confirms the results of previous resolution studies (Müller et al., 2015; Schneider, 2017).

After identifying the necessary resolution, we turn our attention to the required size of a representative volume element. As a result of the manufacturing process and the material, fiber-reinforced composites are characterized by randomness in, e.g., their realized fiber lengths, fiber directions and fiber positioning. Consequently, the computed elastic properties are random variables, as well. However, the effective properties as deterministic descriptors are only obtained on cells of

sufficient size, the so-called representative volume elements (RVEs) (Hill, 1963; Drugan and Willis, 1996; Kanit et al., 2003).

When working with cells of finite size, the incurring error naturally decomposes into two terms. The standard deviation of the apparent properties is called random error and quantifies their dispersion (Kanit et al., 2003; Gloria and Otto, 2011). This error may be reduced by averaging multiple samples on cells of equal size (Dirrenberger et al., 2014; Jeulin, 2016). The second, so-called systematic, error equals the difference of the mean of the apparent properties and the effective elastic properties (Kanit et al., 2003; Gloria and Otto, 2011). We monitor this error by increasing the unit cell size and observing to what extent the mean is changing. In case of sufficiently small random and systematic errors, the investigated unit cell size is usable for a representative volume element.

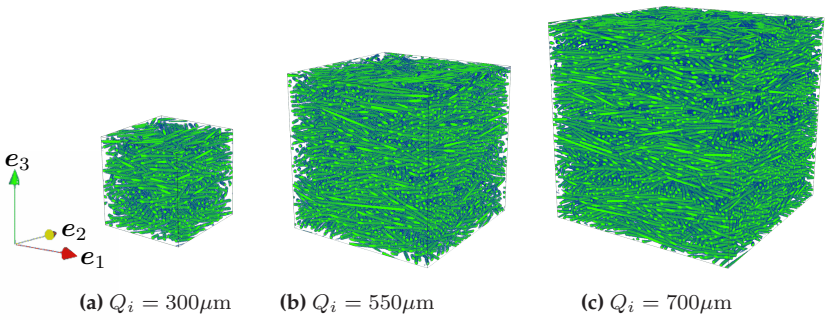


Figure 3.9: Generated microstructures with the second-order fiber orientation tensor $\boldsymbol{A}_1 \mathrel{\hat{=}} \mathrm{diag}(0.49, 0.49, 0.02)$ for three different cubic cell-sizes. Figure adapted from Figure 9 of Lauff et al. (2023).

For reducing the representativity errors, we enforce a high accuracy regarding the prescribed properties, for example the fiber length distribution and the fiber orientation state. According to previous studies,

periodic boundary conditions leads to lower random and systematic errors as well (Sab and Nedjar, 2005; Schneider, 2022). For these reasons, we expect rather low representativity errors.

In the following RVE study, we choose cubic cell-sizes with dimensions $Q_i = 300\mu\mathrm{m}$, $Q_i = 550\mu\mathrm{m}$ and $Q_i = 700\mu\mathrm{m}$ and the previously identified resolution $h = 2\mu\mathrm{m}$. For the fiber orientation tensors $\boldsymbol{A}_1$ and $\boldsymbol{A}_5$, we consider ten realizations for every unit cell size. Figure 3.9 shows generated microstructures for the orientation state $\boldsymbol{A}_1$ and the three cell sizes. To quantify the representativity of the unit cells, we compute the empirical mean and the standard deviation of the approximated engineering constants, see Table 3.6.

	Q_i μm	E_1 GPa	E_2 GPa	E_3 GPa	G_{23} GPa	G_{13} GPa	G_{12} GPa	$\mathrm{err}_{\mathrm{orth}}$ %
$\boldsymbol{A}_1$	300	6.90	6.88	5.22	1.72	1.72	2.54	0.79
		$\pm$ 0.07	$\pm$0.05	$\pm$0.01	$\pm$0.00	$\pm$0.00	$\pm$0.01	$\pm$0.12
	550	6.83	6.81	5.19	1.72	1.72	2.53	0.96
		$\pm$ 0.02	$\pm$0.02	$\pm$0.00	$\pm$0.00	$\pm$0.00	$\pm$0.00	$\pm$0.06
	700	6.82	6.81	5.19	1.72	1.72	2.53	0.94
		$\pm$ 0.02	$\pm$0.02	$\pm$0.00	$\pm$0.00	$\pm$0.00	$\pm$0.00	$\pm$0.07
$\boldsymbol{A}_5$	300	10.86	5.11	4.91	1.63	1.81	1.94	0.63
		$\pm$ 0.08	$\pm$0.04	$\pm$0.01	$\pm$0.00	$\pm$0.00	$\pm$0.01	$\pm$0.06
	550	10.88	5.09	4.91	1.63	1.81	1.94	0.63
		$\pm$ 0.03	$\pm$0.01	$\pm$0.00	$\pm$0.00	$\pm$0.00	$\pm$0.00	$\pm$0.03
	700	10.88	5.09	4.91	1.63	1.81	1.94	0.63
		$\pm$ 0.02	$\pm$0.01	$\pm$0.00	$\pm$0.00	$\pm$0.00	$\pm$0.00	$\pm$0.01

Table 3.6: Approximated effective orthotropic engineering constants for three different cubic cell-sizes and fiber orientation tensors $\boldsymbol{A}_1 \mathrel{\hat{=}} \mathrm{diag}(0.49, 0.49, 0.02)$ and $\boldsymbol{A}_5 \mathrel{\hat{=}} \mathrm{diag}(0.89, 0.09, 0.02)$. Table adapted from Table 6 of Lauff et al. (2023).

The orthotropic error $\mathrm{err}_{\mathrm{orth}}$ is smaller than 1%, showing an adequate orthotropic approximation of the computed effective stiffness. We observe that the shear moduli are almost unaffected by changing the size of the unit cell. Also for the Young's moduli, the dispersion and the bias are rather low and decrease for an increasing unit cell size. The highest systematic error is computed for the Young's modulus E_1 in the mainly-planar isotropic fiber arrangement. Compared to the large-scale modulus a relative error of 1.17% occurs for $Q_i = 300\mu\mathrm{m}$, dropping to 0.15% for $Q_i = 550\mu\mathrm{m}$. The systematic error for the almost aligned case is even lower, not exceeding 0.5% for any engineering constant or unit cell size.

To sum up, the results confirm our expectation that combining periodic boundary conditions and higher accuracy of the descriptive parameters of the microstructure results in low representativity errors. In fact, even the smallest unit cell size $Q_i = 300\mu\mathrm{m}$ leads to acceptable errors for engineering applications.

3.4.5 Effective stiffness compared to the SAM algorithm

In this section, we compare the computed effective stiffness of microstructures generated with the Orientation Corrected Shaking method and the Sequential Addition and Migration (SAM) algorithm (Schneider, 2017; Mehta and Schneider, 2022). Therefore, we reproduce the results of the RVE study in Table 3.6 for microstructures generated by the SAM algorithm.

Already in previous studies (Schneider, 2017; Müller and Böhlke, 2016; Schneider, 2022), it is pointed out that the effective elastic properties are determined by the fiber orientation tensor of fourth order $\mathbb{A}$, i.e., prescribing the fiber orientation tensor of second order $\boldsymbol{A}$ is not sufficient. For this reason, the presented OCS method as well as the SAM algorithm enforce a close match of the fiber orientation tensor of fourth order. However, in practice, only the fiber orientation tensor of second order is

available and the additional information included in the fiber orientation tensor of fourth order is not known. For this reason, the fourth order fiber orientation tensor within the SAM algorithm is estimated by a closure approximation (Folgar and Tucker III, 1984; Cintra and Tucker III, 1995; Kugler et al., 2020; Dray et al., 2007; Breuer et al., 2019). In contrast, for the OCS method the previously presented intrinsic computation of higher-order fiber orientation tensors is applied, see Equation (3.22).

Due to the lack of data, the choice of the closure approximation represents another parameter to be selected. Furthermore, as second-order fiber orientation tensors are either isotropic, transversely isotropic or orthotropic (Cowin, 1985; Bauer and Böhlke, 2022b), closure approximations are restricted on these material symmetries as well (Bauer and Böhlke, 2022a).

In the following study, we investigate the influence of the chosen closure approximation on the computed effective stiffness. Therefore, we consider the intrinsic closure of the OCS method and, for the SAM algorithm, the exact closure (ACG) (Montgomery-Smith et al., 2011a;b) as well as the maximum entropy closure (MEC) (Chaubal and Leal, 1998; Müller and Böhlke, 2016).

We choose $Q_i = 550\mu\mathrm{m}$ as cell size, following the results of the RVE study for the OCS method. In Mehta and Schneider (2022) the necessary RVE size is investigated for the SAM algorithm, as well. It is shown that for a similar material the cell size $Q_i = 300\mu\mathrm{m}$ is already representative for engineering applications. Hence, we assume that the chosen cell size $Q_i = 550\mu\mathrm{m}$ is applicable for the SAM algorithm as RVE, especially as we consider even shorter fibers than Mehta and Schneider (2022).

In Table 3.7, the results for both microstructure generators are shown. We observe that both random and orthotropic error are small for the effective stiffness based on the SAM algorithm, in the same manner as we observed for the OCS method. Hence, the chosen cell size is representative for both generators.

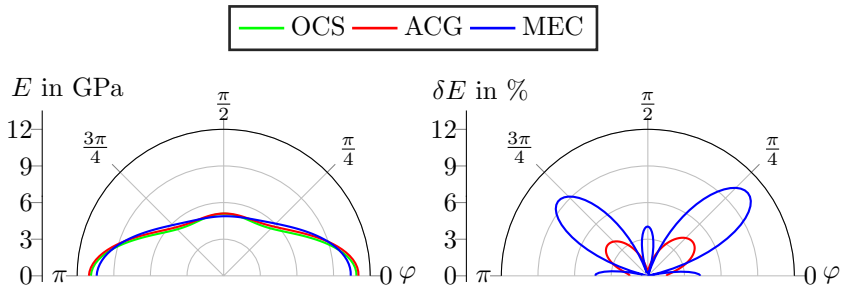
For the mainly-planar isotropic case, the computed moduli for the three closure approximations are comparable. Considering the shear moduli G_{23} and G_{13}, we even notice that all considered closures lead to almost the same results. The remaining moduli turn out to be close, as well.

		E_1 GPa	E_2 GPa	E_3 GPa	G_{23} GPa	G_{13} GPa	G_{12} GPa	err_{orth} %
$\boldsymbol{A}_1$	OCS	6.83	6.81	5.19	1.72	1.72	2.53	0.96
		$\pm$ 0.02	$\pm$0.02	$\pm$0.00	$\pm$0.00	$\pm$0.00	$\pm$0.00	$\pm$0.06
	ACG	7.02	7.02	5.32	1.71	1.71	2.63	1.06
		$\pm$ 0.02	$\pm$0.01	$\pm$0.00	$\pm$0.00	$\pm$0.00	$\pm$0.00	$\pm$0.04
	MEC	6.98	6.98	5.27	1.73	1.73	2.62	1.01
		$\pm$0.01	$\pm$0.01	$\pm$0.00	$\pm$0.00	$\pm$0.00	$\pm$0.00	$\pm$0.03
$\boldsymbol{A}_5$	OCS	10.88	5.09	4.91	1.63	1.81	1.94	0.63
		$\pm$ 0.03	$\pm$0.01	$\pm$0.00	$\pm$0.00	$\pm$0.00	$\pm$0.00	$\pm$0.03
	ACG	11.04	5.11	5.00	1.67	1.76	2.04	0.68
		$\pm$ 0.03	$\pm$0.00	$\pm$0.00	$\pm$0.00	$\pm$0.00	$\pm$0.00	$\pm$0.02
	MEC	10.41	4.88	4.96	1.65	1.82	2.21	0.78
		$\pm$ 0.02	$\pm$0.00	$\pm$0.00	$\pm$0.00	$\pm$0.00	$\pm$0.00	$\pm$0.02

Table 3.7: Approximated effective orthotropic engineering constants of microstructures with fiber orientation tensors $\boldsymbol{A}_1 \doteq \text{diag}(0.49, 0.49, 0.02)$ and $\boldsymbol{A}_5 \doteq \text{diag}(0.89, 0.09, 0.02)$ generated with the OCS method and with the SAM algorithm (based on the exact (ACG) or on the maximum entropy closure (MEC)). Table adapted from Table 7 of Lauff et al. (2023).

The highest relative difference is computed for the shear modulus G_{12} between the OCS method and the exact closure with 3.95%. Higher differences are obtained by investigating the almost aligned case. Even for the shear moduli G_{23} and G_{13}, we observe remarkable differences with a maximum of 3.41% for G_{13} between the exact and the maximum entropy closure. Moreover, the Young's modulus in $\boldsymbol{e}_1$-direction E_1 differs by more than half a GPa, slightly more than six percent. Again, the highest

relative difference is computed for G_{12} with 13.92%, which is about ten percent higher compared to the mainly-planar isotropic case. Bauer and Böhlke (2023) study the influence of the exact and maximum entropy closure on the reconstructed fiber orientation distribution for planar fiber arrangement. Higher differences between the approximations are observed for increasing fiber alignment, corresponding to our results for the computed effective stiffness.



(a) Mean Young's modulus $E(\boldsymbol{p})$

(b) Relative difference $\delta E(\boldsymbol{p})$ to the OCS method

Figure 3.10: Comparison of the computed mean Young's modulus in the $\boldsymbol{e}_1$-$\boldsymbol{e}_2$-plane of microstructures with fiber orientation tensor $\boldsymbol{A}_5 \mathrel{\hat{=}} \operatorname{diag}(0.89, 0.09, 0.02)$ generated with the OCS method and with the SAM algorithm (based on the exact closure (ACG) or on the maximum entropy closure (MEC)). Figure adapted from Figure 10 of Lauff et al. (2023).

Let us focus on the almost unidirectional case to investigate the higher differences more thoroughly. In Figure 3.10(a), the mean of the direction dependent Young's modulus with tensile directions in the $\boldsymbol{e}_1$-$\boldsymbol{e}_2$-plane is shown. For details on the computation of the direction dependent Young's modulus $E(\boldsymbol{p})$, we refer to, e.g., Böhlke and Brüggemann (2001). Notice that the computed effective stiffness, instead of its orthotropic approximation, is used for the computation of direction dependent Young's modulus. Via the visualization, it turns out that the shape of the Young's modulus almost coincides for the OCS method and the exact

closure, whereas it differs for the maximum entropy closure, especially near the angle $\varphi = \pi/2$. By plotting the relative difference to the OCS method

$$\delta E(\boldsymbol{p}) = \frac{\left|E_{\text{OCS}}(\boldsymbol{p}) - E_{\text{ACG/MEC}}(\boldsymbol{p})\right|}{E_{\text{OCS}}(\boldsymbol{p})} \cdot 100\% \tag{3.38}$$

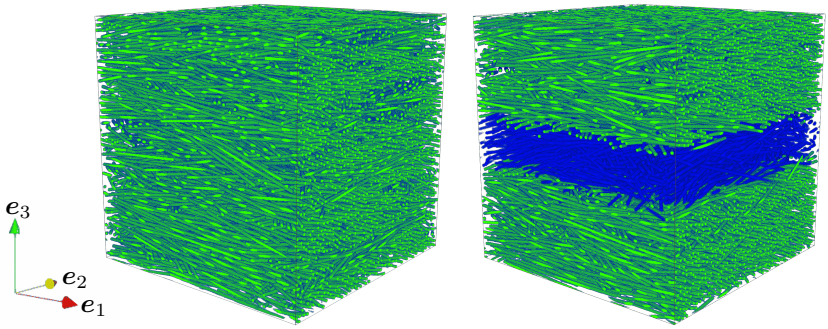
in Figure 3.10(b), we observe that the highest relative differences are computed for the maximum entropy closure for planar tensile directions with angles near $\varphi = \pi/4$, corresponding to the result shown in Table 3.7. Additionally, the plot visualizes that the computed Young's moduli are not exactly orthotropic as the relative difference is not symmetric with respect to the vertical line at $\varphi = \pi/2$, see, e.g, the angles $\varphi = \pi/4$ and $\varphi = 3\pi/4$.

To conclude, it turns out that especially for the almost aligned orientation state the selection of the closure approximation influences the computed effective stiffness noticeably, i.e., up to 10% in this study. As all microstructures represent the prescribed tensors $\boldsymbol{A}_{1,5}$, it is not possible to decide which closure approximation performs best without additional data. For this reason, we emphasize the importance of including additional information on the fiber orientation state to reduce the uncertainty by selecting a closure approximation.

3.4.6 Application to a PA66GF35 material

In this section, we apply the OCS method to an injection molded PA66GF35 composite with experimental data provided by Hessman et al. (2019; 2021). The material is reinforced with fibers of $10\mu\text{m}$ diameter, making up a volume fraction of $\phi = 19.3\%$. Mehta and Schneider (2022) fit the measured length distribution (Hessman et al., 2019) with a Weibull distribution, resulting in a volume-weighted mean $m = 332.16\mu\text{m}$ and a standard deviation $s = 127.64\mu\text{m}$ as distribution parameters. Concerning the fiber orientation state, a skin-core-skin distribution is

observed which is typical for injection molded composites (Bay and Tucker III, 1992a;b; Breuer et al., 2021).



(a) Microstructure with mean data **(b)** Sandwich microstructure

Figure 3.11: Microstructures generated with mean data and with data for a sandwich structure according to Hessman et al. (2019; 2021). Figure adapted from Figure 11 of Lauff et al. (2023).

To analyze the influence of whether the layer structure is explicitly modeled or not, in analogy to Mehta and Schneider (2022), we generate microstructures with a mean fiber orientation tensor

$$\boldsymbol{A}_{\text{mean}} \hat{=} \operatorname{diag}(0.7855, 0.1962, 0.0183) \tag{3.39}$$

over the whole height as well as skin-core-skin layered microstructures with

$$\begin{aligned} \boldsymbol{A}_{\text{skin}} &\hat{=} \operatorname{diag}(0.8602, 0.1227, 0.0171) \\ \boldsymbol{A}_{\text{core}} &\hat{=} \operatorname{diag}(0.2255, 0.7424, 0.0321), \end{aligned} \tag{3.40}$$

where the core layer occupies one sixth of the total height. Both the fiber orientation data and the height of the core layer is extracted from Hessman et al. (2019; 2021). For a comparison with the results given by Mehta

and Schneider (2022), we choose the same cubic cell size $Q_i = 800\mu\mathrm{m}$, a resolution $h = 2\mu\mathrm{m}$ and consider ten realizations. The boundaries between the layers are characterized by a soft constraint forcing the midpoint of a fiber to be in its respective layer. In Figure 3.11, generated mean and sandwich microstructures are shown.

Taking a look at the sandwich microstructure in Figure 3.11(b), we notice the different preferred directions of the fibers for the skin and core layers resulting from the prescribed fiber orientation tensors $\boldsymbol{A}_{\text{skin}}$ and $\boldsymbol{A}_{\text{core}}$.

The computed Young's moduli in $\boldsymbol{e}_1$- and $\boldsymbol{e}_2$-direction are listed in Table 3.8. Mehta and Schneider (2022) use the exact closure. In brackets the relative error of the computed Young's modulus compared to the experimental data is shown.

	E_1 GPa	E_2 GPa
Experiments	10.34 ± 0.40	5.50 ± 0.10
(Hessman et al., 2021, Fig. 2)	-	-
Sandwich	10.17 ± 0.04	5.96 ± 0.01
	[1.64%]	[8.18%]
Mean data	9.99 ± 0.03	5.47 ± 0.01
	[3.38%]	[0.55%]
Sandwich	10.42 ± 0.03	5.78 ± 0.00
(Mehta and Schneider, 2022, Tab. 5)	[0.77%]	[5.09%]
Mean data	9.91 ± 0.03	5.56 ± 0.02
(Mehta and Schneider, 2022, Tab. 5)	[4.16%]	[1.09%]

Table 3.8: Comparison of the experimental results Hessman et al. (2021) and the computed mechanical properties obtained by using the OCS method or the SAM algorithm Mehta and Schneider (2022) with exact closure. Table adapted from Table 8 of Lauff et al. (2023).

Considering the computed standard deviations, we obtain an insignificant random error for all generated microstructures. In fact, the standard

deviation of the experiments is one order of magnitude higher. For the Young's modulus in $\boldsymbol{e}_1$-direction E_1, we observe that by using the sandwich structure a close approximation to the experimental data for both microstructure generators is obtained. Using the mean data leads to an underestimation of the modulus E_1 with higher differences than the sandwich structure, up to 3.38% for the OCS method and 4.16% for the SAM algorithm. In contrast, the transverse Young's modulus E_2 for the mean data fits to the experimental data with high accuracy. However, the sandwich structure leads to a significantly overestimated modulus E_2 with relative errors of 8.18% for the OCS method and 5.09% for the SAM algorithm. For the transverse modulus, there is a remarkable difference between the microstructure generators.

Taking a look at the runtime, for the OCS method, the mean runtime to generate the microstructures is about 100 minutes for the mean structures and 110 minutes for the sandwich structures. In contrast, Mehta and Schneider (2022) compute a runtime below two minutes for all generated microstructures. Notice that for this study a different desktop computer is used. The smaller runtime for the SAM algorithm is characteristic of collective-rearrangement methods, whereas the OCS method is a sequential insertion algorithm. Still, we observe that sequential insertion methods are capable of generating industrially relevant fiber microstructures with a reasonable computational effort, displaying a good agreement with experimental data.

3.5 Summary and conclusion

In this chapter, we presented the Orientation Corrected Shaking method based on the two-stage shaking algorithm by Li et al. (2022) for generating microstructures with almost planar fiber arrangements. As extensions, we consider periodic boundary conditions and implement a scheme that works for general rectangular unit cells, in contrast to

Li et al. (2022). Additionally, the realized fiber orientation states of the OCS method are investigated. Therefore, we uncover the hidden closure structure by revealing an exact expression of the realized fiber orientation tensors of any order ignoring the non-penetration condition. With this insight at hand, we compute the shaking parameters $\Delta\theta$ and $\Delta\varphi_1$ directly instead of selecting them by trial and error. Last but not least, the procedure of single orientation shaking is presented to overcome inaccuracies during the shaking step as result of the non-penetration condition.

The computational investigations included in this work lead to the following conclusions:

- The influence of the semi-analytic shaking parameter estimation and of the procedure of single orientation shaking on the realized fiber orientation tensors is studied. It turns out that a combination of both strategies is necessary to match the fiber orientation state accurately. Otherwise, we observe significant errors for the fiber orientation tensor of second order, e.g., an absolute error of 34.1% in case of equal shaking parameters for both orthogonal layers and single orientation shaking.
- Due to the user-selected rectangular unit cell size of the OCS method, it is possible to investigate the necessary RVE size. The study reveals rather low random and systematic errors, even for the smallest unit cell rather. Additionally, a good approximation of the orthotropic engineering constants is observed. Hence, the OCS method leads to rather small representative volume elements. We emphasize that this is caused by the combination of periodic boundary conditions with an accurate realization of the fiber volume fraction, as well as the fiber length and orientation distributions.
- The computed effective stiffness of the intrinsic closure approximation of the OCS method is compared with the exact and maximum entropy closures implemented within the framework of the SAM (Schneider,

2017; Mehta and Schneider, 2022) algorithm. We observe differences exceeding ten percent between the three approximation closures, although all microstructures represent the same fiber orientation tensors of second order. Hence, it is confirmed that using only a fiber orientation of second order as input is not sufficient to describe a fiber-reinforced composite. To minimize uncertainties introduced by closure approximations, access to the full fiber orientation tensors of fourth order is necessary.

- Applying the OCS method to an injection molded PA66GF35 material with mean aspect ratio of 33 and volume fraction of 19.3%, shows the capability of generating microstructures for industrial produced materials. By comparing the computed effective stiffness to experimental data, a good coincidence of the longitudinal Young's moduli is observed, especially for the layered sandwich structure. Similar to the microstructures generated by the SAM algorithm based on the exact closure (Mehta and Schneider, 2022), the transverse Young's modulus is overestimated for the OCS method as well – by about 8%, which is still adequate for engineering accuracy. According to Mehta and Schneider (2022), possible reasons for the differences are imprecise fiber orientation and length distributions due to the incomplete segmentation of the fibers during the analysis of the Micro-CT scan, the missing fiber orientation tensors of fourth order and the assumption of the fiber length distribution to be uniform for the entire microstructure.

To conclude, the numerical investigations show that the OCS method is capable of generating representative microstructures for industrial volume fractions and aspect ratios in reasonable time. The synthetic microstructures feature accurately realized properties, as volume fraction and fiber length and orientation distributions. Especially the representation of the fiber orientation state is improved significantly as we adapt the shaking step to account for an accurate realization of the fiber

orientation tensor of fourth order. Hence, the generated microstructures are capable of representing the real microstructure adequately, which leads to a close match between experimental data and the results of computational homogenization. Last but not least, the extensions for a user-selected rectangular size of the unit cell and periodic boundary conditions reduce the RVE sizes resulting in smaller runtimes for the microstructure generation and computational homogenization.

Chapter 4

Microstructures generation of long fiber reinforced composites[1]

4.1 Introduction

In this chapter, we address the challenge of generating packings with high fiber volume fractions for long fiber reinforced composites. More precisely, we aim to realize microstructures for industrial composites with fiber volume fractions up to 30% and aspect ratios exceeding 100. For the microstructure generation, we address two further tasks. First, the size of the representative volume element (RVE) needs to be reduced to enable efficient microstructure generation and computational homogenization. Therefore, we require the descriptive components of the microstructure to be realized accurately. Additionally, we wish to generate periodic geometries to decrease artificial artifacts at the boundaries (Kanit et al., 2003; Sab and Nedjar, 2005; Schneider, 2022). Moreover, we aim to account for the fiber bending, as modeling fibers with straight cylinders necessitates RVEs to be rather large (Jeulin, 2016; Willot, 2017). Secondly, we target an adequate modeling of the fiber lengths. Experiments reveal that long fiber reinforced composites feature

[1] This chapter is based on the Sections 1.2 and 2 to 5 of the publication "Generating microstructures of long fiber reinforced composites by the fused sequential addition and migration method" (Lauff et al., 2024).

fiber length distributions with high standard deviations (Nguyen et al., 2008; Fliegener et al., 2014; Senior and Osswald, 2020) leading to a wide range of fiber lengths. Computing the effective properties requires that the fiber length distribution is captured accurately, i.e., assuming constant fiber lengths is not sufficient (Mehta and Schneider, 2022). Thus, we require an adequate representation of the fiber length distribution.

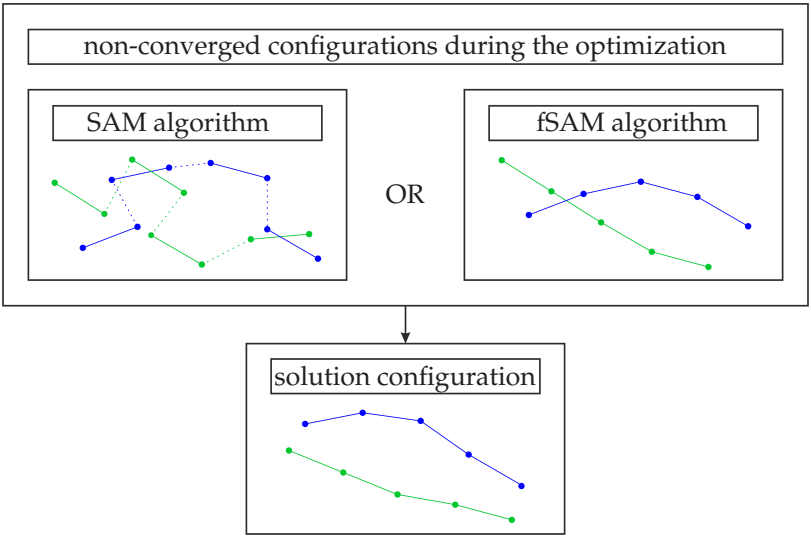
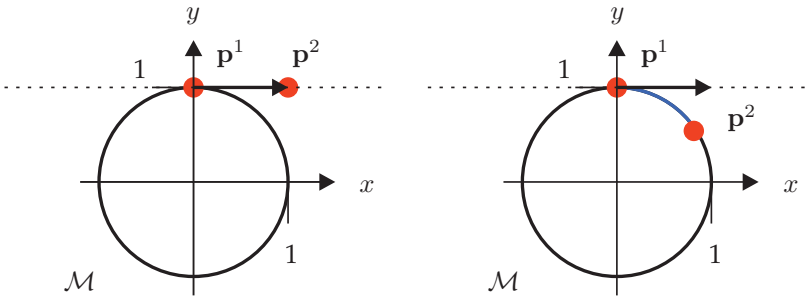


Figure 4.1: Visualization of non-converged configurations during the optimization using the SAM algorithm or the fSAM algorithm as well as of a solution configuration. Figure adapted from Figure 1 of Lauff et al. (2024).

To address these tasks, we present the fused Sequential Addition and Migration (fSAM) algorithm as an alternative approach to the SAM strategy for long curved fibers (Schneider, 2022) in terms of a physically meaningful fiber motion during the optimization. The SAM strategy for long curved fibers discretizes the curved fibers as polygonal chains. Hence, besides other criteria for convergence, e.g., the non-overlap condi-

tion, adjacent segments need to be connected. A *converged* configuration satisfying the non-overlap condition and the coherence condition for all fibers is shown in Figure 4.1. During the optimization procedure with a gradient descent approach, Schneider (2022) moves the segments of each polygonal chain independently. To ensure the coherence condition between adjacent segments, a penalty term is added to the optimization function. As the coherence condition is not fulfilled for all iterative steps, non-converged configurations typically show a positive distance between the fiber segments. A non-converged configuration of the SAM algorithm is shown in Figure 4.1, where we highlight the distance between adjacent segments by the dashed connection lines. Due to the additional penalty term, the SAM strategy for long curved fibers suffers from convergence problems for complex microstructures. To overcome this limitation, we aim to fulfill the coherence condition in every iterative step by moving the polygonal chains in a fused way. Hence, non-converged configurations of the fSAM algorithm involve connected fibers, see Figure 4.1. However, by restricting the movement on the admissible space for a connected polygonal chain, the configuration space, i.e., the admissible set during the optimization, is a curved, i.e., non-flat, manifold. In this context, a basic gradient descent approach may lead to iterates which leave the manifold. We illustrate this issue for an optimization problem where the configuration space for the iterates $\mathbf{p}^k \in \mathbb{R}^2$ is the unit circle, see Figure 4.2(a). For Riemannian manifolds $(\mathcal{M}, g)$ with metric g, an optimization on the manifold may be ensured by moving along the geodesics (Do Carmo, 1992; Petersen, 2016), i.e., the shortest lines between two points on the manifold. These replace the straight lines in vector spaces, where no curvature is present. In Figure 4.2(b), a gradient descent step following the geodesic of the unit sphere is shown. In general, the equations governing the geodesics may be understood as mechanical problems with holonomic constraints and no external forces. Hence, moving along a geodesic means integrating the constrained mechanical system for a

unit time with initial conditions, i.e., the location on the manifold and a tangent vector. For enabling fused fiber movement, we first derive the d'Alembert type constrained mechanical system, which governs the geodesics of the manifold describing a polygonal chain. Then, we introduce an efficient numerical integration for the resulting differential algebraic equations.



(a) Basic approach

(b) Approach with iterates along the geodesic

Figure 4.2: Illustration of a gradient descent step with the iterates $\mathbf{p}^1$ and $\mathbf{p}^2$ for an optimization problem with a unit circle as the configuration space $\mathcal{M}$, using the basic approach (a) and an adapted approach moving along the blue highlighted geodesic (b). Figure adapted from Figure 2 of Lauff et al. (2024).

We account for the fiber length distribution by sampling the fiber lengths from the Gamma distribution. The details comprise Section 4.3.3. As a result, extremely long fibers may occur, discretized with a high number of segments. However, the dimension of the system of equations which is solved for the numerical integration of the constrained mechanical system increases with the number of segments. As the effort of direct solvers scales cubically with the dimension, extremely long fibers lead to a rather long runtime. To handle this issue, we propose a workaround for extremely long fibers. To be more precise, a fiber discretized with

more segments than a maximum number is divided in smaller subchains, which move separately. The coherence conditions between these subchains is only ensured for the final configuration by adding a respective penalty term to the optimization function. We refer to Section 4.3.4 for more details.

For the computational investigations described in Section 4.4, we first discuss the improvements of the microstructure generation with the fSAM algorithm by comparing it to the SAM algorithm for long fibers (Schneider, 2022). After identifying the necessary resolution and RVE size, we study the influence of the maximum segment length which is used to discretize the curved fibers. Moreover, we show the capability of the fSAM algorithm to generate packings with high fiber volume fractions for long fibers. Furthermore, we apply the fSAM algorithm to an industrial PPGF30 material, comprised of a polypropylene matrix reinforced by E-glass fibers with a volume content of 13.22%, accounting for its fiber length distribution.

4.2 Optimization on the configuration space of curved fibers

4.2.1 Riemannian manifolds and submanifolds

In this manuscript, we consider *Riemannian manifolds* $(\mathcal{M}, g)$ (Do Carmo, 1992; Petersen, 2016), i.e., real, smooth manifolds $\mathcal{M}$ equipped with a metric g, which is a family of Euclidean inner products on the tangent spaces $T_{\mathbf{x}}\mathcal{M}$ that depends smoothly on the point $\mathbf{x} \in \mathcal{M}$. With the metric, the energy of a curve $\mathbf{c} : [0, 1] \to \mathcal{M}$, parametrized by arc length t, is defined by

$$E(\mathbf{c}) = \frac{1}{2} \int_0^1 g^{\mathcal{M}}_{\mathbf{c}(t)} \left(\dot{\mathbf{c}}(t), \dot{\mathbf{c}}(t) \right) \, \mathrm{d}t. \tag{4.1}$$

Suppose that a submanifold $\mathcal{M}$ of the n_{dim}-dimensional Euclidean space $\mathbb{R}^{n_{\text{dim}}}$ with scalar product $\langle .,. \rangle_{\mathbb{R}^{n_{\text{dim}}}}$ is given in terms of a constraint function $\mathbf{\Phi}$ which has $\mathbf{0}$ as a regular value. Then, the tangent space $T_{\mathbf{x}}\mathcal{M}$ arises as the null space of the constraint Jacobian

$$T_{\mathbf{x}}\mathcal{M} = \text{null}\left(\frac{\partial \mathbf{\Phi}\left(\mathbf{x}\right)}{\partial \mathbf{x}}\right), \quad \mathbf{x} \in \mathbf{\Phi}^{-1}(\mathbf{0}) \equiv \mathcal{M}. \tag{4.2}$$

The submanifold $\mathcal{M}$ naturally inherits the Riemannian metric of the ambient space

$$g_{\mathbf{x}}\left(\mathbf{v}_1, \mathbf{v}_2\right) = \langle \mathbf{v}_1, \mathbf{v}_2 \rangle_{\mathbb{R}^{n_{\text{dim}}}}, \quad \mathbf{v}_1, \mathbf{v}_2 \in T_{\mathbf{x}}\mathcal{M} \subseteq \mathbb{R}^{n_{\text{dim}}}. \tag{4.3}$$

For such a submanifold $\mathcal{M}$, the geodesic, i.e., the shortest path between two points on the manifold (Do Carmo, 1992; Petersen, 2016), is obtained as the minimum of the energy functional in Equation (4.1)

$$\frac{1}{2}\int_0^1 g_{\mathbf{x}}\left(\dot{\mathbf{c}}(t), \dot{\mathbf{c}}(t)\right)\, \mathrm{d}t \longrightarrow \min_{\mathbf{c}:[0,1]\to\mathbb{R}^{n_{\text{dim}}},\ \text{s.t. } \mathbf{\Phi}(\mathbf{c}(t))=\mathbf{0}} \tag{4.4}$$

subject to the constraints $\mathbf{c}(0) = \mathbf{x}_0$ and $\mathbf{c}(1) = \mathbf{x}_1$ for two given points $\mathbf{x}_0, \mathbf{x}_1 \in \mathcal{M}$. The optimization problem in Equation (4.4) may be interpreted as a constrained mechanical system following Newton's (generalized) laws of motion without a potential or external forces. Hence, the equations governing the geodesic motion on the manifold $\mathcal{M}$ may be formulated in the form of the differential-algebraic equations (DAEs) for a general constrained mechanical system (Angeles and Lee, 1989; Betsch, 2005)

$$\begin{aligned} &\mathbf{M}\ddot{\mathbf{c}}(t) + \mathbf{R}\left(\mathbf{c}(t), \boldsymbol{\lambda}(t)\right) = \mathbf{0} \quad \text{with} \quad \mathbf{R}\left(\mathbf{c}(t), \boldsymbol{\lambda}(t)\right) \equiv \left(\frac{\partial \mathbf{\Phi}\left(\mathbf{c}(t)\right)}{\partial \mathbf{c}}\right)^{\mathsf{T}} \boldsymbol{\lambda}(t), \\ &\mathbf{\Phi}\left(\mathbf{c}(t)\right) = \mathbf{0}, \end{aligned} \tag{4.5}$$

depending on a constant symmetric positive-definite (mass) matrix $\mathbf{M}$, a coordinate vector $\mathbf{c}(t)$, a vector the Lagrangian multipliers $\boldsymbol{\lambda}(t)$ and a vector-valued constraint function $\boldsymbol{\Phi}$. The constraint forces are given with

$$\mathbf{R}\left(\mathbf{c}(t), \boldsymbol{\lambda}(t)\right) \equiv \left(\frac{\partial \boldsymbol{\Phi}\left(\mathbf{c}(t)\right)}{\partial \mathbf{c}}\right)^{\mathsf{T}} \boldsymbol{\lambda}(t) \equiv \mathbf{J}\left(\mathbf{c}(t)\right)^{\mathsf{T}} \boldsymbol{\lambda}\left(t\right), \tag{4.6}$$

where $\mathbf{J}$ denotes the Jacobian of the vector-valued constraint function. Suppose that we parametrize a Riemannian manifold $(\mathcal{M}, g)$ by another manifold $\mathcal{M}_E$ with a smooth map

$$\mathbf{m} : \mathcal{M}_E \longrightarrow \mathcal{M}. \tag{4.7}$$

Then, the manifold $\mathcal{M}_E$ inherits the Riemannian metric g via pull-back (Petersen, 2016)

$$\begin{aligned} &h_{\mathbf{p}}\left(\mathbf{w}_1, \mathbf{w}_2\right) \equiv g_{\mathbf{m}(\mathbf{p})}\left(\,\mathrm{d}\mathbf{m}_{\mathbf{p}}\left(\mathbf{w}_1\right), \mathrm{d}\mathbf{m}_{\mathbf{p}}\left(\mathbf{w}_2\right)\right), \\ &\mathbf{p} \in \mathcal{M}_E, \quad \mathbf{w}_1, \mathbf{w}_2 \in T_{\mathbf{p}}\mathcal{M}_E, \end{aligned} \tag{4.8}$$

where $\mathrm{d}\mathbf{m}_{\mathbf{p}}$ is the differential map from the tangent space $T_{\mathbf{p}}\mathcal{M}_E$ onto the tangent space $T_{\mathbf{m}(\mathbf{p})}\mathcal{M}$ at the point $\mathbf{p} \in \mathcal{M}_E$.

4.2.2 Description and discretization of curved fibers

Following Schneider (2022), we consider a cylindrical fiber with length L and we describe its centerline by a twice continuously differentiable curve

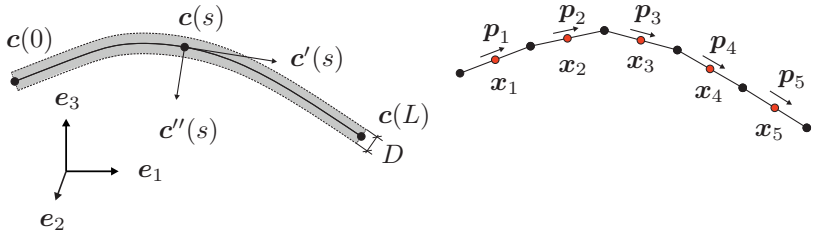
$$\mathbf{c} : [0, L] \longrightarrow Q, \tag{4.9}$$

where we assume a periodic rectangular unit cell $Q = [0, Q_1] \times [0, Q_2] \times [0, Q_3]$. The curve is parametrized by arc length s

$$\|\mathbf{c}'\left(s\right)\| = 1, \quad s \in [0, L], \tag{4.10}$$

and the diameter D is assumed to be constant, see Figure 4.3(a). For the parametrization with the arc length, the curvature is defined as

$$\kappa(s) = \|\mathbf{c}''(s)\|. \tag{4.11}$$



(a) Description of a curved fiber **(b)** Discretization as polygonal chain

Figure 4.3: Description of a curved fiber with a twice continuously differentiable curve parametrized by arc length (a) and discretized polygonal chain (b). Figure adapted from Figure 3 of Lauff et al. (2024).

We discretize a fiber as a polygonal chain with spherocylinders as segments (Schneider, 2022). Then, a fiber consists of n segments with common segment lengths $\ell = L / n$. In the original SAM algorithm for curved fibers (Schneider, 2022), every segment with index $a = 1, \ldots, n$ is parametrized by its midpoint $\mathbf{x}^a \in Q$ and its direction $\mathbf{p}^a \in S^2$, where S^2 denotes the unit sphere, see Figure 4.3(b). This parametrization appears to have $5\,n$ degrees of freedom. However, the condition that consecutive segments have to be connected reduces the degrees of freedom to $3 + 2\,n$. In the SAM algorithm (Schneider, 2022), the connection of consecutive segments is ensured via penalization, which is part of the optimization method used later on.

Alternatively, the connectedness of consecutive segments may be ensured by restricting the coordinate vector

$$\mathbf{f} = \left[\left(\mathbf{x}^1\right)^\mathsf{T} \quad \cdots \quad \left(\mathbf{x}^n\right)^\mathsf{T} \quad \left(\mathbf{p}^1\right)^\mathsf{T} \quad \cdots \quad \left(\mathbf{p}^n\right)^\mathsf{T} \right]^\mathsf{T} \tag{4.12}$$

on the configuration space

$$\mathcal{F} = \left\{ \mathbf{f} \in \mathbb{R}^{6\,n} \,|\, \boldsymbol{\Phi}_1\left(\mathbf{f}\right) = \mathbf{0}, \boldsymbol{\Phi}_2\left(\mathbf{f}\right) = \mathbf{0} \right\}, \tag{4.13}$$

where the n-dimensional vector-valued constraint function $\boldsymbol{\Phi}_1$ ensures that the directions are normed

$$\begin{aligned} &\boldsymbol{\Phi}_1\left(\mathbf{f}\right) = \left[\Phi_1^1\left(\mathbf{f}\right) \quad \cdots \quad \Phi_1^n\left(\mathbf{f}\right) \right]^\mathsf{T} \\ &\text{with} \quad \Phi_1^a\left(\mathbf{f}\right) = \frac{1}{2}\left(\|\mathbf{p}^a\|^2 - 1 \right), \quad a = 1, \ldots, n, \end{aligned} \tag{4.14}$$

and the $3\,(n-1)$-dimensional vector-valued constraint function $\boldsymbol{\Phi}_2$ accounts for the connectedness of the fiber

$$\begin{aligned} &\boldsymbol{\Phi}_2\left(\mathbf{f}\right) = \left[\boldsymbol{\Phi}_2^1\left(\mathbf{f}\right)^\mathsf{T} \quad \cdots \quad \boldsymbol{\Phi}_2^{n-1}\left(\mathbf{f}\right)^\mathsf{T} \right]^\mathsf{T} \\ &\text{with} \quad \boldsymbol{\Phi}_2^a\left(\mathbf{f}\right) = \mathbf{x}^a + \frac{\ell}{2}\,\mathbf{p}^a - \left(\mathbf{x}^{a+1} - \frac{\ell}{2}\,\mathbf{p}^{a+1} \right), \quad a = 1, ..., n-1. \end{aligned} \tag{4.15}$$

We follow this strategy for the fSAM algorithm, and aim to account for the vector-valued constraint function $\boldsymbol{\Phi}_2$ directly by the parametrization of a curved fiber. Therefore, we introduce the notation $\mathbf{x}^0$ for the starting point of the fiber. To obtain a completely dimensionless parametrization, we normalize the starting point with

$$\hat{\mathbf{x}}^0 = \hat{\mathbf{Q}}^{-1}\,\mathbf{x}^0 \quad \text{with} \quad \hat{\mathbf{Q}} = \mathrm{diag}(Q_1, Q_2, Q_3), \tag{4.16}$$

where the matrix $\hat{\mathbf{Q}}$ in the context of microstructure generation comprises the dimensions of the unit cell. Then, each connected polygonal chain

may be parametrized via $\left(\hat{\mathbf{x}}^0, \mathbf{p}^1, \ldots, \mathbf{p}^n\right) \in \mathbb{R}^3 \times \left(S^2\right)^n$. To collect the starting point and the directions of the segments in vector-valued form, we define the coordinate vector $\mathbf{q} \in \mathbb{R}^{n_q}$ as

$$\mathbf{q} = \left[\left(\hat{\mathbf{x}}^0\right)^{\mathsf{T}} \quad \left(\mathbf{p}^1\right)^{\mathsf{T}} \quad \cdots \quad \left(\mathbf{p}^n\right)^{\mathsf{T}}\right]^{\mathsf{T}} \tag{4.17}$$

where the dimension n_q of the coordinate vector is

$$n_q = 3\,(n+1). \tag{4.18}$$

Hence, the admissible configuration space of a polygonal chain parametrized via the vector $\mathbf{q}$ (4.17) is given by the set

$$\mathcal{R} = \left\{\, \mathbf{q} \in \mathbb{R}^{n_q} \mid \boldsymbol{\Phi}_1\left(\mathbf{f}\left(\mathbf{q}\right)\right) = \mathbf{0} \,\right\}, \tag{4.19}$$

where the coordinate vector $\mathbf{f}$ derives from the relation

$$\begin{aligned} &\mathbf{f}\left(\mathbf{q}\right) = \left[\left(\mathbf{x}^1\left(\mathbf{q}\right)\right)^{\mathsf{T}} \quad \cdots \quad \left(\mathbf{x}^n\left(\mathbf{q}\right)\right)^{\mathsf{T}} \quad \left(\mathbf{p}^1\right)^{\mathsf{T}} \quad \cdots \quad \left(\mathbf{p}^n\right)^{\mathsf{T}}\right]^{\mathsf{T}}, \quad \mathbf{q} \in \mathcal{R}, \\ &\text{with} \quad \mathbf{x}^a\left(\mathbf{q}\right) = \hat{\mathbf{Q}}\,\hat{\mathbf{x}}^0 + \sum_{b=1}^{a-1} \ell\,\mathbf{p}^b + \frac{\ell}{2}\,\mathbf{p}^a, \quad a = 1, \ldots n. \end{aligned} \tag{4.20}$$

The configuration space $\mathcal{R}$ (4.19) consists of (products of) the rectangular box $[0,1] \times [0,1] \times [0,1]$ (with periodic boundary conditions) for the normalized starting point $\hat{\mathbf{x}}^0$ and of the unit sphere S^2 for the directions of the segments $\mathbf{p}^a$. As the configuration space $\mathcal{R}$ parametrizes the admissible configuration space for the coordinate vector $\mathbf{f} \in \mathbb{R}^{6\,n}$, it turns out to be a Riemannian manifold $(\mathcal{R}, g)$ (Petersen, 2016) with a natural metric g, inherited from the known scalar product of the Euclidean space. Due to the restriction of the directions on the unit sphere, the tangent space $T_{\mathbf{q}}\mathcal{R}$ at $\mathbf{q} \in \mathcal{R}$ arises as the null space of the constraint Jacobian

$$T_{\mathbf{q}}\mathcal{R} = \operatorname{null}\left(\frac{\partial \boldsymbol{\Phi}_1\left(\mathbf{f}\left(\mathbf{q}\right)\right)}{\partial \mathbf{q}}\right). \tag{4.21}$$

According to the derivation in Appendix B, the Riemannian metric g of the manifold $\mathcal{R}$ is constant $g_{\mathbf{q}} \equiv g$ and given in the explicit form

$$g\left(\dot{\mathbf{q}}_1, \dot{\mathbf{q}}_2\right) = \dot{\mathbf{q}}_1^{\mathsf{T}}\, \mathbf{G}\, \dot{\mathbf{q}}_2, \quad \mathbf{q} \in \mathcal{R}, \quad \dot{\mathbf{q}}_1, \dot{\mathbf{q}}_2 \in T_{\mathbf{q}}\mathcal{R}, \tag{4.22}$$

with the constant metric matrix

$$\mathbf{G} = \begin{bmatrix} n\,\hat{\mathbf{Q}}^2 & f_1\,\ell\,\hat{\mathbf{Q}} & f_2\,\ell\,\hat{\mathbf{Q}} & \cdots & f_n\,\ell\,\hat{\mathbf{Q}} \\ & f_{d,1}\,\mathbf{1}_{3\times3} & f_2\,\ell^2\,\mathbf{1}_{3\times3} & \cdots & f_n\,\ell^2\,\mathbf{1}_{3\times3} \\ & & \ddots & & \vdots \\ & & & \ddots & f_n\,\ell^2\,\mathbf{1}_{3\times3} \\ \text{sym} & & & & f_{d,n}\,\mathbf{1}_{3\times3} \end{bmatrix}$$

$$\text{with} \quad f_a = n - a + \frac{1}{2} \quad \text{and} \quad f_{d,a} = \varepsilon\left(\ell, D\right) + \ell^2\left(n - a + \frac{1}{4}\right). \tag{4.23}$$

Here, $\hat{\mathbf{Q}}$ denotes the normalization matrix for the starting point (4.16), ℓ the segment length and $\varepsilon\left(\ell, D\right)$ the volume-specific moment of inertia of a spherocylinder (García, 2015)

$$\varepsilon\left(\ell, D\right) = \frac{I\left(\ell, D\right)}{V\left(\ell, D\right)} = \frac{D^2}{2/3 + \ell/D}\left[\frac{(\ell/D)^3}{12} + \frac{(\ell/D)^2}{6} + \frac{3\,\ell/D}{16} + \frac{1}{15}\right] \tag{4.24}$$

with the volume $V\left(\ell, D\right)$ and the moment of inertia $I\left(\ell, D\right)$ of a spherocylinder. For an exact expression of the moment of inertia $I\left(\ell, D\right)$, we refer to García (2015). To obtain Equation (4.24), the density of a spherocylinder is set to unity. We remark that the vectors with overdots $\dot{\mathbf{q}}_1, \dot{\mathbf{q}}_2 \in T_{\mathbf{q}}\mathcal{R}$ in Equation (4.22) are no time derivatives, but tangent vectors in the tangent space $T_{\mathbf{q}}\mathcal{R}$, and may be velocity vectors.

4.2.3 Adapted gradient descent approach on the configuration space of curved fibers

We aim to solve an optimization problem

$$F(\mathbf{q}) \longrightarrow \min_{\mathbf{q}\in\mathcal{R}} \tag{4.25}$$

with a gradient descent approach on the configuration space $\mathcal{R}$ (4.19) with constant metric g (4.22), where the coordinate vector $\mathbf{q} \in \mathbb{R}^{n_q}$ is restricted to the manifold $\mathcal{R}$ due to the vector-valued constraint function $\mathbf{\Phi}_1$ (4.14). Proceeding with the standard gradient descent on vector spaces does not respect the constraints, in general, as illustrated in Figure 4.2(a). To compute admissible iterates, the gradient descent approach may be adapted by moving along the geodesics, i.e., the shortest paths between two points on the manifold (Do Carmo, 1992; Petersen, 2016), see Figure 4.2(b). According to Equation (4.4), a geodesic on the manifold $\mathcal{R}$ may be obtained by minimizing the energy functional for a curve $\mathbf{q}(t) \in \mathbb{R}^{n_q}$ under the condition that the curve lies on the manifold, i.e., the vector-valued constraint function $\mathbf{\Phi}_1(\mathbf{f}(\mathbf{q}(t)))$ is the zero vector. Then, the system of equations governing the geodesic equals a constrained mechanical system given in the form of the differential-algebraic equations (DAEs) in Equation (4.5). For the geodesic on the manifold $\mathcal{R}$, an explicit form of the system of equations (4.5) may be derived, see Appendix C. Resulting from this derivation, the geodesics on the Riemannian manifold of curved fibers $\mathcal{R}$ (4.19) is governed by

$$\begin{aligned} \mathbf{G}\,\ddot{\mathbf{q}}(t) + \mathbf{J}(\mathbf{q}(t))^{\mathsf{T}}\boldsymbol{\lambda}(t) &= \mathbf{0}, \\ \mathbf{\Phi}_1(\mathbf{f}(\mathbf{q}(t))) &= \mathbf{0}, \end{aligned} \tag{4.26}$$

depending on the constant symmetric positive-definite metric matrix $\mathbf{G} \in \mathbb{R}^{n_q \times n_q}$ (4.23), the coordinate vector $\mathbf{q}(t) \in \mathbb{R}^{n_q}$ (4.17), the vector of Lagrangian multipliers $\boldsymbol{\lambda}(t)$, the vector of constraints $\mathbf{\Phi}_1(\mathbf{f}(\mathbf{q}(t))) \in \mathbb{R}^n$

defined in Equation (4.14) and the transposed Jacobian of the constraint vector $\mathbf{J}(\mathbf{q}(t))^{\mathsf{T}} \in \mathbb{R}^{n_q \times n}$ in explicit form

$$\mathbf{J}(\mathbf{q}(t))^{\mathsf{T}} = \begin{bmatrix} \mathbf{0}_{3\times1} & \mathbf{0}_{3\times1} & \cdots & \mathbf{0}_{3\times1} \\ \mathbf{p}^1(t) & \mathbf{0}_{3\times1} & \cdots & \mathbf{0}_{3\times1} \\ \mathbf{0}_{3\times1} & \mathbf{p}^2(t) & \cdots & \mathbf{0}_{3\times1} \\ \vdots & \vdots & \ddots & \vdots \\ \mathbf{0}_{3\times1} & \mathbf{0}_{3\times1} & \cdots & \mathbf{p}^n(t) \end{bmatrix}. \tag{4.27}$$

The coordinate vector $\mathbf{q}(t)$ and the vector of the Lagrangian multipliers $\boldsymbol{\lambda}(t)$ are curves parametrized with the arc length t. To shorten the expressions, we will suppress this time-dependency further, i.e., we will write

$$\boldsymbol{\lambda} \equiv \boldsymbol{\lambda}(t) \quad \text{and} \quad \mathbf{q} \equiv \mathbf{q}(t). \tag{4.28}$$

For the geodesically complete Riemannian manifold $(\mathcal{R}, g)$, the *exponential mapping* takes a tangent vector $\mathbf{v} \in T_{\mathbf{q}}\mathcal{R}$ and a point on the manifold $\mathbf{q} \in \mathcal{R}$ and computes

$$\exp_{\mathbf{q}}(\mathbf{v}) = \mathbf{q}_v(1), \tag{4.29}$$

where $\mathbf{q}_v : [0,1] \to \mathcal{R}$ is the unique geodesic with the starting point $\mathbf{q}_v(0) = \mathbf{q}$ and the initial tangent vector $\dot{\mathbf{q}}_v(0) = \mathbf{v}$. With this insight at hand, the iterates of the gradient descent approach may be computed via the scheme

$$\mathbf{q}^{k+1} = \exp_{\mathbf{q}^k}\left(-\tau_k \nabla_{\mathbf{q}} F(\mathbf{q}^k)\right), \quad k = 0, 1, \ldots, \tag{4.30}$$

with step size τ_k to enable an admissible optimization procedure on the Riemannian manifold $\mathcal{R}$.

4.2.4 D'Alembert type constrained mechanical system governing the geodesics

Due to the presence of the Lagrange multipliers $\boldsymbol{\lambda}$ in the system of equations (4.26), we need to solve for $n_q + n$ unknowns, although the system has only $n_q - n$ degrees of freedom. There is a systematic procedure to reduce degrees of freedom to n_q unknowns, called *d'Alembert principle*. This strategy is based on identifying the tangent space $\dot{\mathbf{q}} \in T_{\mathbf{q}}\mathcal{R}$ at $\mathbf{q} \in \mathcal{R}$ explicitly. To do so, we differentiate the condition $\boldsymbol{\Phi}_1(\mathbf{f}(\mathbf{q})) = \mathbf{0}$ with regard to the time

$$\mathbf{J}(\mathbf{q})\,\dot{\mathbf{q}} = \mathbf{0}, \tag{4.31}$$

which uncovers that the tangent space $\dot{\mathbf{q}} \in T_{\mathbf{q}}\mathcal{R}$ at $\mathbf{q} \in \mathcal{R}$ arises as the null space of the constraint Jacobian $\mathbf{J}(\mathbf{q})$. Let the vectors $\mathbf{t}_j \in \mathbb{R}^{n_q}$ ($j = 1, \ldots, n_q - n$) be a basis of the tangent space $T_{\mathbf{q}}\mathcal{R}$. Then, the *null space matrix* $\mathbf{P}(\mathbf{q}) \in \mathbb{R}^{n_q \times (n_q - n)}$ (Betsch, 2005) may be constructed such that its range, also called column space, is equal to the tangent space

$$\text{range}\left(\mathbf{P}(\mathbf{q})\right) \equiv T_{\mathbf{q}}\mathcal{R} = \text{null}\left(\mathbf{J}(\mathbf{q})\right), \tag{4.32}$$

using the basis vectors $\mathbf{t}_j \in \mathbb{R}^{n_q}$ as its column vectors

$$\mathbf{P}(\mathbf{q}) = \begin{bmatrix} \mathbf{t}_0 & \cdots & \mathbf{t}_{n_q - n} \end{bmatrix}. \tag{4.33}$$

By this construction, the null space matrix $\mathbf{P}(\mathbf{q})$ maps any vector $\mathbf{u} \in \mathbb{R}^{n_q - n}$ onto the tangent space $T_{\mathbf{q}}\mathcal{R}$ at $\mathbf{q} \in \mathcal{R}$ (Betsch, 2005)

$$\mathbf{P}(\mathbf{q}) : \mathbb{R}^{n_q - n} \to T_{\mathbf{q}}\mathcal{R}. \tag{4.34}$$

For an arbitrary basis of the tangent space $T_{\mathbf{q}}\mathcal{R}$, the linear mapping in Equation (4.34) is not isometric, in general. To preserve the size of the vector $\mathbf{u}$, we require that the null space matrix is an isometry, i.e., its column vectors correspond to an orthonormal basis (Meyer, 2000). Then,

every tangent vector $\mathbf{v} \in T_{\mathbf{q}}\mathcal{R}$ may be parametrized in the space $\mathbb{R}^{n_q - n}$ with the vector

$$\mathbf{u} = \mathbf{P}^{\mathsf{T}}\,\mathbf{v} \tag{4.35}$$

and the condition $\mathbf{v} = \mathbf{P}\,\mathbf{u}$ holds. Betsch (2005) derives an explicit formulation for the isometric null space matrix of the double spherical pendulum. Extending this formulation to the considered polygonal chain leads to

$$\begin{aligned} \mathbf{P}(\mathbf{q}) &= \begin{bmatrix} \mathbf{1}_{3\times3} & \mathbf{0}_{3\times3} & \cdots & \mathbf{0}_{3\times3} \\ \mathbf{0}_{3\times2} & \mathbf{P}^1(\mathbf{p}^1) & \cdots & \mathbf{0}_{3\times2} \\ \vdots & \vdots & \ddots & \vdots \\ \mathbf{0}_{3\times2} & \mathbf{0}_{3\times2} & \cdots & \mathbf{P}^n(\mathbf{p}^n) \end{bmatrix} \\ \text{with} \quad \mathbf{P}^a(\mathbf{p}^a) &= \begin{bmatrix} \mathbf{r}^a(\mathbf{p}^a) & \mathbf{s}^a(\mathbf{p}^a) \end{bmatrix}, \end{aligned} \tag{4.36}$$

where the column vectors of the submatrices $\mathbf{P}^a(\mathbf{p}^a)$ characterize the tangent space for each segment direction

$$\begin{aligned} &\mathbf{r}^a(\mathbf{p}^a) = \mathbf{R}^a\,\mathbf{e_1}, \quad \mathbf{s}^a(\mathbf{p}^a) = \mathbf{R}^a\,\mathbf{e_2} \\ &\text{with} \quad \mathbf{R}^a = (\mathbf{e}_3 \cdot \mathbf{p}^a)\,\mathbf{1}_{3\times3} + [\mathbf{e}_3 \times \mathbf{p}^a]_\times + \frac{(\mathbf{e}_3 \times \mathbf{p}^a) \otimes (\mathbf{e}_3 \times \mathbf{p}^a)}{1 + \mathbf{e}_3 \cdot \mathbf{p}^a}. \end{aligned} \tag{4.37}$$

Here, the formulation $[\mathbf{e}_3 \times \mathbf{p}^a]_\times$ denotes a skew-symmetric matrix with corresponding axial vector $\mathbf{e}_3 \times \mathbf{p}^a$, see Section 1.4. As the null space matrix $\mathbf{P}(\mathbf{q})$ is constructed such that the product $\mathbf{P}(\mathbf{q})^{\mathsf{T}}\,\mathbf{J}(\mathbf{q})^{\mathsf{T}}$ is a zero matrix, the equivalent form of Equation (4.26)

$$\begin{aligned} \mathbf{P}(\mathbf{q})^{\mathsf{T}}\,\mathbf{G}\,\ddot{\mathbf{q}} &= \mathbf{0}, \\ \mathbf{\Phi}_1\left(\mathbf{f}\left(\mathbf{q}\right)\right) &= \mathbf{0}, \end{aligned} \tag{4.38}$$

leads to a system of equation with n_q unknowns.

4.2.5 Numerical integration of the d'Alembert type constrained mechanical system

For the numerical integration of Equation (4.38), we follow Betsch (2005) and use the energy conserving time integration scheme introduced by Gonzalez (1999). We briefly introduce the main aspects of the numerical integration scheme, especially with respect to the considered use case. For more details, we refer to Betsch (2005).

We are interested in the evolution of the coordinate vector $\mathbf{q}$ in the time interval $I = [0, 1]$. For the numerical integration, we divide the time interval I into n_t subintervals of length $\Delta t = 1 \,/\, n_t$. On a single time interval $I_j = [t_j, t_{j+1}]$, we approximate the coordinate vector and its first time derivative via

$$\begin{aligned} \mathbf{q}(t) &\approx \mathbf{q}_j + \frac{t - t_j}{\Delta t} \left(\mathbf{q}_{j+1} - \mathbf{q}_j \right), \\ \dot{\mathbf{q}}(t) &\approx \mathbf{v}_j + \frac{t - t_j}{\Delta t} \left(\mathbf{v}_{j+1} - \mathbf{v}_j \right), \end{aligned} \tag{4.39}$$

with given quantities $\mathbf{q}_j \in \mathcal{R}$ and $\mathbf{v}_j \in \mathbb{R}^{n_q}$ at time node t_j. To obtain the coordinate vector at time node t_{j+1}, we solve the discretized differential-algebraic equations

$$\begin{aligned} \mathbf{P}(\mathbf{q}_j, \mathbf{q}_{j+1})^{\mathsf{T}} \, \mathbf{H}(\mathbf{q}_j, \mathbf{q}_{j+1}) &= \mathbf{0}, \\ \boldsymbol{\Phi}_1 \left(\mathbf{f} \left(\mathbf{q}_{j+1} \right) \right) &= \mathbf{0}, \\ \text{with} \quad \mathbf{H}(\mathbf{q}_j, \mathbf{q}_{j+1}) &= \frac{2}{\Delta t} \, \mathbf{G} \left[\mathbf{q}_{j+1} - \mathbf{q}_j \right] - 2 \, \mathbf{G} \, \mathbf{v}_j, \end{aligned} \tag{4.40}$$

via a Newton scheme, see Betsch (2005). $\mathbf{P}\left(\mathbf{q}_j, \mathbf{q}_{j+1}\right)$ denotes the discrete null space matrix and characterizes the null space of the discrete constraint Jacobian $\mathbf{J}(\mathbf{q}_j, \mathbf{q}_{j+1})$. In general, the discrete constraint Jacobian is defined via discrete derivatives (Gonzalez, 1996), see Betsch (2005). For the special case of quadratic constraint function, e.g., as for the considered polygonal chain, the discrete constraint Jacobian simplifies

and is equal to the constraint Jacobian evaluated at the coordinate vector at the midpoint of the time interval $\mathbf{q}_{j+\frac{1}{2}}$

$$\mathbf{J}\left(\mathbf{q}_j, \mathbf{q}_{j+1}\right) = \mathbf{J}\left(\mathbf{q}_{j+\frac{1}{2}}\right). \tag{4.41}$$

Accordingly, the discrete null space matrix $\mathbf{P}\left(\mathbf{q}_j, \mathbf{q}_{j+1}\right)$ equals the null space matrix $\mathbf{P}\left(\mathbf{q}_{j+\frac{1}{2}}\right)$. As the starting point for the Newton iteration, the coordinate vector at time node t_{j+1} is set to

$$\mathbf{q}_{j+1} = \mathbf{q}_j + \Delta t\, \mathbf{v}_j. \tag{4.42}$$

After solving for the coordinate vector $\mathbf{q}_{j+1}$, the velocity is updated

$$\mathbf{v}_{j+1} = \frac{2}{\Delta t}\left(\mathbf{q}_{j+1} - \mathbf{q}_j\right) - \mathbf{v}_j, \tag{4.43}$$

such that all necessary quantities for the next time step are known.

With respect to the iterative Newton scheme, integrating the d'Alembert type scheme (4.38) instead of the basic constrained scheme (4.26) offers an additional advantage in terms of the conditioning of the iteration matrix. Whereas the basic scheme suffers from an ill-conditioned iteration matrix for small time steps, the condition number of the iteration matrix is independent of the time step for the d'Alembert type scheme.

In our implementation, we initially consider $n_t = 1$ subintervals of the full interval I, subdividing the considered interval whenever the Newton scheme fails to converge. As convergence criterion for the Newton scheme, we choose that the norm of the residual vector is below 10^{-4}. If more than ten Newton iterations are necessary, we stop the Newton scheme and restart the time integration with halved time steps. To ensure convergence, we apply the backtracking strategy (Boyd and Vandenberghe, 2009) with parameters $\alpha = 1/3$ and $\beta = 0.9$. A pseudo-code for the numerical integration of the d'Alembert type constrained mechanical system is given in Algorithm 4.

Algorithm 4: Numerical integration of the d'Alembert type constrained mechanical system. Algorithm adapted from Algorithm 1 of Lauff et al. (2024).

Input: $\mathbf{q}_1$, $\mathbf{v}_1$

1: $n_t \leftarrow 1$, $\Delta t \leftarrow 1$
2: **for** $j \leftarrow 1$ **to** n_t **do**
3: Initial update of the coordinate vector $\mathbf{q}_{j+1}$ ▷ Equation (4.42)
4: Computation of the residual vector
5: **while** norm of residual vector $> 10^{-4}$ **do**
6: **if** $j > 10$ **then**
7: $n_t \leftarrow 2\, n_t$, $\Delta t \leftarrow \frac{1}{2}\Delta t$
8: Return to line 2
9: Newton step with backtracking
10: Computation of the residual vector

4.3 Microstructure generation for long fiber reinforced composites

4.3.1 Description of long fiber reinforced composites

We consider a rectangular cell $Q = [0, Q_1] \times [0, Q_2] \times [0, Q_3]$ containing N curved fibers of constant diameter D in a non-penetrating fiber arrangement. The i^{th}-fiber is discretized as a polygonal chain, see Section 4.2.2. The number of segments n_i is chosen such that the segment length ℓ_i is below a defined maximum segment length $\bar{\ell}$

$$n_i = \left\lceil \frac{L_i}{\bar{\ell}} \right\rceil, \quad \ell_i = \frac{L_i}{n_i}, \tag{4.44}$$

where the type $\lceil \cdot \rceil$ denotes the smallest integer larger or equal to a given real number. The location of the fiber is defined by the coordinate vector $\mathbf{q}_i$ (4.17). As we consider a non-penetrating fiber arrangement, the fiber

volume fraction computes as

$$\phi = \frac{\pi D^2}{4Q_1Q_2Q_3} L_{\text{total}} \quad \text{with the total length} \quad L_{\text{total}} = \sum_{i=1}^{N} L_i, \tag{4.45}$$

which is identical to the formula for straight cylinders (Goodman and Goodman, 1969).

For fiber-reinforced composites, it is convenient to use volume-weighted fiber orientation tensors (Kanatani, 1984; Advani and Tucker III, 1987) as compact characteristics for the fiber orientation distribution. In case of a finite number of curved fibers, the realized volume-weighted fiber orientation tensor of second order $\boldsymbol{A}^{\text{r}}$ and of fourth order $\mathbb{A}^{\text{r}}$ compute as

$$\boldsymbol{A}^{\text{r}} = \frac{1}{L_{\text{total}}} \sum_{i=1}^{N} \sum_{a=1}^{n_i} \ell_i \left(\boldsymbol{p}_i^a\right)^{\otimes 2}, \quad \mathbb{A}^{\text{r}} = \frac{1}{L_{\text{total}}} \sum_{i=1}^{N} \sum_{a=1}^{n_i} \ell_i \left(\boldsymbol{p}_i^a\right)^{\otimes 4} \tag{4.46}$$

in tensorial notation. Typically, the fiber orientation tensors of second order $\boldsymbol{A}^{\text{r}}$ are obtained from micro-CT scans (Krause et al., 2010; Wirjadi et al., 2016; Hessman et al., 2019). However, to predict the effective properties accurately also the fiber orientation tensor of fourth order $\mathbb{A}^{\text{r}}$ is necessary (Dray et al., 2007; Müller and Böhlke, 2016; Bauer and Böhlke, 2022a). To obtain an adequate fourth order orientation tensor, closure approximations are applied (Folgar and Tucker III, 1984; Cintra and Tucker III, 1995; Dray et al., 2007; Breuer et al., 2019; Kugler et al., 2020; Karl et al., 2021; 2023). In this manuscript, we use the exact closure (ACG) (Montgomery-Smith et al., 2011a;b).

4.3.2 Fused sequential addition and migration (fSAM) algorithm

In its original form, the sequential addition and migration (SAM) (Schneider, 2017) algorithm is a method for generating periodic microstructures

of short straight fiber-reinforced composites with constant lengths. Additionally, extensions of the basic scheme enable to account for fiber length distributions (Mehta and Schneider, 2022) and long curved fibers discretized as polygonal chains (Schneider, 2022). Microstructure generation with the SAM algorithm proceeds in consecutive steps until the desired fiber volume fraction is reached. For each step, a specified amount of fibers is added randomly to the cell first. Then, an optimization framework is used, converging provided no overlap between fibers is detected and further criteria, e.g., realization of the prescribed fiber orientation tensor $\mathbb{A}$ up to the defined numerical precision, are fulfilled. Considering the extension of the SAM algorithm for long fibers (Schneider, 2022), convergence problems occur as the coherence of adjacent fiber segments is not intrinsically ensured with the fiber parametrization but with an additional penalty term. In order to enable packings with higher fiber volume fractions for longer fibers, in this work we introduce the fused sequential addition and migration (fSAM) algorithm as alternative approach to the SAM algorithm with respect to a fused fiber description and movement, see Section 4.2.

Therefore, we adapt the objective function introduced by Schneider (2022) to

$$F\left(\mathbf{f}_1,\ldots,\mathbf{f}_N\right) \mathrel{\hat{=}} \frac{1}{2}\sum_{i,j=1}^{N}\sum_{a=1}^{n_i}\sum_{b=1}^{n_j}\left(\delta_{ij}^{ab}\right)^2+\frac{w_{\mathbb{A}}}{8}\,N\,\|\mathbb{A}-\mathbb{A}^{\mathrm{r}}\|^2+\frac{w_\rho}{2}\sum_{i=1}^{N}\sum_{a=1}^{n_i-1}\left(\rho_i^a\right)^2 \tag{4.47}$$

with weights $w_{\mathbb{A}}$ and w_ρ, where $\mathbf{f}_i$ denotes the vector of all midpoints and directions of the i^{th}-fiber (4.17). For the SAM algorithm (Schneider, 2022), an additional term for the coherence between segments is considered, which we leave out as we intrinsically fulfill this condition. The first

term captures the non-overlap condition with the quantity

$$\begin{aligned}\delta_{ij}^{ab} &\equiv \left\langle D - \min_{s_i^a, s_j^b \in [-1,1]} d_Q \left(\boldsymbol{x}_i^a + s_i^a \frac{\ell_i}{2} \boldsymbol{p}_i^a, \boldsymbol{x}_j^b + s_j^b \frac{\ell_j}{2} \boldsymbol{p}_j^b \right) \right\rangle_+ \\ &\equiv \langle D - \| \boldsymbol{k}_{ij}^{ab} \| \rangle_+,\end{aligned} \tag{4.48}$$

where the vector $\boldsymbol{k}_{ab}^{ij}$ relates to the smallest periodic distance between two segments and the Macaulay bracket $\langle h \rangle_+ = \max(0, h)$ are used. The second term of $F(\mathbf{f}_1, \ldots, \mathbf{f}_N)$ in Equation (4.47) accounts for the prescribed fiber orientation tensor. As extremely wide angles between segments are unrealistic, the third term of $F(\mathbf{f}_1, \ldots, \mathbf{f}_N)$ in Equation (4.47) aims to limit the maximum bending angle to the prescribed value $\bar{\alpha}$ with the quantity

$$\rho_i^a \equiv \left\langle \cos \bar{\alpha} - \boldsymbol{p}_i^{a+1} \cdot \boldsymbol{p}_i^a \right\rangle_+ . \tag{4.49}$$

Let us discuss the weights $w_{\mathbb{A}}$ and w_ρ. As the function $F(\mathbf{f}_1, \ldots, \mathbf{f}_N)$ has dimension (length)^2 due to the first term, both weights are required to have dimension (length)^2 as well. Following Schneider (Schneider, 2022), we choose $w_\rho = 0.75\, \varepsilon(\ell_i, D)$, where $\varepsilon(\ell_i, D)$ is the volume-specific moment of inertia of a spherocylinder, see Equation (4.24). For the weight $w_{\mathbb{A}}$, Schneider (2022) uses $w_{\mathbb{A}} = \varepsilon(\ell_i, D)$. However, we observed that the fSAM algorithm and its numerical integration leads to slow convergence of the orientation condition for an increased number of segments. Hence, we choose the weight $w_{\mathbb{A}}$ to depend on the number of segments via the relation

$$w_{\mathbb{A}} \equiv \varepsilon(\ell_i, D) \frac{\varepsilon(n_i \ell_i, D)}{n_i \varepsilon(\ell_i, D)} = \frac{\varepsilon(n_i \ell_i, D)}{n_i}. \tag{4.50}$$

In case of a fiber consisting of a single segment, the weight $w_{\mathbb{A}}$ coincides with the SAM algorithm.

We aim to solve the optimization problem with a gradient descent approach parametrized by the coordinate vectors $\mathbf{q}_i$

$$F\left(\mathbf{f}_1, \ldots, \mathbf{f}_N\right) \longrightarrow \min_{\mathbf{q}_i \in \mathcal{R}} . \tag{4.51}$$

Therefore, we need to compute the respective directional derivatives of the objective function. However, the objective function $F\left(\mathbf{f}_1, \ldots, \mathbf{f}_N\right)$ in Equation (4.47) is given in terms of the midpoints and the directions collected in the coordinate vectors $\mathbf{f}_i$. For this parametrization, the directional derivatives are computed via

$$\begin{aligned}
\frac{\partial F\left(\mathbf{f}_1, \ldots, \mathbf{f}_N\right)}{\partial \mathbf{x}_i^a} &\hat{=} -\sum_{j=1}^{N} \sum_{b=1}^{n_j} \delta_{ij}^{ab} \frac{\boldsymbol{k}_{ij}^{ab}}{\left\|\boldsymbol{k}_{ij}^{ab}\right\|}, \\
\frac{\partial F\left(\mathbf{f}_1, \ldots, \mathbf{f}_N\right)}{\partial \mathbf{p}_i^a} &\hat{=} -\sum_{j=1}^{N} \sum_{b=1}^{n_j} \delta_{ij}^{ab} \frac{\ell_i \, s_{ij}^{ab}}{2} \frac{\boldsymbol{k}_{ij}^{ab}}{\left\|\boldsymbol{k}_{ij}^{ab}\right\|} \\
&\quad - w_{\mathbb{A}} \frac{\ell_i \, N}{L_{\text{total}}} \left(\mathbb{A} - \mathbb{A}^{\mathsf{r}}\right) \left[\left(\boldsymbol{p}_i^a\right)^{\otimes 3}\right] \\
&\quad - w_{\rho} \left(\rho_i^a \, \boldsymbol{p}_i^{a+1} + \rho_i^{a-1} \, \boldsymbol{p}_i^{a-1}\right),
\end{aligned} \tag{4.52}$$

according to the SAM algorithm for curved fibers (Schneider, 2022). To obtain the directional derivatives for the coordinate vectors $\mathbf{q}_i$ from Equation (4.52), we have to account for the dependence between these two parametrizations, see Equation (4.20). Then, we obtain the relation

$$\begin{aligned}
\frac{\partial F\left(\mathbf{f}_1, \ldots, \mathbf{f}_N\right)}{\partial \mathbf{q_i}} &= \left(\frac{\partial \mathbf{f}_i}{\partial \mathbf{q}_i}\right)^{\mathsf{T}} \frac{\partial F\left(\mathbf{f}_1, \ldots, \mathbf{f}_N\right)}{\partial \mathbf{f}_i} \\
&= \begin{bmatrix} \hat{\mathbf{Q}} \sum_{a=1}^{n_i} \dfrac{\partial F\left(\mathbf{f}_1, \ldots, \mathbf{f}_N\right)}{\partial \mathbf{x}_i^a} \\ R_1\left(\mathbf{f}_1, \ldots, \mathbf{f}_N\right) \\ \vdots \\ R_{n_i}\left(\mathbf{f}_1, \ldots, \mathbf{f}_N\right) \end{bmatrix}
\end{aligned} \tag{4.53}$$

with

$$R_a\left(\mathbf{f}_1,\ldots,\mathbf{f}_N\right) = F\left(\mathbf{f}_1,\ldots,\mathbf{f}_N\right)\left(\frac{\partial}{\partial \mathbf{p}_i^a} + \sum_{b=a+1}^{n_i} \ell_i \frac{\partial}{\partial \mathbf{x}_i^b} + \frac{\ell_i}{2}\frac{\partial}{\partial \mathbf{x}_i^a}\right), \tag{4.54}$$

where $\hat{\mathbf{Q}}$ denotes the normalization matrix for the starting point (4.16) and ℓ_i the segment length.

For Riemannian manifolds, the gradient computes as the linear map of the directional derivatives by the inverse of the metric matrix (Petersen, 2016). Hence, the gradient of the objective function $F\left(\mathbf{f}_1,\ldots,\mathbf{f}_N\right)$ with respect to the coordinate vectors $\mathbf{q}_i$ follows as

$$\nabla_{\mathbf{q_i}} F\left(\mathbf{f}_1,\ldots,\mathbf{f}_N\right) = \mathbf{G}_i^{-1}\,\frac{\partial F\left(\mathbf{f}_1,\ldots,\mathbf{f}_N\right)}{\partial \mathbf{q}_i} \tag{4.55}$$

with the metric matrix $\mathbf{G}_i$ (4.23), which differs throughout the polygonal chains in case the segment lengths ℓ_i or the numbers of segments n_i are not constant.

As the motion is restricted to a curved manifold, a basis descent gradient approach may leave the optimization space, see Figure 4.2(a). To ensure a motion on the manifold, we compute the iterates of the gradient descent approach moving along the geodesics and account for the periodicity with respect to the normalized starting points. This iterative procedure may be written in the form

$$\mathbf{q}_i^{k+1} = \exp_{\mathbf{q}_i^k}\left(-\tau\,\nabla_{\mathbf{q}_i} F\left(\mathbf{f}_1^k,\ldots,\mathbf{f}_N^k\right)\right), \quad k = 0,1,\ldots, \tag{4.56}$$

where τ denotes the stepsize and $\exp_{\mathbf{q}}(\mathbf{v})$ refers to the exponential mapping, see Equation (4.29), with a tangent vector $\mathbf{v} \in T_{\mathbf{q}}\mathcal{R}$ and a point on the manifold $\mathbf{q} \in \mathcal{R}$. The exponential mapping is realized by numerically integrating the d'Alembert type mechanical constrained system, explained in Section 4.2.5, using the point $\mathbf{q} \in \mathcal{R}$ and the tangent vector $\mathbf{v} \in T_{\mathbf{q}}\mathcal{R}$ as initial condition at time $t_0 = 0$. As the

exponential mapping of a single fiber's coordinate vector is independent of the remaining fibers, the numerical integration may be computed independently for each fiber, thus, the computation may be parallelized directly. We select the stepsize $\tau = 0.501$ (Schneider, 2017). Additionally, we multiply the directional derivatives $\partial F\left(\mathbf{f}_1^k, \ldots, \mathbf{f}_N^k\right)/\partial \mathbf{p}_i^a$ with the stepsize $\tau_p = 0.3$ to prefer translation over rotation, following the SAM algorithm (Schneider, 2017). A pseudo-code for a single iterative optimization step of the fSAM algorithm is given in Algorithm 5.

Algorithm 5: Iterative optimization step of the fSAM algorithm. Algorithm adapted from Algorithm 2 of Lauff et al. (2024).

Input: Coordinate vector $\mathbf{q}_i^k, \quad i = 1, \ldots, N$
Compute the coordinate vectors $\mathbf{f}_i^k$ ▷ Equation (4.20)
for $i \leftarrow 1$ **to** N **do**
  for $a \leftarrow 1$ **to** n_i **do**
    Compute the directional derivatives $\dfrac{\partial F\left(\mathbf{f}_1^k, \ldots, \mathbf{f}_N^k\right)}{\partial \mathbf{x}_i^a}$ and $\dfrac{\partial F\left(\mathbf{f}_1^k, \ldots, \mathbf{f}_N^k\right)}{\partial \mathbf{p}_i^a}$ ▷ Equation (4.52)
  Compute the directional derivative $\dfrac{\partial F\left(\mathbf{f}_1^k, \ldots, \mathbf{f}_N^k\right)}{\partial \mathbf{q}_i}$ ▷ Equation (4.53)
  Compute the gradient $\nabla_{\mathbf{q_i}} F\left(\mathbf{f}_1^k, \ldots, \mathbf{f}_N^k\right)$ ▷ Equation (4.55)
  Compute the updated coordinate vector $\mathbf{q}_i^{k+1}$ ▷ Equation (4.56)
▷ following Sections 4.2.3 to 4.2.5

When computing the gradients with Equation (4.52), most of the time/effort is spent for the evaluation of the inter-segment distances. To generate periodic microstructures, we use periodic distances between the fiber segments. Assuming the fiber segments are smaller than the half of the minimum of the cell dimensions Q_i, the periodic distance

between two points $\boldsymbol{x}, \boldsymbol{y} \in Q$ may be computed as

$$d_Q(\boldsymbol{x}, \boldsymbol{y}) = \sqrt{\sum_{i=1}^{3} \left(\mathcal{P}\left((\boldsymbol{x} - \boldsymbol{y}) \cdot \boldsymbol{e}_i, Q_i\right)\right)^2}, \quad \boldsymbol{x}, \boldsymbol{y} \in Q, \tag{4.57}$$

with the function

$$\mathcal{P}(\xi, L) = \begin{cases} \xi - L, & \text{for } \xi > L/2, \\ \xi + L, & \text{for } \xi \leq -L/2, \\ \xi, & \text{else}, \end{cases} \tag{4.58}$$

see Schneider (2022). To reduce the effort, two main aspects need to be considered. First, a fast computation of the periodic distances is necessary. Therefore, we use a modified Vega-Lago algorithm (Vega and Lago, 1994) introduced in Pournin et al. (2005). Additionally, the number of distance measurements should be reduced. To check only close segments for collision, we use cell-linked lists (Allen and Tildesley, 2017) in combination with nested Verlet lists (Verlet, 1967; Schneider, 2017). For more details on the implementation of these strategies for the distance computation, we refer to previous publications on the SAM algorithm (Schneider, 2017; Mehta and Schneider, 2022; Schneider, 2022).

4.3.3 Gamma distribution as fiber length distribution

Due to the manufacturing processes of fiber-reinforced composites, the fiber lengths vary throughout the component. For short fiber reinforced composites, Mehta and Schneider (2022) show the importance of capturing the varying fiber lengths when computing the effective properties with minimum effort. As for long fiber reinforced composites the fiber lengths are even more varying (Nguyen et al., 2008; Fliegener et al., 2014; Senior and Osswald, 2020), we aim to realize the fiber lengths adequately.

Typically, only the volume-weighted mean m and standard deviation s are available as statistic quantities measured in experiments. To model a fiber length distribution with these input parameters, a distribution type has to be chosen which captures the main characteristics of the measured fiber length distributions. In case of long fiber reinforced polymers, the fiber length distribution involves a monotonically decreasing curve and high standard deviations (Nguyen et al., 2008; Fliegener et al., 2014; Senior and Osswald, 2020). To model such a qualitative behavior, the Gamma distribution may be used, see Figure 4.4, which is defined via the probability density function

$$\rho_{\alpha,\beta}(L) = \frac{\beta^\alpha}{\Gamma(\alpha)} L^{\alpha-1} \exp\left(-\beta\, L\right), \quad L > 0, \tag{4.59}$$

depending on the shape parameter $\alpha > 0$ and the rate parameter $\beta > 0$. For the problem at hand, we need to compute the distribution parameters α and β from the volume-weighted mean m and the standard deviation s. Provided the volume of the considered objects only varies due to the length, e.g., as it holds for straight cylinders with constant diameter, Mehta and Schneider (2022) derive the conditions

$$m = \frac{\langle \ell^2 \rangle}{\langle \ell \rangle}, \quad s^2 = \frac{\langle \ell^3 \rangle}{\langle \ell \rangle} - m^2, \tag{4.60}$$

where the notation $\langle Z \rangle$ is used for the expectation of the random variable Z. As the volume of a curved cylindrical fiber with constant diameter D coincides with the volume of a straight cylindrical fiber with equal diameter (Goodman and Goodman, 1969), the condition (4.60) holds for the considered polygonal chain. For a random variable Z following the Gamma distribution with distribution parameters α and β, the expectation of the n^{th}-power of the random variable Z is given by the

expression (Papoulis and Pillai, 2002)

$$\langle Z^n \rangle = \frac{1}{\beta^n} \prod_{i=1}^{n} (\alpha + i - 1), \quad n \in \mathbb{N}. \tag{4.61}$$

With the expression (4.61) at hand, we reformulate Equation (4.60) to get the system

$$m = \frac{\alpha + 1}{\beta}, \quad s^2 = \frac{\alpha + 1}{\beta^2} \tag{4.62}$$

of equations. Solving for α in the first equation and inserting this expression into the second equation yields the explicit relations

$$\alpha = \frac{m^2}{s^2} - 1, \quad \beta = \frac{m}{s^2}. \tag{4.63}$$

Due to the asymptotic behavior of the Gamma distribution for high standard deviations shown in Figure 4.4, sampling from the Gamma distribution results in numerous fibers with unrealistically small fiber lengths. To overcome this limitation, we only consider fiber lengths exceeding a chosen minimum fiber length. Attention has to be taken that the minimum fiber length is small enough such that the volume-weighted quantities are not influenced significantly. Hence, we choose the minimum fiber length to be equal to the fiber diameter such that also the smallest fiber length is larger than the diameter.

For an accurate realization of the statistic quantities m and s, it is critical to select an adequate sampling strategy, especially when considering high standard deviations as in long fiber reinforced polymers. Due to the advantages of a sampling strategy with scrambled Sobol sequences (Sobol, 1967; 1976) compared to a classic Monte Carlo approach (Hammersley and Handscomb, 1964), see Mehta and Schneider (2022), we use this scheme for the fiber length sampling.

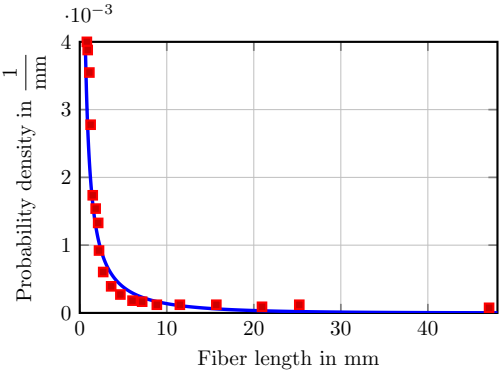


Figure 4.4: Gamma distribution with volume-weighted mean $m = 15.00\text{mm}$ and standard deviation $s = 14.98\text{mm}$ (blue), fitted to fiber length data of a PPGF30 material (Fliegener et al., 2014) (red). Figure adapted from Figure 4 of Lauff et al. (2024).

Besides the Gamma distribution, also other distribution types may be used to model the fiber length distribution of long fiber reinforced polymers, e.g., the Beta, Weibull or log-normal distribution. For the material at hand, the Gamma distribution turns out to be a sufficiently accurate model for the fiber length distribution.

4.3.4 Handling of extremely long fibers

If the fiber lengths are sampled from a fiber length distribution, e.g., the Gamma distribution, extremely long fibers with high numbers of segments n may be present. For the numerical integration of the fiber movement, systems of linear equations of a dimension $n_q = 3(n_i + 1)$ need to be solved. As the effort of direct solvers scales cubically in n_q, it may be extremely time-consuming to determine the fiber movement for fibers with many segments.

To improve the efficiency for increasing aspect ratios, we introduce a *mixed* procedure which combines the advantages of the SAM and fSAM algorithm. If more segments than a prescribed maximum number $\bar{n}$ are

necessary, then the fiber will be divided in

$$n_p = \left\lceil \frac{n_i}{\bar{n}} \right\rceil \tag{4.64}$$

polygonal chains, which will move separately. The first $n_p - 1$ chains comprise $\bar{n}$-segments each, and the last chain collects the remaining segments. To illustrate the separation into multiple chains, a fiber with $n = 15$ segments and a maximum number of segments $\bar{n} = 6$ is shown in Figure 4.5. The distance between adjacent chains is highlighted by the two dashed connection lines.

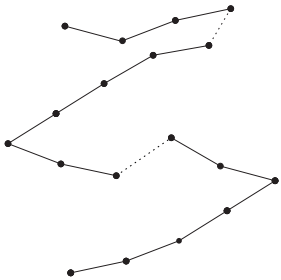


Figure 4.5: Separation of a fiber with $n = 15$ segments and a maximum number of segments $\bar{n} = 6$ into three chains. Figure adapted from Figure 5 of Lauff et al. (2024).

With the introduced separation, we satisfy the coherence condition for the links in each subchain but not between *different* subchains, see Figure 4.5. However, we still require that the coherence is a convergence criterion for the optimization process. To overcome this issue, we account for an additional term in the optimization function with respect to the coherence criterion (Schneider, 2022), which we have left out in

Equation (4.47)

$$F\left(\mathbf{f}_1,\ldots,\mathbf{f}_N\right) \hat{=} \frac{1}{2}\sum_{i,j=1}^{N}\sum_{a=1}^{n_i}\sum_{b=1}^{n_j}\left(\delta_{ij}^{ab}\right)^2 + \frac{w_{\mathbb{A}}}{8}\,N\,\|\mathbb{A}-\mathbb{A}^{\mathrm{r}}\|^2 + \frac{w_\rho}{2}\sum_{i=1}^{N}\sum_{a=1}^{n_i-1}\left(\rho_i^a\right)^2 + \frac{w_\gamma}{2}\sum_{i=1}^{N}\sum_{a=1}^{n_i-1}\left(\gamma_i^a\right)^2. \tag{4.65}$$

The quantity γ_a^i is defined as the smallest periodic distance between two adjacent segments. As we still fulfill the coherence condition within the chains intrinsically, the quantity γ_a^i is only non-zero for adjacent segments which are part of two different subchains. Hence, the quantity γ_a^i may be computed via

$$\gamma_i^a \equiv \left\{ \begin{array}{ll} d_Q\left(\boldsymbol{x}_i^a + \frac{\ell_i}{2}\,\boldsymbol{p}_i^a, \boldsymbol{x}_i^{a+1} - \frac{\ell_i}{2}\,\boldsymbol{p}_i^{a+1}\right), & \text{if } a \in \{\bar{n}, 2\,\bar{n}, 3\,\bar{n}, \ldots\} \\ 0, & \text{else} \end{array} \right\},$$
$$a = 1,\ldots,n_i-1. \tag{4.66}$$

As the fourth term in Equation (4.65) needs to have dimension $(\text{length})^2$, the weight w_γ is dimensionless, and we choose $w_\gamma = 0.75$ (Schneider, 2022). Due to the additional term in the objective function, also the directional derivatives extend

$$\begin{aligned} \frac{\partial F\left(\mathbf{f}_1,\ldots,\mathbf{f}_N\right)}{\partial \mathbf{x}_i^a} &\hat{=} -\sum_{j=1}^{N}\sum_{b=1}^{n_j}\delta_{ij}^{ab}\,\frac{\boldsymbol{k}_{ij}^{ab}}{\left\|\boldsymbol{k}_{ab}^{ij}\right\|} + w_\gamma\left(\boldsymbol{v}_i^a - \boldsymbol{v}_i^{a+1}\right), \\ \frac{\partial F\left(\mathbf{f}_1,\ldots,\mathbf{f}_N\right)}{\partial \mathbf{p}_i^a} &\hat{=} -\sum_{j=1}^{N}\sum_{b=1}^{n_j}\delta_{ij}^{ab}\,\frac{\ell_i\,s_{ij}^{ab}}{2}\,\frac{\boldsymbol{k}_{ij}^{ab}}{\left\|\boldsymbol{k}_{ij}^{ab}\right\|} \\ &\quad - w_{\mathbb{A}}\frac{\ell_i\,N}{L_{\text{total}}}\left(\mathbb{A}-\mathbb{A}^{\mathrm{r}}\right)\left[\left(\boldsymbol{p}_i^a\right)^{\otimes 3}\right] \\ &\quad - w_\rho\left(\rho_i^a\,\boldsymbol{p}_i^{a+1} + \rho_i^{a-1}\,\boldsymbol{p}_i^{a-1}\right) + \frac{w_\gamma\,\ell_i}{2}\,\left(\boldsymbol{v}_i^a + \boldsymbol{v}_i^{a+1}\right), \end{aligned} \tag{4.67}$$

where the vector $\boldsymbol{v}_i^a$ relates to the smallest periodic distance between two adjacent segments.

Attention has to be taken that the maximum number of segments $\bar{n}$ is chosen adequately. On the one hand, if the parameter is too small, convergence problems due to the coherence condition will arise similar to the SAM algorithm. On the other hand, if the maximum number of segments is too large, the runtime for the numerical integration will increase drastically.

4.4 Computational investigations

4.4.1 Setup

For the computational investigations, we use an implementation of the fSAM algorithm in Python with Cython extensions. This implementation features parallelization with OpenMP for collision checks between the fibers and the numerical integration of the fiber movement. The measured runtimes were recorded on a desktop computer with a 8-core Intel i7 CPU and 64GB RAM.

E-glass fibers			PP matrix		
E	$=$	72.0 GPa	E	$=$	1.25 GPa
ν	$=$	0.22	ν	$=$	0.35

Table 4.1: Material properties for the PP matrix and the E-glass fibers (DOW® Chemical Company, 2003; PPG Fiber Glass, 2013). Table adapted from Table 1 of Lauff et al. (2024).

We consider the material parameters of a polypropylene (PP) matrix reinforced by E-glass fibers (DOW® Chemical Company, 2003; PPG Fiber Glass, 2013), see Table 4.1. As our reference setup, we model the

fibers with a diameter of $D = 17\mu\mathrm{m}$. We restrict the segment lengths to $\bar{\ell} = 100\mu\mathrm{m}$ and the maximum angles to $\bar{\alpha} = 60°$. To avoid stress peaks for fibers which are too close (Böhm et al., 2002; Pan et al., 2008), we enforce a minimum inter-fiber distance of 20% of the fiber diameter, i.e., for a diameter of $D = 17\mu\mathrm{m}$ the minimum distance is $3.4\mu\mathrm{m}$. The fiber lengths, the fiber volume fraction and the fiber orientation tensor vary throughout the different studies. As the reference algorithm, we use the pure fSAM algorithm, introduced in Section 4.3.2. Only for the computational studies in the Sections 4.4.5 and 4.4.7, we also use the mixed procedure with a maximum segment number of $\bar{n} = 20$, see Section 4.3.4. For the pure fSAM algorithm and the mixed procedure, we add the fibers which are necessary to reach the desired fiber volume fractions in a single step.

To reduce boundary effects, we generate periodic microstructures. From a computational point of view, this requirement manifests in periodic distance computations between the individual fiber segments. The fiber orientation tensors of fourth order are approximated with the exact closure by a prescribed fiber orientation tensor of second order. As termination criteria for the microstructure generation with the fSAM algorithm, we enforce that the non-overlapping condition is fulfilled strictly. Additionally, the fiber orientation tensor has to be realized with a relative error below 10^{-4} and the angle constraint with an absolute error below 10^{-2}. In case of the mixed procedure, the termination criterion for the coherence condition is a distance between adjacent chains below $10^{-3}D$, where D denotes the fiber diameter.

The effective elastic properties are computed with FFT-based computational homogenization software (Moulinec and Suquet, 1994; 1998). We use a discretization on a staggered grid (Schneider et al., 2016) and a conjugate gradient solver (Zeman et al., 2010; Brisard and Dormieux, 2012) with a relative tolerance of 10^{-5} as termination criterion. Based on six independent load cases, we first compute the effective elasticity tensor.

Second-order fiber orientation tensors are always orthotropic (Cowin, 1985; Bauer and Böhlke, 2022b). Hence, also the fiber orientation tensors of fourth order approximated by the exact closure are at most orthotropic (Bauer and Böhlke, 2022a). For this reason, we report on the effective orthotropic engineering constants approximated from the full effective elastic tensor (Cowin, 1985; Görthofer et al., 2020).

4.4.2 On the difference between the SAM and the fSAM algorithm

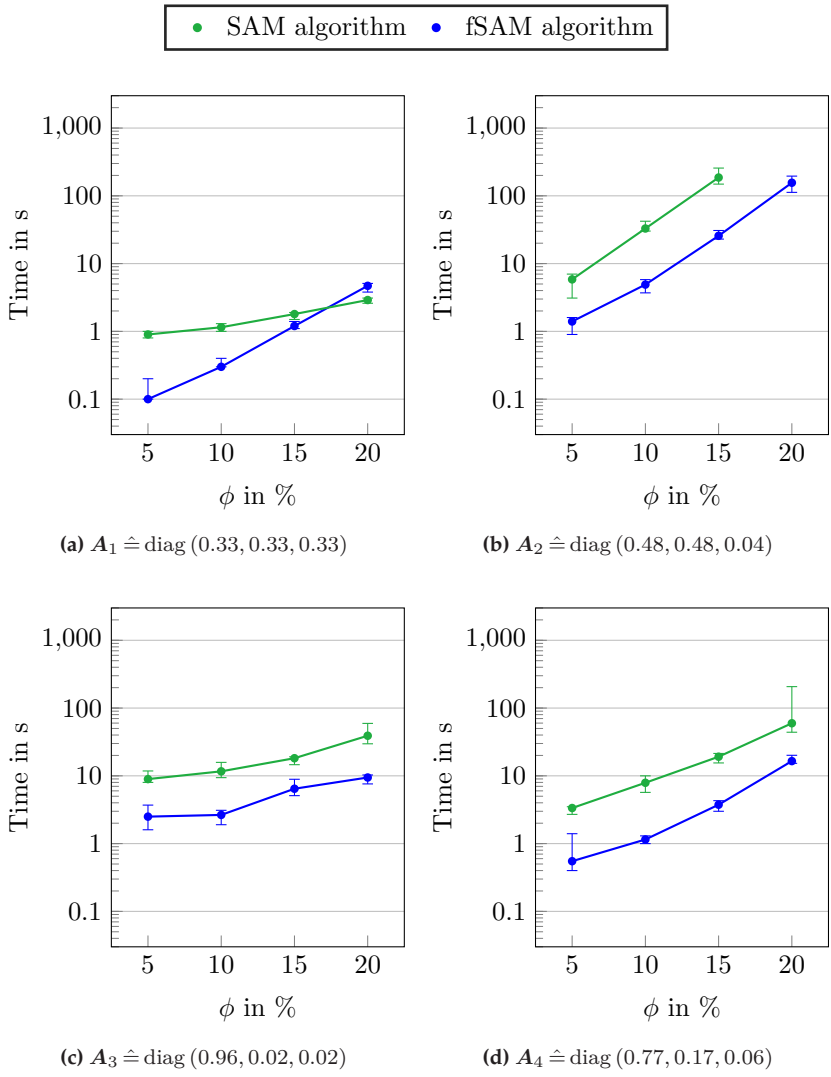
The main goals of the extension towards a fused fiber movement are, on the one hand, to enable faster microstructure generation and, on the other hand, to achieve packings with high fiber volume fractions for long fibers. To assess the improvement, we start our investigations by comparing the efficiency of the microstructure generation for both the SAM and the fSAM algorithm. For this purpose, we generate microstructures with a cubic unit cell and cell dimension $Q_i = 748\mu\mathrm{m}$. The fibers are modeled with a uniform fiber length of $L = 1700\mu\mathrm{m}$, i.e., a fiber aspect ratio of $r_a = 100$. For the study, we consider the fiber volume fractions

$$\phi \in \{5\%, 10\%, 15\%, 20\%\} \tag{4.68}$$

and the second-order fiber orientation tensors

$$\begin{aligned} \boldsymbol{A}_1 &\mathrel{\hat{=}} \mathrm{diag}\,(0.33, 0.33, 0.33)\,, \quad \boldsymbol{A}_2 \mathrel{\hat{=}} \mathrm{diag}\,(0.48, 0.48, 0.04)\,, \\ \boldsymbol{A}_3 &\mathrel{\hat{=}} \mathrm{diag}\,(0.96, 0.02, 0.02)\,, \quad \boldsymbol{A}_4 \mathrel{\hat{=}} \mathrm{diag}\,(0.77, 0.17, 0.06)\,, \end{aligned} \tag{4.69}$$

where the last fiber orientation corresponds to a fiber orientation state experimentally determined for long fiber reinforced thermoplastics (Blarr et al., 2023) manufactured by the LFT-D process (Krause et al., 2003). For every combination of fiber volume fraction, fiber orientation tensor and procedure, we generate ten microstructures. The measured runtimes are visualized in Figure 4.6.



(a) $\boldsymbol{A}_1 \mathrel{\widehat{=}} \mathrm{diag}\,(0.33, 0.33, 0.33)$

(b) $\boldsymbol{A}_2 \mathrel{\widehat{=}} \mathrm{diag}\,(0.48, 0.48, 0.04)$

(c) $\boldsymbol{A}_3 \mathrel{\widehat{=}} \mathrm{diag}\,(0.96, 0.02, 0.02)$

(d) $\boldsymbol{A}_4 \mathrel{\widehat{=}} \mathrm{diag}\,(0.77, 0.17, 0.06)$

Figure 4.6: Comparison of the runtimes for generating microstructures with four different fiber orientation tensors and fiber volume fractions using the SAM algorithm or the fSAM algorithm. Figure adapted from Figure 6 of Lauff et al. (2024).

For all fiber orientation tensors, we observe an increase in effort for packings with higher fiber volume fractions. Also, the considered fiber orientation tensor has an influence on the microstructure generation. According to the study, the easiest fiber orientation tensor to realize is the isotropic case and generating the almost planar isotropic case is the hardest. For example, for the fSAM algorithm and the highest volume fraction it takes on average about 5s to generate the isotropic microstructure but 156s for the almost planar one.

Composites with fiber lengths exceeding the geometry thickness, e.g., industrial long fiber reinforced thermoplastics, feature an almost planar fiber arrangement (Advani and Tucker III, 1990; Görthofer et al., 2019; Dray et al., 2007; Bernasconi et al., 2012). Comparing the two algorithms for the almost planar fiber orientation states $\boldsymbol{A}_2$-$\boldsymbol{A}_4$, it turns out that the microstructure generation with the fSAM algorithm is always faster than using the SAM algorithm. Especially for the highest volume fraction of 20%, tremendous differences in the runtime are measured. Only for a configuration with an isotropic fiber orientation state and a fiber volume fraction of $\phi = 20\%$, the SAM algorithm is slightly faster than the fSAM algorithm. However, this configuration is not representative for typical LFTs.

Let us focus on the almost planar isotropic case shown in Figure 4.6(b) to investigate the differences between the two strategies more thoroughly. For the fiber volume fractions 5%, 10% and 15%, the fSAM algorithm is 4.2, 6.7 and 7.2 times faster than the SAM algorithm. For the highest fiber volume content of 20%, the SAM algorithm fails to converge at all, but the fSAM algorithm is able to generate this microstructure in a mean runtime of 156s. As filler fractions between 20% and 30% are of primary industrial relevance, the SAM algorithm turns out to be incapable of generating the necessary microstructures, whereas the fSAM algorithm reaches this range. The capability of the fSAM algorithm for even higher

fiber volume fractions up to 32% and aspect ratios of 150 is shown in Section 4.4.6.

Due to the numerical integration of the constrained mechanical system, a single optimization step for the fused fiber procedure takes more time than for the SAM algorithm. Still, the fSAM algorithm turns out to be faster overall, which is a result of the significantly lower number of iteration until convergence. Especially, for complex microstructures, e.g., with long fibers or high volume fraction, the SAM algorithm suffers from convergence problems due to the penalty term for the coherence condition. Moving the fibers in a physically meaningful way appears to stabilize the convergence behavior of the optimization algorithm. Hence, we conclude that the adaption of the SAM algorithm with respect to the fSAM algorithm improves the microstructure generation for long fibers immensely. Last but not least, we remark that further reduction in runtime may be achieved by a faster implementation of the numerical integration, e.g., with respect to special strategies for the matrix multiplications or the solution of the linear systems of equations.

4.4.3 Resolution study

When computing effective properties with computational homogenization techniques, the mesh size needs to be chosen fine enough such that an accurate computation of the properties is enabled (Brisard and Dormieux, 2012; Schneider, 2015). For this purpose, we study the influence of the resolution on the effective stiffness with the reference setup from Section 4.4.1 and material parameters listed in Table 4.1. We generate microstructures with a cubic cell-size and cell dimension $Q_i = 612\mu\mathrm{m}$, which turns out to be large enough for representativity in the RVE study in Section 4.4.4. The microstructures are filled with a fiber volume fraction of $\phi = 15\%$. A uniform fiber length of $L = 2550\mu\mathrm{m}$ is considered, i.e., an aspect ratio of $r_a = 150$. Due to the maximum segment length of $\bar{\ell} = 100\mu\mathrm{m}$, the chains consist of 26

segments. We prescribe the fiber orientation tensor of second order $\boldsymbol{A} \mathrel{\hat{=}} \mathrm{diag}(0.77, 0.17, 0.06)$, already used in Section 4.4.2.

For the resolution, we consider four voxel edge-lengths $6.8\mu\mathrm{m}$, $3.4\mu\mathrm{m}$, $2.0\mu\mathrm{m}$ and $1.7\mu\mathrm{m}$. Hence, 2.5 voxels resolve a diameter for the coarsest mesh size, whereas 10 voxels resolve a diameter for the finest mesh size. With respect to the total voxel number per microstructure, this results in 90^3, i.e., more than $72 \cdot 10^4$, voxels for the coarsest mesh size and 360^3, i.e., more than $46 \cdot 10^6$, voxels for the finest mesh size. As the effort for the computational homogenization increases with the total voxel number, the homogenization is significantly more time-consuming for the finest mesh size than for the coarsest mesh size. Comparing the voxel edge-lengths to the minimum segment distance of $3.4\mu\mathrm{m}$, it turns out that the two finest mesh sizes resolve the minimum segment distance with more than one voxel, whereas the voxel edge-length $h = 3.4\mu\mathrm{m}$ equals the minimum segment distance and the coarsest resolution is not sufficient to resolve the minimum segment distance. In Figure 4.7, the same microstructure resolved with different voxel edge-lengths are shown. We observe that the fiber directions show a preference in $\mathbf{e}_1$-direction and are mainly planar, according to the prescribed fiber orientation tensor of second order.

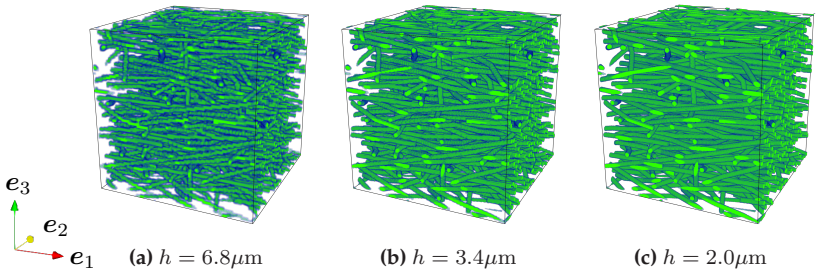


Figure 4.7: Visualization of $(612\mu\mathrm{m})^3$-microstructures resolved with three different voxel edge-lengths h. Figure adapted from Figure 7 of Lauff et al. (2024).

Let us discuss the computed orthotropic engineering constants, see Table 4.2. As we approximate the engineering constants from the full effective elastic tensor, we report on the approximation error err_{orth} to control the quality of the approximation. We observe that the approximation error is 2.35% for the coarsest resolution and decreases below 1% for the three other meshes. Hence, in all cases the approximation is adequate to represent the effective stiffness. For the Young's moduli, it turns out that the Young's modulus in $\mathbf{e}_1$-direction exceeds the moduli in the other directions by about a factor of three due to the preferred fiber arrangement in $\boldsymbol{e}_1$-direction. As the fibers are rather positioned in $\boldsymbol{e}_2$-direction than in $\boldsymbol{e}_3$-direction, the smallest Young's modulus is E_3. Also the shear moduli are notably affected by the anisotropic fiber arrangement. According to the order of the fiber orientation tensor components ($a_1 > a_2 > a_3$), the shear moduli decrease from G_{12} to G_{13} to G_{23}. To assess the error induced by the chosen resolution, we compare the moduli with respect to the finest mesh. The highest error is computed for the Young's modulus E_1 and the coarsest resolution with 14.21%, dropping to 4.08% and 0.70% for the finer resolutions.

h μm	E_1 GPa	E_2 GPa	E_3 GPa	G_{23} GPa	G_{13} GPa	G_{12} GPa	err_{orth} %
6.8	6.10	2.26	2.06	0.75	0.86	1.09	2.35
3.4	6.82	2.32	2.04	0.74	0.85	1.15	0.96
2.0	7.06	2.35	2.03	0.73	0.85	1.17	0.52
1.7	7.11	2.35	2.03	0.73	0.85	1.17	0.44

Table 4.2: Approximated orthotropic engineering constants for the voxel edge-lengths $h = 6.8\mu\text{m}$, $h = 3.4\mu\text{m}$, $h = 2.0\mu\text{m}$ and $h = 1.7\mu\text{m}$. Table adapted from Table 2 of Lauff et al. (2024).

To obtain an error below 3%, we choose a voxel edge-length of $h = 2.0\mu\text{m}$, i.e., 8.5 voxels per diameter. Compared to previous studies for straight

(Müller et al., 2015; Schneider, 2017; Lauff et al., 2023) and curved (Schneider, 2022) fibers with aspect ratios up to 30, where a resolution of 5 voxels per diameter turns out to be sufficient, we observe a higher required resolution for an aspect ratio of 150.

4.4.4 On the size of the representative volume element

A key concept for computational homogenization of materials with random microstructures is the representativity of unit cells. Due to the randomness of the microstructures, the computed apparent elastic properties on cells of finite volume are *random* variables. Only when assuming infinite cell sizes, the apparent properties become *deterministic* descriptors, known as effective properties. For increasing cell sizes, the apparent properties converge to the effective properties (Hill, 1963; Drugan and Willis, 1996; Kanit et al., 2003). In this context, a unit cell is called representative volume element (RVE) if the computed properties are sufficiently close to the effective properties, i.e., the infinite-volume limit of the apparent properties. The computational effort for the homogenization increases with the unit-cell size. Hence, reducing the necessary RVE size is an important factor to ensure time efficient homogenization.

In general, the effective properties are unknown quantities. Hence, it is not possible to compare the apparent properties directly to these quantities. However, the representativity of a unit cell may be assessed without knowing the effective properties in advance. Instead, it is sufficient to monitor two kinds of representativity errors. For a fixed unit-cell size, the *random* error (Kanit et al., 2003; Gloria and Otto, 2011) is quantified by the standard deviation of the apparent properties and measures the differences between the realizations. Increasing the unit-cell size reduces the random error (Dirrenberger et al., 2014; Jeulin, 2016). Besides the random error, the mean of the apparent properties may differ from the effective properties, which is called *systematic* error (Kanit

et al., 2003; Gloria and Otto, 2011). To monitor the systematic error, we compare the mean of the apparent properties for increasing unit-cell sizes until the mean value converges.

For the RVE study, the setup from Section 4.4.3 is considered, where the microstructures are resolved with 8.5 voxels per diameter. We study the representativity of three different cubic cell-sizes with dimensions $Q_i = 476\mu\text{m}$, $Q_i = 612\mu\text{m}$ and $Q_i = 748\mu\text{m}$. Hence, the fibers with length $2550\mu\text{m}$ are several times longer than the cell edge-length, e.g., for the smallest cell by about a factor of 5. With respect to the voxel edge-length of $h = 2\mu m$, the smallest cell is resolved with 238^3, i.e., more than $13 \cdot 10^6$, voxels and the largest cell with 374^3, i.e., more than $52 \cdot 10^6$, voxels. In Figure 4.8, generated microstructures for all three cell sizes are shown.

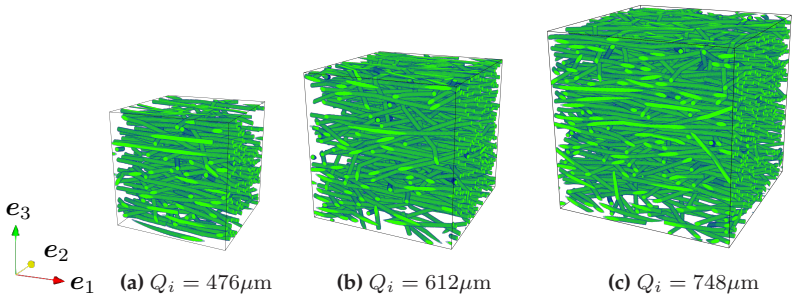


Figure 4.8: Generated microstructures for three different cubic cell-sizes Q_i. Figure adapted from Figure 8 of Lauff et al. (2024).

For each cell size, we compute the mean and the standard deviation of the approximated engineering constants for ten realized microstructures. The results are listed in Table 4.3. Monitoring the orthotropic approximation error shows that the approximation is suitable with an error below 1% for all three cases. Also for the representativity errors, we observe

small deviations, only affecting the second digit. The highest systematic error occurs for the shear modulus G_{12} with a relative error of 0.51%.

Q_i μm	E_1 GPa	E_2 GPa	E_3 GPa	G_{23} GPa	G_{13} GPa	G_{12} GPa	err_{orth} %
476	7.09	2.36	2.03	0.73	0.84	1.17	0.55
	$\pm$0.05	$\pm$0.02	$\pm$0.01	$\pm$0.00	$\pm$0.01	$\pm$0.01	$\pm$0.09
612	7.06	2.35	2.03	0.73	0.84	1.16	0.55
	$\pm$0.03	$\pm$0.01	$\pm$0.00	$\pm$0.00	$\pm$0.00	$\pm$0.01	$\pm$0.06
748	7.06	2.35	2.03	0.73	0.84	1.17	0.54
	$\pm$0.03	$\pm$0.01	$\pm$0.00	$\pm$0.00	$\pm$0.00	$\pm$0.01	$\pm$0.06

Table 4.3: Approximated orthotropic engineering constants for the cubic cell-sizes $Q_i = 476\mu\text{m}$, $Q_i = 612\mu\text{m}$ and $Q_i = 748\mu\text{m}$. Table adapted from Table 3 of Lauff et al. (2024).

It turns out that even the smallest cell size is representative and thus the RVE sizes are small enough to ensure computationally reasonable effort for the homogenization in industrial applications. A further reduction of the cell size is difficult, especially as the smallest cell size only includes 27 fibers and a minimum amount of fibers is necessary to ensure that the microstructure statistics are realized. Additionally, the microstructure generation process is made more challenging as the fibers wrap around the cell even more often. In accordance with previous studies (Schneider, 2022; Lauff et al., 2023), we emphasize that the combination of periodic boundary conditions and an accurate realization of the prescribed descriptors, e.g., as the fourth-order fiber orientation tensor $\mathbb{A}$, lead to extremely small RVE sizes.

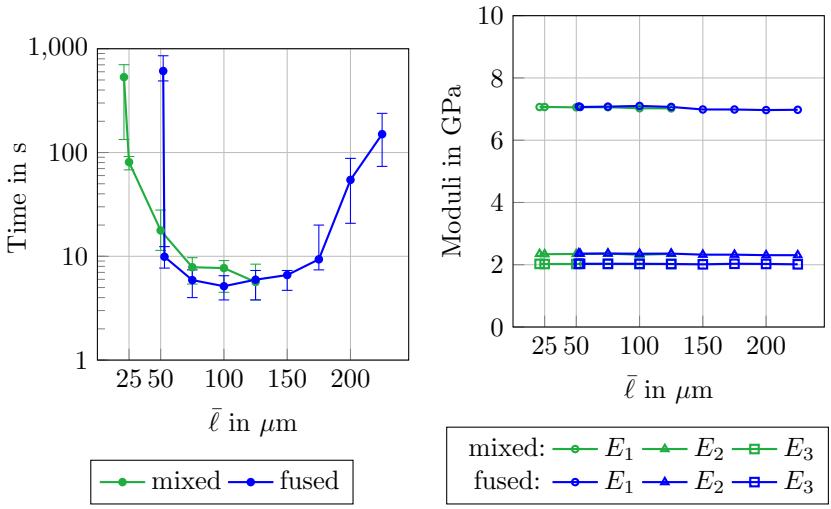
4.4.5 Study on the maximum segment length

In this section, we study the influence of the maximum segment length $\bar{\ell}$ on the runtime for the microstructure generation as well as on the computed effective stiffness. Therefore, we consider the setup from Section 4.4.3 with an edge-length of $Q_i = 612\mu\mathrm{m}$. The selection of the maximum segment length influences the runtime of the microstructure generation significantly. To identify an adequate range for the parameter, we study the runtime for varying maximum segment lengths. The considered maximum segment lengths $\bar{\ell}$ and the resulting numbers of segments n are listed in Table 4.4 with blue color. For all cases, the averaged runtimes of ten microstructure generations are illustrated in Figure 4.9(a) by the blue graph.

$\bar{\ell}$	21	25	50	52	53	75	100	125	150	175	200	225
n	122	102	51	50	49	34	26	21	17	15	13	12

Table 4.4: Considered maximum segment lengths $\bar{\ell}$ and the resulting numbers of segments n. Table adapted from Table 4 of Lauff et al. (2024).

For the mean runtime, we observe a convex shape with a minimum of $5\mathrm{s}$ for a maximum segment length of $\bar{\ell} = 100\mu\mathrm{m}$, i.e., the case where the fibers consist of 26 segments. For higher maximum segment lengths, the runtime is increasing and for $\bar{\ell} = 225\mu\mathrm{m}$, the mean runtime is more than $100\,\mathrm{s}$. On the other hand, the microstructure generation is also more expensive for maximum segment lengths smaller than $\bar{\ell} = 100\mu\mathrm{m}$. Between a maximum segment length of $100\mu\mathrm{m}$ and $52\mu\mathrm{m}$, the gradient is rather small. In contrast, the graph shows an extreme raise for the runtime between $53\mu\mathrm{m}$, i.e., 49 segments, and $52\mu\mathrm{m}$, i.e., 50 segments. The highest mean runtime is measured for $52\mu\mathrm{m}$ of more than $600\,\mathrm{s}$.



(a) Runtimes

(b) Young's moduli

Figure 4.9: Comparison of the runtimes for the microstructure generation (a) and the Young's moduli (b) in terms of different maximum segment lengths $\bar{\ell}$. Figure adapted from Figure 9 of Lauff et al. (2024).

With increasing maximum segment length, fewer but longer segments are considered. Hence, the possibility of the fibers to fill small free spaces within in the unit cell is hindered, which causes an increase in runtime. Especially, for small RVE sizes the maximum segment length needs to be small as fibers wrapping around a unit cell multiple times harden the microstructure generation and more flexibility is necessary. However, for decreasing maximum segment lengths the increasing number of segments leads to more effort for the numerical integration of the constrained mechanical system and the collision checks. Comparing the latter two tasks, the numerical integration of the constrained mechanical system is the main reason for the increase in runtime. For our investigation, the microstructure generation becomes inefficient whenever certain thresholds are exceeded, e.g., the maximum segment

length may not be smaller than $53\mu\mathrm{m}$ and not larger than $175\mu\mathrm{m}$. For this setup, the maximum segment length $\bar{\ell} = 100\mu\mathrm{m}$ is identified as best selection with respect to the runtime. The thresholds and the ideal parameter selection depend on the considered setup.

We aim to study the runtimes for the microstructure generation with even smaller maximum segment lengths. To reduce the effort for the numerical integration due to the high number of segments, we use the mixed procedure, see Section 4.3.4. For the study, we consider a maximum number of segments $\bar{n} = 20$ and the segment lengths listed in Table 4.4 with green text color or boxed in green. Higher maximum segment lengths than $\bar{\ell} = 125\mu\mathrm{m}$ are not considered as the resulting segment numbers are smaller than the maximum number of segments $\bar{n} = 20$. Thus, the fibers are discretized with only one chain and the mixed procedure coincides with the pure fSAM algorithm. The measured runtimes are shown by the green graph in Figure 4.9(a).

We observe that the runtimes for the mixed procedure are always higher than for the maximum segment length $\bar{\ell} = 100\mu\mathrm{m}$ with the fSAM algorithm. Hence, this is still the best parameter and procedure selection for our use case. Considering maximum segment lengths smaller than $\bar{\ell} = 53\mu\mathrm{m}$, where the fibers are discretized with high numbers of segments, the mixed procedure immensely reduces the runtimes. For example, we observe a runtime of $17.8\mathrm{s}$ for the maximum segment length $\bar{\ell} = 50\mu\mathrm{m}$, which is more than 30 times smaller than the runtime for the maximum segment length $\bar{\ell} = 52\mu\mathrm{m}$ using the fSAM algorithm. However, the green graph shows a significant increase in runtime for maximum segment lengths smaller than $\bar{\ell} = 50\mu\mathrm{m}$ as the higher number of chains per fiber results in more violation of the coherence condition. For the smallest considered maximum segment length $\bar{\ell} = 21\mu\mathrm{m}$, a runtime of $533\mathrm{s}$ is needed. A further reduction of the maximum segment length to $\bar{\ell} = 20\mu\mathrm{m}$ is not possible as the segment aspect ratio is only slightly higher than one, but the algorithm requires a pronounced

spherocylindrical, and not a spherical, segment shape. To conclude, it turns out that the mixed procedure enables microstructure generation for high numbers of segments. However, for moderate number of segments, still the lowest runtime is measured for the fSAM algorithm. Hence, we emphasize that the mixed procedure should only be used to handle extremely long fibers, e.g, due to sampling from fiber length distributions.

After studying the influence of the maximum segment length on the runtime of the microstructure generation, we turn our attention to the computed effective stiffnesses. Therefore, we generate microstructures with the maximum segment lengths listed in Table 4.4, using the fSAM algorithm for the blue written maximum segment lengths and the mixed procedure for the green written or boxed ones. Following Section 4.4.3, the generated microstructures are resolved with a voxel edge-length of $h = 2.0\mu\mathrm{m}$. With this setup, the unit cell is representative and the orthotropic approximation is adequate, according to Section 4.4.4. Hence, we generate only one unit cell for each case to compute the approximated orthotropic effective stiffnesses. The Young's moduli are shown in Figure 4.9(b).

The results show that the stiffness of the microstructures is close for all maximum segment lengths. When comparing the differences with the representativity errors, it even turns out that they are in a similar range. This observation corresponds to a previous study (Schneider, 2022), investigating the effective properties between curved fibers with a fixed maximum segment length of $\bar{\ell} = 50\mu m$, i.e., five times the considered diameter of $D = 10\mu\mathrm{m}$, and straight fibers, i.e., the extreme case with a maximum segment length of $\bar{\ell} = \infty$, for different fiber lengths. However, for straight fibers, the microstructure generation and the following homogenization are extremely demanding for high aspect ratios due to the huge necessary unit-cell sizes. Hence, the previous study is restricted to fiber aspect ratios up to $r_a = 90$. By considering rather long maximum

segment lengths instead of completely straight fibers, we are capable of confirming the observation of the previous study (Schneider, 2022) also for a significantly higher aspect ratio of $r_a = 150$. Additionally, it turns out that also using maximum segment lengths which are only slightly larger than the diameter does not influence the effective properties remarkably.

4.4.6 Generation of microstructures with high fiber volume fractions

We aim to study the limits of the microstructure generation using the fSAM algorithm with respect to a packing with high fiber volume fraction. Therefore, we generate microstructures with a cubic cell-size and cell dimension $Q_i = 612\mu\mathrm{m}$, a constant fiber length of $L = 2550\mu\mathrm{m}$ and a fiber orientation tensor of second order $\boldsymbol{A} \mathrel{\hat{=}} \mathrm{diag}(0.77, 0.17, 0.06)$. To pack structures with industrial fiber volume fractions, a high flexibility for the fibers, i.e., a small maximum segment length, is required. Hence, we use the maximum segment length $\bar{\ell} = 53\mu\mathrm{m}$, which is the threshold for an efficient numerical integration of the constrained mechanical system according to Section 4.4.5. Compared to the fiber diameter $D = 17\mu\mathrm{m}$, the segments have an aspect ratio of about 3. To study the efficiency of the algorithm with increasing fiber volume fraction, we generate microstructures starting from 20% in 1% steps up to the fiber volume fraction where the algorithm fails to converge within 10^6 iterations.

In Figure 4.10, the mean and the standard deviation of the runtimes for the microstructure generation are shown, considering ten realizations for each fiber volume fraction. We observe an exponential growth in time for increasing fiber volume fractions. Hence, the smallest runtime is measured for the lowest fiber volume fraction with $21\mathrm{s}$. The limit for the fiber volume fraction is reached for $\phi = 32\%$. Notice that the minimum distance between the fibers of $3.4\mu\mathrm{m}$, i.e., 20% of the

fiber diameter $D = 17\mu\text{m}$, is realized by increasing the diameter of a fiber during the collision checks by 20%. Hence, the minimum distance increases the fiber volume fraction artificially, and without the minimum distance significantly higher fiber volume fractions may be achievable. A microstructure reinforced with $\phi = 32\%$ fiver volume content is shown in Figure 4.11. For this case, the runtime is about $7\,900\text{s}$, i.e., $2\text{h}\,12\text{min}$, which is still a low runtime for a packing with such a high fiber volume fraction generated on an ordinary desktop computer. Typically, long fiber reinforced composites are manufactured up to a fiber volume fraction of 30% (Nguyen et al., 2008; Fliegener et al., 2014). Hence, the study shows the capability of the fSAM algorithm to generate microstructure for industrially used LFTs.

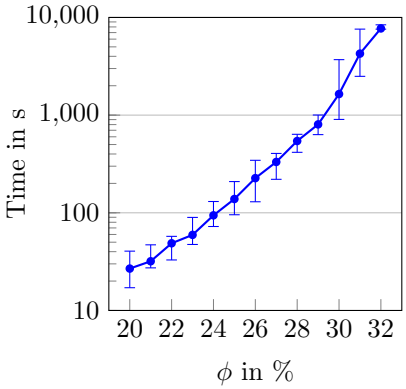


Figure 4.10: Runtimes for the microstructure generation with increasing fiber volume fractions ϕ. Figure adapted from Figure 10 of Lauff et al. (2024).

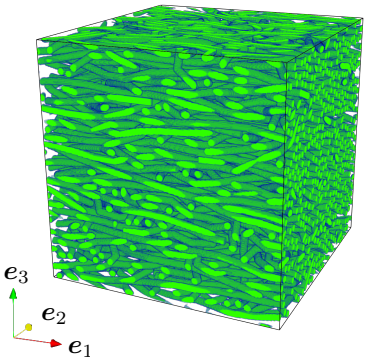


Figure 4.11: Microstructure with aspect ratio $r_a = 150$ and fiber volume fraction $\phi = 32\%$. Figure adapted from Figure 11 of Lauff et al. (2024).

4.4.7 Application to a PPGF30 material accounting for the fiber length distribution

In this section, we apply the fSAM algorithm, see Sections 4.3.2 and 4.3.4, to a PPGF30 material with a fiber volume fraction of $\phi = 13.22\%$ and a second-order fiber orientation tensor $\boldsymbol{A} \hat{=} \operatorname{diag}(0.71, 0.26, 0.03)$ (Fliegener et al., 2014). We model the fiber length distribution given by Fliegener et al. (2014) with a Gamma distribution using a volume-weighted mean of $m = 15.00\mathrm{mm}$ and a standard deviation of $s = 14.98\mathrm{mm}$. The resulting fiber length distribution is shown in Figure 4.4. For the microstructure generation, we consider a rectangular unit cell $Q = [0, 1500\mu\mathrm{m}] \times [0, 1500\mu\mathrm{m}] \times [0, 750\mu\mathrm{m}]$. To ensure an efficient numerical integration of the constrained mechanical systems, we use the mixed procedure with a maximum segment number of $\bar{n} = 20$ and a maximum segment length of $\bar{\ell} = 100$. In Figure 4.12, a generated microstructure is shown. Due to the fiber length distribution, extremely long fibers are realized. For the visualized microstructure, we highlight the longest fiber, which has a length of $L \approx 48\,976\mu\mathrm{m}$, in blue and observe that the fiber wraps around the unit cell multiple times. Also, the oscillation of the fibers is apparent. We aim to realize the volume-weighted mean m and the standard deviation s of the fiber length distribution accurately due to their influence on the effective elastic properties (Mehta and Schneider, 2022). With increasing standard deviation, a higher number of realizations is necessary to obtain adequate statistic quantities. However, when generating microstructures, a large number of fibers results in larger volume element sizes and thus higher computational effort in terms of to the microstructure generation and the subsequent computational homogenization. To reduce the necessary fiber count, we use an improved sampling strategy with scrambled Sobol sequences (Sobol, 1967; 1976) instead of, e.g., the classical Monte Carlo approach. To assess the quality of the realizations, we compare the mean values of the realized statistic

quantities with the desired ones. For the considered ten realizations, we obtain a volume-weighted mean of 14.06mm, which is 6.27% below the desired value of 15.00mm. For the standard deviation, the mean value is 12.50mm, i.e., 16.56% below the desired value of 14.98mm. Hence, the volume-weighted mean is realized quite accurately, whereas we observe significantly higher differences for the standard deviation, which is typical for sampling from distribution functions with high standard deviations.

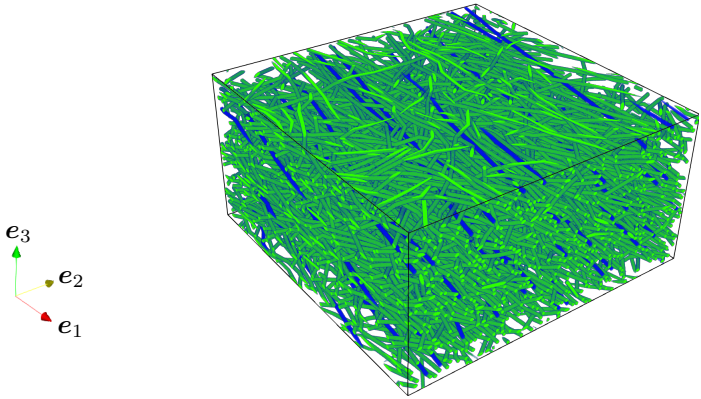


Figure 4.12: Generated microstructure with cell size $Q = [0, 1500\mu\text{m}] \times [0, 1500\mu\text{m}] \times [0, 750\mu\text{m}]$, highlighting the longest fiber with a fiber length of $L \approx 48\,976\mu\text{m}$. Figure adapted from Figure 12 of Lauff et al. (2024).

We wish to compare the stiffness of the generated microstructures with experimental data (Fliegener et al., 2014) and with microstructures generated with the SAM algorithm (Schneider, 2022). Notice that the latter microstructures include fibers with a constant aspect ratio of $r_a = 240$. For this comparison, we generate ten microstructures, where the mean runtime is about 20min. Then, we compute the orthotropic Young's moduli with a voxel edge-length of $h = 2.0\mu\text{m}$, resolving the

generated microstructures with $750 \times 750 \times 375$, i.e., about 211 million, voxels. Following Schneider (2022), we use the material parameters $E = 1.8$GPa and $\nu = 0.35$ (Fliegener et al., 2014; Senior and Osswald, 2020) for the polypropylene matrix. To enable a fair comparison of the runtime with identical hardware, we additionally repeat the study on the SAM algorithm (Schneider, 2022) by generating ten microstructures.

	E_1 GPa	E_2 GPa	E_3 GPa	Runtime min
Experiments (Fliegener et al., 2014)	6.65 -	3.07 -	- -	- -
SAM algorithm (Schneider, 2022)	6.22 $[-6.47\%]$	3.28 $[+6.84\%]$	2.71 -	88.61 ± 35.72 -
fSAM algorithm	6.38 ± 0.02 $[-4.06\%]$	3.30 ± 0.02 $[+7.49\%]$	2.71 ± 0.00 -	19.69 ± 4.14 -

Table 4.5: Comparison of the experimental results (Fliegener et al., 2014) and the computed approximated Young's moduli of microstructures generated with the SAM algorithm (Schneider, 2022) or with the fSAM algorithm. Table adapted from Table 5 of Lauff et al. (2024).

The computed Young's moduli are listed in Table 4.5, where we add the relative difference with respect to the experimental results in brackets. Comparing the Young's modulus E_1, the fSAM algorithm shows a good agreement with the experimental results with a relative underestimation of 4.06%, which is closer than the result for the SAM algorithm with 6.47% deviation. The Young's modulus E_2 is overestimated by both procedures slightly with 6.85% for the SAM and 7.49% for the fSAM algorithm. For the Young's modulus E_3, no experimental results are obtained. However, comparing the two procedures it turns out that the Young's modulus E_3 coincides. Besides the Young's moduli, also the

runtimes of the SAM and the fSAM algorithm are listed in Table 4.5. The mean runtime of the SAM algorithm is about 89min, which is multiple times higher compared to the fSAM algorithm with 20min.

Last but not least, we study the highest realizable fiber volume fraction for the considered setup, still using the fiber length distribution shown in Figure 4.4. Therefore, we increase the fiber volume fraction starting from 15% in 1% steps. For each fiber volume fraction, we consider five realizations. The runtimes are shown in Tab. 4.6. For the highest realizable fiber volume fraction of 19%, the runtime is about 150min, i.e., $2\text{h}30\text{min}$.

ϕ in $\%$	15	16	17	18	19
Runtime	34.14	43.76	57.61	87.15	151.32
min	$\pm$ 5.81	$\pm$ 4.92	$\pm$ 4.06	$\pm$20.95	$\pm$ 23.45

Table 4.6: Runtimes for the microstructure generation of a PPGF material with the fiber length distribution shown in Figure 4.4 and increasing fiber volume fraction. Table adapted from Table 6 of Lauff et al. (2024).

4.5 Summary and conclusion

This work presents the fused sequential addition and migration (fSAM) algorithm to generate microstructures for composites with long, flexible fibers, which is applicable for industrial fiber aspect ratios and volume fractions. Especially, as the fSAM algorithm generates these microstructures in a computationally efficient manner, the approach represents a promising new tool in the field of reconstruction algorithms for long fiber reinforced composites.

According to the SAM algorithm for long curved fibers (Schneider, 2022), we model the fibers as polygonal chains with spherocylinders as

segments and use an optimization framework for the microstructure generation. As main novelty, we enable a physically meaningful fiber movement within the iterative scheme, where the fibers move in a fused way. However, as a result we optimize on a curved manifold. For this case, the iterates of the basic gradient descent approach may leave the optimization space. To ensure admissible iterates, the gradient steps need to move along the geodesic, i.e., the shortest curve between two points on the manifold. In general, such a geodesic is governed by a constrained mechanical system without external forces. Thus, we derive the d'Alembert type constrained mechanical system describing the geodesic of the considered manifold. In a second step, an efficient numerical method for the integration of the constrained mechanical system is presented. Additionally, we discuss the adaption of the SAM algorithm for long curved fibers (Schneider, 2022) to account for the fused fiber movement. For the fiber length distribution, we use the Gamma distribution, which is capable of realizing the main characteristics of the fiber lengths measured for long fiber reinforced microstructures (Nguyen et al., 2008; Fliegener et al., 2014; Senior and Osswald, 2020). In context of extremely long fibers, we introduce a workaround to overcome the high computational effort due to the numerical integration of the constrained mechanical system.

We briefly summarize the findings of the computational investigations:

- First, a study on the efficiency of the SAM algorithm and the fSAM algorithm is provided, considering constant fiber lengths. The results show that generating microstructures with the fSAM algorithm is multiple times faster than with the SAM algorithm. Whereas the SAM algorithm fails to generate microstructures with a fiber volume fraction of 20%, an aspect ratio of about 90 and an almost planar isotropic fiber orientation state, the fSAM algorithm is capable of generating this microstructure in a routine way. The packing with

higher fiber volume fraction is enabled as the fused fiber movement stabilizes the convergence behavior of the optimization algorithm.

- To ensure the representativity of the generated unit cells, even the smallest considered cell size may be used as RVE. In these unit cells only 27 fibers are included. Hence, the fSAM algorithm ensures appropriate cell sizes leading to a reasonable effort for the subsequent computational homogenization.
- A parameter study of the maximum segment length is included in the computational investigations, showing that the selection of the parameter has significant influence on the runtime but almost no effect on the effective properties. On the one hand, the maximum segment length needs to be sufficient small to ensure the necessary flexibility of the fibers. On the other hand, with decreasing maximum segment length more segments are used to discretize the fiber, which leads to an increased effort for the numerical integration of the constrained mechanical system and the collision checks. Hence, for every considered use case an adequate parameter selection is mandatory. Considering the computed effective stiffness for different maximum segment lengths, the deviations are rather small, below 3%.
- To prove the capability of the fSAM algorithm to generate microstructures with industrial fiber volume fraction, a study is included considering constant fiber lengths and an experimentally measured orthotropic fiber orientation tensor of second order $\boldsymbol{A} \hat{=} \operatorname{diag}(0.77, 0.17, 0.06)$ (Blarr et al., 2023). The highest achieved fiber volume fraction is 32% for a fiber aspect ratio of 150, generated in $2\mathrm{h}\,12\mathrm{min}$. Hence, also high-performance materials reinforced by high fiber volume fractions are covered by the algorithm. Indeed, for typical standard materials up to a fiber volume fraction of 25% the runtime is within $3\mathrm{min}$. Studying the maximum fiber volume fractions for varying fiber orientation states may be part of further investigations.

- The method is capable of generating microstructures for an industrial PPGF30 material with a fiber volume fraction of 13.22%, accounting for its fiber length distribution. Sampling from the Gamma distribution leads to extremely long fibers, e.g., in this case up to a length of $49\mathrm{mm}$, i.e., an aspect ratio of $r_a \approx 2\,881$. By comparing the computed effective properties to experimental results, the computed Young's modulus E_1 is in good coincidence with experiments, leading to a relative underestimation by 4.06%. The computed Young's modulus E_2 slightly overestimates the experiments with a relative deviation of 7.49%.

To sum up the numerical investigations, considering physically meaningful fiber motion as the key novelty within the fSAM algorithm improves the capability for generating microstructures of composites with long, curved fibers significantly. Thus, on the one hand, higher fiber volume fractions for long fiber reinforced composites are achievable, enabling microstructure generation also for high-performance LFTs with more than 30% fiber volume content. On the other hand, the microstructure generation is more efficient due to the reduced runtimes. Also, with respect to the subsequent numerical homogenization, reasonable computational effort is ensured by small RVE sizes. The methodology demonstrates to be suitable for industrial materials, featuring fiber length distribution with extremely long fibers, when applied to a PPGF30 material. Moreover, comparing the computed effective properties of generated PPGF30 microstructures to experimental data shows good coincidence.

Chapter 5

Microstructure generation of long fiber reinforced hybrid composites[1]

5.1 Introduction

The microstructure of hybrid fiber-reinforced composites consists of subcells with different characteristics. However, current microstructure generation tools prescribe the desired quantities, like the fiber volume fraction or the fiber orientation distribution, for the *entire* microstructure without distinguishing between specific areas. Hence, these tools are only applicable to composites with location independent descriptors, e.g., to pure discontinuous fiber-reinforced composites with a single fiber volume fraction, fiber length and orientation distribution, but not to materials with location-dependent descriptors. In this chapter, we address the challenge to generate microstructures for hybrid fiber-reinforced composites with continuous and discontinuous long fiber reinforcement, where we target unidirectional fiber orientation states for the continuous fiber-reinforcement. For the microstructure generation tool, we define two additional requirements. First, we aim to minimize the necessary unit cell size for representativity. Therefore, we target microstructures

[1] This chapter is based on the Sections 1.2 and 2 to 5 of the publication "Microstructure generation of long fiber reinforced hybrid composites using the fused sequential addition and migration method" (Lauff et al., 2025b).

with periodic geometry and accurately fulfilled descriptive components, i.e., the fiber volume fraction or the fiber orientation tensor (Kanatani, 1984; Advani and Tucker III, 1987) of desired order. Modeling the fibers with straight geometries leads to unit cell edge-lengths which need to be at least as large as the mean fiber length. As this may be restrictive for long fiber reinforced composites, we account for the fiber bending of long fibers, which permits to decrease the unit cell size compared to straight fibers. As a second task, we need to model the areas between adjacent materials. Depending on the materials and the manufacturing processes, these interfaces may feature a strict separation of the areas or an interlocking where fibers reach into the adjacent layers.

For this purpose, we extend the fused sequential addition and migration algorithm (Lauff et al., 2024) to generate hybrid long fiber reinforced composites. The classical fSAM algorithm (Lauff et al., 2024) models the fibers as polygonal chains and positions the fibers within a periodic unit cell without further restrictions on the fibers' location. To distinguish between different subcells of a hybrid composite, we assign each fiber to a specific subcell and restrict the location of the fiber by enforcing box constraints. In this manuscript, we introduce two types of box constraints. On the one hand, *hard box constraints* require that a fiber is completely located within its subcell, which leads to a strict separation between adjacent subcells. On the other hand, *soft box constraints* enforce that only the midpoints of the segments are within the respective subcell, which enables an interlocking between adjacent subcells. For soft box constraints, the degree of interlocking decreases with decreasing segment lengths. To ensure that interlocking is still possible for small segment lengths, we additionally consider an adapted soft constraint type where only specific midpoints of the segments are restricted.

During the optimization procedure of the fSAM algorithm, the box constraints may be considered in two ways. On the one hand, only the solution configuration at convergence fulfills the box constraints,

which may be realized by adding a penalty term to the objective function. Hence, we call this procedure the *penalty approach*. On the other hand, the box constraints may be fulfilled by using an iteration rule which computes admissible iterates on the configuration space of constrained polygonal chains. For the latter case, the box constraints are enforced via an *intrinsic approach*, and a penalty term is not necessary. Due to the box constraints, the configuration space of a constrained polygonal chain is a manifold with boundary. However, the original iteration rule of the fSAM algorithm (Lauff et al., 2024) is only applicable to smooth manifolds including equality constraints in their description. To obtain an iteration rule to move along the geodesics respecting the box constraints, we extend the integration scheme of the fSAM algorithm for manifolds with boundary. Therefore, we formulate the box constraints as inequality constraints for the numerical integration of the d'Alembert type constrained mechanical system, using the Karush-Kuhn-Tucker (KKT) conditions. Then, we solve the discretized system of equations with a non-smooth Newton scheme (Qi and Sun, 1993; Robinson, 1994; Ito, 2008) in every time step. For the penalty and the intrinsic approach, we discuss the integration into the framework of the fSAM algorithm. Additionally, we provide information on further extensions of the fSAM algorithm to generate microstructures of hybrid composites, e.g., the adaption of the objective function to account for subcells with varying desired characteristics.

We start the computational investigations by studying the performance of the microstructure generator handling the box constraints with either the penalty or the intrinsic approach. Subsequently, we investigate the necessary resolution and RVE size for a two-layered CoDicoFRP. Furthermore, we compare the interface between adjacent subcells as well as the effective properties of the entire microstructure when using the hard or soft box-constraint type. Last but not least, we validate the computed effective elastic properties of a CoDicoFRP with discontinuous core and

continuous shell layers by comparing the stiffness with experimentally measured data.

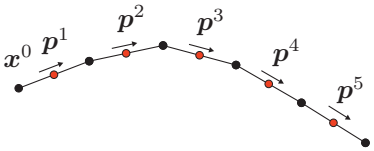


Figure 5.1: Discretization of a curved fiber as a polygonal chain. Figure adapted from Figure 1 of Lauff et al. (2025b).

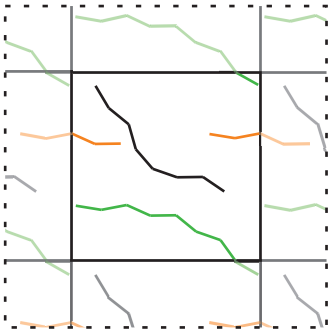


Figure 5.2: Fibers in a two-dimensional periodic unit cell. Figure adapted from Figure 2 of Lauff et al. (2025b).

5.2 Optimization on the configuration space of curved and constrained fibers

5.2.1 Parametrization of curved and constrained fibers

We consider a curved fiber of length L and diameter D, which we model as a polygonal chain with n congruent spherocylinders, i.e., cylinders with hemispherical ends (Schneider, 2022; Lauff et al., 2024). Hence, each segment has a segment length of $\ell = L/n$. For the parametrization of such a polygonal chain, following Section 4.2.2, we normalize the starting point $\mathbf{x}^0$ of a fiber, see Equation (4.16). Then, a fiber may be parametrized via the coordinate vector $\mathbf{q} \in \mathbb{R}^{n_q}$ (4.17) with dimension n_q (4.18). For an illustration of the core idea of the used discretization, see Figure 5.1. The considered fiber is modeled with $n = 5$ segments

and parametrized via its starting point and the five directions of its segments. With the coordinate vector $\mathbf{q}$, the midpoints of the segments may be expressed explicitly via Equation (4.20). As the directions $\mathbf{p}^a$ are assumed to be unit vectors, the configuration space is described by the set $\mathcal{R}$ (4.19) with the n-dimensional vector-valued constraint function $\mathbf{\Phi}_1$ (4.14).

The configuration space in Equation (4.19) describes fibers residing in the Euclidean space $\mathbb{R}^3$ without further restrictions on their location. Also for periodic unit cells, the description in Equation (4.19) is applicable with little extra effort, see Lauff et al. (2024). An example for a two-dimensional periodic unit cell with fibers as inclusions is shown in Figure 5.2. However, when considering fibers with restrictions on their location, i.e., due to the layered structure of a continuous-discontinuous fiber reinforced polymer (CoDicoFRP), the configuration space in Equation (4.19) needs to be adapted according to the underlying box constraints.

In this manuscript, we aim to consider *hard* and *soft box constraints*. In case of hard box constraints, an entire fiber is restricted to its respective cell

$$\begin{aligned} &C = [B_1, T_1] \times [B_2, T_2] \times [B_3, T_3]\,, \\ &0 \leq B_i \leq T_i \leq Q_i, \quad i = 1, 2, 3, \end{aligned} \tag{5.1}$$

e.g., to the bottom or the upper layer of a two-layered CoDicoFRP. An admissible configuration of a fiber within its cell is shown in Figure 5.3(a). Hard box constraints are enforced by restricting the starting point of a fiber and the endpoints of the individual segments to lie within the unit cell. Such a condition may be formulated via the vectorial constraint function

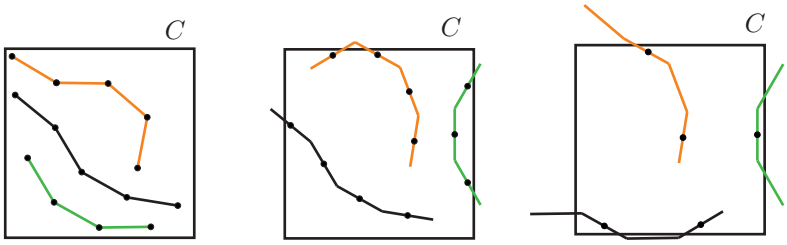
$$\mathbf{\Phi}_{\mathrm{H}}(\mathbf{q}) = \left[\mathbf{\Phi}_{\mathrm{H}}^{0}(\mathbf{q})^{\mathsf{T}} \quad \mathbf{\Phi}_{\mathrm{H}}^{1}(\mathbf{q})^{\mathsf{T}} \quad \cdots \quad \mathbf{\Phi}_{\mathrm{H}}^{n}(\mathbf{q})^{\mathsf{T}} \right]^{\mathsf{T}} \tag{5.2}$$

with

$$\boldsymbol{\Phi}_{\mathrm{H}}^{0}(\mathbf{q}) = \begin{bmatrix} -\mathbf{x}^{0} + \begin{bmatrix} B_1 \\ B_2 \\ B_3 \end{bmatrix} \\ +\mathbf{x}^{0} - \begin{bmatrix} T_1 \\ T_2 \\ T_3 \end{bmatrix} \end{bmatrix}, \quad \boldsymbol{\Phi}_{\mathrm{H}}^{a}(\mathbf{q}) = \begin{bmatrix} -\left(\mathbf{x}^{a}(\mathbf{q}) + \ell \dfrac{\mathbf{p}^{a}}{2}\right) + \begin{bmatrix} B_1 \\ B_2 \\ B_3 \end{bmatrix} \\ +\left(\mathbf{x}^{a}(\mathbf{q}) + \ell \dfrac{\mathbf{p}^{a}}{2}\right) - \begin{bmatrix} T_1 \\ T_2 \\ T_3 \end{bmatrix} \end{bmatrix},$$

$a = 1, \ldots, n.$ (5.3)

Thus, hard constraints are fulfilled if each component of the vectorial constraint function (5.2) is smaller or equal than zero.



(a) Hard box constraints **(b)** Soft box constraints ($n_{\mathrm{SBC}} = 0$) **(c)** Soft box constraints ($n_{\mathrm{SBC}} = 2$)

Figure 5.3: Illustrative unit cells with hard box constraints (a), soft box constraints with control parameter $n_{\mathrm{SBC}} = 0$ (b) and soft box constraints with control parameter $n_{\mathrm{SBC}} = 2$ (c), where the black dots represent the constrained fiber points. Figure adapted from Figure 3 of Lauff et al. (2025b).

In case of soft constraints, only the segments' midpoints of a fiber are restricted to their respective unit cell, see Figure 5.3(b), and, e.g., an interlocking between two adjacent layers may be realized. Then, the

vectorial constraint function is defined by

$$\boldsymbol{\Phi}_{\mathrm{S}}(\mathbf{q}) = \left[\boldsymbol{\Phi}_{\mathrm{S}}^{1}(\mathbf{q})^{\mathsf{T}} \quad \cdots \quad \boldsymbol{\Phi}_{\mathrm{S}}^{n}(\mathbf{q})^{\mathsf{T}}\right]^{\mathsf{T}}$$
$$\text{with} \quad \boldsymbol{\Phi}_{\mathrm{S}}^{a}(\mathbf{q}) = \begin{bmatrix} -\mathbf{x}^{a}(\mathbf{q}) + \begin{bmatrix} B_1 \\ B_2 \\ B_3 \end{bmatrix} \\ +\mathbf{x}^{a}(\mathbf{q}) - \begin{bmatrix} T_1 \\ T_2 \\ T_3 \end{bmatrix} \end{bmatrix}, \quad a = 1, \ldots, n. \tag{5.4}$$

If a fiber is modeled with short segments, most parts of the fiber will not penetrate the cell boundaries. Hence, the difference between hard and soft box constraints decreases for smaller segment lengths. To enable an interlocking also for small segment lengths, we adapt the soft box constraints such that not all midpoints are constrained to their cell, see Figure 5.3(c). Therefore, we introduce the parameter $n_{\mathrm{SBC}} \geq 0$ to control the amount of constrained midpoints. Depending on this parameter, the vectorial constraint function in Equation (5.4) accounts for the midpoints $\mathbf{x}^a$ with

$$\left\{ \begin{array}{ll} a = 1, \ldots, n, & \text{if } n_{\mathrm{SBC}} = 0 \\ a = n_{\mathrm{SBC}} + 1, \ldots, (1 + 2\,k)\, n_{\mathrm{SBC}} + 1 \leq n, & \text{if } 0 < n_{\mathrm{SBC}} < n/2 \\ a = \lfloor n/2 \rfloor, & \text{else} \end{array} \right\}, \tag{5.5}$$

where $\lfloor \cdot \rfloor$ denotes the floor function. Thus, e.g., for a fiber with $n = 30$ segments, in case of $n_{\mathrm{SBC}} = 3$ the midpoints $\mathbf{x}^a$ ($a = 4, 10, 16, 22, 28$) are restricted and in case of $n_{\mathrm{SBC}} \geq 15$ only the midpoint $\mathbf{x}^{15}$ is restricted.

We permit to mix the box-constraint types coordinate-wise, e.g., by using no box constraints for the $\boldsymbol{e}_1$, soft box constraints for the $\boldsymbol{e}_2$-direction and hard constraints for the $\boldsymbol{e}_3$-direction. Hence, the constraint functions (5.2) and (5.4) may not be active in all directions and the inactive parts need to

be deleted from the formulations. To shorten the expressions, we merge the box constraints to

$$\boldsymbol{\Phi}_{\mathrm{BC}}(\mathbf{q}) = \begin{bmatrix} \boldsymbol{\Phi}_{\mathrm{H}}(\mathbf{q}) \\ \boldsymbol{\Phi}_{\mathrm{S}}(\mathbf{q}) \end{bmatrix} \leq \mathbf{0} \tag{5.6}$$

with the dimension n_{BC}, where the inequality is to be understood component-wise. Then, the configuration space of a curved and constrained fiber is given by the manifold with boundary

$$\mathcal{R}^{\mathrm{BC}} = \{\, \mathbf{q} \in \mathbb{R}^{n_q} \mid \boldsymbol{\Phi}_1(\mathbf{q}) = \mathbf{0},\ \boldsymbol{\Phi}_{\mathrm{BC}}(\mathbf{q}) \leq \mathbf{0} \,\}. \tag{5.7}$$

5.2.2 Adapted gradient descent approach on the configuration space of curved and constrained fibers

We consider an objective function

$$F : \mathcal{R}^{\mathrm{BC}} \to \mathbb{R}, \quad \mathbf{q} \mapsto f(\mathbf{q}), \tag{5.8}$$

optimized in the configuration space $\mathbf{q} \in \mathcal{R}^{\mathrm{BC}}$ (5.7). To minimize the objective function, we aim to use a gradient descent approach. However, the standard, i.e., *Euclidean*, gradient descent method may compute iterates that violate the constraints in Equation (5.7). To ensure an optimization procedure on the optimization space, the gradient descent approach needs to compute iterates along the geodesics, i.e., the locally shortest paths between two points on a manifold (Petersen, 2016). The equations governing these geodesics follow from minimizing the kinetic energy functional on the manifold, which may be understood as a constrained mechanical system without external forces and driven solely by the kinetic energy (Betsch, 2005; Angeles and Lee, 1989). For the manifold of a double spherical pendulum, Betsch (2005) derived the equations governing the geodesics in the form of a d'Alembert type

constrained mechanical system. Based on this formulation, we extended in Section 4.2.4 the equations for a polygonal chain parametrized via $\mathbf{q} \in \mathcal{R}$, i.e., without box constraints, which read

$$\begin{aligned} \mathbf{P}(\mathbf{q})^{\mathsf{T}}\, \mathbf{G}\, \ddot{\mathbf{q}} &= \mathbf{0}, \\ \boldsymbol{\Phi}_1\left(\mathbf{q}\right) &= \mathbf{0} \end{aligned} \tag{5.9}$$

with the null space matrix $\mathbf{P}(\mathbf{q})$ and the constant symmetric positive-definite metric matrix $\mathbf{G}$. For a detailed derivation of Equation (5.9) and the explicit formulas for the matrices $\mathbf{P}$ and $\mathbf{G}$, we refer to Section 4.2.4. Proceeding from Equation (5.9), the geodesics on the configuration space $\mathcal{R}^{\mathrm{BC}}$ may be obtained by enforcing that at each point along the path fulfills the box constraints (5.6).

With the equations governing the geodesics at hand, we may compute the exponential mapping

$$\exp_{\mathbf{q}}(\mathbf{v}) = \mathbf{q}_v(1) \tag{5.10}$$

for prescribed points $\mathbf{q} \in \mathcal{R}^{\mathrm{BC}}$ on the manifold and admissible tangent vectors $\mathbf{v} \in T_{\mathbf{q}}\mathcal{R}^{\mathrm{BC}}$. Here, $\mathbf{q}_v(1)$ refers to the endpoint of the geodesic $\mathbf{q}_v : [0,1] \to \mathcal{R}^{\mathrm{BC}}$ with the starting point $\mathbf{q}_v(0) = \mathbf{q}$ and the initial tangent vector $\dot{\mathbf{q}}_v(0) = \mathbf{v}$. Using the exponential mapping to ensure admissible iterates, we adapt the intrinsic gradient descent approach (Lauff et al., 2024) with the iterative procedure

$$\mathbf{q}^{k+1} = \exp_{\mathbf{q}^k}\left(-\tau_k\, \nabla_{\mathbf{q}} F(\mathbf{q}^k)\right), \quad k \in \mathbb{N}, \tag{5.11}$$

where τ_k stands for a selected positive stepsize.

5.2.3 Exponential mapping on the configuration space of curved and constrained fibers

In this section, we introduce a numerical integration scheme for computing the exponential mapping of the manifold with boundary $\mathcal{R}^{\mathrm{BC}}$ (5.10). Following previous publications which consider the exponential mapping of manifolds describing a double spherical pendulum (Betsch, 2005) and a polygonal chain (Lauff et al., 2024), we use the energy conserving time integration scheme presented by Gonzalez (1999).

We consider the time interval $I = [0, 1]$, which we decompose into n_t subintervals of equal time steps $\Delta t = 1 \,/\, n_t$. For each subinterval $I_j = [t_j, t_{j+1}]$ starting at time t_j, the coordinate vector $\mathbf{q}(t) \in \mathcal{R}^{\mathrm{BC}}$ and its time derivative $\dot{\mathbf{q}}(t) \in T_{\mathbf{q}}\mathcal{R}^{\mathrm{BC}}$ are approximated by the linear approximation formulas in Equation (4.39). With this time discretization scheme, the discretized form of the differential-algebraic equations (5.9) takes the form

$$\begin{aligned} \mathbf{P}(\mathbf{q}_{j+\frac{1}{2}})^{\mathsf{T}}\, \hat{\mathbf{H}}(\mathbf{q}_j, \mathbf{q}_{j+1}) &= \mathbf{0}, \\ \boldsymbol{\Phi}_1\left(\mathbf{q}_{j+1}\right) &= \mathbf{0} \end{aligned} \tag{5.12}$$

with the vector-valued function

$$\hat{\mathbf{H}}(\mathbf{q}_j, \mathbf{q}_{j+1}) = \frac{2}{\Delta t}\, \hat{\mathbf{G}}\, [\mathbf{q}_{j+1} - \mathbf{q}_j] - 2\, \hat{\mathbf{G}}\, \mathbf{v}_j \tag{5.13}$$

under the additional inequality constraint accounting for the box constraints (5.6). The matrix $\mathbf{P}(\mathbf{q}_{j+\frac{1}{2}})$ denotes the null space matrix evaluated for the coordinate vector

$$\mathbf{q}_{j+\frac{1}{2}} = \frac{\mathbf{q}_j + \mathbf{q}_{j+1}}{2} \tag{5.14}$$

and $\hat{\mathbf{G}}$ represents the normalized metric matrix

$$\hat{\mathbf{G}} = \begin{bmatrix} n & \hat{\mathbf{Q}}^{-2}\left[f_1\,\ell\,\hat{\mathbf{Q}}\right] & \hat{\mathbf{Q}}^{-2}\left[f_2\,\ell\,\hat{\mathbf{Q}}\right] & \cdots & \hat{\mathbf{Q}}^{-2}\left[f_n\,\ell\,\hat{\mathbf{Q}}\right] \\ & \hat{\mathbf{Q}}^{-2}\left[f_{d,1}\,\mathbf{1}_{3\times3}\right] & \hat{\mathbf{Q}}^{-2}\left[f_2\,\ell^2\,\mathbf{1}_{3\times3}\right] & \cdots & \hat{\mathbf{Q}}^{-2}\left[f_n\,\ell^2\,\mathbf{1}_{3\times3}\right] \\ & & \ddots & & \vdots \\ & & & \ddots & \hat{\mathbf{Q}}^{-2}\left[f_n\,\ell^2\,\mathbf{1}_{3\times3}\right] \\ \text{sym} & & & & \hat{\mathbf{Q}}^{-2}\left[f_{d,n}\,\mathbf{1}_{3\times3}\right] \end{bmatrix}$$

$$\text{with} \quad f_a = n - a + \frac{1}{2} \quad \text{and} \quad f_{d,a} = \varepsilon\left(\ell, D\right) + \ell^2\left(n - a + \frac{1}{4}\right), \tag{5.15}$$

where $\varepsilon\left(\ell, D\right)$ denotes the volume-specific moment of inertia of a spherocylinder (García, 2015). For more details on the derivation of the discretized differential-algebraic equations (5.12), we refer to Betsch (2005) and Lauff et al. (2024). The additional inequality constraint accounting for the box constraints (5.6) leads to the Karush-Kuhn-Tucker (KKT) conditions

$$\begin{aligned} \mathbf{P}(\mathbf{q}_{j+\frac{1}{2}})^{\mathsf{T}}\left[\hat{\mathbf{H}}(\mathbf{q}_j, \mathbf{q}_{j+1}) + \frac{\partial \hat{\mathbf{\Phi}}_{\text{BC}}\left(\mathbf{q}_{j+1}\right)}{\partial \mathbf{q}}^{\mathsf{T}} \boldsymbol{\lambda}_j\right] &= \mathbf{0}, \\ \mathbf{\Phi}_1\left(\mathbf{q}_{j+1}\right) &= \mathbf{0}, \\ \boldsymbol{\lambda}_j \geq \mathbf{0}, \quad \hat{\mathbf{\Phi}}_{\text{BC}}\left(\mathbf{q}_{j+1}\right) \leq \mathbf{0}, \quad \boldsymbol{\lambda}_j \odot \hat{\mathbf{\Phi}}_{\text{BC}}\left(\mathbf{q}_{j+1}\right) &= \mathbf{0}, \end{aligned} \tag{5.16}$$

where we use the normalized vectorial constraint function

$$\hat{\mathbf{\Phi}}_{\text{BC}}\left(\mathbf{q}\right) = \begin{bmatrix} \hat{\mathbf{Q}}^{-1} & \mathbf{0}_{3\times3} & \cdots & \mathbf{0}_{3\times3} \\ \mathbf{0}_{3\times3} & \hat{\mathbf{Q}}^{-1} & \cdots & \mathbf{0}_{3\times3} \\ \vdots & \vdots & \ddots & \mathbf{0}_{3\times3} \\ \mathbf{0}_{3\times3} & \mathbf{0}_{3\times3} & \cdots & \hat{\mathbf{Q}}^{-1} \end{bmatrix} \mathbf{\Phi}_{\text{BC}}\left(\mathbf{q}\right). \tag{5.17}$$

In Equation (5.16), $\boldsymbol{\lambda} \in \mathbb{R}^{n_{\text{BC}}}$ denotes the additional vector of unknown Lagrangian multipliers and the notation $() \odot ()$ represents the element-

wise multiplication of two vectors, see Section 1.4. For any fixed parameter vector $\boldsymbol{\mu} \in \left(\mathbb{R}^{>0}\right)^{n_{\mathrm{BC}}}$, the conditions

$$\boldsymbol{\lambda}_j \geq \mathbf{0}, \quad \hat{\boldsymbol{\Phi}}_{\mathrm{BC}}\left(\mathbf{q}_{j+1}\right) \leq \mathbf{0}, \quad \boldsymbol{\lambda}_j \odot \hat{\boldsymbol{\Phi}}_{\mathrm{BC}}\left(\mathbf{q}_{j+1}\right) = \mathbf{0} \tag{5.18}$$

hold if and only if the equation

$$\left\langle \boldsymbol{\lambda}_j + \boldsymbol{\mu} \odot \hat{\boldsymbol{\Phi}}_{\mathrm{BC}}\left(\mathbf{q}_{j+1}\right) \right\rangle_+ = \boldsymbol{\lambda}_j \tag{5.19}$$

is satisfied, where $\langle h \rangle_+ = \max(0, h)$ denotes the Macaulay bracket, applied component-wise to a vector. Hence, the system of equations and inequalities (5.16) may be equivalently rewritten as a system of *equations*

$$\begin{aligned} \mathbf{P}(\mathbf{q}_{j+\frac{1}{2}})^{\mathsf{T}} \left[\hat{\mathbf{H}}(\mathbf{q}_j, \mathbf{q}_{j+1}) + \frac{\partial \hat{\boldsymbol{\Phi}}_{\mathrm{BC}}\left(\mathbf{q}_{j+1}\right)}{\partial \mathbf{q}}^{\mathsf{T}} \boldsymbol{\lambda}_j \right] &= \mathbf{0}, \\ \boldsymbol{\Phi}_1\left(\mathbf{q}_{j+1}\right) &= \mathbf{0}, \\ \left\langle \boldsymbol{\lambda}_j + \boldsymbol{\mu} \odot \hat{\boldsymbol{\Phi}}_{\mathrm{BC}}\left(\mathbf{q}_{j+1}\right) \right\rangle_+ - \boldsymbol{\lambda}_j &= \mathbf{0}. \end{aligned} \tag{5.20}$$

For each subinterval $I_j = [t_j, t_{j+1}]$, the coordinate vector $\mathbf{q}_j \in \mathcal{R}^{\mathrm{BC}}$ and the velocity vector $\mathbf{v}_j \in \mathbb{R}^{n_q}$ are given quantities at time $t = t_j$. The coordinate vector $\mathbf{q}_{j+1}$ is obtained by solving the system of equations (5.20) with a non-smooth Newton scheme (Qi and Sun, 1993; Robinson, 1994; Ito, 2008). As initial guess for the coordinate vector $\mathbf{q}_{j+1}$, we follow Equation (4.42). At convergence of the non-smooth Newton scheme, the velocity vector for the next time step is obtained via Equation (4.43).

For the parameter vector $\boldsymbol{\mu}$, we use $\boldsymbol{\mu} = 10 \cdot \mathbf{1}_{n_{\mathrm{BC}}}$. As convergence criteria of the Newton scheme, we choose that the norm of the residual vector is below 10^{-8} and that the inequality constraints are strictly satisfied. Following Lauff et al. (2024), we initially consider the complete time interval I with a single time step $\Delta t = 1$. If the non-smooth Newton scheme does not converge in ten iterations, we repeat the time integration with

doubled subintervals. For Newton's method applied to find roots of a sufficiently smooth function, backtracking (Boyd and Vandenberghe, 2009) is a popular strategy to globalize the convergence properties of Newton's method, which is only characterized by local convergence in its traditional undamped form. For non-smooth problems, however, backtracking is not guaranteed to help upgrading the local convergence behavior of Newton's method to global convergence. Therefore, backtracking is only used in the case that the inequality constraints are not violated in a time step at all. If backtracking is applied, we use the backtracking parameter $\beta = 0.9$, taken from literature (Görthofer et al., 2022). Thus, in each backtracking step, the stepsize is moderately reduced by 10%. For the fixed backtracking parameter $\beta = 0.9$, we have investigated the influence of the second backtracking parameter $\alpha \in (0, 0.5)$ on the runtime to solve the system of equations (5.20). The study has shown that the effect of the parameter α is negligible and we select $\alpha = 1/3$. To still ensure global convergence of the non-smooth Newton's method, we rely on a homotopy method, i.e., the previously described adaptive reduction of the time-step size, which permits us to remain in the basin of attraction of the sought root.

Please note that considering the unknown Lagrangian multipliers in Equation (5.20) increases the dimension of the system equations significantly. Hence, it is important for the performance to consider only those components which are active in the current time step. If a fiber does not touch the boundary of its containing cell, the inequality constraints are considered inactive and should be deleted from the formulation to decrease the dimension and thus the runtime for solving the equations.

5.3 Microstructure generation of long fiber reinforced hybrid composites

5.3.1 Description of long fiber reinforced hybrid composites

We consider periodic microstructures comprising a rectangular cell $Q = [0, Q_1] \times [0, Q_2] \times [0, Q_3]$, which is divided into m non-overlapping subcells with rectangular cell dimensions

$$C^c = [B_1^c, T_1^c\,] \times [B_2^c, T_2^c\,] \times [B_3^c, T_3^c\,], \quad c = 1, \ldots, m. \tag{5.21}$$

Hence, the volume of a subcell computes as

$$V_c = (T_1^c - B_1^c\,)\,(T_2^c - B_2^c\,)\,(T_3^c - B_3^c\,)\,. \tag{5.22}$$

In each cell, N_c long, curved fibers of constant diameter D_c without fiber-overlap are given. Thus, the total number of fibers inside the entire unit cell Q equals the sum

$$N = \sum_{c=1}^{m} N_c. \tag{5.23}$$

The ordering of the fibers is chosen such that the first N_1 fibers belong to the first cell, the next N_2 fibers to the second cell and so on. The smallest fiber-index corresponding to the c^{th}-cell is denoted by i_c.

The fibers are modeled as polygonal chains with spherocylindrical segments and are parametrized via the coordinate vector $\mathbf{q}$, see Equation (4.17). The fiber lengths follow a prescribed fiber length distribution, e.g, the uniform, Gamma or Weibull distribution. In this manuscript, we consider cells filled with discontinuous or continuous fibers, where we assume a unidirectional fiber arrangement for the continuous fibers. To

model the discontinuous fibers, we select the number of segments of the i^{th}-fiber such that the segment lengths ℓ_i is below a defined maximum segment length $\bar{\ell}_c$

$$n_i = \left\lceil \frac{L_i}{\bar{\ell}_c} \right\rceil, \quad \ell_i = \frac{L_i}{n_i}, \quad i = 1, \dots, N, \tag{5.24}$$

where the functional $\lceil \cdot \rceil$ computes the smallest integer larger or equal to a given real number. For the continuous and unidirectional fibers, we use a single segment, i.e., we model the fiber as a straight cylindrical geometry.

The fiber volume fraction within a subcell computes as

$$\phi_c = \frac{\pi D_c^2}{4 V_c} L_c^{\text{total}} \quad \text{with the total length} \quad L_c^{\text{total}} = \sum_{i=i_c}^{i_c+N_c} L_i \tag{5.25}$$

according to the Pappus' theorem (Goodman and Goodman, 1969). The fiber orientation state is typically represented by the fiber orientation tensors (Advani and Tucker III, 1987; Kanatani, 1984), where the realized volume-weighted fiber orientation tensors of second $\boldsymbol{A}_c^{\text{r}}$ and fourth order $\mathbb{A}_c^{\text{r}}$ of each cell compute as

$$\boldsymbol{A}_c^{\text{r}} = \frac{1}{L_c^{\text{total}}} \sum_{i=i_c}^{i_c+N_c} \sum_{a=1}^{n_i} \ell_i \left(\boldsymbol{p}_i^a\right)^{\otimes 2}, \quad \mathbb{A}_c^{\text{r}} = \frac{1}{L_c^{\text{total}}} \sum_{i=i_c}^{i_c+N_c} \sum_{a=1}^{n_i} \ell_i \left(\boldsymbol{p}_i^a\right)^{\otimes 4}, \tag{5.26}$$

where the vector $\boldsymbol{p}_i^a$ denotes the direction of the a^{th}-segment of the i^{th}-fiber. For fiber reinforced composites, the fiber orientation tensor of second order may be identified via micro-CT imaging (Krause et al., 2010; Wirjadi et al., 2016; Hessman et al., 2019). To obtain an adequate approximation of the fiber orientation tensor of fourth order, closure approximation (Folgar and Tucker III, 1984; Cintra and Tucker III, 1995; Dray et al., 2007; Breuer et al., 2019; Kugler et al., 2020; Karl et al., 2021; 2023) may be used. For cells with unidirectional fiber arrangement,

e.g., oriented in $\boldsymbol{e}_1$ direction, the fiber orientation tensor of second order is given by $\boldsymbol{A}^{\mathrm{r}} \hat{=} \mathrm{diag}(1,0,0)$. In Figure 5.4, an example for a hybrid composite with two layers in $\boldsymbol{e}_3$-direction is shown. The bottom layer is reinforced with discontinuous fibers and the upper layer is reinforced with continuous fibers in a unidirectional fiber arrangement in $\boldsymbol{e}_1$-direction.

5.3.2 Extension of the fused sequential addition and migration (fSAM) algorithm

In this section, we provide information on the extensions to the original fused sequential addition and migration (fSAM) algorithm (Lauff et al., 2024) to generate periodic hybrid microstructures composed in multiple cells with different prescribed characteristics, e.g., varying fiber length and orientation distributions or fiber volume fractions.

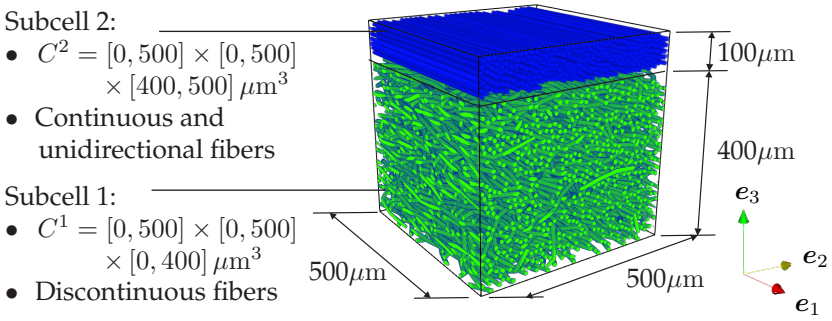


Figure 5.4: Hybrid composite with two layers in $\boldsymbol{e}_3$-direction. Figure adapted from Figure 4 of Lauff et al. (2025b).

Comment on the fiber orientation term within the objective function
The fSAM algorithm aims to minimize the objective function (4.47), where the first term accounts for the non-overlap condition between the fiber segments, the second term considers the fiber orientation tensor and the third term restricts the angle between adjacent segments to the maximum angle $\bar{\alpha}$. The coordinate vector $\mathbf{f}_i$ denotes an alternative parametrization of a fiber, which is obtained from the coordinate vector $\mathbf{q}_i$ by computing the midpoints of the segments $\mathbf{x}_i^a$, see Equation (4.20). Typically, we prescribe a tolerance for the relative error of the fiber orientation tensor $\epsilon_{\mathbb{A}}$ as a termination criterion for the optimization problem. However, due to the formulation in Equation (4.47), the fiber orientation will be further corrected during the gradient descent scheme even if the orientation error is below the tolerance, but the other criteria are not fulfilled. As the fiber orientation term leads to non-zero gradients of the objective function for all fiber directions, it is necessary to numerically integrate the d'Alembert constrained mechanical system for all fibers. Thus, the fiber orientation term may result in the computation of the exponential mapping for fibers which already satisfy the maximum angle condition and do not intersect with other fibers, although the fiber orientation tensor is already satisfying its convergence criterion. As a result, the runtime increases significantly, especially at the end of the optimization procedure, as the fiber orientation condition converges first most of the time. To decrease the runtime, we formulate the objective function

$$F_{\langle\cdot\rangle_+}(\mathbf{f}_1,\ldots,\mathbf{f}_N) \hat{=} \frac{1}{2}\sum_{i,j=1}^{N}\sum_{a=1}^{n_i}\sum_{b=1}^{n_j}\left(\delta_{ij}^{ab}\right)^2 + \frac{w_{\mathbb{A}}}{8}N\left\langle\|\mathbb{A}-\mathbb{A}^{\mathrm{r}}\|^2-\epsilon_{\mathbb{A}}\right\rangle_+ + \frac{w_\rho}{2}\sum_{i=1}^{N}\sum_{a=1}^{n_i-1}\left(\left\langle\cos\bar{\alpha}-\boldsymbol{p}_i^{a+1}\cdot\boldsymbol{p}_i^a\right\rangle_+\right)^2 \tag{5.27}$$

such that the term for the fiber orientation tensor is only be considered if the orientation error exceeds the prescribed tolerance $\epsilon_{\mathbb{A}}$.

Extension of the objective function for multiple subcells with different characteristics

The objective function in Equation (5.27) only accounts for a single fiber orientation distribution and a uniform maximum angle within the entire cell. As we aim to consider m subcells with different characteristics, we need to distinguish between these areas. Hence, the objective function in Equation (5.27) turns to

$$\begin{aligned} F_{\text{hybrid}}\left(\mathbf{f}_1,\ldots,\mathbf{f}_N\right) \hat{=} & \frac{1}{2}\sum_{i,j=1}^{N}\sum_{a=1}^{n_i}\sum_{b=1}^{n_j}\left(\delta_{ij}^{ab}\right)^2 \\ & + \frac{w_{\mathbb{A}}}{8}\sum_{c=1}^{m} N_c\left\langle \|\mathbb{A}_c - \mathbb{A}_c^{\mathsf{r}}\|^2 - \epsilon_{\mathbb{A}}\right\rangle_+ \\ & + \frac{w_\rho}{2}\sum_{c=1}^{m}\sum_{i=i_c}^{i_c+N_c}\sum_{a=1}^{n_i-1}\left(\left\langle \cos\bar{\alpha}_c - \boldsymbol{p}_i^{a+1}\cdot\boldsymbol{p}_i^{a}\right\rangle_+\right)^2, \end{aligned} \tag{5.28}$$

where $\mathbb{A}_c$ denotes the desired fiber orientation tensor of fourth order of the c^{th}-subcell and $\bar{\alpha}_c$ the maximum angle of the c^{th}-subcell. The term for the non-overlap condition does not distinguish between different subcells, as the fibers may reach into adjacent subcells, depending on their box constraints. Thus, fibers of different subcells may intersect during the optimization procedure which is not admissible for convergence.

Implementation of soft and hard box constraints

Let us discuss the implementation of the soft and hard box constraints as part of the fSAM algorithm. Therefore, we consider two different procedures. On the one hand, the box constraints may be fulfilled in every iterative step, which we call the *intrinsic* approach. Then, the gradient steps are restricted on the adapted configuration space of the

fibers $\mathcal{R}^{\text{BC}}$, see Equation (5.7). Hence, moving along the geodesics of this manifold requires the numerical integration of the d'Alembert type constrained mechanical system in Equation (5.9) under the condition that the box constraints (5.6) are fulfilled. In our investigations, it turned out that the term for the fiber orientation tensor converges slowly if fibers are close to their boundaries. Thus, we increase the weight of this term for all fibers which violate the inequality conditions during the previous numerical integration of the d'Alembert constrained mechanical system by a factor of 2.5.

Alternatively, the box constraints may only be enforced via the convergence criterion of the optimization problem, but not in every iterative step. Hence, we consider the d'Alembert type constrained mechanical system in Equation (5.9) without the box constraints during the exponential mapping. To enforce the box constraints, we extend the objective function by a term accounting for the soft and hard box constraints

$$F_{\text{penalty,BC}}\left(\mathbf{f}_1, \ldots, \mathbf{f}_N\right) \mathrel{\hat{=}} F_{\text{hybrid}}\left(\mathbf{f}_1, \ldots, \mathbf{f}_N\right) + \frac{w_{\text{BC}}}{2} \sum_{i=1}^{N} \left\| \mathbf{\Phi}_{\text{BC}}\left(\mathbf{q}_i\right) \right\|^2, \tag{5.29}$$

where the coordinate vector $\mathbf{q}_i$ is computed from the coordinate vector $\mathbf{f}_i$. For this change of fiber parametrization, the normalized starting point computes as

$$\hat{\mathbf{x}}_i^0\left(\boldsymbol{f}_i\right) = \hat{\mathbf{Q}}^{-1} \left(\mathbf{x}_i^1 - \frac{\ell_i}{2} \mathbf{p}_i^1 \right). \tag{5.30}$$

The objective function $F_{\text{penalty,BC}}\left(\mathbf{f}_1, \ldots, \mathbf{f}_N\right)$ has dimension $(\text{length})^2$. Hence, the weight of the box constraints term w_{BC} needs to be dimensionless and we select $w_{\text{BC}} = 5$. Due to the additional penalty term within the objective function, we call this procedure the *penalty* approach.

Sampling and pre-optimization step

Before the main optimization problem is solved, a sampling step is

conducted. Therefore, we first sample fiber lengths according to the prescribed fiber length distribution of each cell until the desired fiber volume fraction is reached. Then, we sample the midpoints and the directions of the fibers, assuming straight fibers first. Therefore, we follow Schneider (2022), by sampling the midpoints from a uniform distribution within the subcells and by sampling the directions from the ACG closure (Montgomery-Smith et al., 2011a;b), accounting for the prescribed fiber orientation tensors of second order. Subsequently, the segment number of each fiber is determined, see Equation (5.24), and the fibers decompose into segments without changing their location in the cell.

Due to the sampling procedure, the realized fiber orientation tensors may differ from the desired ones. Additionally, the fibers may violate their box constraints, as only the fiber's midpoints are surely located within their respective cell. To stabilize the convergence behavior of the algorithm, we aim to ensure that the initial fiber orientation tensor of the main optimization problem is within the prescribed tolerance. Furthermore, moving along a geodesic requires the starting configuration to be admissible, i.e., to lie on the manifold of curved and constrained fibers. To obtain a starting configuration for the main optimization according to these requirements, we consider a pre-optimization step subsequent to the sampling step. Therefore, we solve an optimization problem with the objective function

$$
\begin{aligned}
F_{\text{pre}}\left(\mathbf{f}_1, \ldots, \mathbf{f}_N\right) \mathrel{\hat{=}} & \frac{w_{\mathbb{A}}}{8} \sum_{c=1}^{m} N_c \left\langle \left\| \mathbb{A}_c - \mathbb{A}_c^{\mathrm{r}} \right\|^2 - \epsilon_{\mathbb{A}} \right\rangle_+ \\
& + \frac{w_\rho}{2} \sum_{c=1}^{m} \sum_{i=i_c}^{i_c+N_c} \sum_{a=1}^{n_i-1} \left(\left\langle \cos \bar{\alpha}_c - \boldsymbol{p}_i^{a+1} \cdot \boldsymbol{p}_i^{a} \right\rangle_+ \right)^2 \\
& + \frac{w_{\text{BC}}}{2} \sum_{i=1}^{N} \left\| \boldsymbol{\Phi}_{\text{BC}}\left(\mathbf{q}_i\right) \right\|^2 ,
\end{aligned}
\tag{5.31}
$$

which coincides with the objective function of the penalty approach, see Equation (5.29), except for the term of the non-overlap condition. For the weights, we follow the main optimization problem, except for the weight of term for the box constraints $w_{\mathrm{BC}} = 0.5$. Solving the optimization problem in Equation (5.31) results in a fiber arrangement with accurate fiber orientation realization where the fibers are in admissible configurations on the spaces $\mathcal{R}_i^{\mathrm{BC}}$, but may be overlapping.

Handling of the continuous and unidirectional fibers

Continuous and unidirectional fibers are modeled with a single straight cylindrical segment, which is arranged in one of the three coordinate directions $\boldsymbol{e}_i$. The segment has the length of the parallel edge of its cell $(T_i^c - B_i^c)$. Due to this special resulting configuration, the ends of the segments are in touch when periodically repeating the subcell in fiber direction. Hence, the fiber is continuous.

The fSAM algorithm (Lauff et al., 2024) prescribes a minimum distance to avoid stress peaks between close fibers. Additionally, a self-intersection scheme (Mehta and Schneider, 2022) is used to detect long fibers intersecting themselves. Thus, the algorithm would detect self-intersections for the continuous fibers, although they shall touch at their end. To overcome this limitation, the self-intersection scheme is turned off for continuous fibers.

For subcells reinforced with continuous fibers, we prescribe a unidirectional fiber orientation state. Hence, we know that all segment directions need to be unidirectional for convergence. Thus, we do not change the fiber directions within the main optimization problem. To find a fiber arrangement with no fiber overlap, only the midpoints of the fibers are changed.

5.4 Computational investigations

5.4.1 Setup

E-glass fibers			PP matrix		
E	$=$	72.0 GPa	E	$=$	1.25 GPa
ν	$=$	0.22	ν	$=$	0.35

Table 5.1: Material properties for the PP matrix and the E-glass fibers (DOW® Chemical Company, 2003; PPG Fiber Glass, 2013). Table adapted from Table 1 of Lauff et al. (2025b).

We use an implementation of the fSAM algorithm written in Python with Cython extensions, where the collision checks between the segments and the numerical integration of the exponential mapping are parallelized with OpenMP. The runtimes were measured on a desktop computer with a 8-core Intel i7 CPU and 64GB RAM.

As our reference setup, we work with a two-layered CoDicoFRP comprising a discontinuously fiber-reinforced bottom layer and a continuously fiber-reinforced upper layer. For both subcells, we consider a polypropylene (PP) matrix reinforced by E-glass fibers. Table 5.1 records the corresponding elastic moduli (DOW® Chemical Company, 2003; PPG Fiber Glass, 2013). The fiber diameter is assumed to be $D = 10\mu\mathrm{m}$ for all fibers. For the discontinuous phase, the fibers are modeled with a uniform fiber length of $L = 1500\mu\mathrm{m}$, i.e., a fiber aspect ratio of 150, the maximum segment length is set to $\bar{\ell} = 50\mu\mathrm{m}$ and the maximum angle is chosen as $\bar{\alpha} = 60°$. Between all fibers, we ensure a minimum distance of 20% of the fiber diameter, i.e., $2.0\mu\mathrm{m}$.

The fiber orientation tensor of fourth order is obtained by a closure approximation from a prescribed fiber orientation tensor of second order. As we use the exact closure (Montgomery-Smith et al., 2011a;b) and fiber

orientation tensors of second order are orthotropic, in general, the fiber orientation tensors of fourth order are orthotropic as well (Bauer and Böhlke, 2022a). For the convergence of the optimization procedure of the fSAM algorithm, it is necessary that no fiber overlap is detected. Additionally, the relative error in the fiber orientation tensor of fourth order needs to be below 10^{-4} and the absolute error of the angle constraint is enforced to be below 10^{-2}. For the penalty approach, we enforce that the constrained fiber points exceed their boundaries $10^{-3}D$ at most.

To compute the effective elastic properties, we use an FFT-based computational homogenization software (Moulinec and Suquet, 1994; 1998) with a discretization on a staggered grid (Schneider et al., 2016) and a conjugate gradient solver (Zeman et al., 2010; Brisard and Dormieux, 2012). As termination criterion for the solver, we choose a relative tolerance of 10^{-5}. The effective elasticity tensor is computed using six independent load cases. Based on the effective elastic stiffness, we approximate the effective orthotropic engineering constants (Cowin, 1985; Görthofer et al., 2020) due to the orthotropic material symmetry of the microstructures.

5.4.2 On the algorithmic handling of the box constraints

In this section, we compare the intrinsic and the penalty approach enforcing the box constraints. Therefore, we generate two-layered microstructures with a cubic unit cell and cell dimensions $Q_i = 500\mu\mathrm{m}$. The bottom layer with discontinuous fiber-reinforcement has cell dimension $C^1 = [0, 500] \times [0, 500] \times [0, 400]\,\mu\mathrm{m}^3$ and we consider the fiber volume fractions

$$\phi_1 \in \{20\%, 21\%, 22\%, 23\%, 24\%, 25\%\}. \tag{5.32}$$

We prescribe the fiber orientation tensor of second order

$$\boldsymbol{A} \hat{=} \operatorname{diag}(0.77, 0.17, 0.06)\,, \tag{5.33}$$

experimentally measured for long fiber reinforced thermoplastics (Blarr et al., 2023). The upper layer with continuous and unidirectional fiber-reinforcement has cell dimension $C^2 = [0, 500] \times [0, 500] \times [400, 500]\ \mu\text{m}^3$ and a fiber volume fraction of $\phi_2 = 35\%$. The principal direction of the continuous fibers is the $\boldsymbol{e}_1$-direction. For both layers, we consider no box constraints for the $\boldsymbol{e}_1$-direction and $\boldsymbol{e}_2$-direction. Hence, the fibers may wrap around the unit cell due to the periodic boundary conditions. For the $\boldsymbol{e}_3$-direction, we apply hard constraints at height $0\mu\text{m}$ and $500\mu\text{m}$, as well as soft box constraints at height $400\mu\text{m}$. A generated microstructure is shown in Figure 5.4.

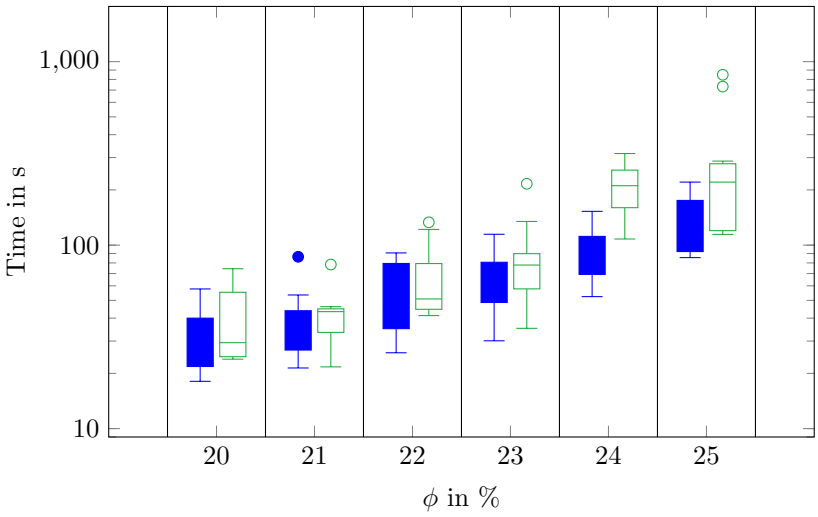


Figure 5.5: Runtimes for the microstructure generation using an approach with intrinsic box constraints control or via a penalty term. Figure adapted from Figure 5 of Lauff et al. (2025b).

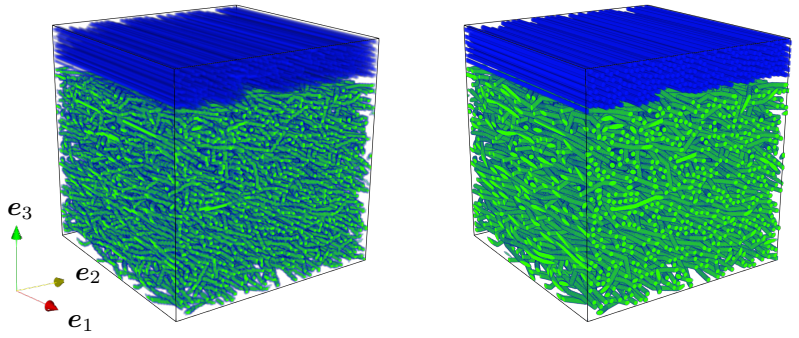
For each fiber volume fraction and procedure, we consider ten generated microstructures and report on the measured runtimes in Figure 5.5. We observe an increase in runtime for packings with higher fiber volume

fractions. For the lowest fiber volume fractions $\phi_1 \in \{20\%, 21\%\}$, both procedures have similar runtimes, e.g., the penalty procedure generates microstructures with $\phi_1 = 21\%$ in about 43s on average. However, for higher fiber volume fractions the runtime of the intrinsic approach is always below the runtime of the penalty approach. Additionally, the penalty approach has outliers with extremely high runtimes. For the fiber volume fractions $22\%, 23\%, 24\%$ and 25%, the intrinsic approach is 1.23, 1.33, 2.26 and 2.21 times faster than the penalty approach, when including the outliers to this consideration.

Let us focus on the packing with the highest fiber volume fraction of $\phi_1 = 25\%$ to have a detailed look on the runtimes. For this case, the minimum measured runtime is 86s for the intrinsic approach and 114s for the penalty approach. The maximal measured runtime is 221s for the intrinsic approach and 849s for the penalty approach. Hence, we observe that the minimum runtime observed for both approaches is rather close. However, this is not the case for the maximal runtime as the penalty approach suffers from extreme outliers. For both approaches, the variability in runtime mainly depends on the starting configuration of the fibers, which results from both the sampling and the pre-optimization step. If the starting configuration is challenging with respect to the main optimization problem, e.g., due to a high number of collisions or high angles between the segments, the runtime will increase. Whereas the intrinsic approach is capable of dealing with challenging starting configurations, the penalty approach suffers from convergence problems, especially with increasing complexity, e.g., higher fiber volume fractions. However, still the penalty approach leads to reasonable runtimes for the microstructure generation. Due to the better performance of the intrinsic approach, we will use this procedure for the following investigations.

5.4.3 Resolution study

To predict the effective properties with FFT-based computational homogenization methods, a mesh size needs to be chosen which is sufficiently fine to enable an accurate prediction of the effective properties (Brisard and Dormieux, 2012; Schneider, 2015). For the resolution study, we consider the setup from the previous subsection with the fiber volume fraction $\phi_1 = 25\%$ and material parameters from Table 5.1. The cubic cell with cell dimensions $Q_i = 500\mu\mathrm{m}$ turns out to be representative, see Table 5.3. To select an adequate mesh size, we compute the effective properties for the four voxel edge-lengths $h = 4.00\mu\mathrm{m}$, $2.00\mu\mathrm{m}$, $1.25\mu\mathrm{m}$ and $1.00\mu\mathrm{m}$. Compared to the fiber diameter $D = 10\mu\mathrm{m}$, a fiber is resolved with 2.5, 5, 8, 10 voxels for decreasing mesh size. As the effort of the homogenization increases with the total voxel number, the finest mesh size with 500^3, i.e., $125 \cdot 10^6$, voxels lead to a significantly higher runtime than the coarsest mesh size with 125^3, i.e., about $2 \cdot 10^6$, voxels. In Figure 5.6, the same microstructure resolved with the different voxel-edge lengths $h = 4.00\mu\mathrm{m}$ and $h = 1.25\mu\mathrm{m}$ is shown.



(a) $h = 4.00\mu\mathrm{m}$ **(b)** $h = 1.25\mu\mathrm{m}$

Figure 5.6: Two-layered microstructures resolved with the voxel edge-lengths $h = 4.00\mu\mathrm{m}$ (a) and $h = 1.25\mu\mathrm{m}$ (b). Figure adapted from Figure 6 of Lauff et al. (2025b).

We report on the approximated orthotropic engineering constants for all four voxel-edge lengths in Table 5.2. To assess the quality of the orthotropic approximation, also the orthotropic approximation error is listed. For the two coarsest mesh sizes, the orthotropic approximation error is 2.76% and 1.07%, dropping below 1% for the two finer mesh sizes. Hence, it turns out that the approximation of the orthotropic engineering constants is adequate. Due to the fiber-reinforcement in $\boldsymbol{e}_1$-direction of the upper layer and the preferred fiber arrangement in $\boldsymbol{e}_1$-direction of the bottom layer, the Young's modulus E_1 exceeds the remaining Young's moduli by multiples. To select a sufficiently fine mesh size, we compare the elastic moduli of the three coarser mesh sizes to the finest mesh size. For the shear modulus G_{13}, the highest relative difference is measured with 16.50% for the coarsest mesh size, reducing to 4.85% and 0.97% for the two finer mesh sizes. As the computed orthotropic approximation error and the resolution induced error is below 1% for the voxel-edge length $h = 1.25\mu\text{m}$, we select this voxel-edge length as our mesh size.

h μm	E_1 GPa	E_2 GPa	E_3 GPa	G_{23} GPa	G_{13} GPa	G_{12} GPa	err_{orth} %
4.00	12.53	3.13	2.76	1.03	1.20	1.62	2.76
2.00	13.32	3.02	2.57	0.94	1.08	1.49	1.07
1.25	13.53	3.00	2.54	0.91	1.04	1.47	0.56
1.00	13.60	3.00	2.53	0.90	1.03	1.46	0.44

Table 5.2: Approximated orthotropic engineering constants for the voxel edge-lengths $h = 4.00\mu\text{m}$, $h = 2.00\mu\text{m}$, $h = 1.25\mu\text{m}$ and $h = 1.00\mu\text{m}$. Table adapted from Table 2 of Lauff et al. (2025b).

5.4.4 RVE study

For computational homogenization of random materials, the selected unit cell size is of key importance to ensure representativity. Due to practical reasons the unit cell needs to be finite, and the apparent effective properties of random materials include a certain degree of randomness as well. However, to obtain the effective properties as deterministic descriptors, the unit cell size needs to be large enough to cover the entire material statistics and ensure that the boundary conditions do not impact the results (Hill, 1963; Drugan and Willis, 1996). Such a unit cell is called *representative volume element* (RVE). As the computational effort for the homogenization depends on the unit cell size, the smallest possible RVE size should be selected.

To assess the representativity of a unit cell, two errors need to be monitored (Kanit et al., 2003; Gloria and Otto, 2011). On the one hand, the *random* error, or dispersion, measures the variability of the realized apparent properties for a fixed unit cell size, i.e., may be monitored by the standard deviation of multiple realizations. On the other hand, the *systematic* error, or bias, quantifies the difference between the mean apparent properties and the effective properties. Typically, the effective properties are not known. However, to quantify the systematic error, the mean apparent properties of increasing unit cell sizes may be monitored.

For the RVE study, we work with the two-layered microstructure already used in the previous two sections. To study the representativity of different unit cell sizes, we consider cubic cells with cell dimensions $Q_i = 300\mu\mathrm{m}$, $500\mu\mathrm{m}$ and $700\mu\mathrm{m}$, where the boundary between the two layers is always at height $0.8\,Q_3$, i.e., at $240\mu\mathrm{m}$, $300\mu\mathrm{m}$ and $560\mu\mathrm{m}$, respectively, for increasing cell dimensions. To ensure a sufficiently fine resolution, we use a voxel edge-length of $h = 1.25\mu\mathrm{m}$, according to the resolution study in Table 5.2. Thus, 240^3, i.e., about $14 \cdot 10^6$, voxels resolve the

smallest unit cell and 560^3, i.e., $176 \cdot 10^6$, resolve the largest unit cell. For each unit cell size, a generated microstructure is shown in Figure 5.7.

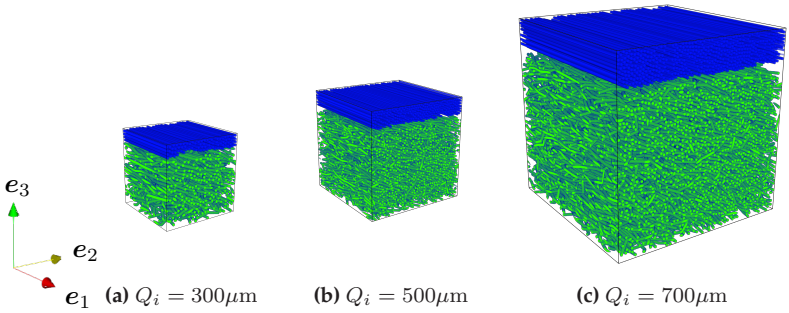


Figure 5.7: Generated microstructures for three different cubic cell-sizes Q_i. Figure adapted from Figure 7 of Lauff et al. (2025b).

To investigate the representativity errors, we consider ten microstructures for each unit cell size. The mean and the standard deviation of the approximated engineering constants are listed in Table 5.3. We observe that the orthotropic approximation is suitable for all three unit cell sizes as the error is always below 1%. Also, the standard deviation is low for all unit cell sizes. For the systematic error, we report the highest relative error for the smallest unit cell size $Q_i = 300\mu\text{m}$ and the shear modulus G_{13} with 2.86%, dropping to 0.95% for the unit cell size $Q_i = 500\mu\text{m}$. Hence, even the smallest unit cell size has rather small representativity errors. To ensure that both the systematic and the random error are well below 1%, we select the unit cell size with cell dimensions $Q_i = 500\mu\text{m}$ for the further investigations.

We remark that the fSAM algorithm generates periodic microstructures, regardless which box constraints are applied to the fibers. Already in previous publications (Schneider, 2022; Lauff et al., 2023) it is emphasized

that periodic microstructures with accurately realized characteristics, i.e., the fiber volume fraction or the fiber orientation tensor of fourth order, combined with periodic boundary conditions for the displacement field during the homogenization are advantageous for decreasing the RVE size.

Q_i μm	E_1 GPa	E_2 GPa	E_3 GPa	G_{23} GPa	G_{13} GPa	G_{12} GPa	err_{orth} %
300	13.48	3.02	2.53	0.90	1.02	1.47	0.69
	$\pm$ 0.04	$\pm$0.04	$\pm$0.01	$\pm$0.00	$\pm$0.01	$\pm$0.02	$\pm$0.20
500	13.54	3.02	2.54	0.91	1.04	1.48	0.60
	$\pm$ 0.05	$\pm$0.03	$\pm$0.00	$\pm$0.00	$\pm$0.01	$\pm$0.01	$\pm$0.08
700	13.55	3.02	2.56	0.92	1.05	1.48	0.57
	$\pm$ 0.04	$\pm$0.02	$\pm$0.01	$\pm$0.00	$\pm$0.00	$\pm$0.01	$\pm$0.04

Table 5.3: Approximated orthotropic engineering constants for the cubic cell-sizes $Q_i = 300\mu\text{m}$, $Q_i = 500\mu\text{m}$ and $Q_i = 700\mu\text{m}$. Table adapted from Table 3 of Lauff et al. (2025b).

5.4.5 On the difference between soft and hard box constraints

In this section, we study the influence of the selected box constraints on the generated microstructures. Therefore, we work with the two-layered CoDicoFRP already used in the previous sections, see Figure 5.4, and change the box-constraint type between the bottom and the top layer. For the study, we compare four different box-constraint types. First, we use the hard box constraints, where the complete fiber is enforced to be within its cell. Then, we consider the soft box-constraint type with three different parameter selections of n_{SBC}, which controls the amount

of restricted midpoints. In Table 5.4, the three considered parameter selections of n_{SBC} and the corresponding restricted midpoints $\mathbf{x}^a$ are listed.

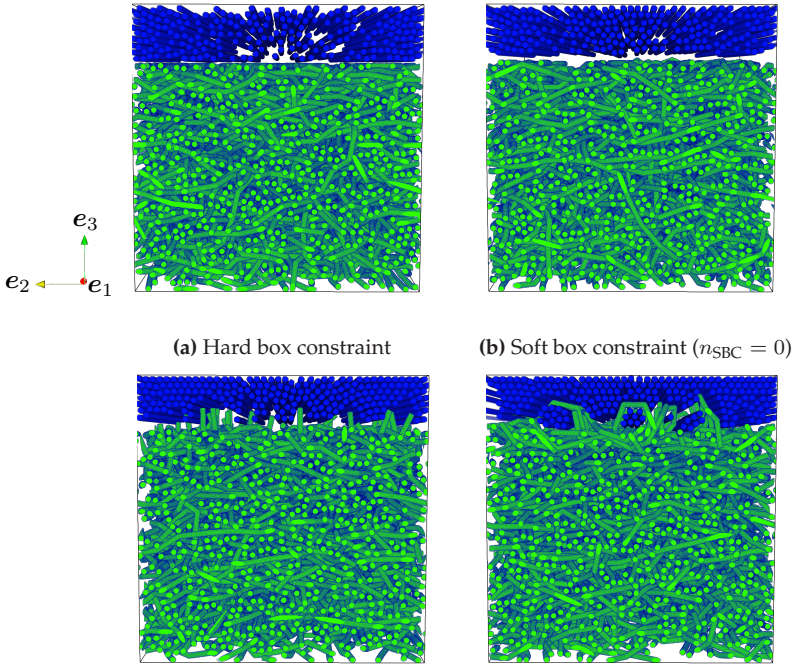
n_{SBC}	Restricted midpoints $\mathbf{x}^a$
0	$a = 1, 2, 3, \ldots$
1	$a = 2, 4, 6, \ldots$
2	$a = 3, 7, 11, \ldots$

Table 5.4: Parameter selections of n_{SBC} for the soft box-constraint type and the corresponding restricted midpoints. Table adapted from Table 4 of Lauff et al. (2025b).

For each box-constraint type, one of the ten generated microstructures is shown in Figure 5.8. We observe that for the hard box constraint in Figure 5.8(a) the boundary between the two layers is extremely straight and all fibers are completely in their cell, as enforced. For the soft box constraint with $n_{\text{SBC}} = 0$, the microstructure in Figure 5.8(b) looks quite similar. Due to the small maximum segment length of $\bar{\ell} = 50\mu\text{m}$, the fibers are mainly located in their respective layer and interlocking is suppressed.

During the compression molding of CoDicoFRP, the material flow leads to ply migration between the two phases (Corbridge et al., 2017). To model such a ply migration, we also consider higher parameter selections of n_{SBC}, restricting less segment midpoints to their cell, see Table 5.4. Figure 5.8(c) shows a microstructure generated with $n_{\text{SBC}} = 1$. We observe that the discontinuous fibers reach into the adjacent layer. Hence, this parameter selection may be suitable to realize the interlocking of the CoDicoFRP layers. When further increasing the parameter n_{SBC} to 2, the discontinuous fibers wrap around the continuous fiber-reinforcement, see Figure 5.8(d). Whereas

this is not representative for CoDicoFRP, such a strong connection may appear for other use cases, i.e., the layer boundaries of discontinuous fiber-reinforced materials with a skin-core–skin structure (Hessman et al., 2019; Bay and Tucker III, 1992b; Breuer et al., 2021).



(a) Hard box constraint

(b) Soft box constraint ($n_{\mathrm{SBC}} = 0$)

(c) Soft box constraint ($n_{\mathrm{SBC}} = 1$)

(d) Soft box constraint ($n_{\mathrm{SBC}} = 2$)

Figure 5.8: Two-layered continuous-discontinuous fiber-reinforced composite with different box constraints at the layer interface. Figure adapted from Figure 8 of Lauff et al. (2025b).

Besides a visual comparison of the generated microstructures, we also study the influence of the box constraints on the effective elastic properties. Therefore, we consider ten microstructures for each box constraint and report on the approximated orthotropic engineering constants in

Table 5.5. It turns out that the effective stiffness increases slightly with higher interlocking, where the differences are rather small and below 1% for all cases. However, the influence of the box constraints may be higher, e.g., when considering the damage behavior of the inter-laminar region (Ernesti and Schneider, 2022; 2023).

	E_1 GPa	E_2 GPa	E_3 GPa	G_{23} GPa	G_{13} GPa	G_{12} GPa
hard box constraint	13.53 $\pm$ 0.03	2.99 $\pm$0.02	2.54 $\pm$0.00	0.91 $\pm$0.00	1.05 $\pm$0.00	1.47 $\pm$0.01
soft box constraint ($\ell_{\text{SBC}} = 150\mu\text{m}$)	13.54 $\pm$ 0.05	3.02 $\pm$0.04	2.54 $\pm$0.01	0.91 $\pm$0.00	1.04 $\pm$0.00	1.48 $\pm$0.01
soft box constraint ($\ell_{\text{SBC}} = 250\mu\text{m}$)	13.58 $\pm$ 0.03	3.05 $\pm$0.03	2.56 $\pm$0.01	0.91 $\pm$0.00	1.05 $\pm$0.00	1.50 $\pm$0.02

Table 5.5: Approximated orthotropic engineering constants for different box constraints. Table adapted from Table 5 of Lauff et al. (2025b).

5.4.6 Comparison to experimental data

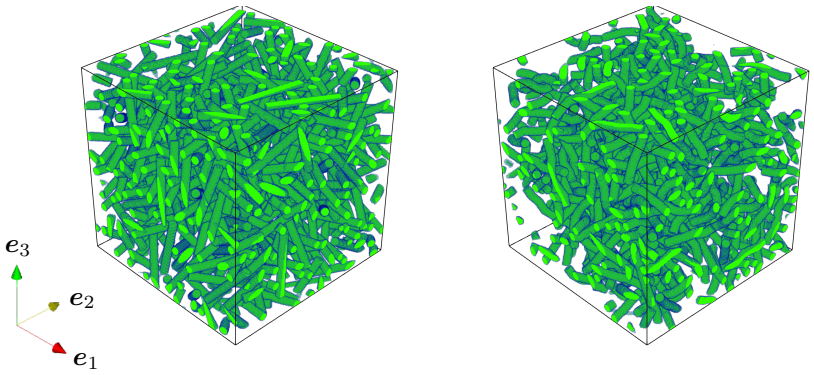
Hemp-fiber reinforced DicoFRP

	E GPa	ν -
PP matrix	1.18	0.36
hemp fibers	35.00	0.25

Table 5.6: Elastic parameters for the PP matrix and the hemp fibers (Bourgogne, 2024). Table adapted from Table 6 of Lauff et al. (2025b).

We start the validation section by comparing the effective properties of microstructures with either straight or curved fibers to experimental

data. Therefore, we consider a hemp-fiber reinforced DicoFRP with polypropylene (PP) as the matrix. The elastic parameters of the materials are listed in Table 5.6. According to Bourgogne (2024), the fibers have a diameter of $D = 30\mu\mathrm{m}$, come with a fiber length of $L = 250\mu\mathrm{m}$ and are processed with a fiber volume content of 17.3%. Hence, we consider short fibers with a fiber aspect ratio of $r_a \approx 8.3$. Following the suggestion by Bourgogne (2024), we use an isotropic fiber orientation state for the considered composite. For the microstructure generation, we enforce a minimum distance between the fibers of 20%, i.e., $6.0\mu\mathrm{m}$, and use a maximum segment length of $40\mu\mathrm{m}$ in case of curved fibers. Straight fibers are realized with a single segment per fiber. We select a cubic cell with cell dimensions $Q_i = 750\mu\mathrm{m}$ and resolve the microstructures with a voxel edge-length of $3.75\mu\mathrm{m}$, i.e., according to the resolution study, eight voxels per diameter. In Figure 5.9, microstructures with straight and curved fibers are shown. Based on ten realizations, the mean runtime to generate a microstructure with straight fibers is $2\mathrm{s}$ and to generate a microstructure with curved fibers is $19\mathrm{s}$.



(a) Straight fibers **(b)** Curved fibers

Figure 5.9: Microstructures with straight (a) and curved (b) fibers. Figure adapted from Figure 9 of Lauff et al. (2025b).

The experiments (Bourgogne, 2024) revealed a Young's modulus E_1 of about 2.06GPa for the hemp-fiber reinforced composite. To compare the mechanical behavior of the generated microstructures with the experimental data, we also report on the mean Young's modulus E_1 obtained from ten realizations. For the microstructures with straight fibers, we obtained a mean Young's modulus of $E_1 = 2.03\text{GPa}$ and for the curved fibers we obtained a mean Young's modulus of $E_1 = 1.98\text{GPa}$. Hence, we observe that the influence of the curvature is rather small with a relative decrease of 2.5% compared to straight fibers. Additionally, the results show a good agreement with the experimental data for both cases.

Carbon-fiber reinforced CoDicoFRP

Besides the hemp-fiber reinforced DicoFRP, we consider a CoDicoFRP with two continuous fiber-reinforced shell layers and a core layer with discontinuous fiber-reinforcement. For the materials, we use a polyamide 6 (PA6) matrix (Technyl®star, DOMO Chemicals GmbH) reinforced with carbon fibers (PX35, ZOLTEK). The considered elastic parameters for both materials are listed in Table 5.7.

	E	ν			
	GPa	-			
PA6 matrix	3.7	0.4			
	E_1	E_2	G_{12}	ν_{23}	ν_{12}
	GPa	GPa	GPa	-	-
carbon fibers	242	28	32.4	0.23	0.23

Table 5.7: Elastic parameters for the PA6 matrix (Altech®, 2020; Tschoegl et al., 2002) and the carbon fibers (ZOLTEK Corporation, 2019; Fiedler et al., 2004). Table adapted from Table 7 of Lauff et al. (2025b).

We model the matrix with isotropic material parameters, taking the Young's modulus E from the data sheet of a commercially available polyamide 6 (Altech®, 2020) and the Poisson's ratio ν from the literature (Tschoegl et al., 2002). For the carbon fibers, we assume a transversely isotropic material symmetry and use the elastic modulus E_1 from the data sheet of the PX35 carbon fibers (ZOLTEK Corporation, 2019). For the remaining parameters, we use the material data of HTA carbon fibers (Toho Tenax) (Fiedler et al., 2004) with similar elastic modulus E_1. Fiedler et al. (2004) report on the orthotropic engineering constants of the HTA carbon fibers. Based on the corresponding orthotropic stiffness, the transversely isotropic engineering constants in Table 5.7 are obtained by a projection on the transverse isotropic stiffness space (Cowin, 1985; Görthofer et al., 2020). The diameter of the carbon fibers is $D = 7.2\mu\mathrm{m}$ (ZOLTEK Corporation, 2019).

The CoDicoFRP parts were manufactured with the *long fiber reinforced thermoplastic direct* (LFT-D) compression molding process (Krause et al., 2003; Christ et al., 2024) at the Fraunhofer ICT in Pfinztal, Germany, co-molding the LFT plastificate with the continuous and unidirectional fiber-reinforced tapes. The tapes include a fiber mass fraction of 60% (DOMO, 2025), i.e., a fiber volume fraction of 48%, and are fiber-reinforced in the flow direction, which is the $\boldsymbol{e}_1$-direction. For the Dico material, fiber content and fiber length measurements were conducted at the Fiber Institute Bremen (FIBRE), Germany, see Scheuring et al. (2024) for more details. The fiber volume content measurement revealed a fiber volume fraction of 23.5% on average. With respect to the fiber lengths, a number-weighted mean fiber length of $L = 1550\mu\mathrm{m}$ and a median value of $L = 540\mu\mathrm{m}$ was measured. Additionally, the fiber orientation tensors of the Dico material were analyzed and tensile tests for the manufactured CoDicoFRP parts conducted at the IAM, KIT, Germany. For more details on the procedures for the fiber orientation determination and the tensile tests, we refer to Blarr et al. (2023) and

Scheuring et al. (2024). Compression molding leads to parts which may be separated in two areas, depending on the initial charge of the LFT plastificate, the charge and the flow area. For the fiber orientation determination and the tensile tests, at least five samples were taken from both areas. In this investigation, we consider the results of the flow area. The mean fiber orientation tensor of second order is

$$\boldsymbol{A}_{\text{Dico}} \mathrel{\hat{=}} \begin{bmatrix} 0.85 & 0.07 & 0.00 \\ 0.07 & 0.14 & 0.00 \\ 0.00 & 0.00 & 0.01 \end{bmatrix}. \tag{5.34}$$

The experimental results for the planar Young's modulus are shown in Figure 5.11, where the angle φ represents the deviation from the flow direction. The measuring points

$$\varphi \in \{0°, 22.5°, 45°, 90°, 135°, 157.5°\} \tag{5.35}$$

were considered. Due to the continuous fiber-reinforcement in flow direction and the highest eigenvalue a_1 of the fiber orientation tensor (5.34), the Young's modulus in flow direction at $\varphi = 0°$ is the highest modulus with 43.14GPa. The smallest planar Young's modulus is at $\varphi = 90°$ with 7.95GPa.

We aim to generate RVEs for the considered CoDicoFRP. Therefore, we select the subcell dimensions

$$\begin{aligned} C^1 &= [0, 600] \times [0, 600] \times [\ \ 0,\ \ 25]\,\mu\text{m}, \\ C^2 &= [0, 600] \times [0, 600] \times [\ 25, 275]\,\mu\text{m}, \\ C^3 &= [0, 600] \times [0, 600] \times [275, 300]\,\mu\text{m}, \end{aligned} \tag{5.36}$$

such that the height of the cell (and of the subcells) is ten times smaller than the manufactured parts. According to the manufactured part, we pack the shell layers with a fiber volume fraction of 48% and prescribe a

unidirectional fiber arrangement in e_1-direction. For the core layer, we prescribe the measured fiber volume fraction of 23.5% and the second-order fiber orientation tensor in Equation (5.34). To stay between the measured mean and median fiber length, we use a uniform fiber length of $720\mu\mathrm{m}$, i.e., a fiber aspect ratio of 100. With respect to the algorithmic choices, we use the soft box-constraint type with $n_{\mathrm{SBC}} = 1$ to model the interface between the subcells. Due to the decreased diameter of $D = 7.2\mu m$, we consider a smaller minimum distance of $1.44\mu\mathrm{m}$. In Figure 5.10, a synthetic microstructure for a CoDicoFRP is shown, including 1073 fibers with a total number of 11167 segments. For the ten generated microstructures, the mean runtime for the microstructure generation is $156\mathrm{min}$.

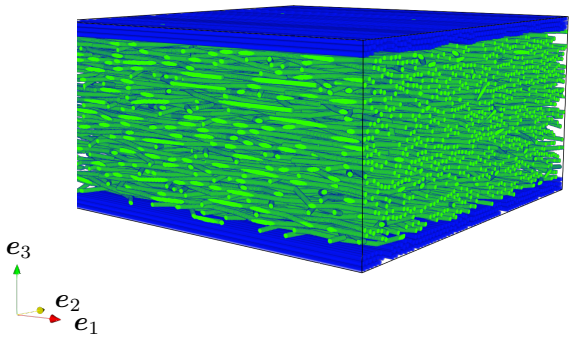


Figure 5.10: Synthetic microstructure of a CoDicoFRP using experimentally measured characteristics. Figure adapted from Figure 11 of Lauff et al. (2025b).

Let us compare the effective stiffness of the synthetic microstructures with the manufactured parts. For the resolution, we use $h = 0.8\mu\mathrm{m}$, i.e., the diameter is resolved by 9 voxels and the entire cell consists of $750^2 \times 375 \approx 211 \cdot 10^6$ voxels. Based on the computed stiffness of the ten

generated microstructures, we compute the direction dependent planar Young's modulus (Böhlke and Brüggemann, 2001) and report on the mean values in Figure 5.11.

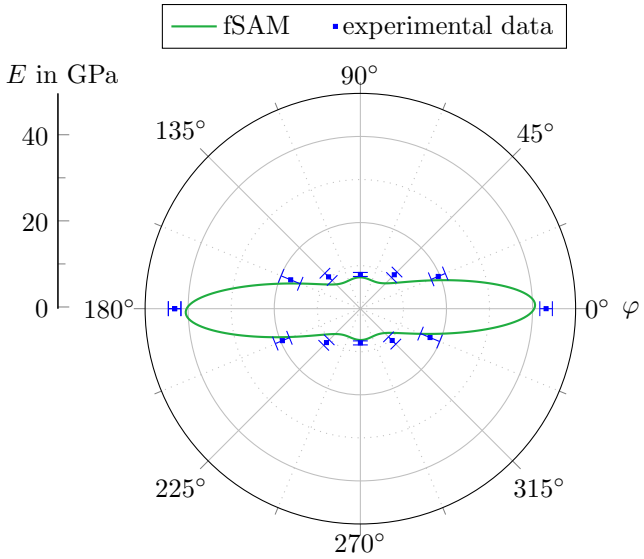


Figure 5.11: Comparison of the Young's modulus in the e_1-e_2-plane of the CoDicoFRP. Figure adapted from Figure 10 of Lauff et al. (2025b).

We observe that the highest Young's modulus is not computed at the angle $\varphi = 0°$ but at the angle $\varphi \approx 1.5°$. This shift results from the compression molding process of the LFT plastificates and is known in the literature (Bondy et al., 2017; Schelleis et al., 2023; Blarr et al., 2023; Scheuring et al., 2024). Notice that the generated microstructures are still orthotropic as we prescribe a fiber orientation tensor of second order and use an exact closure (Montgomery-Smith et al., 2011a;b) to obtain the fiber orientation of fourth order (Bauer and Böhlke, 2022a). However,

the considered bases $\{\boldsymbol{e}_1, \boldsymbol{e}_2, \boldsymbol{e}_3\}$ does not represent the orthotropic axes as the second-order fiber orientation tensor of the Dico phase (5.34) is not given in its principle axis system, i.e., its matrix-representation is not diagonalized. The orthotropic axis system of the generated microstructures may be obtained with a normal right rotation of the bases $\{\boldsymbol{e}_1, \boldsymbol{e}_2, \boldsymbol{e}_3\}$ by about $1.5°$ around the $\boldsymbol{e}_3$-axes. Compared to the experimental data, it turns out that the shape of the planar Young's modulus shows good agreement but the quantitative values are slightly underestimated. For the Young's modulus at $\varphi = 0°$, the computed value is $40.41\mathrm{GPa}$, which is a relative difference to the experiments of 6.3%, and at $\varphi = 90°$, the computed value is $7.28\mathrm{GPa}$, i.e., a relative underestimation of 8.4%.

5.5 Summary and conclusion

This chapter deals with an extension of the fused sequential addition and migration (fSAM) (Lauff et al., 2024) algorithm to generate hybrid composites with long fiber reinforcement. The fSAM algorithm models the fibers as polygonal chains and uses an optimization procedure on the configuration space of a polygonal chain to generate microstructures. To distinguish between different cells of hybrid composites, an adapted configuration space of a polygonal chain is used to account for box constraints, which restrict the location of a fiber to its respective subcell. Depending on the considered material system, the subcells may be strictly separated or interlocked by fibers reaching into adjacent subcells. To enable different interfaces, the fSAM algorithm works with multiple box-constraint types. In case of the *hard box constraints*, the entire fiber is restricted to its cell, whereas for the *soft box constraints* only the segment midpoints of a polygonal chain are enforced to be within their cell. Hence, for the latter box constraint, an interlocking between adjacent subcells is enabled. However, when considering small segment lengths, the degree of interlocking is rather small as the fibers are mainly located

within their subcell. To ensure interlocking also for decreasing segment lengths, an adapted soft box-constraint type may be selected where only selected segment midpoints are restricted.

Due to the connectivity constraint of a polygonal chain, the optimization problem of the original fSAM algorithm is defined on a curved, i.e., non-flat, configuration space. To compute admissible iterates, an adapted gradient descent approach is used, moving along the geodesics, i.e., the shortest path between two points on the configuration space. To account for the box constraints, the extended fSAM algorithm provides two alternative approaches. On the one hand, the *penalty* approach uses the original iteration rule which leads to iterates violating the box constraints. To ensure that the solution configuration at convergence is admissible, an additional penalty term accounting for the box constraints is added to the objective function. On the other hand, the *intrinsic* approach is based on an iteration rule which accounts directly for the box constraints. As the original iteration rule of the fSAM algorithm is only capable of handling equality constraints, a novel strategy is included in this manuscript to move along the geodesics of manifolds whose descriptions include inequality constraints as well, e.g., the box constraints. Hence, each iterate of the intrinsic approach is admissible on the configuration space of a curved and constrained fiber, i.e., a penalty term for the box constraints is not necessary. A detailed derivation of the extended iteration rule is given within the work at hand. For both strategies, the manuscript includes a discussion on the implementation within the framework of the fSAM algorithm. Additionally, information on further adaptions, which are necessary to generate hybrid composites, is provided, concerning the sampling, the pre-optimization step and the adaption of the objective function.

The computational investigations lead to the following findings:

- Due to the faster microstructure generation, the intrinsic approach is advantageous compared to the penalty approach to handle the box

constraints. Especially for complex microstructures with high fiber volume fractions, the penalty approach suffers from convergence problems in case of challenging starting configurations, e.g., with many fiber collisions.

- The fSAM algorithm for hybrid composites generates fiber microstructures with high confidence in the desired properties, e.g., the fiber volume fraction or the fiber orientation tensor. Thus, even small unit cell sizes are representative and may be used as RVEs. As the runtime for the microstructure generation and the computational homogenization increases for larger unit cell sizes, the small RVE sizes ensure a computationally efficient prediction of the effective mechanical behavior of the material.
- The shape of the interfaces between adjacent subcells strongly depends on the selected box-constraint type. Whereas the hard box-constraint type leads to a strict separation, the soft box-constraint type enables interlocking, which increases with less restricted segment midpoints. Although the visual comparison results in significant differences, the effective elastic stiffness is in a close range for all implemented box-constraint types. However, the box-constraint type may have a higher influence, e.g., when investigating the damage behavior of the inter-laminar region.
- The microstructures generated by the fSAM algorithm are capable of representing the mechanical behavior of long fiber reinforced hybrid composites. The computed effective stiffness of a synthetic CoDicoFRP with shell-core-shell structure shows a good agreement with experimental measured data. The computed Young's moduli E_1 and E_2 are $40.41\mathrm{GPa}$ and $7.28\mathrm{GPa}$, slightly underestimating the experimental results with a relative difference of 6.3% and 8.4%, respectively.

To conclude, the studies demonstrate the capability of the extended fSAM algorithm to generate representative volume elements for long

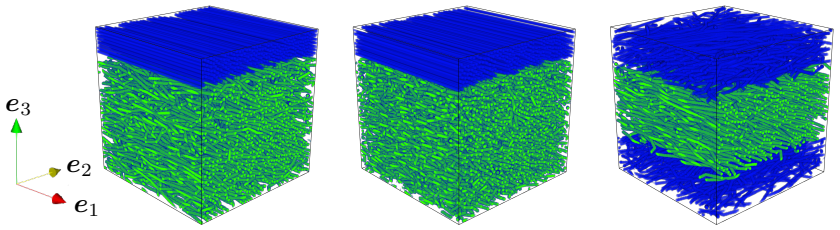
fiber reinforced hybrid composites in an efficient manner. Due to the possibility of choosing the box-constraint type, the interface may be modeled according to the considered material system. Hence, either strictly separated areas or interlocked areas can be realized by the microstructure model. With respect to the computational effort of the subsequent homogenization, the fSAM algorithm is a resource-saving method due to the small RVE sizes. By comparing the mechanical behavior of synthetic and manufactured CoDicoFRPs, the novel methodology permits to predict the measured elastic properties with high fidelity.

Besides CoDicoFRPs with long, curved fibers, as shown in Figure 5.12(a), the fSAM algorithm is also applicable to other material systems. Let us give two examples. For CoDicoFRPs with short fibers in the discontinuous fiber-reinforced phase, bending is typically negligible. Thus, the fSAM algorithm generates the corresponding microstructures by modeling the fibers with one cylindrical segment, see Figure 5.12(b). Another field of application are purely discontinuous fiber-reinforced materials with a skin-core–skin structure (Hessman et al., 2019; Bay and Tucker III, 1992b; Breuer et al., 2021), where the descriptors vary in each layer, see Figure 5.12(c).

As a future development, one could account for the generation of interphases between the fibers and the matrix material (Riaño and Joliff, 2019), especially when investigating interphase damage (Bourgogne et al., 2021). Additionally, strategies are necessary to generate microstructures with higher fiber volume fractions and fiber aspect ratios as, e.g., highly aligned fiber-reinforced microstructures are manufactured with fiber volume fractions above 50% and fiber aspect ratios above 500 (Cender et al., 2024; Yarlagadda et al., 2019). Throughout this manuscript, only the linear elastic material behavior of the composites was investigated. In perspective, it also might be of interest to study the damage behavior (Görthofer et al., 2022; Ernesti and Schneider, 2022; 2023) of the

generated microstructures and to take the nonlinear thermoviscoelastic behavior of the matrix material (Kehrer et al., 2023) into consideration.

As a key feature, the fSAM algorithm models the fibers as flexible structures including curvature. Different studies (Zhang et al., 2018; Schneider, 2022; Dai et al., 2023; Bourgogne, 2024) report that microstructures with varying degrees of curvature show differences in their mechanical properties. Hence, it is important to study the influence of the fiber curvature on the computed effective stiffness. The fSAM algorithm permits only to decide whether fibers can be curved or not. Prescribing the degree of curvature is not (yet) possible. Additionally, for long fibers, the fiber volume content that can be achieved with straight fibers is extremely limited. Hence, for high fiber aspect ratios and fiber volume fractions, the influence of the curvature cannot be studied at all. To overcome these limitations, it could be part of future research to extend the fSAM algorithm by curvature control such that the influence of the fiber curvature is assessable and the degree of curvature may be prescribed as additional desired characteristic.



(a) CoDicoFRP with long fibers **(b)** CoDicoFRP with short fibers **(c)** DicoFRP with layered structure

Figure 5.12: Three examples for hybrid or multilayer fiber-reinforced composites generated with the fSAM algorithm. Figure adapted from Figure 12 of Lauff et al. (2025b).

Chapter 6

On the influence of the fiber curvature on the stiffness[1]

6.1 Introduction

This chapter investigates the influence of different degrees of average fiber curvature on elastic properties of fiber-reinforced microstructures. To generate microstructures with a specific curvature, a quantitative curvature parameter needs to be defined. The mean of the local curvature, which would be a straightforward choice, is unsuitable. High local curvature values can be realized by frequently alternating changes of fiber direction along the fiber length. Thus, the mean of the local curvature can be increased without changing the overall shape of the fiber, as shown in Figure 6.1. However, for real fibers we typically observe smooth transitions in the fiber directions and significant changes in the overall shape. Thus, the fiber zig-zagging shown in Figure 6.1 is not representative of physical fiber bending. To avoid this pathological behavior, we introduce the deviation from straight curve (DSC) as a novel curvature measure for fiber composites, which computes as the trace of the local second-order fiber orientation tensor's covariance for

[1] This chapter is based on the Sections 1.2 and 2 to 5 of the publication "On the influence of the fiber curvature on the stiffness of long fiber reinforced composites" (Lauff et al., 2025a).

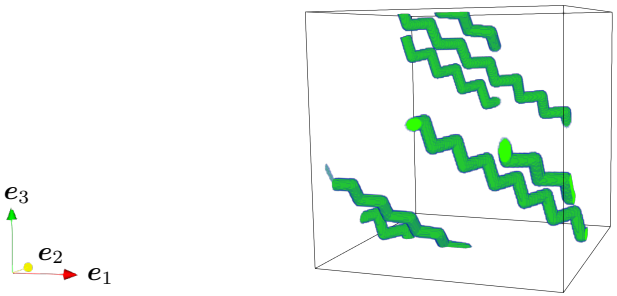


Figure 6.1: Single fiber with a high mean of the local curvature. Figure adapted from Figure 1 of Lauff et al. (2025a).

a single fiber, and show that constraints on this parameter serve as constraints on the mean of the local curvature. To avoid excessively high local curvature values, which would lead to real fibers breaking, we also restrict the local curvature to a critical threshold. With the condition of the local curvature constraint, prescribing the DSC leads to fibers with physically meaningful fiber bending, especially without zig-zagging or sharp bends.

In Section 6.3, we implement the global curvature objective and local curvature constraint into the fused Sequential Addition and Migration (fSAM) (Lauff et al., 2024) algorithm for generating curved fiber microstructures. The fSAM algorithm is already capable of generating periodic microstructures containing curved fibers; however, the average curvature of the fibers cannot be controlled directly and results indirectly from other parameters such as fiber volume fraction and length distribution. As the fSAM algorithm discretizes fibers as chains of straight segments, the local curvature cannot be computed exactly, and we find a suitable approximation. Implementing the curvature objective and constraint amounts to adding two additional terms to the objective function. To minimize this novel objective function, we adapt

the optimization procedure from the non-curvature-controlled version of the fSAM algorithm, requiring minimal changes.

Section 6.4 contains computational studies of the curvature-controlled fSAM algorithm for glass-fiber reinforced polypropylene. For realistic example values of the fiber aspect ratio and volume fraction, we investigate the realizable limits of curvature. At both high and low curvature values, we quantify the error due to RVE size and voxel resolution. We also discuss the effect of the segment length, which is a numerical parameter arising from the discretization of the fibers as chains of straight segments. Using the results from the numerical parameter studies, we finally quantify the influence of fiber curvature on the mechanical properties of the glass-fiber reinforced polypropylene.

6.2 Description and discretization of curved fibers

6.2.1 Quantifying the orientation and the curvature of a single fiber

We consider a fiber with length L and constant diameter D whose centerline may be described by a twice continuously differentiable curve

$$\boldsymbol{c} : [0, L] \longrightarrow Q \tag{6.1}$$

within the periodic unit cell $Q = [0, Q_1] \times [0, Q_2] \times [0, Q_3]$. Such a representation is illustrated in Figure 4.3(a).

We assume that the curve $\boldsymbol{c}$ is parametrized by arc length s, i.e., the first derivative of the curve has unit length

$$\| \boldsymbol{c}' (s) \| = 1, \quad s \in [0, L] . \tag{6.2}$$

According to Pappus' theorem (Goodman and Goodman, 1969), the fiber volume fraction of a fiber with circular cross-section equals the fiber volume fraction of a straight cylinder regardless of the curved shape of the fiber, i.e., the expression

$$\phi_f = \frac{\pi L D^2}{4 Q_1 Q_2 Q_3} \tag{6.3}$$

is valid. As a consequence, in case all fibers have equal diameter, the fiber-volume fraction of a collection of non-overlapping fibers is solely determined by the total fiber length.

The statistics of the fiber orientation state of fiber ensembles is compactly described by the fiber orientation tensors of second order $\boldsymbol{A}_f$ and of fourth order $\mathbb{A}_f$ (Kanatani, 1984; Advani and Tucker III, 1987). For a single fiber, these tensors take the form

$$\boldsymbol{A}_f = \frac{1}{L} \int_0^L \boldsymbol{c}'(s) \otimes \boldsymbol{c}'(s) \, \mathrm{d}s \quad \text{and} \quad \mathbb{A}_f = \frac{1}{L} \int_0^L \boldsymbol{c}'(s)^{\otimes 4} \, \mathrm{d}s. \tag{6.4}$$

Due to the normalization condition (6.2) satisfied by the vector $\boldsymbol{c}'(s)$, the relations

$$\mathbb{A}_f [\boldsymbol{I}] = \boldsymbol{A}_f \quad \text{and} \quad \mathrm{tr}(\boldsymbol{A}_f) = 1 \tag{6.5}$$

hold. As the fiber orientation tensor of second order is symmetric, the tensor may be diagonalized

$$\boldsymbol{A}_f \hat{=} \mathrm{diag}(a_1, a_2, a_3) \tag{6.6}$$

by a rotation into the eigenbasis where we use the ordering convention

$$a_3 \leq a_2 \leq a_1 \tag{6.7}$$

for convenience. The eigenvalues are constrained by the condition,

$$a_1 + a_2 + a_3 = 1, \tag{6.8}$$

a reformulation of Equation (6.5), and are non-negative because the fiber orientation tensor is positive semi-definite by Equation (6.4).

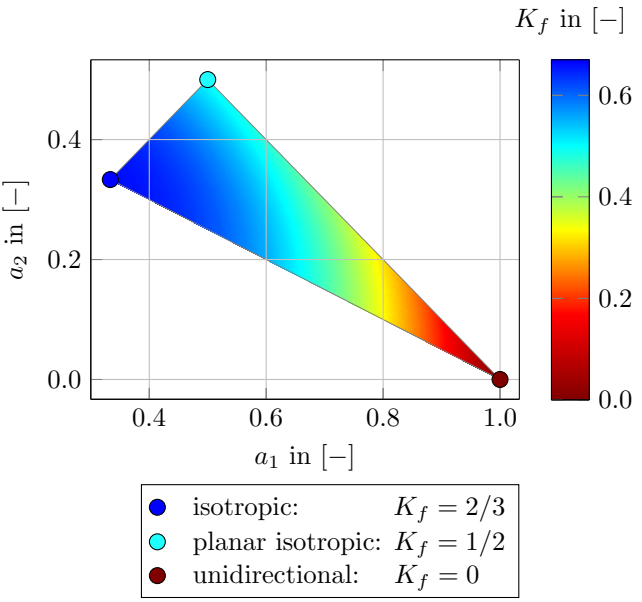


Figure 6.2: Fiber orientation triangle with the corresponding values of the deviation from straight curve K_f (6.18). Figure adapted from Figure 3 of Lauff et al. (2025a).

As a consequence of Equation (6.8), the fiber orientation tensor of second order is completely determined by two eigenvalues, e.g., a_1 and a_2. With the ordering convention (6.7), the two-dimensional configuration space of the fiber orientation tensor of second order may be visualized by the *fiber orientation triangle* (Cintra and Tucker III, 1995; Bauer and

Böhlke, 2022b), see Figure 6.2. The vertices mark the three extreme fiber orientation states, namely the isotropic state ($a_i = 1/3$, $i = 1, 2, 3$), the planar isotropic state ($a_1 = a_2 = 1/2, a_3 = 0$) and the unidirectional state ($a_1 = 1, a_2 = a_3 = 0$).

Whereas short fibers are accurately modeled by straight cylinders, longer fibers require taking the fiber curvature into account. Classically, the curvature (Pinkall and Gross, 2024; Araújo, 2024) of a curve (6.1) parametrized by arc length is defined via

$$\kappa(s) = \|\boldsymbol{c}''(s)\|, \quad s \in [0, L]. \tag{6.9}$$

With the goal of generating suitable fiber microstructures in mind, we would like to prescribe a suitable statistical measure of fiber curvature. However, this quest is not straightforward, for a number of reasons. For a start, the fiber orientation and the fiber curvature are not independent. Suppose, for instance, that the fiber orientation state is unidirectional, i.e., described by the fiber orientation tensor

$$\boldsymbol{A} = \boldsymbol{p} \otimes \boldsymbol{p} \tag{6.10}$$

for some unit vector $\boldsymbol{p}$. Then, all fibers need to be straight and point in direction $\pm\boldsymbol{p}$, see Schneider (2017). In particular, the curvature $\boldsymbol{c}'' \equiv \boldsymbol{0}$ needs to vanish for all fibers. The average curvature

$$\bar{\kappa}_f = \frac{1}{L} \int_0^L \|\boldsymbol{c}''(s)\| \, \mathrm{d}s \tag{6.11}$$

serves as an educated guess for a curvature measure, but does not turn out to be robust with respect to the discretization of the fibers as polygonal chains, see Section 6.2.2.

As a convenient alternative for quantifying the fiber curvature, we consider the deviation from straight curve (DSC). The latter computes as

the trace of the local second-order fiber orientation tensor's covariance for a single fiber

$$K_f \equiv \operatorname{tr}\left(\frac{1}{L}\int_0^L \left(\boldsymbol{A}_f - \boldsymbol{c}'(s)\otimes\boldsymbol{c}'(s)\right)^{\otimes 2}\,\mathrm{d}s\right), \tag{6.12}$$

which we may reformulate to

$$K_f = \frac{1}{L}\int_0^L \|\boldsymbol{A}_f - \boldsymbol{c}'(s)\otimes\boldsymbol{c}'(s)\|^2\,\mathrm{d}s. \tag{6.13}$$

This measure comes with a number of favourable properties.

1. The DSC is non-negative and vanishes only for straight fibers. More precisely, the bounds
$$0 \le K_f \le \frac{2}{3} \tag{6.14}$$
hold, and we have the characterization
$$K_f = 0 \quad \text{if and only if} \quad \boldsymbol{c}''(s) = \boldsymbol{0} \quad \text{for all} \quad s \in [0, L]. \tag{6.15}$$

2. The DSC serves as a lower bound to the average curvature in the sense that the inequality
$$K_f \le 2\left(L\,\bar{\kappa}_f\right)^2 \tag{6.16}$$
holds.

3. The DSC admits the equivalent representation
$$K_f = 1 - \|\boldsymbol{A}_f\|^2 \tag{6.17}$$
in terms of the second order fiber orientation tensor (6.4). Assuming that the fiber orientation tensor of second order is given in its diago-

nalized form (6.6), the DSC may be computed with two of the three eigenvalues, e.g.,

$$K_f = 1 - \left(a_1^2 + a_2^2 + a_3^2\right) = 1 - \left(a_1^2 + a_2^2 + (1 - a_1 - a_2)^2\right), \quad (6.18)$$

where the configuration space of the DSC is given by the points on the fiber orientation triangle. The values of the DSC are shown in Figure 6.2. We observe that the value $2/3$ is only obtained in case of an isotropic fiber orientation state.

The first property (6.14)–(6.15) enables us to use the DSC as a curvature measure, i.e., to quantify the deviation of the curve from being straight. The second property (6.16) relates the DSC to more classical measures of curvature. In particular, a positive value of the DSC enforces the average curvature to be positive, as well. Last but not least, the expression (6.17) is convenient for calculating the DSC in practice.
Establishing the validity of these statements is straightforward. For the convenience of the reader, the derivations are included in Appendix D.

6.2.2 Discretization of the curved fibers

We discretize the twice continuously differentiable curve $\boldsymbol{c}$ describing a curved fiber as a polygonal chain (Schneider, 2022). The polygonal chain consists of n spherocylinders, i.e., cylinders with hemispheres at their ends, as segments, which have the uniform segment length $\ell = L/n$ and the diameter D. Following Section 4.2.2, we parametrize the polygonal chain with the starting point $\mathbf{x}^0$ in the normalized form (4.16) and the directions of the segments $\mathbf{p}^a \in S^2$ $(a = 1, \ldots, n)$. The normalized starting point $\hat{\mathbf{x}}^0$ and the directions $\mathbf{p}^a$ are collected in the coordinate vector $\mathbf{q} \in \mathbb{R}^{n_q}$ (4.17) with the dimension n_q (4.18) to describe a polygonal chain in vector-valued form. As the directions need to be normalized, the admissible configuration space of a curved fiber is a curved, i.e., non-flat, manifold, see Equation (4.19). The discretization as

a polygonal chain and the parametrization with the coordinate vector $\mathbf{q}$ are visualized in Figure 5.1.

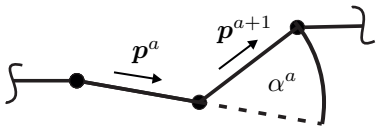


Figure 6.3: Angle α^a between the a^{th}- and the $(a+1)^{\text{th}}$-segment. Figure adapted from Figure 4 of Lauff et al. (2025a).

Based on this discretization, the local curvature (6.9) at the connection point of the a^{th} and the $(a+1)^{\text{th}}$ segment may be approximated by finite differences (Schneider, 2022)

$$\kappa^a \equiv \frac{\|\mathbf{p}^{a+1} - \mathbf{p}^a\|}{\ell}, \quad a = 1, \dots, n-1, \tag{6.19}$$

which we rewrite as

$$\kappa^a = \frac{\sqrt{2\,(1 - \mathbf{p}^a \cdot \mathbf{p}^{a+1})}}{\ell}, \quad a = 1, \dots, n-1, \tag{6.20}$$

using the normalization condition of the directions. In terms of the angle α^a between the a^{th}- and the $(a+1)^{\text{th}}$-segment, see Figure 6.3, the expression (6.20) may be reformulated

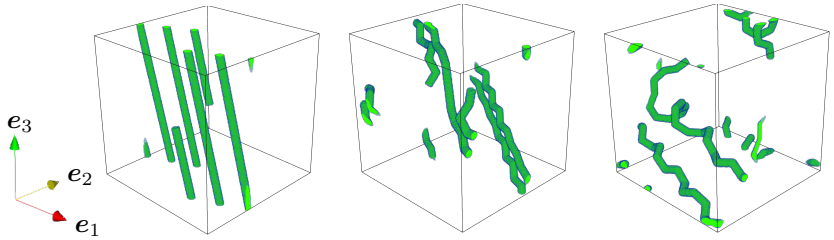
$$\kappa^a = \frac{\sqrt{2\,(1 - \cos\alpha^a)}}{\ell}, \quad a = 1, \dots, n-1. \tag{6.21}$$

For the discretized curve, the fiber orientation tensors of second order and fourth order compute as

$$\boldsymbol{A}_f = \frac{1}{n}\sum_{a=1}^{n} \boldsymbol{p}^a \otimes \boldsymbol{p}^a \quad \text{as well as} \quad \mathbb{A}_f = \frac{1}{n}\sum_{a=1}^{n} \boldsymbol{p}^{\otimes 4}, \tag{6.22}$$

and the DSC is computed with the formula

$$K_f = \frac{1}{n}\sum_{a=1}^{n} \|\boldsymbol{A}_f - \boldsymbol{p}^a \otimes \boldsymbol{p}^a\|^2 = 1 - \|\boldsymbol{A}_f\|^2. \tag{6.23}$$



(a) $K_f = 0$ **(b)** $K_f = \frac{1}{3}$ **(c)** $K_f = \frac{2}{3}$

Figure 6.4: Cells filled with single fibers and varying deviations from straight curve K_f. Figure adapted from Figure 5 of Lauff et al. (2025a).

In Figure 6.4, single fibers discretized as polygonal chains with the DSCs $K_f = 0$, $K_f = 1/3$ and $K_f = 2/3$ are shown. As the fiber lengths exceed the selected cell size, the fibers wrap around the periodic cell multiple times. In accordance with our previous discussion, the selection of the DSC to be $K_f = 0$ leads to straight fibers, i.e., no fiber curvature is realized, see Figure 6.4(a). With increasing DSC, we observe that the degree of curvature of the fibers is also increasing, see Figure 6.4(b) and Figure 6.4(c). For $K_f = 2/3$, the highest degree of curvature is realized.

As the DSC only takes the value $2/3$ for the extreme case of an isotropic fiber orientation state, the fiber is formed as a three-dimensional spiral.

6.3 Generating microstructures filled with curved fibers

6.3.1 Description of fiber-reinforced composites with long and curved fibers

We consider a periodic unit cell $Q = [0, Q_1] \times [0, Q_2] \times [0, Q_3]$ which should contain N curved fibers in a non-overlapping configuration. The fibers have the uniform fiber diameter D and their centerline is described by polygonal chains, see Section 6.2.2. For the parametrization of the polygonal chain describing the i^{th}-fiber ($i = 1, \dots, N$), we use the coordinate vector $\mathbf{q}_i$ (4.17). The fiber lengths L_i are described in terms of a fiber length distribution, e.g., the Dirac, the Weibull or the log-normal distribution. A prescribed maximum segment length $\bar{\ell}$ is used to select the number of segments for each fiber depending on the fiber length L_i, see Equation (4.44). Due to the non-penetrating fiber arrangement, the total fiber volume fraction computes as the sum over the fiber volume fraction of the single fibers (4.45). The volume-weighted fiber orientation tensors of second order and of fourth order compute as

$$\boldsymbol{A} = \frac{1}{L_{\text{total}}} \sum_{i=1}^{N} L_i \, \boldsymbol{A}_f^i \quad \text{and} \quad \mathbb{A} = \frac{1}{L_{\text{total}}} \sum_{i=1}^{N} L_i \mathbb{A}_f^i, \tag{6.24}$$

where $\boldsymbol{A}_f^i$ and $\mathbb{A}_f^i$ are the fiber orientation tensors (6.22) of the i^{th}-fiber. The information on the fiber orientation state of fiber-reinforced composites is typically obtained from micro-CT imaging (Krause et al., 2010; Fliegener et al., 2014; Wirjadi et al., 2016; Pinter et al., 2018; Hessman et al., 2019; Blarr et al., 2023) or from filling simulations (Kennedy and

Zheng, 2013; Görthofer et al., 2019; Meyer et al., 2020). Whereas from micro-CT imaging also the fiber orientation tensors of higher orders may be extracted, filling simulations typically only provide the fiber orientation tensor of second order $\boldsymbol{A}$. However, to estimate the effective elastic stiffness, fiber orientation tensors of higher order are required as they include additional information (Müller and Böhlke, 2016; Bauer and Böhlke, 2022a). Based on a given second-order fiber orientation tensor, the required fiber orientation tensors of higher order may be approximated by closures (Cintra and Tucker III, 1995; Dray et al., 2007; Breuer et al., 2019; Kugler et al., 2020; Karl et al., 2021; 2023)

$$\mathbb{A} = \mathbb{F}(\boldsymbol{A}). \tag{6.25}$$

However, such approaches do not provide a fiber orientation distribution, which is required to sample fiber directions, e.g., during the microstructure generation. Thus, alternative approaches, e.g., the exact (ACG) closure (Montgomery-Smith et al., 2011a;b) or the maximum entropy closure (Chaubal and Leal, 1998; Müller and Böhlke, 2016), first approximate the fiber orientation distribution and subsequently compute the desired fiber orientation tensors form the fiber orientation distribution. In this manuscript, we use the exact closure to obtain an approximation for the fiber orientation distribution as well as for the fiber orientation tensor of fourth order.

Additionally, the volume-weighted DSC is introduced as

$$\bar{K} = \frac{1}{L_{\text{total}}} \sum_{i=1}^{N} L_i \, K_f^i, \tag{6.26}$$

where K_f^i denotes the DSC (6.23) of the i^{th}-fiber. Due to the non-negativity of the lengths L_i and the range of the parameter K_f^i (6.14),

the volume-weighted DSC also satisfies the bounds

$$0 \leq \bar{K} \leq \frac{2}{3}. \tag{6.27}$$

To prevent excessively high fiber bending, we require that the approximated curvatures κ_i^a (6.21) between two adjacent segments do not exceed a predefined maximum curvature $\bar{\kappa}$

$$\kappa_i^a \leq \bar{\kappa}, \quad i = 1, \ldots, N, \quad a = 1, \ldots, n_i - 1. \tag{6.28}$$

6.3.2 Objective function with extended curvature control

According to the core procedure of the fused sequential addition and migration (fSAM) method (Lauff et al., 2024; 2025b), we use an optimization algorithm to find admissible fiber arrangements. Therefore, we introduce a non-negative objective function F such that all fiber configurations characterized by the roots of the objective function

$$F(\mathbf{f}_1, \ldots, \mathbf{f}_N) = 0 \tag{6.29}$$

are admissible solutions of the optimization problem. The vector $\mathbf{f}_i$ is an alternative parametrization of the i^{th}-fiber comprising the midpoints $\mathbf{x}_i^a$ and direction $\mathbf{p}_i^a$ of all segments (4.12). With a given coordinate vector $\mathbf{q}_i$, the midpoints of the segments may be computed via Equation (4.20). The original objective function of the fSAM algorithm (Lauff et al., 2024) does only include a maximum angle constraint to prevent excessively high kinks between adjacent segments. However, prescribing a desired degree of fiber curvature is not possible. Thus, we aim to extend the objective function by a term taking the desired volume-weighted DSC $\bar{K}$ into account. More precisely, we aim to satisfy the non-overlap condition, the maximum curvature constraint (6.28) as well as the desired fiber

orientation and curvature states

$$\mathbb{A} \stackrel{!}{=} \mathbb{A}^{\mathsf{r}} \quad \text{and} \quad \bar{K} \stackrel{!}{=} \bar{K}^{\mathsf{r}}, \tag{6.30}$$

where we distinguish between the desired states $\mathbb{A}$ or $\bar{K}$ and the currently realized states $\mathbb{A}^{\mathsf{r}}$ or $\bar{K}^{\mathsf{r}}$.

We start the discussion with the introduction of the objective function (Schneider, 2022; Lauff et al., 2024) of dimension $(\text{length})^2$, see Section 4.3.2,

$$F\left(\mathbf{f}_1, \ldots, \mathbf{f}_N\right) \hat{=} \frac{1}{2} \sum_{i,j=1}^{N} \sum_{a=1}^{n_i} \sum_{b=1}^{n_j} \left(\delta_{ij}^{ab}\right)^2 + \frac{w_{\mathbb{A}}}{8} N \left\|\mathbb{A} - \mathbb{A}^{\mathsf{r}}\right\|^2, \tag{6.31}$$

including a term for the non-overlap condition and the fiber orientation tensor of fourth order. Whereas the term for the non-overlap condition is considered until a non-penetrating arrangement is found, the fiber orientation term is only active if the convergence criterion

$$\frac{\left\|\mathbb{A} - \mathbb{A}^{\mathsf{r}}\right\|}{\left\|\mathbb{A}\right\|} \leq \epsilon_{\mathbb{A}} \tag{6.32}$$

with the tolerance $\epsilon_{\mathbb{A}}$ does not hold.

To account for the desired volume-weighted DSC $\bar{K}$ (6.26) and the maximum curvature constraint (6.28), we extend the objective function by two additional terms

$$\begin{aligned} F_{\text{curvature}}\left(\mathbf{f}_1, \ldots, \mathbf{f}_N\right) \hat{=} & \frac{1}{2} \sum_{i,j=1}^{N} \sum_{a=1}^{n_i} \sum_{b=1}^{n_j} \left(\delta_{ij}^{ab}\right)^2 + \frac{w_{\mathbb{A}}}{8} N \left\|\mathbb{A} - \mathbb{A}^{\mathsf{r}}\right\|^2 \\ & + \frac{w_{\bar{K}}}{8} n_s \left(\bar{K} - \bar{K}^{\mathsf{r}}\right)^2 \\ & + \frac{w_{\bar{\kappa}} \, \ell_{\text{mean}}^4}{2} \sum_{i=1}^{N} \sum_{a=1}^{n_i - 1} \left(\left\langle \left(\kappa_i^a\right)^2 - \bar{\kappa}^2 \right\rangle_+ \right)^2 . \end{aligned} \tag{6.33}$$

The third term accounts for the desired volume-weighted DSC $\bar{K}$ with the empirical weight $w_{\bar{K}} = 20\, w_{\mathbb{A}}$. The maximum curvature constraint is realized by the fourth term, where the mean segment length computes as

$$\ell_{\text{mean}} = \frac{L_{\text{total}}}{n_s} \quad \text{with} \quad n_s = \sum_{i=1}^{N} n_i, \tag{6.34}$$

and we choose the weight to be $w_{\bar{\kappa}} = 1.5\, \varepsilon(\ell_i, D)$. Within the objective function $F_{\text{curvature}}$ (6.33), the terms for the desired fiber curvature parameter and the maximum angle constraint are taken into account via the convergence criteria

$$\begin{aligned} &\frac{\|\bar{K} - \bar{K}^{\mathrm{r}}\|}{\bar{K}} \leq \epsilon_{\bar{K}} \quad \text{and} \quad \frac{\langle \kappa_i^a - \bar{\kappa} \rangle_+}{\bar{\kappa}} \leq \epsilon_{\bar{\kappa}}, \\ &i = 1, \ldots, N, \quad a = 1, \ldots, n_i - 1, \end{aligned} \tag{6.35}$$

respectively. The convergence criterion for the maximum curvature constraint is evaluated for all adjacent segments individually. In case of a desired DSC $\bar{K}$, the weights for the fiber orientation term $w_{\mathbb{A}}$ and for the maximum curvature constraint $w_{\bar{\kappa}}$ need to be increased and we select a factor of two for both weights. Selecting the weights for the individual terms within the objective function to ensure a stable convergence behavior of the algorithm is critical. We selected the weights by trial and error, investigating numerous different combinations of microstructural descriptors to ensure that the weighting factors work for a wide range of desired microstructures. In fact, the algorithm is quite sensitive with respect to the selection of the weighting factors, underlining the importance of an adequate choice.

For the optimization procedure of the fSAM algorithm (Lauff et al., 2024), the directional derivatives of the objective function with respect to the coordinate vector $\mathbf{f}_i$ are necessary. According to the extended objective

function $F_{\text{curvature}}$ (6.33), the directional derivatives compute as

$$
\begin{aligned}
\frac{\partial F_{\text{curvature}}\left(\mathbf{f}_1, \ldots, \mathbf{f}_N\right)}{\partial \mathbf{x}_i^a} &\hat{=} -\sum_{j=1}^{N} \sum_{b=1}^{n_j} \delta_{ij}^{ab} \frac{\boldsymbol{k}_{ij}^{ab}}{\left\| \boldsymbol{k}_{ij}^{ab} \right\|}, \\
\frac{\partial F_{\text{curvature}}\left(\mathbf{f}_1, \ldots, \mathbf{f}_N\right)}{\partial \mathbf{p}_i^a} &\hat{=} -\sum_{j=1}^{N} \sum_{b=1}^{n_j} \delta_{ij}^{ab} \frac{\ell_i \, s_{ij}^{ab}}{2} \frac{\boldsymbol{k}_{ij}^{ab}}{\left\| \boldsymbol{k}_{ij}^{ab} \right\|} \\
&\quad - w_{\mathbb{A}} \frac{\ell_i \, N}{L_{\text{total}}} \left(\mathbb{A} - \mathbb{A}^{\mathsf{r}}\right) \left[(\boldsymbol{p}_i^a)^{\otimes 3} \right] \\
&\quad + w_{\bar{K}} \frac{\ell_i}{\ell_{\text{mean}}} \left(\bar{K} - \bar{K}^{\mathsf{r}}\right) \boldsymbol{A}_f^i \, \boldsymbol{p}_i^a \\
&\quad - w_{\bar{\kappa}} \frac{2 \, \ell_{\text{mean}}^4}{\ell_i^2} \left(\left\langle (\kappa_i^a)^2 - \bar{\kappa}^2 \right\rangle_+ \boldsymbol{p}_i^{a+1} \right. \\
&\qquad \left. + \left\langle \left(\kappa_i^{a-1}\right)^2 - \bar{\kappa}^2 \right\rangle_+ \boldsymbol{p}_i^{a-1} \right).
\end{aligned}
\tag{6.36}
$$

6.3.3 Pre-optimization step

The procedure of the fSAM algorithm (Lauff et al., 2024) starts with the sampling of straight fibers which are described by a single segment (Schneider, 2022). More precisely, the fiber midpoints are distributed uniformly within the unit cell, the fiber directions are sampled from the approximated fiber orientation distribution and the fiber lengths follow the desired fiber length distribution. After the sampling step, the fibers are segmented into n_i segments following Equation (4.44). Although the sampling of the fiber directions accounts for the desired fiber orientation distribution, the realized fiber orientation state may differ from the desired one as we consider a finite number of fibers. To ensure an adequate fiber orientation state before starting the main optimization procedure, a pre-optimization step is executed, minimizing the objective function without considering the non-overlap condition.

For the extended objective function $F_{\text{curvature}}$ (6.33), the objective function of the pre-optimization step is defined as

$$F_{\text{pre,1}}\left(\mathbf{f}_1,\ldots,\mathbf{f}_N\right) \hat{=} \frac{w_{\mathbb{A}}}{8} N \left\|\mathbb{A}-\mathbb{A}^{\text{r}}\right\|^2 + \frac{w_{\bar{K}}}{8} n_s \left(\bar{K}-\bar{K}^{\text{r}}\right)^2 + \frac{w_{\bar{\kappa}}\,\ell_{\text{mean}}^4}{2} \sum_{i=1}^{N} \sum_{a=1}^{n_i-1} \left(\left\langle \left(\kappa_i^a\right)^2 - \bar{\kappa}^2 \right\rangle_+ \right)^2, \tag{6.37}$$

dropping the term for the non-overlap condition. However, in our studies it turned out that the pre-optimization step with already segmented fibers leads to drastically increased runtimes for the main optimization procedure when prescribing small volume-weighted DSCs. To improve the efficiency of the algorithm, we use straight fibers with a single segment for the pre-optimization step and subsequently conduct the decomposition into n_i segments. For this alternative approach, the objective function reads

$$F_{\text{pre,2}}\left(\mathbf{f}_1,\ldots,\mathbf{f}_N\right) \hat{=} \frac{w_{\mathbb{A}}}{8} N \left\|\mathbb{A}-\mathbb{A}^{\text{r}}\right\|^2. \tag{6.38}$$

Compared to the original formulation (6.37), two terms are missing. As the fibers are straight, the realized volume-weighted DSC $\bar{K}^{\text{r}}$ equals zero, and we take the desired DSC $\bar{K}$ into consideration once the main optimization starts. Furthermore, the maximum curvature constraint is intrinsically ensured as the local curvature of the fiber vanishes.

The decision to use straight fibers for the pre-optimization step enables the microstructure generation for small DSCs, i.e., almost straight fibers. In addition, in our studies it turned out that the generation time for higher fiber curvatures is not influenced significantly by this choice. With respect to the generated fibers within the final microstructure, the pre-optimization step with straight fibers may lead to smaller mean values of the local fiber curvature. However, at this point generating microstructures for a wide range of DSCs is only possible efficiently when making the algorithmic choice of straight fibers in the pre-optimization step.

6.4 Computational investigations

6.4.1 Setup

The fSAM algorithm is written in Python with Cython extensions and partly parallelized with OpenMP. The numerical studies were conducted on a desktop computer with a 8-core Intel i7 CPU and 64GB RAM.

E-glass fibers			PP matrix		
E	$=$	$72.0\,\mathrm{GPa}$	E	$=$	$1.25\,\mathrm{GPa}$
ν	$=$	0.22	ν	$=$	0.35

Table 6.1: Isotropic elastic moduli for the PP matrix and the E-glass fibers (DOW® Chemical Company, 2003; PPG Fiber Glass, 2013; Garesci and Fliegener, 2013). Table adapted from Table 1 of Lauff et al. (2025a).

As the reference material system, we use an E-glass fiber reinforced polypropylene (PP) matrix with the elastic constants listed in Table 6.1. We consider the fiber diameter $D = 10\,\mu\mathrm{m}$ and the fiber length $L = 1000\,\mu\mathrm{m}$, i.e., a fiber aspect ratio of $r_a = 100$. The composite has a fiber volume fraction of $\phi = 20\,\%$. For the fiber orientation tensor of second order, we prescribe $\boldsymbol{A} \mathrel{\hat{=}} \mathrm{diag}\,(0.75, 0.15, 0.1)$ and approximate the fiber orientation tensor of fourth order with the ACG closure. Thus, the fiber orientation tensor of fourth order is orthotropic (Bauer and

Böhlke, 2022a;b) and reads

$$\mathbb{A} \mathrel{\hat{=}} \begin{bmatrix} 0.6514 & 0.0584 & 0.0402 & 0 & 0 & 0 \\ 0.0584 & 0.0733 & 0.0182 & 0 & 0 & 0 \\ 0.0402 & 0.0182 & 0.0416 & 0 & 0 & 0 \\ 0 & 0 & 0 & 0.0182 & 0 & 0 \\ 0 & 0 & 0 & 0 & 0.0402 & 0 \\ 0 & 0 & 0 & 0 & 0 & 0.0584 \end{bmatrix} \tag{6.39}$$

in Voigt's notation. Furthermore, we choose the maximum curvature $\bar{\kappa} = 0.02\,1/\mu\mathrm{m}$, i.e., in case of the segment lengths $\ell = 40\,\mu\mathrm{m}$, $25\,\mu\mathrm{m}$ and $15\,\mu\mathrm{m}$, the maximum angle $\bar{\alpha}$ between adjacent segments is about $47°$, $29°$ and $17°$, respectively. The maximum segment length $\bar{\ell}$ and the desired volume-weighted DSC $\bar{K}$ are selected in the individual studies. As an algorithmic choice, we select a minimum distance between the fibers of $20\,\%$ of the fiber diameter, i.e., $2.0\,\mu\mathrm{m}$. Additionally, we insist that the relative error of the fiber orientation tensor needs to be below $\epsilon_{\mathbb{A}} = 10^{-4}$. The tolerances for the curvature parameter $\bar{K}$ and the maximum curvature constraint are fixed as $\epsilon_{\bar{K}} = \epsilon_{\bar{\kappa}} = 10^{-3}$. For small maximum segment lengths, the number of segments n may be extremely high. As for each optimization step linear equations of dimension $3\,(n+1)$ need to be solved, the original fSAM algorithm slows down (Lauff et al., 2024). Thus, the fSAM algorithm includes a procedure where each fiber with more than a prescribed maximum segment number $\bar{n}$ is divided into separately moving subchains (Lauff et al., 2024). The coherence condition between the subchains is taken into consideration by an additional term in the objective function. We use this procedure in case that the maximum segment length $\bar{\ell} = 15\,\mu\mathrm{m}$ is selected and choose the maximum segment number to be $\bar{n} = 35$. For convergence, the distance between adjacent subchains needs to be below $10^{-3}D$.

Based on the generated microstructures, we compute the effective linear elastic moduli with an FFT-based computational homogenization software (Moulinec and Suquet, 1994; 1998). More precisely, we rely on a staggered grid for the discretization (Schneider et al., 2016) and apply a conjugate gradient solver (Zeman et al., 2010; Brisard and Dormieux, 2012; Schneider, 2020a). The iterative procedure stops provided the convergence criterion (Schneider, 2021) is below 10^{-5}. To obtain the effective elasticity tensor, we use six linearly independent strain-load cases. As the material law is isotropic and the desired fiber orientation tensor of fourth order is orthotropic, see Equation (6.39), the effective elasticity tensor is orthotropic, as well. However, due to the approximate realization of the orthotropic fiber orientation tensor of fourth order, the computed apparent stiffness is not completely orthotropic. Thus, we approximate the effective orthotropic engineering constants from the effective elasticity tensor (Cowin, 1985; Görthofer et al., 2020). In addition, to assess the error induced by the orthotropic approximation, we monitor the approximation error

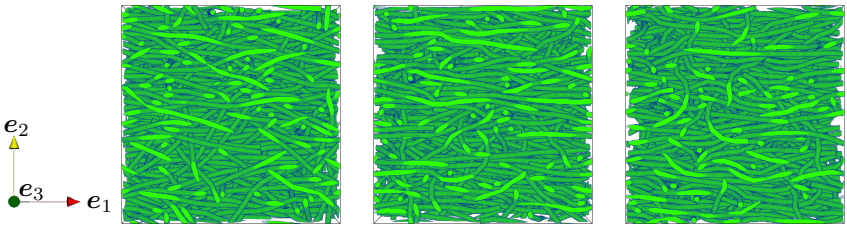
$$\mathrm{err}_{\mathrm{orth}} = \frac{\|\mathbb{C}^{\mathrm{r}} - \mathbb{C}^{\mathrm{r}}_{\mathrm{orth}}\|}{\|\mathbb{C}^{\mathrm{r}}\|} \cdot 100\%, \tag{6.40}$$

where $\mathbb{C}^{\mathrm{r}}$ denotes the realized effective stiffness and $\mathbb{C}^{\mathrm{r}}_{\mathrm{orth}}$ its orthotropic approximation.

6.4.2 Resolution study

To compute the effective elasticity tensor adequately, a sufficiently fine resolution is necessary. However, with decreasing mesh size, the computational effort of the computational homogenization increases, as well. Thus, we aim to use a resolution which is fine enough to provide reliable results but still leads to reasonable runtimes of the algorithm. For the resolution study, we use the reference setup from Section 6.4.1 and generate cubic microstructures with cell dimensions $Q_i = 400\,\mu\mathrm{m}$.

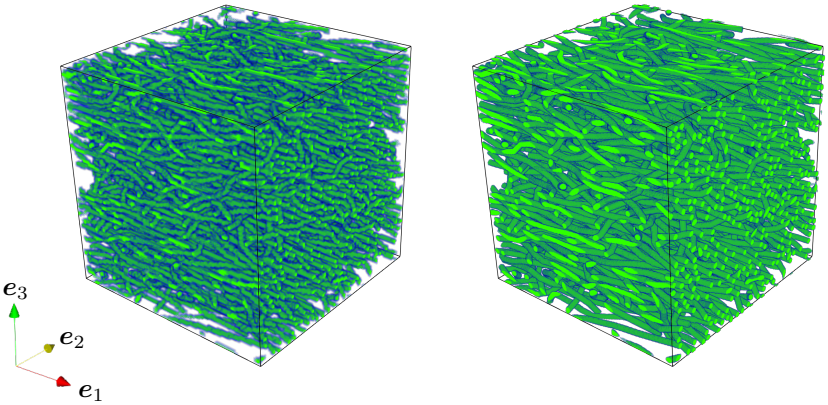
To investigate the necessary resolution for microstructures with small and high degrees of curvature, we consider for the volume-weighted DSC $\bar{K} = 0.06$ and $\bar{K} = 0.25$. Microstructures generated with these volume-weighted DSCs are shown in Figure 6.5. The maximum segment length is selected as $\bar{\ell} = 25\,\mu\mathrm{m}$, i.e., the fibers of length $L = 1000\,\mu\mathrm{m}$ are divided into 40 segments.



(a) $\bar{K} = 0.06$ **(b)** $\bar{K} = 0.15$ **(c)** $\bar{K} = 0.25$

Figure 6.5: Microstructures with varying volume-weighted deviations from straight curve $\bar{K}$. Figure adapted from Figure 6 of Lauff et al. (2025a).

We study the voxel-edge lengths $h = 1.0\,\mu\mathrm{m}$, $1.25\,\mu\mathrm{m}$, $2.0\,\mu\mathrm{m}$ and $4.0\,\mu\mathrm{m}$ and show microstructures with the volume-weighted DSC $\bar{K} = 0.25$ for the finest and the coarsest mesh size in Figure 6.6. Compared to the fiber diameter of $D = 10\,\mu\mathrm{m}$, the selected resolutions have 10, 8, 5 and 2.5 voxels per diameter from the finest to the coarsest mesh size. As the effort for the computational homogenization procedure is mainly driven by the total amount of voxels, which is 400^3, i.e., $64 \cdot 10^6$, for the finest resolution and $1 \cdot 10^6$ for the coarsest resolution, the runtime is significantly smaller for the coarser resolution.



(a) $h = 4.00\,\mu\mathrm{m}$ **(b)** $h = 1.25\,\mu\mathrm{m}$

Figure 6.6: Microstructures with volume-weighted deviation from straight curve $\bar{K} = 0.25$ resolved with the voxel edge-lengths $h = 4.00\,\mu\mathrm{m}$ (a) and $h = 1.25\,\mu\mathrm{m}$ (b). Figure adapted from Figure 7 of Lauff et al. (2025a).

The results of the computations are listed in Table 6.2. First, we assess the approximation quality of the orthotropic engineering constants from the computed elasticity tensor by computing the approximation error $\mathrm{err}_{\mathrm{orth}}$. We observe that the approximation error is above $1\,\%$ for the two voxel-edge lengths $h = 4\,\mu\mathrm{m}$ and $2\,\mu\mathrm{m}$ and decreases below $1\,\%$ for the voxel-edge lengths $h = 1.25\,\mu\mathrm{m}$ and $1\,\mu\mathrm{m}$. Thus, the results demonstrate that the orthotropic approximation is justified. The necessary resolution is chosen by comparing the mechanical properties of the coarser mesh sizes with the results of the finest mesh size. Based on this procedure, we select the coarsest mesh size whose elastic properties only differ with a relative difference below $1\,\%$ from the finest resolution as the necessary resolution. For the volume-weighted DSC $\bar{K} = 0.06$, the Young's modulus E_1 reveals the highest relative underestimation with $13.11\,\%$ for the coarsest resolution. With decreasing voxel-edge length, the error

reduces to $3.71\,\%$ for $h = 2\,\mu\mathrm{m}$ and $0.93\,\%$ for $h = 1.25\,\mu\mathrm{m}$. Hence, for small degrees of fiber curvature the voxel-edge length $h = 1.25\,\mu\mathrm{m}$ turns out be sufficient. With respect to the higher volume-weighted DSC $\bar{K} = 0.25$, the Young's modulus E_1 is also most affected by the resolution. For the coarsest resolution, the relative underestimation is $10.39\,\%$, dropping to $2.86\,\%$ and $0.78\,\%$ with refining mesh size. As the voxel-edge length $h = 1.25\,\mu\mathrm{m}$ results in relative errors below $1\,\%$ for both curvature parameters, we use this resolution for the following investigations.

$\bar{K}$	h	E_1	E_2	E_3	G_{23}	G_{13}	G_{12}	$\mathrm{err}_{\mathrm{orth}}$
$-$	μm	GPa	GPa	GPa	GPa	GPa	GPa	%
	4.00	7.49	2.60	2.46	0.92	1.15	1.29	3.06
0.06	2.00	8.30	2.59	2.40	0.89	1.13	1.31	1.22
	1.25	8.54	2.60	2.39	0.88	1.12	1.32	0.70
	1.00	8.62	2.60	2.39	0.88	1.13	1.32	0.56
	4.00	6.90	2.47	2.37	0.90	1.07	1.17	2.94
0.25	2.00	7.48	2.40	2.29	0.85	1.02	1.13	1.17
	1.25	7.64	2.38	2.27	0.83	1.01	1.12	0.68
	1.00	7.70	2.38	2.27	0.82	1.00	1.12	0.55

Table 6.2: Approximated orthotropic engineering constants for the voxel edge-lengths $h = 4.00\,\mu\mathrm{m}$, $h = 2.00\,\mu\mathrm{m}$, $h = 1.25\,\mu\mathrm{m}$ and $h = 1.00\,\mu\mathrm{m}$. Table adapted from Table 2 of Lauff et al. (2025a).

6.4.3 RVE study

In computational homogenization, we analyze the material properties of a microstructure using unit cells. The concept of representativity refers to the ability of specific unit cells to accurately reflect the material's *effective* properties, which are the deterministic macroscopic properties

that emerge as the volume of the unit cell tends to infinity (Hill, 1963; Drugan and Willis, 1996; Kanit et al., 2003). On finite-sized unit cells, the computed *apparent* properties are random due to the inherent randomness in the microstructure, i.e., they vary for different realizations. As the size of the unit cell increases, the apparent properties converge to the effective properties almost surely, reducing the randomness in the computed values. In this context, a *representative volume element* (RVE) is a unit cell large enough such that its apparent properties closely match the effective properties of the material. To reduce the effort of the computational homogenization, the smallest RVE size should be used. In the context of microstructure generation, periodic geometries in combination with accurately realized descriptors, e.g., the fiber volume fraction and fiber orientation tensor of fourth order, enable a reduction of the RVE size (Mehta and Schneider, 2022; Schneider, 2022; Lauff et al., 2024).

The representativity of a unit cell may be assessed by a statistical approach (Kanit et al., 2003; Gloria and Otto, 2011), monitoring the *random* and the *systematic* error. The random error, or dispersion, measures the variance of multiple realizations on a fixed unit cell size. With increasing unit cell size, the variance converges to zero, i.e., the apparent properties converge to deterministic values. On the other hand, the systematic error, or bias, quantifies the difference between the mean value of the apparent properties for a fixed unit cell and the effective properties. As the effective properties are typically unknown quantities, we compare the mean apparent properties for increasing cell-sizes until convergence.

We use the setup from the previous section 6.4.2 and study the representativity of the unit cells with cell dimensions $Q_i = 300\,\mu\mathrm{m}$, $400\,\mu\mathrm{m}$, $500\,\mu\mathrm{m}$. We resolve the microstructures with the voxel-edge length $h = 1.25\,\mu\mathrm{m}$, according to the results of the resolution study 6.4.2. Based on this resolution, the three unit cells contain the voxel numbers listed in

Table 6.3, i.e., the largest unit cell comprises about 4.6 times more voxels than the smallest unit cell.

Q_i μm	Voxel number –
300	$240^3 \approx 14 \cdot 10^6$
400	$320^3 \approx 33 \cdot 10^6$
500	$400^3 = 64 \cdot 10^6$

Table 6.3: Number of voxels for varying cell dimensions Q_i. Table adapted from Table 3 of Lauff et al. (2025a).

As all three unit cells are rather small compared to the fiber length $L = 1000\,\mu\text{m}$, the fibers are multiple times larger than the edge lengths. Realizations with the three varying unit cell sizes are shown in Figure 6.7 for the volume-weighted DSC $\bar{K} = 0.25$.

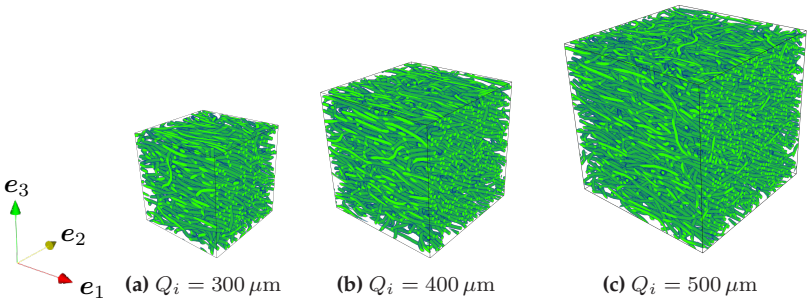


Figure 6.7: Generated microstructures for three different cubic cell-sizes Q_i. Figure adapted from Figure 8 of Lauff et al. (2025a).

We report on the mean and the standard deviation of the approximated orthotropic engineering constants in Table 6.4, generating ten realizations

for each unit cell size. In all cases, we observe that the orthotropic approximation error is below $1\,\%$, i.e., the effective elastic material behavior may be considered as orthotropic. With respect to the representativity error, it turns out that both the random and the systematic error only concern the third significant digit. Thus, even the smallest unit cell size may be considered representative for engineering purposes.

$\bar{K}$	Q_i	E_1	E_2	E_3	G_{23}	G_{13}	G_{12}	$\mathrm{err}_{\mathrm{orth}}$
$-$	μm	GPa	GPa	GPa	GPa	GPa	GPa	%
	300	8.54	2.60	2.39	0.88	1.13	1.32	0.65
		$\pm$0.03	$\pm$0.01	$\pm$0.01	$\pm$0.00	$\pm$0.00	$\pm$0.01	$\pm$0.09
0.06	400	8.53	2.60	2.39	0.88	1.13	1.32	0.69
		$\pm$0.01	$\pm$0.01	$\pm$0.00	$\pm$0.00	$\pm$0.00	$\pm$0.00	$\pm$0.05
	500	8.52	2.60	2.39	0.88	1.13	1.32	0.68
		$\pm$0.01	$\pm$0.00	$\pm$0.00	$\pm$0.00	$\pm$0.00	$\pm$0.00	$\pm$0.04
	300	7.66	2.38	2.27	0.83	1.01	1.12	0.62
		$\pm$0.03	$\pm$0.01	$\pm$0.00	$\pm$0.00	$\pm$0.01	$\pm$0.01	$\pm$0.07
0.25	400	7.66	2.38	2.27	0.83	1.01	1.12	0.63
		$\pm$0.02	$\pm$0.01	$\pm$0.00	$\pm$0.00	$\pm$0.00	$\pm$0.00	$\pm$0.05
	500	7.65	2.38	2.27	0.83	1.01	1.12	0.59
		$\pm$0.02	$\pm$0.00	$\pm$0.00	$\pm$0.00	$\pm$0.00	$\pm$0.00	$\pm$0.05

Table 6.4: Approximated orthotropic engineering constants for the cubic cell-sizes $Q_i = 300\,\mu$m, $Q_i = 400\,\mu$m and $Q_i = 500\,\mu$m. Table adapted from Table 4 of Lauff et al. (2025a).

As the fiber lengths may exceed the edge-lengths, self-intersection of a fiber needs to be considered when computing the quantity δ_{ij}^{ab}, see Equation (4.48), to characterize the non-overlap condition. As a result, we exclude fiber arrangements which are not admissible due to the resulting self-intersection. An example is a straight fiber in, e.g., $\boldsymbol{e}_1$-direction which is longer than the edge-length in $\boldsymbol{e}_1$-direction. Excluding self-

intersection gets more challenging the smaller the unit cell gets, and may affect the resulting microstructures as well as the predicted mechanical behavior. In computational practice, self-intersecting fibers only occur rarely, i.e., for individual fibers. Therefore, its influence on the effective stiffness seems to be limited. However, excluding self-intersection is vital for finding a non-intersecting configuration, i.e., without proper means the algorithm would not converge on a regular basis.

6.4.4 On the realized fiber curvatures and their effect on the mechanical properties

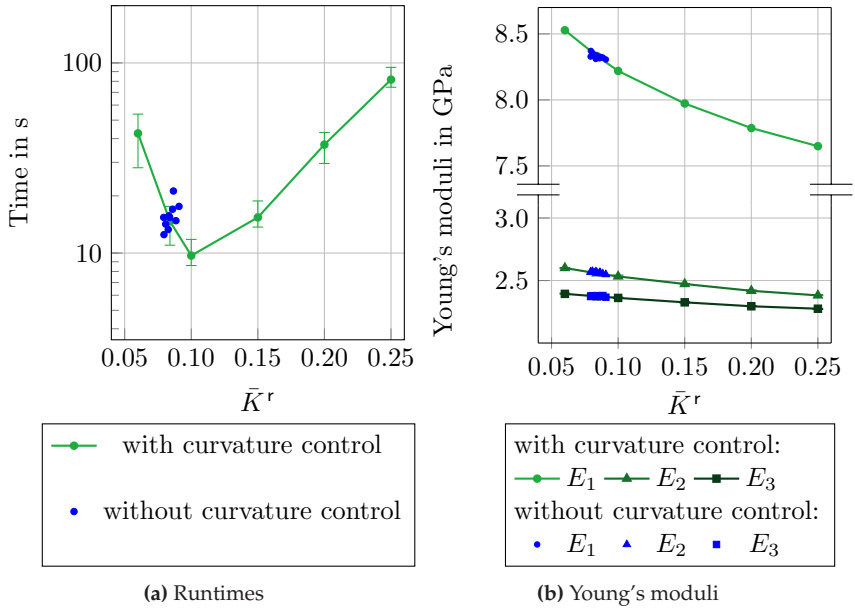
In this section, we compare the realized fiber curvature of the microstructures generated with the fSAM algorithm with or without the introduced fiber curvature control. Additionally, we aim to study the influence of the fiber curvature on the effective properties. Therefore, we first generate ten microstructures without the fiber curvature control. We consider the setup described in Section 6.4.2 with the cubic cell dimensions $Q_i = 400\,\mu\mathrm{m}$, which is sufficient for representativity, see Section 6.4.3. The individual runtimes to generate the ten microstructures as well as the realized volume-weighted DSCs $\bar{K}^{\mathrm{r}}$ are plotted in Figure 6.8(a), represented by the blue dots. We observe a mean runtime of about $16\,\mathrm{s}$. Furthermore, the realized volume-weighted DSCs $\bar{K}^{\mathrm{r}}$ are in a close range with a small mean value of 0.084. Thus, the fibers are rather straight.

In addition, we aim to compare the results with the novel formulation of the fSAM algorithm including the fiber curvature control. Therefore, we consider the volume-weighted DSCs in the set

$$\bar{K} \in \{0.06, 0.084, 0.1, 0.15, 0.2, 0.25\}, \tag{6.41}$$

where we also account for the mean volume-weighted DSC of the microstructures generated without fiber curvature control. Microstructures generated with three different volume-weighted DSCs are shown in

Figure 6.5. For each value in Equation (6.41), we generate ten realizations and plot the runtime in Figure 6.8(a).



(a) Runtimes **(b)** Young's moduli

Figure 6.8: Runtimes for the microstructure generation (a) and the Young's moduli (b) using the fSAM algorithm with or without the curvature control. Figure adapted from Figure 9 of Lauff et al. (2025a).

We observe that the runtime has a convex shape with a minimum at $\bar{K} = 0.1$, where the mean runtime is $9.7\,\mathrm{s}$. For the lower bound of the volume-weighted DSC $\bar{K} = 0.06$, the mean runtime is $42.6\,\mathrm{s}$ and for the upper bound of the volume-weighted DSC $\bar{K} = 0.25$, the mean runtime is even higher with $81.7\,\mathrm{s}$. Still, all microstructures are generated in less than two minutes. Let us compare the runtime at $\bar{K} = 0.084$ with

the runtime of the microstructure generation without curvature control. Then, we observe that the runtimes are within the same range, which underlines that the additional term in the objective function retains the efficiency of the algorithm.

We aim to discuss the reasons for the higher runtimes for very low and extremely high DSCs. Generating microstructures with low fiber curvature is more demanding especially due to two reasons. First, microstructure generation for long fiber reinforced composites with straight fibers is known to be a difficult task in general due to the inflexibility of the fibers to fill small spaces. The second reason concerns the opposing algorithmic fiber movement induced by minimizing the non-overlap condition and the DSC constraint, which disturbs the convergence behavior of the fSAM algorithm. To be more precise, the non-overlap condition leads to a change in fiber geometry towards more bent fibers, as they are easier to pack without fiber-overlap, whereas the DSC constraint aims to straighten the fibers. The increase in runtime for higher DSCs is mainly caused by the local curvature constraint, which is violated more often when a higher DSC is desired, increasing the complexity of the root finding.

The plot Figure 6.8(a) shows another advantage of the extension for a fiber curvature control. Whereas the realizable degrees of curvature are extremely limited when generating microstructures without curvature control, the novel formulation is capable of generating microstructures with volume-weighted DSCs in a wide range. Thus, it is possible to study the influence of the fiber curvature on the effective elastic behavior, and we visualize the computed Young's moduli in Figure 6.8(b). First, we notice that the realizations without curvature control are close to the results for the microstructure generation with fiber curvature control. Furthermore, the results reveal a significant influence of the fiber curvature on the Young's moduli. To be more precise, the Young's moduli are decreasing with increasing fiber curvature and the highest

relative difference is observed for the Young's modulus E_1. Whereas the Young's modulus E_1 is $8.53\,\mathrm{GPa}$ on average for the volume-weighted DSC $\bar{K} = 0.06$, the modulus drops to $7.65\,\mathrm{GPa}$ for the volume-weighted DSC $\bar{K} = 0.25$, which is a relative decrease of $10.31\,\%$. Also, the Young's moduli E_2 and E_3 reveal a relative decrease of $8.46\,\%$ and $5.02\,\%$ between the smallest and the highest fiber curvature. At a first glance, it may appear counterintuitive that increasing the curvature decreases the stiffness in the transversal directions as well. When one imagines a straight fiber becoming curved, this seems to increase the amount of fibers in the transversal directions, which should lead to an increase of stiffness in those directions. However, because our microstructure generation algorithm controls the fiber orientation tensor separately from the curvature, it compensates those effects by also re-orienting segments of other fibers, thereby increasing curvature without increasing the amount of fibers in the transversal directions. Therefore, the only effect on the transversal stiffness is due to the fibers in all directions being more bent, i.e., less stiff to loading along the fiber direction. Thus, the effective properties in all directions are significantly lower if the fiber curvature is more emphasized and the study reveals that the influence of the fiber curvature needs to be considered when generating representative volume elements for long fiber reinforced composites. Comparing the results to the influence of other microstructural descriptors of fiber-reinforced composites, the stiffness appears to be more sensitive to the fiber curvature than to the mean fiber length in case of long fibers (Schneider, 2022; Fliegener et al., 2014), but less sensitive than to the fiber orientation distribution or the fiber volume fraction (Schneider, 2017).

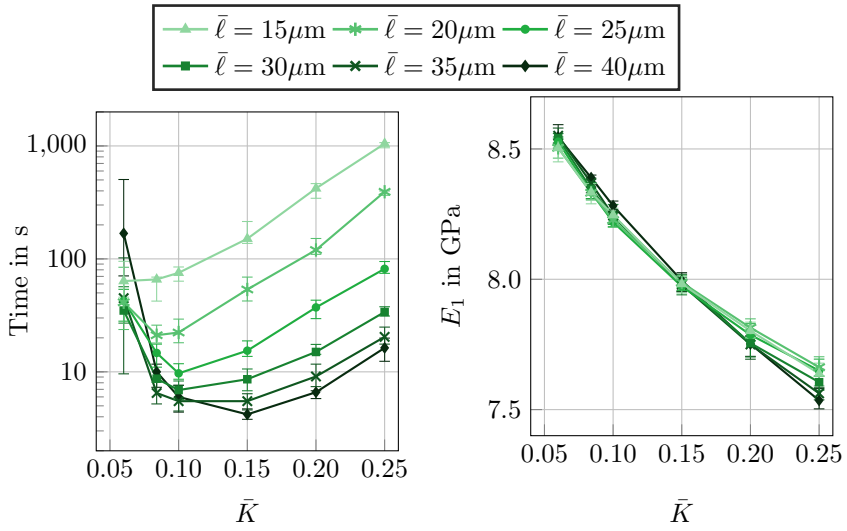
6.4.5 Study on the maximum segment length for varying degrees of curvature

We investigate the influence of the maximum segment length both on the runtime of the microstructure generation and the effective elastic properties of the microstructures. According to a previous study (Lauff et al., 2024) considering rather small fiber curvature, the maximum segment length has a significant influence on the runtime but a negligible influence on the effective properties. In this section, we aim to investigate whether this conclusion may also be drawn for varying degrees of curvature.

Therefore, we extend the study from Section 6.4.4 and consider the maximum segment lengths

$$\bar{\ell} \in \{15\,\mu\mathrm{m}, 20\,\mu\mathrm{m}, 25\,\mu\mathrm{m}, 30\,\mu\mathrm{m}, 35\,\mu\mathrm{m}, 40\,\mu\mathrm{m}\}. \tag{6.42}$$

The runtime for ten generated microstructures is plotted in Figure 6.9(a). We consider the configurations with the volume-weighted DSC $\bar{K} \in [0.15, 0.25]$ first. For this range, we observe a monotonic increase of the mean runtime for all maximum segment lengths. For example for the maximum segment length $\bar{\ell} = 15\,\mu\mathrm{m}$, we observe an increase in the mean runtime from $150.8\,\mathrm{s}$ to $1047.4\,\mathrm{s}$. Thus, the generation of microstructures with higher degree of curvature turns out to be more challenging. Additionally, the mean runtime is smaller for larger maximum segment lengths, i.e., when fewer segments are considered. For the maximum segment length $\bar{\ell} = 40\,\mu\mathrm{m}$ and the volume-weighted DSC $\bar{K} = 0.25$, the mean runtime is only $16.3\,\mathrm{s}$, which 64 times smaller than for the maximum segment length $\bar{\ell} = 15\,\mu\mathrm{m}$. Due to the smaller segment number, less collision checks are necessary. Additionally, the movement of the fibers in each optimization step is computationally less expensive for a coarser segmentation of the fibers (Lauff et al., 2024).



(a) Runtimes

(b) Young's modulus E_1

Figure 6.9: Comparison of the runtimes for the microstructure generation (a) and the Young's moduli (b) in terms of different maximum segment lengths $\bar{\ell}$. Figure adapted from Figure 10 of Lauff et al. (2025a).

For the lower range of the volume-weighted DSC $\bar{K} \in [0.06, 0.15]$, we still observe a monotonic increase for the smallest maximum segment length $\bar{\ell} = 15\,\mu\text{m}$. However, the highest maximum segment length $\bar{\ell} = 40\,\mu\text{m}$ shows a monotonic decrease. Fibers with small segments offer a high flexibility to use empty spaces even for small degrees of curvature. In contrast, it is quite challenging to pack microstructures with the considered combination of the fiber volume fraction, the fiber lengths and the fiber orientation distribution with large maximum segment lengths and small degrees of curvature. Considering the smallest volume-weighted DSC $\bar{K} = 0.06$, it turns out that the mean runtime for the maximum segment length $\bar{\ell} = 40\,\mu\text{m}$ is even higher than for the maximum segment length $\bar{\ell} = 15\,\mu\text{m}$. With decreasing maximum

segment lengths, we observe that the mean runtimes fall below the runtime for the maximum segment length $\bar{\ell} = 15\,\mu\mathrm{m}$ as more flexibility is induced.

Besides the effect on the runtimes of the microstructure generator, we aim to study the influence of the maximum segment lengths on the effective elastic properties. Therefore, we report on the Young's modulus E_1 in Figure 6.9(b). For the lower range of the volume-weighted DSC $\bar{K} \in [0.06, 0.20]$, we observe a close match below $1\,\%$ relative difference for all maximum segment lengths. For the upper bound of the volume-weighted DSC $\bar{K} = 0.25$, the results reveal a slightly larger deviation, which is still below $1.5\,\%$. Due to the elevated degree of fiber curvature, higher angles between adjacent segments are formed, especially for larger maximum segment lengths. These increased angles may induce stress peaks during the computational homogenization and thus may lead to a reduction of the effective Young's modulus. Hence, it is emphasized that, for higher curvature values, the chosen maximum segment length (which acts as a discretization parameter) must be carefully considered. If the segment length is too large, it may lead to a distortion of the results, making it critical to ensure that the segment length is small enough to avoid these stress-induced reductions in elasticity.

Let us connect the discussion on the influence of the maximum segment length to the approximation of the local curvature for a polygonal chain, see Equation (6.20). As the segment length serves as the stepsize of the finite differences formulation, the accuracy of the local curvature approximation significantly depends on the selected segment length. In case of small segment lengths, the curvature approximation is rather reliable, because the directional changes are well captured. However, for large segment lengths, the approximation does not reflect the actual local geometry anymore: the local discontinuities in the direction are averaged over longer distances, leading to a significant underestimation

of the local curvature. Especially for pronounced curvature, this effect leads to a loss of geometrical detail as the sharp angles between adjacent segments are smoothed out. Transferred to the curvature constraint (3.8), the local curvature approximation leads to an increase of the admissible angles between adjacent segments for increasing segment lengths. Eventually, in case of too large segment lengths, the actual local curvature is not constrained to such a degree that stress peaks at the junction between two segments are prevented. Thus, the aforementioned stress peaks for high DSCs may be induced.

6.5 Summary and conclusion

This section presents an algorithm for generating curvature-controlled microstructures of long fiber reinforced composites. As this algorithm allows the control of average fiber curvature as a separate parameter from the usually considered fiber volume fraction, aspect ratio and orientation distribution, it allows to investigate the relationship between curvature and composite properties.

The algorithm is based on the fused Sequential Addition and Migration (fSAM) algorithm for fiber-reinforced composite generation. Accordingly, we model the fibers as polygonal chains consisting of spherocylinder segments, which are parametrized by relative orientations, such that they always remain connected, with only the starting point of the chain being an absolute position. As this parameter space is a curved manifold, we describe how gradient calculations for the optimization process take into account the manifold's metric. Adding to this optimization algorithm, we extended the objective function by the volume-weighted deviation from straight curve (DSC), which we compute as the trace of the local second-order fiber orientation tensor's covariance for each single fiber, and then averaging. This particular choice of average curvature parameter leads to gradually

curved fibers without zig-zagging or sharp bends. In addition, we found that specifying the DSC imposes a lower bound on the average local curvature, such that increasing the DSC increases the curvature of the microstructure. With the novel DSC measure and its implementation within the framework of the fSAM algorithm, we significantly improve the curvature control methods integrated in microstructure generation tools compared to previous algorithms, e.g., the SAM algorithms for long fibers (Schneider, 2022) or the fSAM algorithm (Lauff et al., 2024), which only constrain the maximum angle between adjacent segments, or the microstructure generation tool introduced by Fliegener et al. (2014), which includes no curvature control at all.

We applied the algorithm to an example material consisting of a polypropylene matrix reinforced with glass fibers to study the realizability of extreme values of the curvature parameter and its influence on the stiffness of the composite. To briefly summarize:

- For the strongly textured fiber orientation distribution considered, the non-curvature-controlled fSAM algorithm tends towards a small curvature, with a mean of the realized volume-weighted DSCs $\bar{K}^{\mathrm{r}} = 0.084$ and a low variance. By comparison, DSCs from 0.064 to 0.25 are realizable with the new algorithm.
- The new algorithm has comparable runtimes to the non-curvature-controlled fSAM at similar curvature values. Both high and low curvature microstructures are computationally expensive to realize, with mean runtimes up to eight times longer than for medium-curvature microstructures.
- Resolution studies show that for both high and low average curvatures, the resolution-induced stiffness error is of the same order of magnitude, meaning that high-curvature microstructures do not appear to require particularly fine resolutions.
- The magnitude of the representativity error appears to be similar at both extremes of fiber curvature. We found periodic microstructures

containing roughly 340 fibers to be within 1 % representativity error, i.e., microstructures generated by our algorithm do not need to be particularly large to deliver accurate results.

- The segment length, a numerical parameter arising from the discretized fiber description, appears to have a negligible effect on the effective mechanical properties for low curvatures, as for the non-curvature-controlled fSAM algorithm. For higher curvatures, large segment lengths lead to underestimation of the stiffness, which we explain by sharp angles between adjacent segments, which lead to stress concentration in the adjacent material. The segment length's effect on the runtime is considerable, with longer segments leading to order-of-magnitude quicker calculations except for very low curvature values. Careful consideration of the segment length is therefore necessary when dealing with strongly curved fibers.
- Finally, we quantified the effect of the curvature on the stiffness, showing a monotonically decreasing stiffness with increasing curvature. This effect was most pronounced for the Young's modulus in the preferred fiber alignment direction, which showed a difference between both extremes of about 10 %. With the stiffness being this sensitive to curvature, we consider curvature control an important aspect of fiber-reinforced microstructure generation.

To summarize, we extended the fSAM algorithm by adding curvature control. This does not noticeably increase the numerical expense, yet allows for control over an important microstructural parameter, the average fiber curvature, which can significantly affect the elastic properties of fiber composites. For future research, it would be valuable to include DSC measurements for manufactured long fiber reinforced composites and to validate the effective behavior of the generated microstructures with experimental data. Furthermore, we may investigate further curvature measures (Hartmann and Liese, 2021; Kumar et al., 2024) and assess their robustness when integrated into the fSAM algorithm.

Chapter 7

Numerically robust local continuum damage models via convex relaxation[1]

7.1 Introduction

This chapter contributes to the field of phenomenological continuum-damage mechanics with a novel class of scalar damage models. Due to the convex and coercive formulation, these models are capable of reproducing strain softening behavior while avoiding localization effects, which is a long-standing challenge in damage modeling. Thus, the damage models enable modeling materials which exhibit softening, such as quasi-brittle solids or polymers.

There are a number of advantages which make a convexified damage model attractive:

- The model is local, i.e., no filtered averages or damage-gradient terms are necessary.
- The material evaluation involves conventional internal variables only, is thermodynamically consistent and operates on material point level.

[1] This chapter is based on the Sections 1.2 and 2 to 5 of the publication "Numerically robust local continuum damage models with softening response via convex relaxation" (Lauff et al., 2026).

- The formulation does not involve internal length scale parameters, which may be challenging to calibrate experimentally.
- The implementation in standard commercial FE software, e.g., Abaqus, is straightforward via user material subroutines.
- The novel class of damage models is suitable for computational multiscale modeling frameworks due to its mesh-objective response and the absence of a length scale parameter. Thus, it may be directly embedded into FE^2 (Feyel, 1999; Feyel and Chaboche, 2000; Feyel, 2003) or FE-FFT (Spahn et al., 2014; Kochmann et al., 2016) codes.

However, there are two issues which must be taken care of. For a start, the model must be able to reproduce softening behavior. Otherwise, the damaging behavior observed in experiments cannot be reproduced accurately. Moreover, the (cross-)convex hull must be determined by some means (Fonseca et al., 1994; Le Dret and Raoult, 2000; Carstensen et al., 2002). Previous works used computationally convenient approximations: a pre-defined finite number of damageable phases (Schwarz et al., 2021) or an a-priori restriction to 1D with subsequent direction averaging (Köhler and Balzani, 2023; Melchior et al., 2026).

The key contribution of the work at hand is that we compute the (cross-)convex envelope of the considered local damage models explicitly and analytically. In general, solving the latter problem is considered hard because it involves computing the absolute minimum of a non-convex variational problem. It appears therefore surprising that a closed-form solution could be found.

To be more precise, we compute the convex envelope of a rate-limited, non-convex standard scalar damage model in a time-discretized setting in Section 7.2, completing the conceptual agenda initiated by Schwarz et al. (2021). To do so, we impose a condition which is satisfied by a variety of reasonable damage models: The reciprocal function of the

damage-degradation function should be convex. Under this condition, the regularization approach leads to a family of convex damage models.

As a central outcome of the convexification process, the damage models are formulated based on one-dimensional damage-distribution functions instead of a scalar damage variable, and the effective degradation computes as the harmonically averaged degradation function. Interestingly, the time evolution of the damage-distribution functions turns out to possess the structure of an optimal transport problem (Villani, 2009), which naturally emerges from the variational formulation of the convexified energy. Due to the structural analogy to optimal transport theory, we call the damage models *optimal transport* (OT) damage models.

We provide arguments for the existence of minimizers to the associated mechanical boundary value problems, which is essential for a reliable numerical approximation. The existence of a solution results from the convexity and the coercivity of the condensed incremental energy, see Section 7.3.3.

In Section 7.3, we derive the damage models for a constant time-step size explicitly. Additionally, we introduce an efficient numerical procedure to solve the constrained linear optimization problem using a one-dimensional Newton-type method. We also discuss the convexity properties of the incremental energy and the existence of continuous minimizers to the associated mechanical boundary-value problems. Section 7.3 also provides critical insights into the structure of the derived class of models: In contrast to traditional phenomenological continuum-damage models, which use damage variables of a specific tensor order as arguments, the emerging model involves a *damage-distribution function*. Moreover, this distribution enters the free energy via a harmonic average as a prefactor to the Hookean undamaged free energy. This harmonic averages emerge naturally as a consequence of the convex relaxation process. From a continuum mechanical point of view, the appearance of both the damage distribution and the harmonic average does not come

as a surprise: If we pursued a quasi-convexification, we would expect damage(d) microstructures to form. As we carry out a convexification process - which ignores kinematic compatibility of the strains and thus anisotropic spatial correlations - the harmonic mean emerges naturally as the dedicated homogenization operator in one spatial dimension of elastic rods connected in series. Alternatively, the harmonic average may also be considered as a realized Reuss bound on the effective stiffness. However, some care has to be taken, as we also obtain an evolution for the emerging damage distributions naturally. It is well known that the Hookean free energy gives rise to a convex function in terms of the strain and the compliance tensor (Görthofer et al., 2022). As the compliance tensor of the convexified damage model is linear w.r.t. the damage distribution, the convexity of the model at hand is readily apparent, and the variety of advantages which comes with convexity is directly available.

In Section 7.4, we conduct computational investigations with respect to the novel class of scalar damage models, using methods of FFT-based computational micromechanics (Moulinec and Suquet, 1994; 1998; Schneider, 2021). We start with computations on material point level, studying the influence of the damage model parameters and different damage-degradation functions. To take heterogeneous stress states into consideration, we first apply the damage model to the matrix material of composites with a single circular inclusion and subsequently to the matrix material of long fiber reinforced composites. The OT damage models lead to mesh-independent results even in the regime of softening, preventing localization. Thus, the models may be used to predict the mechanical behavior on continuum scale including materials with softening behavior in a reliable and efficient manner. In addition, the mesh-independence ensures that the OT damage model is applicable for homogenization problems as representative volume elements will emerge for increasing unit cell size.

7.2 Convex relaxation of a class of damage models

7.2.1 A rate-dependent damage model to be convexified

As our point of departure, we consider an isotropic scalar damage model (Schwarz et al., 2021) at small strains in an isothermal setting. We restrict to isotropic damage to keep the formulation as simple as possible to focus on the structure of the novel regularization technique and to avoid further complications. In general, a tensorial damage variable (Voyiadjis and Kattan, 2006) could be used to model anisotropic damage processes.

We use the framework of generalized standard materials (GSM) (Halphen and Nguyen, 1975; Nguyen, 2000), and consider the free energy (density) as a function of the strain $\boldsymbol{\varepsilon}$ and the damage variable d

$$\psi : \mathrm{Sym}(n_{\mathrm{dim}}) \times [0, d_{\max}) \to \mathbb{R}_{\geq 0}, \quad \psi(\boldsymbol{\varepsilon}, d) = \frac{f(d)}{2}\, \boldsymbol{\varepsilon} \cdot \mathbb{C}\, [\boldsymbol{\varepsilon}]\,, \tag{7.1}$$

where $\mathrm{Sym}(n_{\mathrm{dim}})$ stands for the vector space of symmetric second-order tensors in $\mathbb{R}^{n_{\mathrm{dim}}}$ with $n = 2, 3$ spatial dimensions. The considered dissipation potential reads

$$\Psi : \mathbb{R} \to \mathbb{R}_{\geq 0} \cup \{+\infty\}, \quad \Psi\left(\dot{d}\right) = \begin{cases} r\,\dot{d}, & 0 \leq \dot{d} \leq \dot{d}_{\max}, \\ +\infty, & \text{otherwise.} \end{cases} \tag{7.2}$$

Here, $\dot{d}$ denotes the material time derivative of the internal variable d describing the damage, $d_{\max}$ refers to a positive number or plus infinity and determines the maximum attainable value of damage, $\mathbb{C}$ stands for an elastic stiffness tensor, corresponding to the undamaged state, and r is a positive dissipation parameter. Moreover, the phenomenological

model involves a damage-degradation function

$$f : [0, d_{\max}) \to [0, 1], \tag{7.3}$$

which we assume to be continuous, strictly monotonically decreasing and to satisfy the "boundary conditions"

$$f(0) = 1 \quad \text{and} \quad \lim_{d \to d_{\max}} f(d) = 0. \tag{7.4}$$

For the work at hand, the following three mathematical equations are used for the degradation function, taken from the literature (Kachanov, 1999; Dimitrijevic and Hackl, 2011; Brepols et al., 2017):

1. Exponential degradation:

$$f(d) = e^{-d}, \quad d \geq 0. \tag{7.5}$$

2. Linear degradation:

$$f(d) = 1 - d, \quad 0 \leq d \leq 1. \tag{7.6}$$

3. Quadratic degradation:

$$f(d) = (1 - d)^2, \quad 0 \leq d \leq 1. \tag{7.7}$$

As the damage degradation function modulates the remaining stiffness of the material, the stress-strain response of the damage model may be tailored to a specific material by selecting an adequate degradation function. Besides the three introduced functions (7.5)–(7.7), further options are available in literature, see for example Wu and Nguyen (2018).

Last but not least, the model (7.1)–(7.2) involves a rate limitation $\dot{d}_{\max}$, which we assume positive and finite. Here, we follow the suggestion

of Allix (2013), who introduced the rate limitation $\dot{d}_{\max}$ to ensure the coercivity of the condensed energy, i.e., that the condensed energy tends to infinity as the norm of the strain tensor becomes arbitrarily large. If coercivity does not hold, minimizers might lie "at infinity", i.e., are trivial, and existence of minimizers for the model might fail (Dacorogna, 1982). We wish to stress that the rate limitation makes the model generally rate-dependent. Indeed, a generalized standard model is rate independent if and only if the dissipation potential (7.2) is positively homogeneous of degree one. Due to the damage rate limitation, the dissipation potential is not homogeneous and the damage model is rate-dependent.

In accordance with the setting of a GSM (Halphen and Nguyen, 1975), the dissipation potential (7.2) is non-negative, lower semicontinuous as well as convex and fulfills the condition $\Psi(0) = 0$.

To ensure that the model is thermodynamically consistent, we take the Clausius-Duhem inequality (CDI) (Haupt, 2002, Chapter 13) for an isothermal model approach

$$0 \overset{!}{\leq} \boldsymbol{\sigma} \cdot \dot{\boldsymbol{\varepsilon}} - \dot{\psi}\left(\boldsymbol{\varepsilon}, d\right) \equiv \left[\boldsymbol{\sigma} - \frac{\partial \psi}{\partial \boldsymbol{\varepsilon}}\left(\boldsymbol{\varepsilon}, d\right)\right] \cdot \dot{\boldsymbol{\varepsilon}} - \frac{\partial \psi}{\partial d} \cdot \dot{d} \tag{7.8}$$

into account, which has to hold for all strain rates and damage rates. Derived from the CDI (7.8), the associated stress computes as

$$\boldsymbol{\sigma} \equiv \frac{\partial \psi}{\partial \boldsymbol{\varepsilon}}(\boldsymbol{\varepsilon}, d) = f(d)\, \mathbb{C}\left[\boldsymbol{\varepsilon}\right], \tag{7.9}$$

for the model at hand, i.e., the undamaged stiffness $\mathbb{C}$ is uniformly weakened via the degradation function (7.3). To satisfy the non-negativity of the second term of the CDI, we assume the damage evolution to be governed by Biot's equation (Biot, 1965)

$$-\frac{\partial \psi}{\partial d}(\boldsymbol{\varepsilon}, d) \in \partial \Psi\left(\dot{d}\right) \tag{7.10}$$

for a prescribed strain path and a given initial condition for the damage variable, where $\partial\Psi$ stands for the subdifferential (Rockafellar, 1970) of the (convex) dissipation potential (7.2) and the quantity $-\partial\psi(\boldsymbol{\varepsilon}, d)/\partial d$ is called *driving force*.
We consider an implicit Euler discretization in time, i.e., a sequence $t_0, t_1, \ldots$ of increasing time steps and wish to determine solutions to the time-discrete equivalent of Biot's equation (7.10)

$$-\frac{\partial\psi}{\partial d}(\boldsymbol{\varepsilon}, d) \in \partial\Psi\left(\frac{d-d^k}{\triangle t_k}\right) \quad \text{with} \quad \triangle t_k = t_{k+1} - t_k, \tag{7.11}$$

where we write $d \equiv d^{k+1}$ for simplicity and assume the previous value d^k to be known. The condition (7.11) characterizes critical points of the optimization problem (Ortiz and Stainier, 1999; Miehe, 2002)

$$\psi(\boldsymbol{\varepsilon}, d) + \triangle t_k\, \Psi\left(\frac{d-d^k}{\triangle t_k}\right) \longrightarrow \min_{d\in[0,d_{\max})}, \tag{7.12}$$

where the minimum of the function is called *condensed incremental energy* (Miehe, 2002)

$$\psi_{\text{cond}}(\boldsymbol{\varepsilon}) = \min_{d\in[0,d_{\max})} \psi(\boldsymbol{\varepsilon}, d) + \triangle t_k\, \Psi\left(\frac{d-d^k}{\triangle t_k}\right), \quad \boldsymbol{\varepsilon} \in \text{Sym}(n_{\text{dim}}). \tag{7.13}$$

Considering the model at hand, the optimization problem (7.12) takes the form

$$\frac{f(d)}{2}\, \boldsymbol{\varepsilon} \cdot \mathbb{C}\,[\boldsymbol{\varepsilon}] + \mathcal{D}\left(d^k, d\right) \longrightarrow \min_{0\le d-d^k\le \triangle t_k\, \dot{d}_{\max}} \tag{7.14}$$

with the *dissipation distance*

$$\mathcal{D}\left(d^k, d\right) = r(d-d^k), \tag{7.15}$$

which may be understood as the energy dissipated during the damage progression from the damage state d^k to d. For the degradation func-

tions (7.5)–(7.7), the discrete evolution of the damage variable d may be determined analytically. For instance, the exponential degradation function (7.5) leads to the prescription

$$d = \min\left(\max\left(d^k, \ln\frac{\psi_0\left(\boldsymbol{\varepsilon}\right)}{r}\right), d^k + \triangle t_k\, \dot{d}_{\max}\right) \tag{7.16}$$

with the undamaged elastic energy

$$\psi_0 : \mathrm{Sym}(n_{\mathrm{dim}}) \to \mathbb{R}_{\geq 0}, \quad \psi_0\left(\boldsymbol{\varepsilon}\right) = \frac{1}{2}\boldsymbol{\varepsilon} \cdot \mathbb{C}\left[\boldsymbol{\varepsilon}\right]. \tag{7.17}$$

For the quadratic degradation (7.7), one computes

$$d = \min\left(\max\left(d^k, 1 - \frac{r}{2\,\psi_0\left(\boldsymbol{\varepsilon}\right)}\right), d^k + \triangle t_k\, \dot{d}_{\max}\right), \tag{7.18}$$

whereas the linear degradation function (7.6) yields the result

$$d = \begin{cases} d^k, & \psi_0\left(\boldsymbol{\varepsilon}\right) < r, \\ d^k < d < d^k + \triangle t_k\, \dot{d}_{\max}, & \psi_0\left(\boldsymbol{\varepsilon}\right) = r, \\ d^k + \triangle t_k\, \dot{d}_{\max}, & \psi_0\left(\boldsymbol{\varepsilon}\right) > r. \end{cases} \tag{7.19}$$

As the linear degradation function leads to a driving force which is independent of the damage variable

$$-\frac{\partial \psi}{\partial d}(\boldsymbol{\varepsilon}, d) = \psi_0\left(\boldsymbol{\varepsilon}\right), \tag{7.20}$$

the damage evolution equation is ill-posed, resulting in an indeterminate damage state if the undamaged elastic energy exactly equals the damage parameter r, see Equation (7.19). However, in our numerical simulations this case did not occur. For a finite-strain setting without damage-rate limitation, (Melchior et al., 2026, Section 2.4) reported a similar phenomenon due to the applied linear degradation function, where a phase of the material tends to the maximal energetically possible damage

evolution.

Let us consider an undamaged material with $d^0 = 0$ and compute the minimum value of the undamaged elastic energy $\psi_0(\boldsymbol{\varepsilon})$ which is required for damage onset. For both the exponential and the linear degradation function, the undamaged elastic energy needs to satisfy the equation

$$\psi_0(\boldsymbol{\varepsilon}) = r, \tag{7.21}$$

whereas the required undamaged elastic energy equals

$$\psi_0(\boldsymbol{\varepsilon}) = r/2 \tag{7.22}$$

for the quadratic degradation function. Hence, we observe that the model parameter r limits the elastic range, i.e., it determines the onset of inelastic deformation. According to Equations (7.21) and (7.22), the quadratic degradation function leads to an earlier onset of damage compared to the other two degradation functions when selecting the same value for the parameter r. In case that all three degradation functions are requested to start the damage evolution at an equal level of undamaged elastic energy, the parameter r needs to be selected twice as high for the quadratic degradation function.

Although these models lead to sensible results on a material-point level – thanks to the rate limitation (7.2) – producing a well-defined evolution on the continuum scale, when used as a constitutive model for a component, for instance, is more challenging. Under suitable growth conditions on the integrand, a celebrated result of Morrey (1952) states that a necessary and sufficient condition for the existence of minimizers to the variational problem involving such an integrand is the quasi-convexity of the integrand. Whether the condensed incremental energy of the considered damage model is quasi-convex or not is not known to the authors. Presumably, it is not.

A possible way to construct a well-posed evolution is to compute a

suitable quasi-convex envelope of the condensed incremental energy. Unfortunately, we are neither aware of an explicit analytical solution for this problem nor an efficient computational scheme, despite recent progress (Balzani et al., 2024; Köhler et al., 2024). Therefore, we follow the route sketched by Schwarz et al. (2021): We compute the convex envelope of the condensed incremental energy. Every convex function is also quasi-convex (Dacorogna, 2008), so the incremental problems will be amenable to Morrey's existence result. The price to pay is that the model becomes less physically interpretable and that the models we started out with may be significantly altered by the convexification process. Fortunately, computational experiments will permit us to gain insight into the differences which are created and show that the alteration is small for the considered material and load cases, see Section 7.3.

7.2.2 The convex envelope

The purpose of this section is to compute the convex envelope for the damage model (7.1)–(7.2) under natural conditions on the damage-degradation function (7.3).
Suppose that a specific function

$$F : \mathbb{R}^m \to \mathbb{R} \tag{7.23}$$

is given. Then, the convex envelope F^c is defined as the largest convex function whose graph is point-wise less or equal than the graph of the given function F. Geometrically, the epigraph of the convex envelope F^c corresponds to the convex hull of the epigraph of the function F, see Figure 7.1.

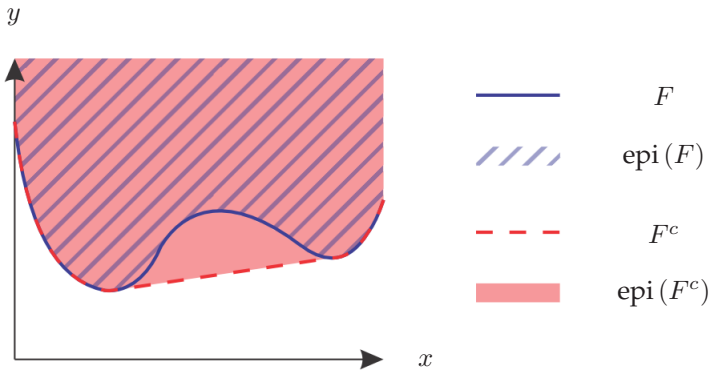


Figure 7.1: Illustration of a one-dimensional non-convex function F, its convex envelope F^c and the epigraphs of both functions epi (F) and epi (F^c). Figure adapted from Figure 1 of Lauff et al. (2026).

Thus, the following explicit characterization

$$F^c(\bar{\boldsymbol{x}}) = \min \left\{ \sum_{i=0}^{m} c_i \, F(\boldsymbol{x}_i) \,\middle|\, \boldsymbol{x}_i \in \mathbb{R}^m,\ c_i \geq 0 \text{ for } i = 0, 1, \ldots, m, \right. \\ \left. \sum_{i=0}^{m} c_i = 1 \text{ and } \sum_{i=0}^{m} c_i \, \boldsymbol{x}_i = \bar{\boldsymbol{x}} \right\} \tag{7.24}$$

of the convex envelope F^c for $\bar{\boldsymbol{x}} \in \mathbb{R}^m$ emerges. Thus, for any point $\bar{\boldsymbol{x}} \in \mathbb{R}^m$, one considers all convex combinations

$$\bar{\boldsymbol{x}} = \sum_{i=0}^{m} c_i \, \boldsymbol{x}_i \tag{7.25}$$

of the point $\bar{\boldsymbol{x}}$, where $m + 1$ terms are sufficient in m dimensions to represent a general convex combination by Caratheodory's Theorem (Carathéodory, 1911), and seeks the smallest convex combination of the corresponding objective values.

For the problem (7.1)–(7.2) at hand, we start with the first time step with index $k = 0$ and consider the condensed incremental energy

$$\psi_{\text{cond}}(\bar{\boldsymbol{\varepsilon}}) = \min \left\{ \frac{f(d)}{2}\, \bar{\boldsymbol{\varepsilon}} \cdot \mathbb{C}\, [\bar{\boldsymbol{\varepsilon}}] + r\left(d - d^0\right) \,\middle|\, 0 \leq d - d^0 \leq \triangle t_0\, \dot{d}_{\max} \right\}, \quad \bar{\boldsymbol{\varepsilon}} \in \text{Sym}(n_{\text{dim}}), \tag{7.26}$$

for $m = n_{\text{dim}}(n_{\text{dim}} + 1)/2$ dimensions. Thus, the convex envelope (7.24) of the condensed incremental energy (7.26) becomes

$$\begin{aligned} \psi^c_{\text{cond}}(\bar{\boldsymbol{\varepsilon}}) = \min \Bigg\{ & \sum_{i=0}^{m} c_i \left(\frac{f\left(d_i\right)}{2}\, \boldsymbol{\varepsilon}_i \cdot \mathbb{C}_i\, [\boldsymbol{\varepsilon}_i] + r\left(d_i - d^0\right) \right) \,\Bigg| \\ & \sum_{i=0}^{m} c_i\, \boldsymbol{\varepsilon}_i = \bar{\boldsymbol{\varepsilon}}, \quad 0 \leq d_i - d^0 \leq \triangle t_0\, \dot{d}_{\max} \Bigg\} \end{aligned} \tag{7.27}$$

for $m = n_{\text{dim}}(n_{\text{dim}} + 1)/2$, $\bar{\boldsymbol{\varepsilon}} \in \text{Sym}(n_{\text{dim}})$ and weighting coefficients c_i which satisfy the simplex constraint (7.24).

Thus, we observe that the "mixing" which is intrinsic to computing a convex envelope (7.24) also entails a "mixing" of internal variables in the sense of creating a "microstructure". Indeed, instead of a *single value* of the internal variable d, up to $n_{\text{dim}}(n_{\text{dim}} + 1)/2 + 1$ internal variables may appear in the first load step due to the convexification. For the second load step, each of the internal variables may decompose further - leading to a process of more and more internal variables for the subsequent time steps. Put differently, a $(n_{\text{dim}}(n_{\text{dim}} + 1)/2 + 1)$-ary tree whose depth corresponds to the number of time steps is created.

To avoid these technicalities, it is actually more convenient to work with a continuum than with a possibly large number of discrete variables. More precisely, returning to the abstract setting (7.23) for clarity, we consider fields

$$\boldsymbol{x} : [0, 1] \to \mathbb{R}^m \tag{7.28}$$

on the unit interval. This domain has no intrinsic physical meaning, but permits us to express the convex envelope (7.24) in the form

$$F^c(\bar{\boldsymbol{x}}) = \min \left\{ \langle F(\boldsymbol{x}) \rangle_{[0,1]} \,\middle|\, \boldsymbol{x} : [0,1] \to \mathbb{R}^m, \quad \langle \boldsymbol{x} \rangle_{[0,1]} = \bar{\boldsymbol{x}} \right\} \tag{7.29}$$

for a prescribed vector $\bar{\boldsymbol{x}} \in \mathbb{R}^m$, where the symbol

$$\langle q \rangle_{[0,1]} = \int_0^1 q(s) \, \mathrm{d}s \tag{7.30}$$

encodes the mean of a function q on the unit interval $[0,1]$. The equivalence of the two expressions (7.24) and (7.29) is readily seen. The right-hand side in Equation (7.29) is certainly not larger than the right-hand side in equation (7.24), as one may define the piece-wise constant function

$$\begin{aligned} &\boldsymbol{x} : [0,1] \to \mathbb{R}^m, \quad \boldsymbol{x}(s) = \boldsymbol{x}_i \text{ if } \sum_{j=0}^{i} c_i \le s < \sum_{j=0}^{i+1} c_i \\ &\text{for} \quad i = 0, 1, \ldots, m-1. \end{aligned} \tag{7.31}$$

On the other hand, the right-hand side in Equation (7.24) is certainly not larger than the right-hand side in equation (7.29), as any continuous convex combination

$$\bar{\boldsymbol{x}} = \langle \boldsymbol{x} \rangle_{[0,1]} \tag{7.32}$$

may be represented by a finite convex combination

$$\bar{\boldsymbol{x}} = \sum_{i=0}^{m} c_i \, \boldsymbol{x}_i, \quad \boldsymbol{x}_i \in \mathbb{R}^m, \quad c_i \ge 0, \quad \sum_{i=0}^{m} c_i = 1, \tag{7.33}$$

with no more than $m+1$ terms as a consequence of Caratheodory's Theorem (Carathéodory, 1911).
Returning to the problem (7.27) at hand, we thus consider the following

convex envelope

$$\psi^c_{\text{cond}}(\bar{\boldsymbol{\varepsilon}}) = \min \left\{ \left\langle \frac{f(d)}{2}\, \boldsymbol{\varepsilon} \cdot \mathbb{C}\left[\boldsymbol{\varepsilon}\right] + r\left(d - d^-\right) \right\rangle_{[0,1]} \,\middle|\, \langle \boldsymbol{\varepsilon} \rangle_{[0,1]} = \bar{\boldsymbol{\varepsilon}}, \quad d^- \leq d \leq d^+ \right\} \tag{7.34}$$

Here, $d^{\pm} : [0,1] \to [d, d_{\text{max}})$ are piece-wise constant functions. For the first load step, we have $d^- \equiv d^0$ and $d^+ = d^0 + \triangle t_0\, \dot{d}_{\text{max}}$. The introduction of the fields d^- and d^+ permits to treat subsequent time steps in a uniform fashion.

7.2.3 Computing the convex envelope explicitly

The goal of this section is to compute the convex envelope (7.34)

$$\psi^c_{\text{cond}}(\bar{\boldsymbol{\varepsilon}}) = \min \left\{ \left\langle \frac{f(d)}{2}\, \boldsymbol{\varepsilon} \cdot \mathbb{C}\left[\boldsymbol{\varepsilon}\right] + r\left(d - d^-\right) \right\rangle_{[0,1]} \,\middle|\, \langle \boldsymbol{\varepsilon} \rangle_{[0,1]} = \bar{\boldsymbol{\varepsilon}}, \quad d^- \leq d \leq d^+ \right\} \tag{7.35}$$

for a prescribed strain $\bar{\boldsymbol{\varepsilon}} \in \text{Sym}(n_{\text{dim}})$ and given piece-wise constant functions $d^{\pm} : [0,1] \to [d, d_{\text{max}})$ which we assume to satisfy the inequality $d^- \leq d^+$ point-wise. Physically speaking, the problem (7.35) may be imagined as a single initially elastic rod which undergoes damage. The domain $[0,1]$ represents the "material points" of the rod, and the stiffness at each material point is degraded by the local damage variable $d(s)$ at the location $s \in [0,1]$, see Figure 7.2. The mental image of the rod makes sense because the strains appearing in the problem (7.35) do not account for kinematic compatibility as a result for considering the *convex* envelope, and not the quasi-convex one.

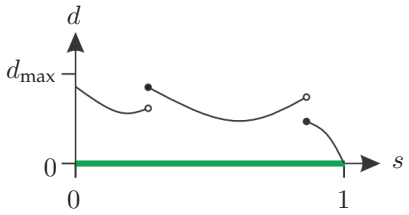


Figure 7.2: Rod with local damage variable d. Figure adapted from Figure 2 of Lauff et al. (2026).

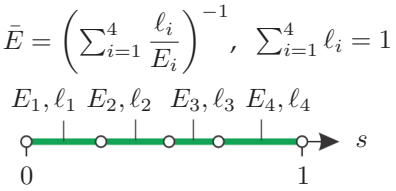


Figure 7.3: Elastic rods connected in series with elastic moduli E_i, lengths ℓ_i and cross-sectional area $A_i = A$. Figure adapted from Figure 3 of Lauff et al. (2026).

As a first step, Schwarz et al. (2021) observed the identity

$$\min_{\langle \boldsymbol{\varepsilon} \rangle_{[0,1]} = \bar{\boldsymbol{\varepsilon}}} \left\langle \frac{f(d)}{2}\, \boldsymbol{\varepsilon} \cdot \mathbb{C}\, [\boldsymbol{\varepsilon}] \right\rangle_{[0,1]} = \frac{\bar{f}(d)}{2}\, \bar{\boldsymbol{\varepsilon}} \cdot \mathbb{C}\, [\bar{\boldsymbol{\varepsilon}}] \tag{7.36}$$

with the harmonically averaged degradation function

$$\bar{f}(d) = \left\langle f(d)^{-1} \right\rangle_{[0,1]}^{-1}. \tag{7.37}$$

For the convenience of the reader, the mathematical arguments are collected in Appendix E. From a homogenization point-of-view in one spatial dimension, the harmonic average (7.37) emerges naturally as the homogenization operator of elastic rods connected in series (Mittelstedt, 2025), illustrated in Figure 7.3. With this insight at hand, we are left to evaluate the minimization problem

$$\bar{f}(d)\, \psi_0(\bar{\boldsymbol{\varepsilon}}) + r\, \left\langle d - d^- \right\rangle_{[0,1]} \longrightarrow \min_{d^- \leq d \leq d^+} \tag{7.38}$$

with the elastic energy ψ_0 of the undamaged state (7.17). To proceed beyond the state of the art (Schwarz et al., 2021), we need to make an additional assumption.

We require that the function

$$g : [d, d_{\max}) \to [0, \infty), \quad g(d) = \frac{1}{f(d)}, \tag{7.39}$$

is well-defined and **convex**. This assumption is readily seen to hold for the three specific cases (7.5)–(7.7) of damage-degradation functions which we have in mind. For the exponential degradation function (7.5), the function g takes the form $g(d) = e^d$, which is clearly a convex function. For the linear and the quadratic degradation functions, the reciprocal function (7.39) takes the form $g(d) = (1-d)^{-m}$ for $m = 1$ and $m = 2$. This function is convex on the interval $[0, 1)$, as can be read off the second derivative

$$g''(d) = m(m+1)\frac{1}{(1-d)^{m+2}}, \tag{7.40}$$

which turns out to be positive for $d \in [0, 1)$.
Under the convexity assumption on the function (7.39), the following alternative expression

$$\begin{aligned}\psi^c_{\text{cond}}(\bar{\boldsymbol{\varepsilon}}) = \min_{\phi^{\text{mix}}:[0,1]\to[0,1]} &\left\langle (1-\phi^{\text{mix}}) f\left(d^-\right)^{-1} + \phi^{\text{mix}} f\left(d^+\right)^{-1} \right\rangle^{-1}_{[0,1]} \psi_0(\bar{\boldsymbol{\varepsilon}}) \\ &+ r\left\langle \phi^{\text{mix}}\left(d^+ - d^-\right)\right\rangle_{[0,1]}\end{aligned} \tag{7.41}$$

is valid. The derivation of this result comprises Appendix F. In fact, when preparing the revised manuscript we discovered that Francfort and co-workers (Francfort and Marigo, 1993; Francfort and Garroni, 2006) provided a result that is equivalent to the expression (7.41) for the linear degradation function (7.6) and the first time step.
Let us discuss the ramifications of the formula (7.41). The result (7.41) may be understood readily via the previously introduced analogy with an elastic rod whose stiffness is heterogeneous along the rod. At every continuum point of the rod with Young's modulus $E(d^-)$, there is a

maximum damage to be attained during this time step, which would lead to the Young's modulus $E(d^+)$ (during unloading), which is lower than $E(d^-)$. The model (7.41) predicts that either the continuum point remains undamaged or is damaged as much as possible. The "volume fraction" ϕ^{mix} in Equation (7.41) indicates the fraction of such continuum points which damage fully, and the remaining $1 - \phi^{\text{mix}}$ fraction of continuum points remain unscathed.
To be more explicit, we study the first time step, where the bounding functions $d^{\pm}$ are actually constant with values

$$d^- = d^0 \quad \text{and} \quad d^+ = d^0 + \triangle t_0 \, \dot{d}_{\max}. \tag{7.42}$$

Then, the optimization problem (7.41) takes the form

$$\psi^c_{\text{cond}}(\bar{\boldsymbol{\varepsilon}}) = \min_{\phi_0^{\text{mix}} \in [0,1]} \Big[\Big(\big(1 - \phi_0^{\text{mix}}\big) \, f \left(d^0\right)^{-1} + \phi_0^{\text{mix}} \, f \left(d^0 + \triangle t_0 \, \dot{d}_{\max}\right)^{-1} \Big)^{-1} \psi_0(\bar{\boldsymbol{\varepsilon}}) + r \, \phi_0^{\text{mix}} \, \triangle t_0 \, \dot{d}_{\max} \Big] \tag{7.43}$$

with $\phi_0^{\text{mix}} = \left\langle \phi^{\text{mix}} \right\rangle_{[0,1]}$. Thus, we observe that intermediate damage states in the interior of the interval $[d^0, d^0 + \triangle t_0 \, \dot{d}_{\max}]$ are not attained. Rather, a mixing of the extreme states, i.e., the end points of the interval, with mixing coefficients $1 - \phi_0^{\text{mix}}$ and ϕ_0^{mix} occur. In the mental rod model, a fraction of ϕ_0^{mix} of continuum points within the rod are damaged as much as possible, and the remaining $1 - \phi_0^{\text{mix}}$ points remain in their virgin state. Here, the role of the damage-rate limitation $\dot{d}_{\max}$ becomes apparent: The model (7.43) predicts that certain points damage as much as possible. If there was no limitation to the damage increment, the specimen would fail instantly, leading to *complete damage* and recovering the ill-posed damage-evolution problem we started out with.
Subsequent time steps also follow such a mixing, triggering a further splitting of the attainable states, leading to *damage distributions*. In case the time increment is constant, an explicit expression of the resulting

damage model can be constructed, see Section 7.3.1. Whereas the damage model is rate-dependent, in general, for the specific case with unlimited damage rate $\dot{d} \to \infty$, the damage model becomes rate-independent. In addition, the damage model may remain rate-independent, even for finite damage rate limitations, in case the actual damage increments are smaller than the maximum admissible damage increments, i.e., the damage rate limitation is inactive.
The model formulation in Equation (7.41) only includes the macroscopic strain $\bar{\varepsilon}$ explicitly, and the distinction between the microscopic strains ε_i and the macroscopic strain $\bar{\varepsilon}$ is not required anymore. Thus, we omit the bar over the macroscopic strain throughout the remaining manuscript for simplicity, i.e., the notation ε is used for the macroscopic strain.

7.2.4 The optimal transport point-of-view

The transition from discrete attained states (7.24) to a continuum description (7.29) turned out to be beneficial for the mathematical treatment of the convex relaxation problem. Indeed, we could reduce the technicalities and arrive at a unified description of the emerging constitutive model which is valid for all time steps. Despite these advantages of the continuum description in terms of damage *fields*, there are some downsides, in particular in terms of the uniqueness and interpretation of the results. More precisely, as we consider a convex envelope, and not a quasi-convex one, there is no natural spatial "order" on the attained damage values. In particular, for a given damage state realizing the minimum (7.35), we may re-order this state in an arbitrary way and obtain another optimal damage state. This circumstance is a direct consequence of the lacking spatial correlation of th convex envelope.
Thus, one observes that the spatial arrangement of the damage values is not relevant. However, the *distribution* of the damage values turns out to be the expressive value of significance. In mathematical terms, instead

of a field

$$d : [0,1] \to [0, d_{\max}), \tag{7.44}$$

we consider the probability measure μ on the set $[0, d_{\max})$ of attainable damage values. In particular, for a continuous function $\Phi : [0, d_{\max}) \to \mathbb{R}$, we notice the equality

$$\int_0^1 \Phi(d(s)) \, \mathrm{d}s = \int_0^{d_{\max}} \Phi(d) \, \mathrm{d}\mu(d), \tag{7.45}$$

where the letter d on the left-hand side stands for the damage field d, whereas the right-hand side involves the letter d as the variable of integration. The equation (7.45) may be interpreted as some form of the co-area formula.

In view of the equation (7.45), the relevant integral quantities of the field d may be expressed equivalently via statistics of the associated probability measure μ. Moreover, under a re-ordering of the domain $[0,1]$, the probability measure μ remains unaltered.

These observations motivate us to consider the probability measure μ as the primary quantity of interest describing the phase space of the relaxed damage model. In fact, we may express the free energy (7.1) in the form

$$\psi(\boldsymbol{\varepsilon}, \mu) = \left(\int_0^{d_{\max}} f(d)^{-1} \, \mathrm{d}\mu(d) \right)^{-1} \psi_0(\boldsymbol{\varepsilon}), \tag{7.46}$$

where we abuse notation and retain the letter ψ for the free energy, although it has been reserved for damage *functions* previously. With respect to the framework of a GSM, the time derivative of the free energy

with respect to the evolution of the probability measure μ follows as

$$\frac{\partial \psi}{\partial \mu}(\boldsymbol{\varepsilon}, \mu)\, \dot{\mu} = -\frac{\displaystyle\int_0^{d_{\max}} f(d)^{-1}\, d\dot{\mu}(d)}{\left(\displaystyle\int_0^{d_{\max}} f(d)^{-1}\, d\mu(d)\right)^2}\, \psi_0(\boldsymbol{\varepsilon}), \tag{7.47}$$

implicitly defining the thermodynamical driving force.

For a fixed time step k, the transition from the previous measure μ^k to the current measure μ involves optimal transportation (Fonseca et al., 1994; Le Dret and Raoult, 2000; Carstensen et al., 2002; Villani, 2009; Santambrogio, 2015). In this context, a *transportation plan* between the probability measures μ^k and μ is a measure π on the product space $[0, d_{\max}) \times [0, d_{\max}) \equiv [0, d_{\max})^2$ which satisfies the push-forward conditions

$$\left(\mathrm{pr}_1\right)_* \pi = \mu^k \quad \text{and} \quad \left(\mathrm{pr}_2\right)_* \pi = \mu \tag{7.48}$$

in terms of the projections $\mathrm{pr}_i(d_1, d_2) = d_i$ $(i = 1, 2)$. The conditions (7.48) state that the transportation plan π distributes the mass from the measure μ^k to the measure μ. An equivalent formulation of the conditions (7.48) is that for any continuous function $\Phi : [0, d_{\max}) \to \mathbb{R}$ and any bounded interval I, the conditions

$$\begin{aligned} \int_{I \times [0, d_{\max})} \Phi(d_1)\ \mathrm{d}\pi(d_1, d_2) &= \int_I \Phi(d_1)\ \mathrm{d}\mu^k(d_1) \quad \text{and} \\ \int_{[0, d_{\max}) \times I} \Phi(d_2)\ \mathrm{d}\pi(d_1, d_2) &= \int_I \Phi(d_2)\ \mathrm{d}\mu^k(d_2) \end{aligned} \tag{7.49}$$

must hold true. With the notation of transportation plan at hand, we may describe the transition from the previous state μ^k to the current state μ mathematically. More precisely, the probability measure μ minimizes

the functional

$$\left(\int_0^{d_{\max}} f(d)^{-1} \, \mathrm{d}\mu(d) \right)^{-1} \psi_0(\boldsymbol{\varepsilon}) + \mathcal{D}(\mu^k, \mu), \tag{7.50}$$

where the dissipation distance $\mathcal{D}\left(\mu^k, \mu\right)$ is the minimum of the Monge-Kantorovich problem (Kantorovich, 2006)

$$\mathcal{D}\left(\mu^k, \mu\right) = \min \left\{ \int_{[0, d_{\max})^2} \kappa_{\text{cost}}(d_1, d_2) \, \mathrm{d}\pi(d_1, d_2) \,\middle|\, \pi \text{ is a transportation plan from } \mu^k \text{ to } \mu \right\}, \tag{7.51}$$

formulated in terms of the cost function

$$\kappa_{\text{cost}}(d_1, d_2) = \begin{cases} r(d_2 - d_1), & d_1 \leq d_2 \leq d_1 + \triangle t_k \, \dot{d}_{\max}, \\ +\infty, & \text{otherwise.} \end{cases} \tag{7.52}$$

The formulation (7.50) highlights the convexity of the considered model. Indeed, the traditional Hookean free energy

$$\psi^{\text{Hooke}}(\boldsymbol{\varepsilon}, \mathbb{S}) = \frac{1}{2} \boldsymbol{\varepsilon} \cdot \mathbb{S}^{-1} \left[\boldsymbol{\varepsilon} \right], \tag{7.53}$$

formulated in terms of the strain $\boldsymbol{\varepsilon}$ and the compliance tensor $\mathbb{S}$, turns out to be a convex function of both arguments, see Görthofer et al. (2022). In particular, the free energy (7.46) is also a convex function of its arguments $\boldsymbol{\varepsilon}$ and μ. First, the undamaged elastic energy $\psi_0\left(\boldsymbol{\varepsilon}\right)$ is convex in its argument $\boldsymbol{\varepsilon}$. Secondly, the harmonic mean of the function $f(d)$ is also convex in the argument μ, essentially as the integration against a probability measure is a linear operation and the reciprocal function is convex for positive input values. As the minimum value of a Monge-Kantorovich problem is a convex function of the marginals μ^k and μ (Villani, 2009; Santambrogio, 2015), the dissipation distance (7.51) is convex in the argument μ too. Thus, the incremental minimization

problem (7.50) is a convex optimization problem, as well. As a result, the condensed incremental energy

$$\psi_{\text{cond}}(\boldsymbol{\varepsilon}) = \min \left\{ \left(\int_0^{d_{\max}} f(d)^{-1} \, \mathrm{d}\mu(d) \right)^{-1} \psi_0(\boldsymbol{\varepsilon}) + \mathcal{D}(\mu^k, \mu) \,\middle|\, \mu \text{ is a probability measure on } [0, d_{\max})\} \right. \tag{7.54}$$

turns out to be a convex function.

We wish to close this excursion to the world of mathematical optimal transport with an interpretation of the results discussed in Section 7.2.3. Under the convexity assumption (7.39) on the reciprocal of the damage-degradation function, the solution μ of the optimization problem (7.50) will be a sum of Dirac measures, provided the previous internal variable μ^k was a sum of Dirac measures, as well. In particular, if the first time step involves a fully intact material, i.e.,

$$\mu^0 = \delta_0, \tag{7.55}$$

where δ_d stands for the Dirac measure on the set $[0, d_{\max})$ concentrated at the damage value d, the first time step will lead to a damage distribution

$$\mu^1 = (1 - \phi^{\text{mix}})\, \delta_0 + \phi^{\text{mix}}\, \delta_{\triangle t_0 \, \dot{d}_{\max}} \quad \text{for some} \quad \phi^{\text{mix}} \in [0, 1]. \tag{7.56}$$

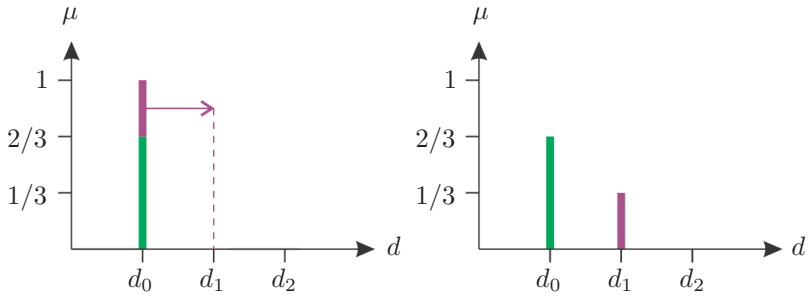
Suppose the k-th time step is described by the discrete measure

$$\mu^k = \sum_{j=1}^{N} \rho_j \, \delta_{d_j}, \quad \rho_j \geq 0, \quad \sum_{j=1}^{N} \rho_j = 1, \tag{7.57}$$

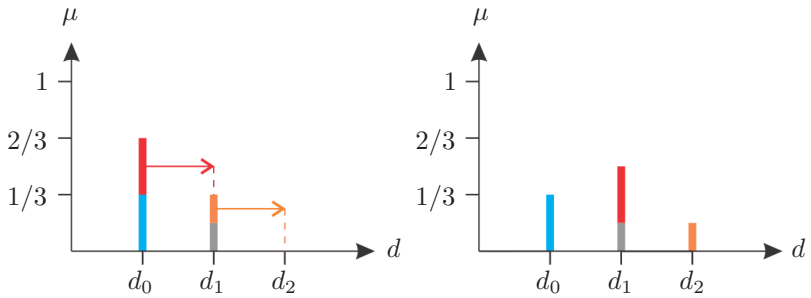
and distinct damage values $d_j \in [0, d_{\max})$, the subsequent time step will have the form

$$\mu^k = \sum_{j=1}^{N} \rho_j \left[(1 - \phi_j^{\text{mix}}) \delta_{d_j} + \phi_j^{\text{mix}} \delta_{d_j + \triangle t_k \dot{d}_{\max}} \right] \tag{7.58}$$

with suitable "fractions" $\phi_j^{\text{mix}} \in [0, 1]$. Due to the connection of the convexified damage model with the theory of optimal transport, we call it *optimal transport* (OT) damage model.



(a) First time step with $\mu^0 = \delta_{d_0}$ and $\mu^1 = \frac{2}{3}\delta_{d_0} + \frac{1}{3}\delta_{d_1}$



(b) Second time step with $\mu^1 = \frac{2}{3}\delta_{d_0} + \frac{1}{3}\delta_{d_1}$ and $\mu^2 = \frac{1}{3}\delta_{d_0} + \frac{1}{2}\delta_{d_1} + \frac{1}{6}\delta_{d_2}$

Figure 7.4: Evolution of a discrete damage distribution with three damage values for two time steps. Figure adapted from Figure 4 of Lauff et al. (2026).

In Figure 7.4, the evolution of a discrete damage distribution with the three damage values d_i ($i = 0, 1, 2$) is shown for two time steps. The initial discrete damage distribution is described by the measure $\mu^0 = \delta_{d_0}$, i.e., the damage fractions are $\rho_0^0 = 1$ and $\rho_1^0 = \rho_2^0 = 0$. During the first time step, see Figure 7.4(a), damage mass is transferred from the damage value d_0 to the damage value d_1 with the transition fraction $\left(\phi_0^{\text{mix}}\right)^0 = 1/3$. The damage distribution at the end of the first time step is $\mu^1 = 2/3\,\delta_{d_0} + 1/3\,\delta_{d_1}$. In the second time step, see Figure 7.4(b), the evolution of the damage distribution is characterized by a damage transportation from the damage value d_0 to the damage value d_1 as well as a damage transportation from the damage value d_1 to the damage value d_2, both with the transition fraction $\left(\phi_0^{\text{mix}}\right)^1 = \left(\phi_1^{\text{mix}}\right)^1 = 1/2$. The updated damage distribution reads $\mu^2 = 1/3\,\delta_{d_0} + 1/2\,\delta_{d_1} + 1/6\,\delta_{d_2}$.

The section at hand is mostly informative, i.e., it puts the results on the convex envelope (7.41) into perspective. Such a formulation appears to be imperative if we were interested in recovering a limit for vanishing time steps $\triangle t_i \to 0$, i.e., a time-continuous model. Indeed, we started out with a time-continuous model (7.23)–(7.24), and performed a convex relaxation at a time-discrete level. The resulting model may be treated numerically - and we will provide details in Section 7.3. However, from a continuum mechanical point of view, it is desirable to recover a time-continuous description, as well. We shall not do so here explicitly. Rather, we remark that the mathematical theory of optimal transport is the natural framework for such a task: The time-continuous model naturally involves probability measures as internal variables. These measures encode a *damage distribution* in a natural way. The latter insight might provide a reasonable continuum-mechanical interpretation of the convex relaxation process.

7.3 Computational mechanics of the damage model

7.3.1 Discussion of the model

In this section, we work out the mechanical aspects of the continuum-damage model resulting from the relaxation procedure (7.41) under the assumption that the time-step size $\triangle t_k \equiv \triangle t$ is constant. In particular, assuming initial damage of zero, the attainable damage states of the model are given by the sequence

$$0, \triangle t\, \dot{d}_{\max}, 2\triangle t\, \dot{d}_{\max}, 3\triangle t\, \dot{d}_{\max}, \ldots \tag{7.59}$$

As we are considering a finite number of time steps, and we also enforce a maximum damage value $d_{\max}$, it is sufficient to restrict to a finite number

$$d_0, d_1, \ldots, d_N \tag{7.60}$$

or *ordered* damage states

$$d_j = \min\left(j \triangle t\, \dot{d}_{\max}, d_{\max}\right), \quad j = 0, 1, \ldots, N, \tag{7.61}$$

i.e., which satisfy the inequalities

$$d_j < d_{j+1} \quad \text{for} \quad j = 0, 1, \ldots, N-1. \tag{7.62}$$

The phase-space of the internal variables comprises all damage fractions

$$\boldsymbol{\rho} \equiv \left[\begin{array}{ccc} \rho_0 & \cdots & \rho_N \end{array}\right]^{\mathsf{T}} \tag{7.63}$$

which satisfy the simplex constraints

$$\rho_j \geq 0 \quad (j = 0, 1, \ldots, N) \quad \text{and} \quad \sum_{j=0}^{N} \rho_j = 1. \tag{7.64}$$

The number $\rho_j \in [0, 1]$ indicates the fraction of damage residing in the damage state d_j (7.61). Initially, we have $\rho_0 = 1$ and all other ρ_j's vanish. For any such damage-distribution state $\boldsymbol{\rho}$, the effective degradation function $\bar{f}$ computes as

$$\bar{f}\,(\boldsymbol{\rho}) \equiv \left(\sum_{j=0}^{N} \rho_j \, g_j \right)^{-1} \quad \text{where} \quad g_j = f(d_j)^{-1}, \tag{7.65}$$

and the associated free energy reads

$$\psi\,(\boldsymbol{\varepsilon}, \boldsymbol{\rho}) = \bar{f}\,(\boldsymbol{\rho}) \, \frac{1}{2} \, \boldsymbol{\varepsilon} \cdot \mathbb{C}\,[\boldsymbol{\varepsilon}] \tag{7.66}$$

with corresponding stress tensor

$$\boldsymbol{\sigma} \equiv \frac{\partial \psi}{\partial \boldsymbol{\varepsilon}}\,(\boldsymbol{\varepsilon}, \boldsymbol{\rho})\,, \quad \text{i.e.,} \quad \boldsymbol{\sigma} = \bar{f}\,(\boldsymbol{\rho}) \; \mathbb{C}\,[\boldsymbol{\varepsilon}]\,, \tag{7.67}$$

compare Equation (7.9). The change from one time step to the next is governed by a suitable dissipation distance. More precisely, the transition from the internal-variable state at the previous step $\boldsymbol{\rho}^k$ to the value at the current time step $\boldsymbol{\rho}^{k+1} \equiv \boldsymbol{\rho}$ is handled via suitable mixing coefficients

$$\phi_j^{\text{mix}} \in [0, 1], \quad j = 0, 1, \ldots, N - 1, \tag{7.68}$$

which we collect in a vector $\boldsymbol{\phi}^{\text{mix}} \in [0,1]^N$. Then, the damage fractions at the next time step are parameterized as follows

$$\rho_j(\boldsymbol{\phi}^{\text{mix}}) = \begin{cases} \left(1-\phi_0^{\text{mix}}\right)\rho_0^k, & j=0, \\ \left(1-\phi_j^{\text{mix}}\right)\rho_j^k + \phi_{j-1}^{\text{mix}}\,\rho_{j-1}^k, & 0<j<N, \\ \rho_N^k + \phi_{N-1}^{\text{mix}}\,\rho_{N-1}^k, & j=N. \end{cases} \tag{7.69}$$

Thus, the volume fractions (7.68) determine the fraction of damage "mass" which is transferred to the next higher level, see Figure 7.4 for an illustration. For a fixed level j, there is a fraction ϕ_{j-1}^{mix} coming from the previous level and a fraction $1-\phi_j^{\text{mix}}$ of remaining "mass". The lowest and the highest level with indices $j=0$ and $j=N$ deserve a special treatment. As there is no negative state, the lowest level $j=0$ does not receive any "inflow" of damage. Thus, it can only lose damage "mass". The highest level, on the other hand, cannot lose damage "mass". Thus, there is no outflow of damage to a higher level, explaining why the index j in Equation (7.68) runs only up to the limit $N-1$. An example for the evolution of a discrete damage distribution with three damage values is shown in Figure 7.4 for two time steps.
The dissipation distance between the damage states $\boldsymbol{\rho}^k$ and $\boldsymbol{\rho} \equiv \boldsymbol{\rho}^{k+1}$ is actually a function of the transition coefficients (7.68)

$$\mathcal{D}(\boldsymbol{\phi}^{\text{mix}}) = r\sum_{j=0}^{N-1} \rho_j^k\,\phi_j^{\text{mix}}\,\triangle d_j \quad \text{with} \quad \triangle d_j = d_{j+1} - d_j. \tag{7.70}$$

In view of Equation (7.69), the dissipation (7.70) encodes the fraction of damage "mass" which dissipates to the next damage level, parameterized by the transition fractions $\boldsymbol{\phi}^{\text{mix}}$.
All in all, the incremental potential P for the k-th load step takes the

form

$$P\left(\boldsymbol{\varepsilon}, \boldsymbol{\Phi}^{\text{mix}}\right) = \left(\sum_{j=0}^{N} \rho_j \left(\boldsymbol{\Phi}^{\text{mix}}\right) g_j\right)^{-1} \frac{1}{2}\, \boldsymbol{\varepsilon} \cdot \mathbb{C}\left[\boldsymbol{\varepsilon}\right] + r \sum_{j=0}^{N-1} \rho_j^k\, \phi_j^{\text{mix}} \triangle d_j, \tag{7.71}$$

where $\boldsymbol{\varepsilon} \in \text{Sym}(n_{\text{dim}})$ denotes a strain tensor, the damage "masses" $\boldsymbol{\rho}$ are parameterized by Equation (7.69) and the transition fractions $\boldsymbol{\Phi}^{\text{mix}}$ are elements of the unit cube (7.68). The discrete evolution of the internal variables, the damage "masses", is thus governed by the optimization problem

$$\psi_{\text{cond}}(\boldsymbol{\varepsilon}) = \min_{\boldsymbol{\Phi}^{\text{mix}} \in [0,1]^N} P\left(\boldsymbol{\varepsilon}, \boldsymbol{\Phi}^{\text{mix}}\right), \tag{7.72}$$

where the minimum of the functional is the condensed incremental energy ψ_{cond}, see Equations (7.34) and (7.43). Notice that we drop the superscript c and the bar over the strain for notational convenience.

7.3.2 Computational aspects on material-point level

For a computational treatment of the model (7.72), the following remarks are helpful.

1. The effective degradation function $\bar{f}$ may be re-written in the form

$$\begin{aligned} \bar{f}\left(\boldsymbol{\Phi}^{\text{mix}}\right) &\equiv \left(\sum_{j=0}^{N} \rho_j \left(\boldsymbol{\Phi}^{\text{mix}}\right) g_j\right)^{-1} \\ &= \left(\sum_{j=0}^{N-1} \left(\left(1-\phi_j^{\text{mix}}\right) \rho_j^k\, g_j + \phi_j^{\text{mix}} \rho_j^k\, g_{j+1}\right) + \rho_N^k g_N\right)^{-1} \\ &= \left(\sum_{j=0}^{N} \rho_j^k\, g_j + \sum_{j=0}^{N-1} \phi_j^{\text{mix}} \rho_j^k \left(g_{j+1} - g_j\right)\right)^{-1}, \end{aligned} \tag{7.73}$$

which we may also express in the compressed form

$$\bar{f}\left(\boldsymbol{\phi}^{\mathrm{mix}}\right) = \left(\bar{f}\left(\mathbf{0}\right)^{-1} + \boldsymbol{\phi}^{\mathrm{mix}} \cdot \boldsymbol{\xi}\right)^{-1} \tag{7.74}$$

in terms of the vector $\boldsymbol{\xi} \in \mathbb{R}^N$ with non-negative components

$$\xi_j = \rho_j^k \left(g_{j+1} - g_j\right), \quad j = 0, 1, \ldots, N-1. \tag{7.75}$$

2. Similarly, the dissipation distance may be expressed in the form

$$r \sum_{j=0}^{N-1} \rho_j^k \, \phi_j^{\mathrm{mix}} \triangle d_j = \boldsymbol{\phi}^{\mathrm{mix}} \cdot \boldsymbol{\eta} \tag{7.76}$$

with the vector $\boldsymbol{\eta} \in \mathbb{R}^N$ whose components read

$$\eta_j = r \rho_j^k \triangle d_j, \quad j = 0, 1, \ldots, N-1. \tag{7.77}$$

These components are non-negative, as well.

Thus, in terms of the undamaged elastic energy ψ_0, see Equation (7.17), the optimization problem (7.72) may be written in the compact vector form

$$P\left(\boldsymbol{\varepsilon}, \boldsymbol{\phi}^{\mathrm{mix}}\right) = \left(\bar{f}\left(\mathbf{0}\right)^{-1} + \boldsymbol{\phi}^{\mathrm{mix}} \cdot \boldsymbol{\xi}\right)^{-1} \psi_0(\boldsymbol{\varepsilon}) + \boldsymbol{\phi}^{\mathrm{mix}} \cdot \boldsymbol{\eta} \to \min_{\boldsymbol{\phi}^{\mathrm{mix}} \in [0,1]^N}. \tag{7.78}$$

To derive the necessary (and sufficient) conditions for this optimization problem, we first take a look at the derivatives of the effective degradation function (7.73). This task is handled easily by re-writing Equation (7.74) in the form

$$\frac{1}{\bar{f}\left(\boldsymbol{\phi}^{\mathrm{mix}}\right)} = \frac{1}{\bar{f}\left(\mathbf{0}\right)} + \boldsymbol{\phi}^{\mathrm{mix}} \cdot \boldsymbol{\xi}. \tag{7.79}$$

Differentiating both hands of the identity with respect to the variable ϕ_j^{mix}, we arrive at the equation

$$-\frac{1}{\bar{f}\left(\boldsymbol{\Phi}^{\text{mix}}\right)^2}\frac{\partial \bar{f}\left(\boldsymbol{\Phi}^{\text{mix}}\right)}{\partial \phi_j^{\text{mix}}} = \xi_j, \tag{7.80}$$

i.e., we are led to the expression

$$\frac{\partial \bar{f}\left(\boldsymbol{\Phi}^{\text{mix}}\right)}{\partial \phi_i^{\text{mix}}} = -\xi_i\, \bar{f}\left(\boldsymbol{\Phi}^{\text{mix}}\right)^2, \quad i = 0, 1, \ldots, N-1. \tag{7.81}$$

For the second derivative, we deduce

$$\frac{\partial \bar{f}\left(\boldsymbol{\Phi}^{\text{mix}}\right)}{\partial \phi_i^{\text{mix}}\, \partial \phi_j^{\text{mix}}} = -2\,\xi_i \bar{f}\left(\boldsymbol{\Phi}^{\text{mix}}\right) \frac{\partial \bar{f}\left(\boldsymbol{\Phi}^{\text{mix}}\right)}{\partial \phi_j^{\text{mix}}} = 2\,\xi_i\,\xi_j\,\bar{f}\left(\boldsymbol{\Phi}^{\text{mix}}\right)^3, \tag{7.82}$$
$$i, j = 0, 1, \ldots, N-1.$$

We observe that the Hessian of the objective function (7.78)

$$\frac{\partial^2 P\left(\boldsymbol{\varepsilon}, \boldsymbol{\Phi}^{\text{mix}}\right)}{\partial \left(\boldsymbol{\Phi}^{\text{mix}}\right)^2} = 2\,\bar{f}\left(\boldsymbol{\Phi}^{\text{mix}}\right)^3 \psi_0(\boldsymbol{\varepsilon})\, \boldsymbol{\xi} \otimes \boldsymbol{\xi} \tag{7.83}$$

is a positive semi-definite matrix. Indeed, both the degradation function (7.73) and the undamaged free energy (7.17) take non-negative values, and a dyadic product of a vector leads to a positive semi-definite matrix.

The positive semidefiniteness of the Hessian (7.83) reveals that the objective function P is convex in the argument $\boldsymbol{\Phi}^{\text{mix}}$. In particular, every critical point of the optimization problem (7.72) is a global minimum. We derived this fact by more general arguments in Section 7.2.4, but come across it at this point, as well.

To find a critical point of the problem (7.72), we first study the case of an interior critical point. Such a point satisfies the equation

$$\mathbf{0} \stackrel{!}{=} \frac{\partial P\left(\boldsymbol{\varepsilon}, \boldsymbol{\phi}^{\mathrm{mix}}\right)}{\partial \boldsymbol{\phi}^{\mathrm{mix}}} = -\bar{f}\left(\boldsymbol{\phi}^{\mathrm{mix}}\right)^2 \psi_0(\boldsymbol{\varepsilon})\, \boldsymbol{\xi} + \boldsymbol{\eta}. \tag{7.84}$$

Apparently, such an interior critical point can only exist in case the vectors $\boldsymbol{\xi}$ and $\boldsymbol{\eta}$ are collinear. Still, to find a root of the vector field on the right-hand side (7.84), we take a look at a Newton-type method

$$\begin{aligned} \mathbf{0} &\stackrel{!}{=} -\bar{f}\left(\boldsymbol{\phi}^{\mathrm{mix}} + \triangle\boldsymbol{\phi}^{\mathrm{mix}}\right)^2 \psi_0(\boldsymbol{\varepsilon})\, \boldsymbol{\xi} + \boldsymbol{\eta} \\ &\approx -\bar{f}\left(\boldsymbol{\phi}^{\mathrm{mix}}\right)^2 \psi_0(\boldsymbol{\varepsilon})\, \boldsymbol{\xi} + \eta + 2\,\bar{f}\left(\boldsymbol{\phi}^{\mathrm{mix}}\right)^3 \psi_0(\boldsymbol{\varepsilon})\, (\boldsymbol{\xi} \otimes \boldsymbol{\xi}) \triangle\boldsymbol{\phi}^{\mathrm{mix}}, \end{aligned} \tag{7.85}$$

i.e.,

$$(\boldsymbol{\xi} \otimes \boldsymbol{\xi}) \triangle\boldsymbol{\phi}^{\mathrm{mix}} = \frac{\bar{f}\left(\boldsymbol{\phi}^{\mathrm{mix}}\right)^2 \psi_0(\boldsymbol{\varepsilon})\, \boldsymbol{\xi} - \boldsymbol{\eta}}{2\,\bar{f}\left(\boldsymbol{\phi}^{\mathrm{mix}}\right)^3 \psi_0(\boldsymbol{\varepsilon})}. \tag{7.86}$$

Due to the degeneracy of the left-hand side, we consider the diagonal components of the matrix $\boldsymbol{\xi} \otimes \boldsymbol{\xi}$ only. To account for the box constraints $0 \leq \phi_j^{\mathrm{mix}} \leq 1$, we use a projection onto the interval $[0, 1]$. We are thus led to the update scheme

$$\begin{aligned} &\phi_j^{\mathrm{mix}} \leftarrow \max\left(0, \min\left(\phi_j^{\mathrm{mix}} + s_j \left(\bar{f}\left(\boldsymbol{\phi}^{\mathrm{mix}}\right)^2 \psi_0(\boldsymbol{\varepsilon})\, \xi_j - \eta_j\right), 1\right)\right), \\ &j = 0, 1, \ldots, N-1, \end{aligned} \tag{7.87}$$

with the step size

$$s_j = \begin{cases} \left(2\,\bar{f}\left(\boldsymbol{\phi}^{\mathrm{mix}}\right)^3 \psi_0(\boldsymbol{\varepsilon})\, \xi_j^2\right)^{-1}, & \rho_j^k > 0, \\ 0, & \text{otherwise.} \end{cases} \tag{7.88}$$

Put differently, we consider a projected gradient method (Nocedal and Wright, 2006, 16.6) with an adaptive step size which recovers Newton's method in 1D. The algorithmic approach is summarized in Algorithm 6. The designed computational treatment is simple, yet resolves the incremental problem (7.72) quickly. In the computational practice, we observe convergence of the numerical scheme to a unique fixed point. We do not, however, have a mathematical argument for uniqueness at our disposal.

Algorithm 6: Evaluation of the OT damage model on material point level. Algorithm adapted from Algorithm 1 of Lauff et al. (2026).

Input: current strain $\boldsymbol{\varepsilon}$, damage masses $\boldsymbol{\rho}^k$ of the previous time step
Parameters of the damage model: $\mathbf{d}$, $\mathbf{g}$, r
▷ Equations (7.60), (7.65) and (7.2)

1: Initialize the damage volume fractions $\boldsymbol{\phi}^{\text{mix}} = \mathbf{0}$
2: Compute the undamaged elastic energy $\psi_0(\boldsymbol{\varepsilon})$ ▷ Equation (7.17)
3: Compute $\boldsymbol{\xi}$, and $\boldsymbol{\eta}$ ▷ Equations (7.75) and (7.77)
4: **while** $\left\| \triangle \boldsymbol{\phi}^{mix} \right\| > 10^{-8}$ **do**
5: Update the damage fractions $\boldsymbol{\rho}\left(\boldsymbol{\phi}^{\text{mix}}\right)$ ▷ Equation (7.69)
6: Compute the effective degradation $\bar{f}\left(\boldsymbol{\phi}^{\text{mix}}\right)$ ▷ Equation (7.73)
7: Update the damage volume fractions $\boldsymbol{\phi}^{\text{mix}}$ ▷ Equations (7.87) and (7.88)
8: Compute the stress $\boldsymbol{\sigma}(\boldsymbol{\varepsilon}, \boldsymbol{\rho})$ ▷ Equation (7.67)

Output: current stress $\boldsymbol{\sigma}$, damage masses $\boldsymbol{\rho}$ of the current time step

7.3.3 Convexity properties of the condensed incremental energy

In this section, we take a look at the mathematical properties of the condensed incremental energy (7.72)

$$\psi_{\text{cond}}(\boldsymbol{\varepsilon}) = \min_{\boldsymbol{\Phi}^{\text{mix}} \in [0,1]^N} P\left(\boldsymbol{\varepsilon}, \boldsymbol{\Phi}^{\text{mix}}\right), \quad \boldsymbol{\varepsilon} \in \text{Sym}(n_{\text{dim}}), \tag{7.89}$$

with the incremental potential (7.71)

$$P\left(\boldsymbol{\varepsilon}, \boldsymbol{\Phi}^{\text{mix}}\right) = \left(\sum_{j=0}^{N} \rho_j \left(\boldsymbol{\Phi}^{\text{mix}}\right) g_j\right)^{-1} \frac{1}{2}\, \boldsymbol{\varepsilon} \cdot \mathbb{C}\left[\boldsymbol{\varepsilon}\right] + r \sum_{j=0}^{N-1} \rho_j^k \, \phi_j^{\text{mix}} \triangle d_j, \tag{7.90}$$

which governs the mechanical subproblem associated to each discrete time step with the parametrization (7.69). The condensed incremental energy has the following properties:

(1) There are positive constants α_-, α_+ and C_+, s.t. the two-sided estimate

$$\frac{\alpha_-}{2}\, \boldsymbol{\varepsilon} \cdot \mathbb{C}\left[\boldsymbol{\varepsilon}\right] \leq \psi_{\text{cond}}(\boldsymbol{\varepsilon}) \leq C_+ + \frac{\alpha_+}{2}\, \boldsymbol{\varepsilon} \cdot \mathbb{C}\left[\boldsymbol{\varepsilon}\right] \tag{7.91}$$

is valid for all strains $\boldsymbol{\varepsilon} \in \text{Sym}(n_{\text{dim}})$.

(2) The condensed incremental energy (7.89) is convex, but not strictly convex.

(3) The naturally associated mechanical boundary-value problem admits minimizers. More precisely, suppose a domain $\Omega \subseteq \mathbb{R}^{n_{\text{dim}}}$ is given, whose sufficiently smooth boundary

$$\partial\Omega = \Gamma_D \cup \Gamma_N \tag{7.92}$$

decomposes into non-overlapping subsets Γ_D and Γ_N which serve as the locations where Dirichlet and Neumann boundary conditions

are imposed. In case the function

$$H^1_D(\Omega)^{n_{\text{dim}}} \to \mathbb{R}, \quad \boldsymbol{u} \mapsto \|\boldsymbol{u}\|_{H^1_D} := \|\nabla^s \boldsymbol{u}\|_{L^2}, \tag{7.93}$$

defines a norm on the Sobolev space

$$H^1_D(\Omega)^{n_{\text{dim}}} = \left\{ \boldsymbol{u} \in H^1(\Omega) \,\middle|\, \boldsymbol{u}\big|_{\Gamma_D} \equiv \boldsymbol{0} \right\} \tag{7.94}$$

with vanishing trace on the Dirichlet boundary, for any boundary-condition enforcing displacement field $\boldsymbol{u}_0 \in H^1(\Omega)^{n_{\text{dim}}}$, body-force field $\boldsymbol{f} \in H^{-1}_D(\Omega)^{n_{\text{dim}}} \equiv \left(H^1_D(\Omega)^{n_{\text{dim}}}\right)'$ and traction field $\boldsymbol{t} \in H^{-\frac{1}{2}}(\Gamma_N)^{n_{\text{dim}}}$, there is a minimizer to the variational problem

$$\int_\Omega \psi_{\text{cond}}(\nabla^s(\boldsymbol{u}_0 + \boldsymbol{u})) + \boldsymbol{f} \cdot \boldsymbol{u} \, \mathrm{d}V + \int_{\Gamma_N} \boldsymbol{t} \cdot \boldsymbol{u} \, \mathrm{d}A \longrightarrow \min_{\boldsymbol{u} \in H^1_D(\Omega)^{n_{\text{dim}}}}. \tag{7.95}$$

The first property (7.91) ensures that the incremental energy is sandwiched between two quadratic functions, ensuring both a coercivity condition and a growth estimate. Together with the second property, the weak lower semicontinuity of the functional (7.95) is ensured, see standard textbooks on the calculus of variations like Dacorogna (1982). In particular, these two properties are responsible for the validity of the third statement, i.e., the existence of minimizers to the mechanical boundary problem (7.95), associated to each time step of a component made of a homogeneous OT damage material. A simple sufficient condition for the uniqueness of solutions to the problem (7.95) is strict convexity. Such a condition is not satisfied by the incremental energy (7.89), as stated in condition (2) and demonstrated explicitly for the first time step in Appendix G.3.

For the sake of readability, the arguments supporting the claimed properties (1)–(3) were out-sourced to Appendix G.

7.4 Computational investigations

7.4.1 Setup

We consider matrix-inclusion materials within a fixed unit cell

$$Q = [0, Q_1] \times [0, Q_2] \times [0, Q_3]\,, \tag{7.96}$$

i.e., we suppose that two open subsets – corresponding to the matrix and the inclusion – are given, which are disjoint and whose closure covers the entire cell. Then, we consider heterogeneous generalized standard materials, s.t. the fibers are purely elastic and the matrix is governed by a damageable material. More precisely, we consider different material models, encompassing the original damage model (7.1)–(7.2) (with $\dot{d}_{\max} = +\infty$), the rate-limitation approach (7.1)–(7.2) (with $\dot{d}_{\max} < +\infty$) proposed by Allix (2013), the relaxation-type model by Schwarz et al. (2021) and the novel optimal transport (OT) model introduced in the manuscript at hand, and discussed in Section 7.3.
Within every time step, kinematic compatibility enforces the local strain field within the unit cell to possess the form

$$\boldsymbol{\varepsilon}(\boldsymbol{x}) = \bar{\boldsymbol{\varepsilon}} + \nabla^s \boldsymbol{u}(\boldsymbol{x})\,, \quad \boldsymbol{x} \in Q, \tag{7.97}$$

involving the symmetrized gradient of a periodic displacement-fluctuation field $\boldsymbol{u}$. In particular, the macroscopic strain $\bar{\boldsymbol{\varepsilon}}$ computes as the volume average of the microscopic strain field $\boldsymbol{\varepsilon}$

$$\bar{\boldsymbol{\varepsilon}} = \frac{1}{Q_1\, Q_2\, Q_3} \int\limits_Q \boldsymbol{\varepsilon}(\boldsymbol{x})\, \mathrm{d}V. \tag{7.98}$$

We assume the material to be undamaged in the initial state. For a prescribed loading path of macroscopic strains $\bar{\boldsymbol{\varepsilon}}$, we seek, for each time step, the associated strain field (7.97) and field of damage variables, such

that the static balance of linear momentum without volume forces

$$\operatorname{div}(\boldsymbol{\sigma})(\boldsymbol{x}) = \mathbf{0} \tag{7.99}$$

is satisfied, where the stress tensor is related to the strain tensor and the internal variables through the governing constitutive law. Subsequently, the macroscopic stress tensor $\bar{\boldsymbol{\sigma}}$ arises via volume averaging (Gross and Seelig, 2018)

$$\bar{\boldsymbol{\sigma}} = \frac{1}{Q_1\, Q_2\, Q_3} \int_Q \boldsymbol{\sigma}(\boldsymbol{x})\, \mathrm{d}V. \tag{7.100}$$

To solve the static balance of linear momentum (7.99), we use an implementation of the proposed damage model as a user-defined subroutine within an FFT-based computational homogenization code. The code (Schneider, 2019; Schneider et al., 2019) is written in Python with Cython extensions and parallelized with OpenMP. For the numerical homogenization within the FFT-based computational homogenization framework (Moulinec and Suquet, 1994; 1998), we discretize the problem by finite differences on a staggered grid (Schneider et al., 2016). The resulting nonlinear equations are solved with a conjugate gradient scheme (Zeman et al., 2010; Brisard and Dormieux, 2012; Wicht et al., 2020; Schneider, 2020a) with a relative tolerance of 10^{-5} as termination criterion. The investigations were conducted on a desktop computer equipped with an 8-core Intel i7 CPU, 64 GB RAM, and enabled Hyper-Threading with a total number of 16 threads. For the computations related to the long fiber reinforced composite material at the end of the computational investigations, we used a workstation with two AMD EPYC 9534 CPUs, each with 64 physical cores, enabled SMT, 256 threads total, and 1024 GB of DRAM.

As the standard material, we consider a polyamide (PA) matrix reinforced with E-glass fibers. For the matrix material and the fibers, we use isotropic elastic parameters (Doghri et al., 2011), see Table 7.1. Whereas

the fibers are modeled in a purely linear elastic way, we apply the introduced damage model to the matrix material and define the damage parameters r and $\dot{d}_{\max}$ as part of the considered studies.

E-glass fibers			PA matrix		
E	$=$	$72.0\,\mathrm{GPa}$	E	$=$	$2.1\,\mathrm{GPa}$
ν	$=$	0.22	ν	$=$	0.3

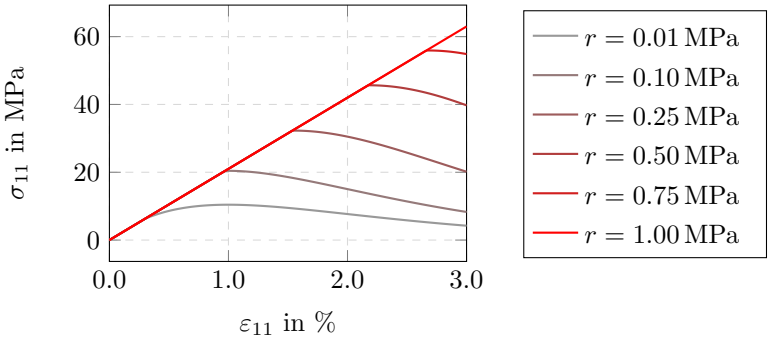
Table 7.1: Isotropic material properties for the PA matrix and the E-glass fibers, both taken from Doghri et al. (2011). Table adapted from Table 1 of Lauff et al. (2026).

We limit the minimum of the effective degradation function $\bar{f}$ to be greater or equal than the threshold 10^{-10}, which leads to a maximum damage $d_{\max} \approx 23.03$ for the exponential degradation function, $d_{\max} = 1 - 10^{-10}$ for the linear degradation function and $d_{\max} \approx 0.99999$ for the quadratic degradation function. If not specified otherwise, the exponential degradation function is used for the damage model at hand.

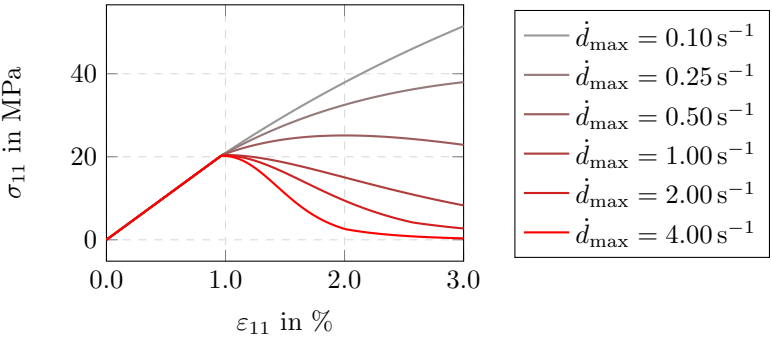
7.4.2 Studies on material point level

In this section, we investigate the influence of the damage parameters r and $\dot{d}_{\max}$ as well as the degradation-function type on the damage model. Therefore, we investigate the stress-strain behavior of the matrix material at material point level. As the loading condition, we select an uniaxial extension in $\boldsymbol{e}_1$-direction with maximum strain of $\varepsilon_{11} = 3\,\%$. The loading is applied in 200 linear loading steps with a time increment of $\Delta t = 0.015\,\mathrm{s}$. As the standard setup, we select the damage parameters $r = 0.10\,\mathrm{MPa}$ and $\dot{d}_{\max} = 1.00\,\mathrm{s}^{-1}$.

Influence of the damage parameters



(a) Model parameter r



(b) Model parameter $\dot{d}_{\max}$

Figure 7.5: Stress-strain curve for varying model parameters on material point level. Figure adapted from Figure 5 of Lauff et al. (2026).

Let us start with the investigation of the model parameter r. According to Equation (7.16), the undamaged energy ψ_0 needs to be greater or equal to the value r for damage to initiate in case of an exponential degradation function. As the undamaged energy computes as

$$\psi_0(\boldsymbol{\varepsilon}) = \frac{1}{2} E \varepsilon_{11}^2 \tag{7.101}$$

for the considered unidirectional tensile test, damage starts at the applied strain level

$$\varepsilon_{11} = \sqrt{\frac{2\,r}{E}}. \tag{7.102}$$

Thus, the model parameter r may be interpreted as a limit for damage initiation. The obtained stress-strain curves for varying model parameters r are given in Figure 7.5(a). In accordance with Equation (7.102), we observe that with increasing parameter r, the damage initiation is activated at a higher strain level ε_{11}. For instance, the required strain with respect to damage initiation is $\varepsilon_{11} \approx 0.31\,\%$ for the parameter $r = 0.01\,\mathrm{MPa}$ and $\varepsilon_{11} \approx 2.67\,\%$ for the parameter $r = 0.75\,\mathrm{MPa}$. In fact, for the highest parameter value $r = 1.00\,\mathrm{MPa}$ investigated, the required strain is above the maximum strain of $\varepsilon_{11} = 3\,\%$, i.e., the material shows a completely linear elastic behavior within the considered range.

For the smallest considered parameter value $r = 0.01\,\mathrm{MPa}$, taking a look beyond the elastic region, we observe first a positive slope, i.e., a region of hardening, and then a negative slope, i.e., softening. In all other cases, no significant initial hardening is observable. Let us compute the critical value for r which marks the transition from hardening to softening at the damage initiation. To simplify the discussion, we investigate the non-convex damage model instead of the OT damage model. At the start of the damage initiation (7.102), the corresponding stress level reads

$$\sigma_{11}^k\left(\varepsilon_{11}^k\right) = \sqrt{2\,r\,E}, \tag{7.103}$$

where k denotes the time step of the damage initiation. For the strain increment $\Delta\varepsilon_{11}$, the strain level of the subsequent time step becomes

$$\varepsilon_{11}^{k+1} = \varepsilon_{11}^k + \Delta\varepsilon_{11}, \tag{7.104}$$

and the damage variable increases from zero to the value $d^{k+1}\left(\varepsilon_{11}^{k+1}\right)$. Using the formula for the damage evolution (7.16) and the positivity of

the increment $\Delta\varepsilon_{11}$, the stress at the subsequent time step follows:

$$\sigma_{11}^{k}\left(\varepsilon_{11}^{k}\right) \equiv f\left(d^{k+1}\right) E\, \varepsilon_{11}^{k+1} = f\left(d^{k+1}\right) E\left(\varepsilon_{11}^{k} + \Delta\varepsilon_{11}\right). \tag{7.105}$$

The stress-strain curve shows hardening if and only if σ_{11}^{k} is smaller than σ_{11}^{k+1} and softening otherwise. Thus, the condition

$$f\left(d^{k+1}\right)\, E\, \Delta\varepsilon_{11} - \sqrt{2\, r\, E}\left(1 - f\left(d^{k+1}\right)\right) = 0 \tag{7.106}$$

characterizes the transition between hardening and softening behavior. For the considered study setup, the nonlinear equation (7.106) is satisfied for the model parameter $r \approx 0.103$, i.e., only the two smallest parameter selections start with hardening, confirming our computational observations.

The influence of the model parameter $\dot{d}_{\max}$ on the stress-strain behavior of the damage model is shown in Figure 7.5(b). As we fix the model parameter r, all models leave the linear elastic regime at the same level. After the damage onset, the model parameter $\dot{d}_{\max}$ affects the shape of the curve. For small parameters $\dot{d}_{\max}$, the damage progression is limited in a stronger way, and thus the stiffness degradation is less pronounced. For the models with the parameter values $\dot{d}_{\max} = 0.10\,\mathrm{s}^{-1}$ and $\dot{d}_{\max} = 0.25\,\mathrm{s}^{-1}$, we observe a large region of hardening, but no softening. However, these models would also include a softening behavior in case of higher applied strains. With increasing rate limit $\dot{d}_{\max}$, the stiffness reduction gets more apparent, the region of hardening decreases and a pronounced softening behavior is observed.

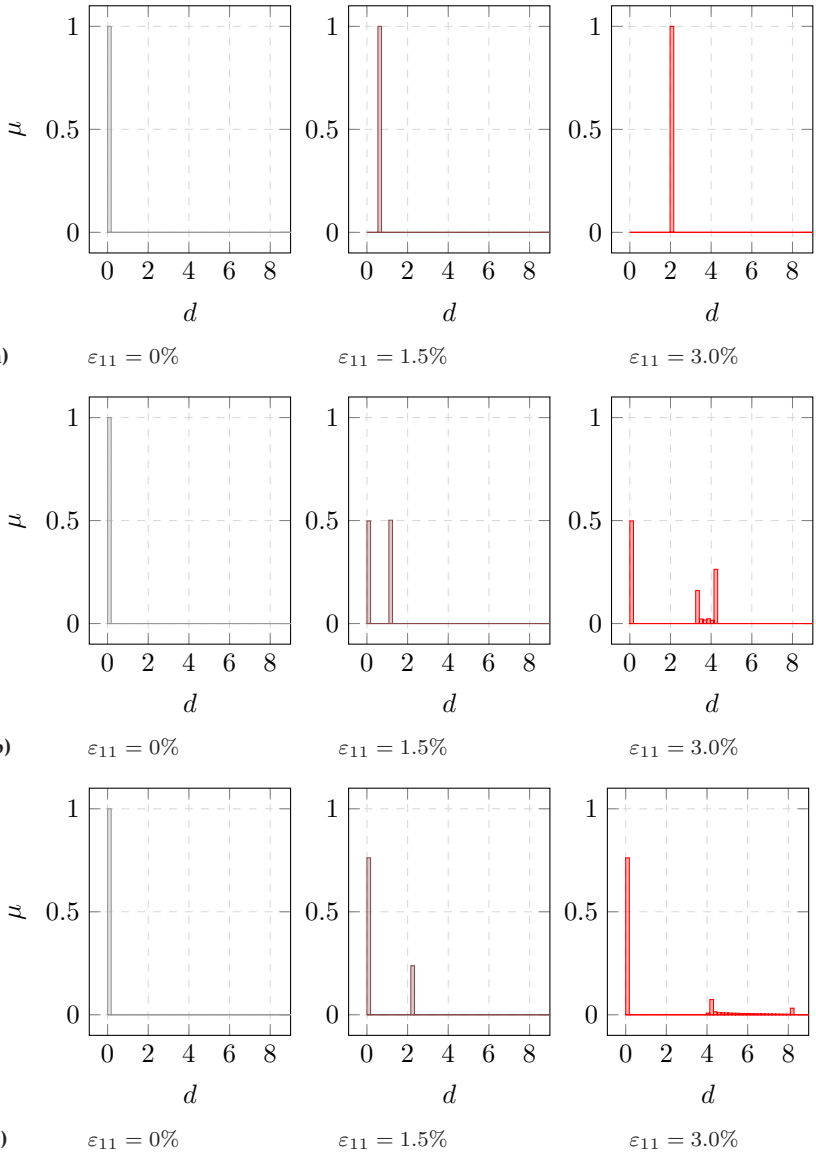


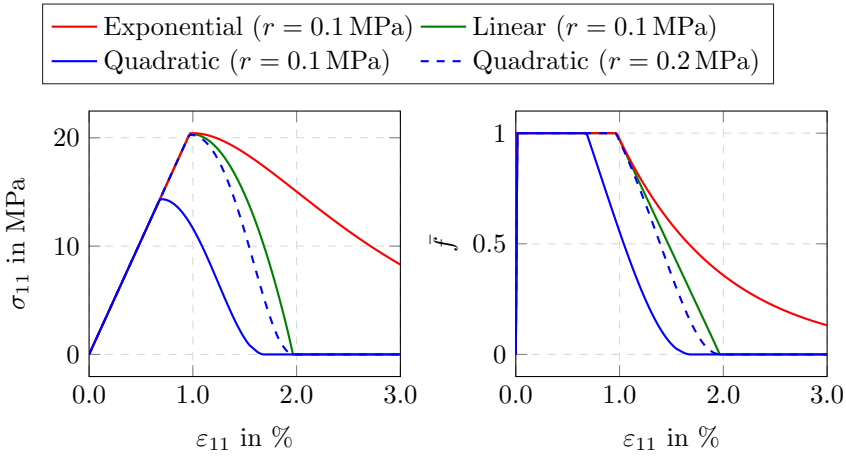
Figure 7.6: Damage distribution for increasing strain levels with different enforced damage-rate limitations $\dot{d}_{\max} = 1.0\,\mathrm{s}^{-1}$ (a), $\dot{d}_{\max} = 2.0\,\mathrm{s}^{-1}$ (b) and $\dot{d}_{\max} = 4.0\,\mathrm{s}^{-1}$ (c). Figure adapted from Figure 6 of Lauff et al. (2026).

In addition, we study the influence of the model parameter $\dot{d}_{\max}$ on the realized damage distribution, see Figure 7.6. For the three considered maximum damage rates, the unloaded material is completely undamaged, i.e., the damage distribution takes the form $\mu = \delta_0$. For increasing applied strain, we observe that the entire damage mass propagates to the maximum damage level for each time step in Figure 7.6(a), when limiting the damage rate to $\dot{d}_{\max} = 1.0\,\mathrm{s}^{-1}$. In contrast, for the two higher maximum damage rates $\dot{d}_{\max} = 2.0\,\mathrm{s}^{-1}$ and $\dot{d}_{\max} = 4.0\,\mathrm{s}^{-1}$, it turns out that the damage distributions are characterized by higher variances and that a significant fraction of the damage mass always remains undamaged, while only smaller fractions propagate to complete failure, see Figures 7.6(b) and 7.6(c). These observations are caused by the definition of the effective degradation as the harmonic mean of the damage distribution. In fact, the effective degradation tends to zero in case any subset - independent of its damage fraction - tends to the maximum damage value. Transferring these insights about the harmonic mean to the minimization problem to be solved (7.72), for a fixed dissipation distance the incremental potential gets smaller in case larger damage increments are permitted (but for smaller damage fractions), compared to a scenario where the total damage is distributed over many smaller steps. As a result, transporting smaller damage fractions over larger damage increments is energetically more favorable than transporting larger fractions over smaller damage increments. As increasing the maximum damage rate $\dot{d}$ permits higher damage increments, the evolution of the damage distribution changes from transporting the total damage over many smaller steps, see Figure 7.6, towards transporting decreasing damage fractions over increasing damage steps, see Figures 7.6(b) and 7.6(c). Consequently, an increasing damage mass remains at low damage states. For the extreme case with unlimited damage rate $\dot{d}_{\max} \to \infty$, almost the entire damage mass is concentrated at low damage states, whereas only an infinitesimal fraction propagates

to the maximum damage state, which may be interpreted as damage localization.

Influence of the selected degradation function

Besides the model parameters, we also study the differences when using different types of degradation functions. To do so, we fix the model parameters $r = 0.1\,\mathrm{MPa}$ and $\dot{d}_{\max} = 1.0\,\mathrm{s}^{-1}$, but consider all three types of degradation functions.



(a) Stress-strain curves

(b) Effective degradation-function

Figure 7.7: Comparison of three degradation functions on material point level. Figure adapted from Figure 7 of Lauff et al. (2026).

In Figure 7.7(a), the stress-strain curves are shown. For the linear and the exponential function, damage initiates at the energy level $\psi_0(\boldsymbol{\varepsilon}) = r$, see Equations (7.16) and (7.19). Thus, both curves share the linear elastic regime. In contrast, the quadratic damage function features a damage

onset at the level $\psi_0(\boldsymbol{\varepsilon}) = r/2$, see Equation (7.18), which manifests in a smaller linear elastic regime. To compare the three degradation functions with equal damage onset, we also plot the stress-strain curve for the quadratic damage function with $r = 0.2\,\mathrm{MPa}$. We observe that the damage model strongly depends on the selected damage degradation function. Whereas similar stress-strain curves with complete damage at $\varepsilon_{11} \approx 1.97\,\%$ emerge for the linear and the quadratic damage function, the exponential degradation function leads to a significantly slower stiffness degradation, and thus to higher remaining stresses.

Let us have a look at the effective degradation $\bar{f}$, see Figure 7.7(b), to study the differences with respect to the remaining stiffness more thoroughly. It turns out that the exponential degradation function still leads to an effective degradation of $\bar{f} \approx 0.37$ when the material already fails for the other two degradation functions. Even at the highest applied strain of $\varepsilon_{11} = 3\,\%$, about $13\,\%$ of the undamaged stiffness remains for the exponential degradation function.

The derivatives of the quadratic degradation function

$$f'(d) = -2(1-d), \quad 0 \leq d \leq 1, \tag{7.107}$$

and the exponential degradation function

$$f'(d) = -\exp(-d), \quad d \geq 0, \tag{7.108}$$

converge to zero for $d \to d_{\max}$. As a result, the effective degradation curves reveal an asymptotic behavior for $\varepsilon_{11} \to \varepsilon_{11}^{\text{fail}}$, where $\varepsilon_{11}^{\text{fail}}$ denotes the strain at material failure. In contrast, the derivative of the linear degradation function

$$f'(d) = \begin{cases} -1, & 0 \leq d < 1, \\ 0, & d = 1, \end{cases} \tag{7.109}$$

has no convergence behavior, but is discontinuous at $d_{\max} = 1$, which transfers to the slope of the effective degradation curve.

7.4.3 Implications of the OT damage model for boundary value problems

To discuss the OT damage model as a constitutive model for components with heterogeneous stress states, we consider a matrix material with a single circular inclusion, which is furnished with the material parameters of E-glass, see Table 7.1. The diameter of the circle is assumed to be $d = 10\,\mu\mathrm{m}$ and the quadratic unit cell has an edge length of $Q_i = 20\,\mu\mathrm{m}$ $(i = 1, 2)$. We apply the macroscopic normal strain $\bar{\varepsilon}_{11} = 3\,\%$ via periodic boundary conditions in 100 loading steps with the time increment $\Delta t = 0.03\,\mathrm{s}$. For the damage parameters, we use $r = 1.00\,\mathrm{MPa}$ and $\dot{d}_{\max} = 4.00\,\mathrm{s}^{-1}$.

On the mesh-independence of the non-convex and the OT damage model

Let us start the investigations with a study on the mesh-size effect by varying the pixel count per direction of the rectangular grid

$$N \in \{20, 40, 80, 160, 320\}. \tag{7.110}$$

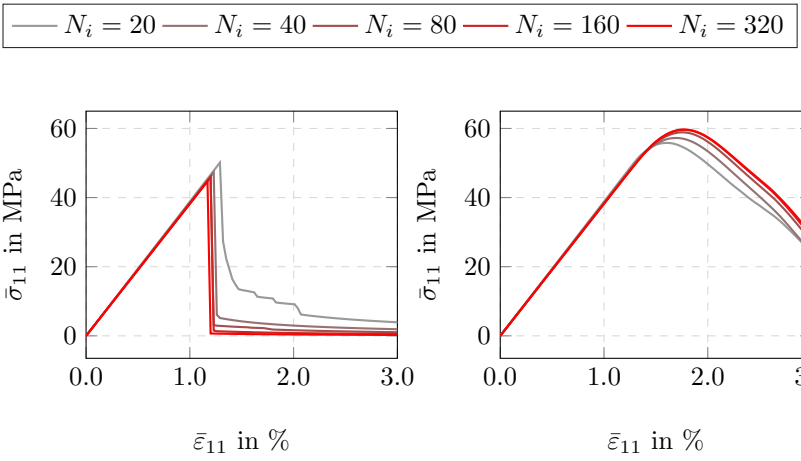
We consider the non-convex damage model (7.1)–(7.2) either without or with damage rate limitation as well as the OT damage model. To obtain the results for the non-convex damage model, we used the FFT-based homogenization technique with the basic scheme (Moulinec and Suquet, 1994) as the conjugate gradient solver did not converge for those material models. The mean and the standard deviation of the solver's iteration count for a single time step are shown in Table 7.2. We observe that the iteration count increases for refined resolutions. Due to the

numerical stability of the FFT-based computational micromechanics with the OT damage model and the applicability of the superior (non-linear) conjugate gradient solver, the iteration count is significantly decreased compared to the other two damage models. The small iteration count below 240 on average highlights the improved convergence behavior of the algorithm with the OT damage model. Comparing the mean iteration number for 320^2 pixels, the non-convex damage model without damage rate limitation leads to $14\,160$ iterations and the non-convex damage model with damage rate limitation results in $6\,876$ iterations, whereas for the OT damage model 239 iterations are required, i.e., only 1.7% and 3.5% of the other two damage models, respectively.

Resolution	20^2	40^2	80^2	160^2	320^2
Non-convex damage	1595	1205	3096	7567	14160
($\dot{d}_{\max} = \infty$)	$\pm$2882	$\pm$3935	$\pm$ 9317	$\pm$30637	$\pm$92676
Non-convex damage	696	2440	4963	6481	6876
($\dot{d}_{\max} = 4.00\,\mathrm{s}^{-1}$)	$\pm$1048	$\pm$5271	$\pm$10521	$\pm$16890	$\pm$17656
ERVE damage model	401	1415	2219	2465	2528
	$\pm$ 589	$\pm$3309	$\pm$ 5665	$\pm$ 6727	$\pm$ 6714
OT damage model	50	89	128	163	239
	$\pm$ 54	$\pm$ 120	$\pm$ 195	$\pm$ 270	$\pm$ 435

Table 7.2: Per time-step mean and standard deviation of the solver iteration-count for a matrix material with a single circular inclusion. We compare different damage models for the matrix materials and resolutions of the composite. Table adapted from Table 2 of Lauff et al. (2026).

In addition to the iteration numbers, we assess the total runtime to discuss whether the lower iteration count of the OT damage compensates for the increase in runtime due to the convexification process. The computations were conducted on a desktop computer, see Section 7.4.1 for more details on the hardware configuration, using four threads.



(a) Non-convex damage without damage rate limitation

(b) Non-convex damage with damage rate limitation

(c) OT damage model

(d) ERVE damage model (Schwarz et al., 2021)

Figure 7.8: Mesh size study for different models and pixel counts for the circular inclusion. Figure adapted from Figure 8 of Lauff et al. (2026).

For a pixel count of 320^2, the runtime with the non-convex damage model without damage-rate limitation was about $864\,\mathrm{min}$, decreasing to $483\,\mathrm{min}$ for the non-convex damage model with damage-rate limitation. In contrast, the OT damage model required $74\,\mathrm{min}$, i.e., only 15% of the runtime of the non-convex damage model with damage-rate limitation. Thus, the study demonstrates that the reduction in the iteration number significantly outweighs the cost of the convexification process.

Besides the algorithmic convergence behavior, we also study the effect of the mesh-size on the mechanical response for the different resolutions in Figure 7.8. For all damages models, we observe that the stress-strain curves of all four mesh-sizes almost coincide in the elastic regime, i.e., the results are mesh-independent.

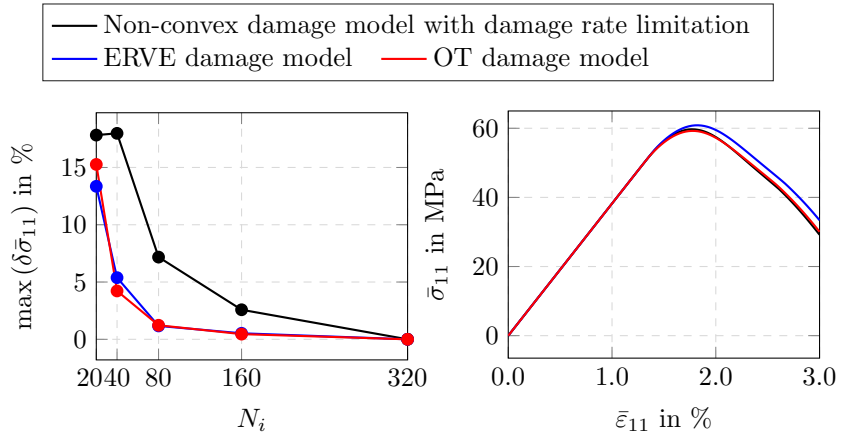
When softening effects start, the results for the non-convex model without damage rate limitation no longer converges due to the onset of localization, which leads to mesh dependency (Gitman et al., 2007), see Figure 7.8(a). For the non-convex model with damage rate limitation in Figure 7.8(b), we observe a converging trend, however the differences between the resolutions are still quite high. In contrast, the results for the OT damage model in Figure 7.8(c) reveal a significantly improved convergence behavior.

To examine the convergence behavior of the non-convex damage model with damage rate limitation and the OT damage model more closely, we analyze the absolute relative mesh-size error of the stress-strain curves compared to the finest resolution

$$\delta\bar{\sigma}_{11} = \left| \frac{\bar{\sigma}_{11,N_i} - \bar{\sigma}_{11,320}}{\bar{\sigma}_{11,320}} \right| \cdot 100\% \tag{7.111}$$

and report on the maximum of the error $\delta\bar{\sigma}_{11}$ for each pixel count in Figure 7.9(a). It turns out that the error is always lower for the OT damage model compared to the non-convex damage model, which is a result of the convexification procedure. Targeting an error below 3%,

we may use the resolution $N_i = 80$ for the OT damage model with a relative error of 1.22%. However, for the non-convex damage model the relative error is still 7.18% for the resolution $N_i = 80$ and 2.58% for the resolution $N_i = 160$. Thus, we need to resolve the structure with at least $N_i = 160$ pixels per axis for the non-convex damage model to ensure the convergence criterion of 3%. Due to the higher voxel count, the less stable convergence behavior and the inability to use the efficient conjugate gradient solver, the computational effort is tremendously higher for the non-convex damage model compared to the OT damage model.



(a) Maximum relative mesh-size error **(b)** Stress-strain curve ($N_i = 320$)

Figure 7.9: Comparing stress-strain curves and errors for the non-convex damage model with damage rate limitation, the OT damage model and the ERVE damage model (Schwarz et al., 2021). Figure adapted from Figure 9 of Lauff et al. (2026).

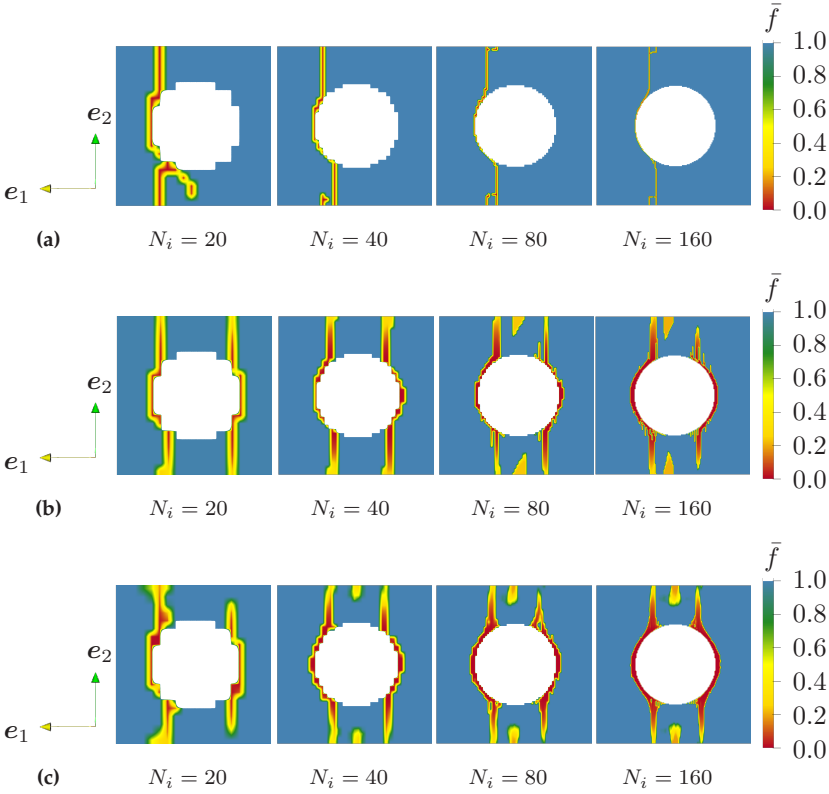


Figure 7.10: Distribution of the effective degradation for varying resolutions, using the non-convex damage model without damage rate limitation (a), the non-convex damage model with damage rate limitation (b) and the OT damage model (c) for the circular inclusion. Figure adapted from Figure 10 of Lauff et al. (2026).

To study the localization as well as the differences in the convergence behavior with respect to the damage degradation, we plot the effective degradation field $\bar{f}$ at the strain level $\bar{\varepsilon}_{11} = 3.0\,\%$ for the three damage models and varying pixel counts in Figure 7.10. For the non-convex damage model without damage rate limitation, the progressive localization with decreasing voxel edge-length is clearly visible in Figure 7.10(a). Due to damage rate limitation, localization is prevented in Figure 7.10(b). However, in contrast to the effective degradation field of the convexified OT damage model, see Figure 7.10(c), finer resolutions are necessary for an adequate approximation of the quantity, which leads to the higher error in Figure 7.9(a).

The considered study may lead to the impression that the non-convex damage model with damage-rate limitation does not suffer from convergence problem under grid refinements for regular meshes. This observation may, however, be very specific to the problem at hand. There is no guarantee that this positive behavior transfers to other cases. In contrast, the convexification process of the OT damage model ensures salient mathematical properties - coercivity and (quasi-)convexity - to hold, in general.

Comparison to the damage model introduced by Schwarz et al. (2021)

In this section, we compare the OT damage model with a damage model introduced by Schwarz et al. (2021), which is also derived by applying a convexification scheme to the non-convex damage model in Equations (7.1)–(7.2). To approximate the convex hull, Schwarz et al. (2021) model the damage variable at each material point in a microstructured fashion with n_{ERVE} discrete damage states defined on an *emulated representative volume element* (ERVE). The attained condensed incremental energy is equivalent to Equation (7.27) with constant weighting coefficients $c_i = 1/n_{\text{ERVE}}$ $(i = 1, \dots, n_{\text{ERVE}})$. In addition to the

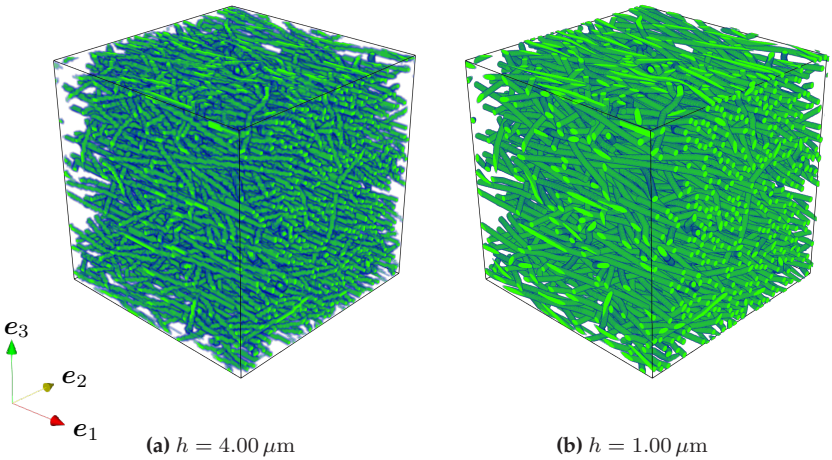
parameters r and $\dot{d}_{\max}$, the number of discrete damage states n_{ERVE} needs to be selected. In this work we use $n_{\text{ERVE}} = 20$, consistent with the computational investigation conducted by Schwarz et al. (2021). To solve the static balance of linear momentum (7.99), we use the FFT-based homogenization framework with the basic scheme (Moulinec and Suquet, 1994) as the conjugate gradient solver failed to converge for the ERVE damage model. Due to the convexification scheme, also the ERVE damage model shows a favorable convergence behavior with respect to mesh refinement, see Figure 7.8(d) and 7.9(a). In addition, the iteration count is decreased compared due to the non-convex damage models, see Table 7.2, but increased compared to the OT damage model. Having a look at the runtime of $466\,\text{min}$ for the pixel count of 320^2, we observe that the computational cost of the ERVE damage model is between the costs of the non-convex damage models and of the OT damage model.

In Figure 7.9(b), we plot the stress-strain curves for both convexified damage models as well as for the non-convex damage model with damage rate limitation, using a pixel count of $N_i = 320$ per axis. We observe that the non-convex damage model and the OT damage model lead to almost coinciding curves, i.e., the convexification process does not alter the stress-strain behavior significantly. For the ERVE damage model, the convexification process has a greater influence on the results, leading to a slightly higher predicted stress-strain response compared to the other two damage models.

7.4.4 Validation of the representativity for stochastic homogenization

In this section, we apply the OT damage model to discontinuously fiber-reinforced composites, which exhibit a heterogeneous and random microstructure, to investigate the representativity of the predicted material behavior within the framework of stochastic homogenization. We use the material data summarized in Table 7.1 for the matrix material

and the fibers, and select the damage parameters $r = 1.00\,\mathrm{MPa}$ and $\dot{d}_{\max} = 4.00\,\mathrm{s}^{-1}$.



(a) $h = 4.00\,\mu\mathrm{m}$ **(b)** $h = 1.00\,\mu\mathrm{m}$

Figure 7.11: Microstructure resolved with two different voxel-edge lengths h. Figure adapted from Figure 11 of Lauff et al. (2026).

For the periodic microstructure generation, we use the fused sequential addition and migration (fSAM) algorithm (Lauff et al., 2024; 2025a). The synthetic packings are filled with a fiber volume fraction of $\phi^{\mathrm{mix}} = 20\,\%$. We model the fibers as polygonal chains with the fiber length $L = 1000\,\mu\mathrm{m}$, the constant fiber diameter $D = 10\,\mu\mathrm{m}$ and a maximum segment length $\bar{\ell} = 25\,\mu\mathrm{m}$. To avoid extremely high angles between adjacent segments, we prescribe the maximum curvature $\bar{\kappa} = 0.02\,\mu\mathrm{m}^{-1}$. Additionally, we choose a minimum distance between the fibers of $20\,\%$ of the fiber diameter, i.e., $2.0\,\mu\mathrm{m}$. For the fiber orientation tensor (Bauer et al., 2023) of second order, we target the tensor $\boldsymbol{A} \mathrel{\hat{=}} \mathtt{diag}\,(0.75, 0.15, 0.1)$, and use the exact closure to approximate the

fiber orientation tensor of fourth order (Montgomery-Smith et al., 2011a;b). The fSAM algorithm is considered to be converged in case no fiber-overlap is detected, the relative error of the fiber orientation tensor is below $\epsilon_{\mathbb{A}} = 10^{-4}$ and the relative error of the maximum curvature constraint drops below $\epsilon_{\bar{\kappa}} = 10^{-3}$.

We load the structure with the macroscopic normal strain $\bar{\varepsilon}_{22} = 3\,\%$ via periodic boundary conditions in $n_{\Delta t}$ loading steps. The time-step count, the necessary resolution and the required cell size for representativity are studied in the following investigations. Generated microstructures resolved a coarse and a fine mesh-size are shown in Figure 7.11.

Study on the time-step size

The goal of this section is to select a sufficiently fine time-step size. Therefore, we consider a microstructure with cubic cell dimensions $Q_i = 420\,\mu\mathrm{m}$ ($i = 1, 2, 3$). The generated microstructure is resolved with a voxel-edge length $h = 1.25\,\mu\mathrm{m}$. We study the time-step counts $n_{\Delta t} = 20$, 40, 80, 160, i.e., the time increments are $\Delta t = 0.15\,\mathrm{s}$, $0.075\,\mathrm{s}$, $0.0375\,\mathrm{s}$ and $0.01875\,\mathrm{s}$.

In Figure 7.12(a), the computed effective stress-strain responses for the applied time-step counts are shown. We observe that the time increment significantly influences the computed material behavior. However, for increasing time-step count, convergence is obtained. Evaluating the absolute relative difference between the temporal resolutions at $\bar{\varepsilon}_{22} = 3\,\%$ compared to the smallest time increment, we obtain errors of 21.33%, 9.11% and 2.98% for increasing time-step count. To obtain an error below 3%, we choose a time-step count of $n_{\Delta t} = 80$ for the following investigations.

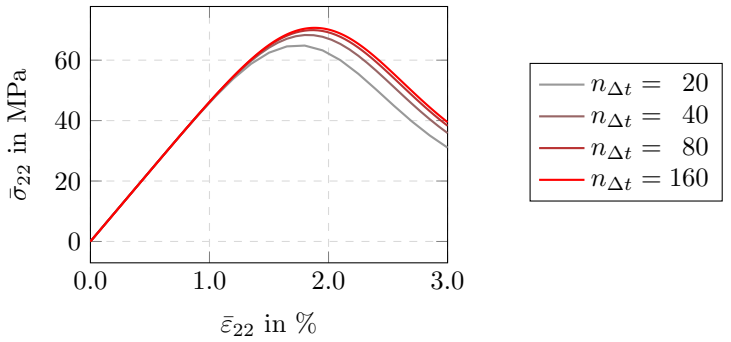
Study on the resolution

A critical aspect of FFT-based homogenization is the spatial resolution of the input microstructure, which directly influences the accuracy of the computed effective properties. Insufficient resolution may fail to capture essential microscale features, while an excessively fine discretization can lead to high computational costs without significant gains in accuracy. The aim of this resolution study is to investigate the impact of the voxel resolution on the homogenized material properties. By evaluating the convergence behavior of the effective stress-strain behavior with increasing resolution, we seek to identify a suitable discretization level that ensures a reliable balance between computational efficiency and numerical accuracy.

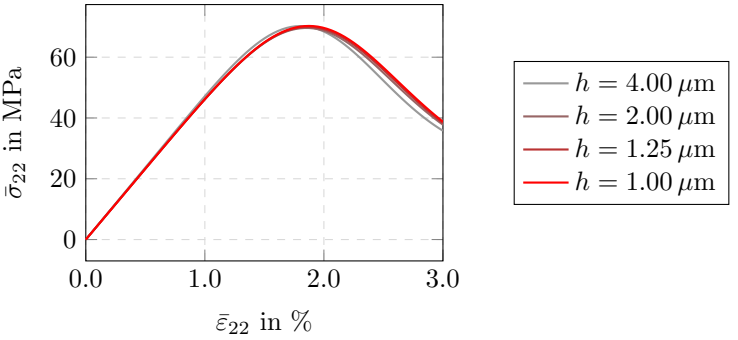
We investigate the voxel-edge lengths $h = 1.0\,\mu\mathrm{m}$, $1.25\,\mu\mathrm{m}$, $2.0\,\mu\mathrm{m}$ and $4.0\,\mu\mathrm{m}$, which resolve the fiber diameter with 10, 8, 5 and 2.5 voxels. For the cubic cell dimensions, we select $Q_i = 420\,\mu\mathrm{m}$. Thus, the microstructure is resolved with 105^3, i.e., about $1.2 \cdot 10^6$, voxels for the coarsest resolution and 420^3, i.e., about $74 \cdot 10^6$, voxels for the finest resolution. Due to the significantly increased number of voxels, the computational effort required to homogenize the finely resolved structure is substantially higher. The considered microstructure resolved with the coarsest and the finest mesh-size are shown in Figure 7.11.

The computed effective stress-strain behavior is shown in Figure 7.12(b). Due to the convexity and coercivity of the OT damage model, convergence for decreasing mesh-size is obtained. Evaluating the maximum relative resolution error of the stress-strain curves compared to the finest resolution reveals an error of 9.00% for the coarsest resolution, dropping to 3.32% and 1.40% with increasing voxel count. We require a resolution error below 3% and thus choose a voxel-edge length of $h = 1.25\,\mu\mathrm{m}$, which is in accordance with previous studies on long fiber

reinforced composites applying a purely elastic material model to the matrix material (Lauff et al., 2024; 2025a).



(a) Time-step size study



(b) Spatial resolution study

Figure 7.12: Sensitivity studies of the stress-strain response for the 3D fiber microstructure. Figure adapted from Figure 12 of Lauff et al. (2026).

RVE study

Understanding the effective behavior of heterogeneous materials at the macroscopic level typically relies on detailed simulations of their microscopic structure. Instead of modeling the entire complexity of a material, computational homogenization uses simplified, smaller-scale models – so-called unit cells – to estimate global properties. A key challenge is ensuring that these unit cells are representative, i.e., that they capture the essential statistical and structural features of the material well enough to enable reliable macroscopic predictions.

In reality, the microstructure introduces randomness, so *apparent* material properties derived from finite unit cells vary across different configurations. As the cell size increases, this variability diminishes, and the results stabilize, approaching the so-called effective properties (Hill, 1963; Drugan and Willis, 1996; Kanit et al., 2003). If a unit cell becomes large enough that further increases no longer affect the computed averages significantly, it is considered a *representative volume element* (RVE). In context of damage modeling with softening phenomena, the apparent properties will only converge to the effective properties if the material behavior is mesh-independent (Gitman et al., 2007). Thus, localization and the concept of representativity are incompatible.

Choosing the smallest possible RVE is the key to minimizing computational cost without sacrificing accuracy. One way to decrease the required unit cell size for representativity is through the use of periodic boundary conditions (Sab and Nedjar, 2005; Schneider et al., 2022) and carefully controlled statistical descriptors, such as the fiber volume fraction or high-order orientation tensors, when generating synthetic microstructures (Schneider, 2022; Lauff et al., 2025a).

To assess whether a unit cell is representative, we need to monitor two types of errors: the *random* and the *systematic* error (Kanit et al., 2003; Gloria and Otto, 2011). The random error (or dispersion) refers to the

variance in the apparent properties across different realizations of a microstructure at fixed cell size and typically vanishes as the domain grows. The systematic error (or bias), on the other hand, measures the discrepancy between the average apparent properties for a fixed unit cell size and the (generally unknown) effective properties. Since the effective properties are rarely available, convergence is evaluated by comparing the mean apparent properties for increasing cell-sizes.

In this RVE study, we consider the three unit cell sizes $Q_i = 280\,\mu\mathrm{m}$, $420\,\mu\mathrm{m}$ and $560\,\mu\mathrm{m}$, and use the resolution $h = 1.25\,\mu\mathrm{m}$. Thus, the smallest unit cell is resolved with 224^3, i.e., about $11 \cdot 10^6$, voxels and the largest unit cell with 448^3, i.e., about $90 \cdot 10^6$, voxels. To assess the representativity of the unit cells, we first generate ten microstructures for each unit cell size, and compute the stress-strain behavior for all generated microstructures. Subsequently, we evaluate the mean and the standard deviation of the stress σ_{22} for each unit cell size with respect to its ten realizations. Last but not least, we compute the relative error of the mean stress compared to the largest unit cell size

$$\delta\overline{\sigma}_{22} = \left| \frac{\text{mean}\left(\bar{\sigma}_{22,Q_i}\right) - \text{mean}\left(\bar{\sigma}_{22,560}\right)}{\text{mean}\left(\bar{\sigma}_{22,560}\right)} \right| \cdot 100\% \tag{7.112}$$

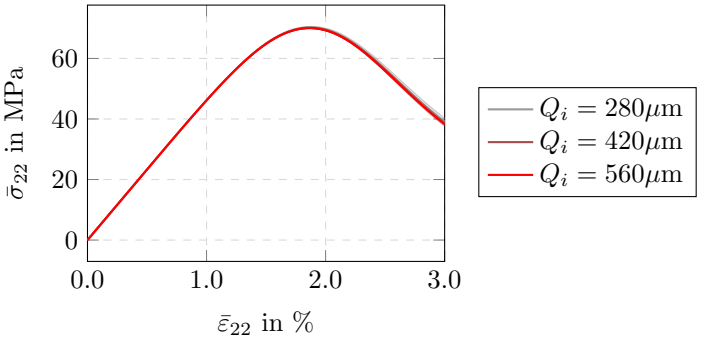
to assess the systematic error and the relative standard deviation

$$\text{RSD} = \frac{\text{std}\left(\bar{\sigma}_{22,Q_i}\right)}{\left|\text{mean}\left(\bar{\sigma}_{22,Q_i}\right)\right|} \cdot 100\% \tag{7.113}$$

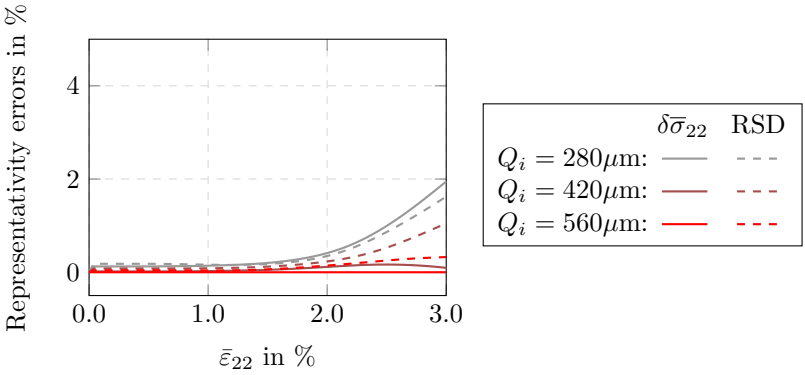
to quantify the random error.

The mean computed stress-strain curves with the resulting scatter bands are plotted in Figure 7.13(a) for all unit cell sizes. We observe that distinguishing between the different curves is barely possible as the curves are in a close range. For a better overview of the differences, we have a look at the representativity errors in Figure 7.13(b). It turns out that the random and the systematic are increasing along the loading

path, but always are below 2%, proving the representativity of all unit cells. Hence, we emphasize that the OT damage model is applicable in the context of homogenization, ensuring moderate necessary resolutions and unit cell sizes for representativity. Such properties are crucial to predict the mechanical behavior in a reliable and efficient manner.



(a) Mean stress-strain curve with the scatter band



(b) Representativity errors

Figure 7.13: On the influence of the unit-cell size for the 3D fiber ensemble. Figure adapted from Figure 13 of Lauff et al. (2026).

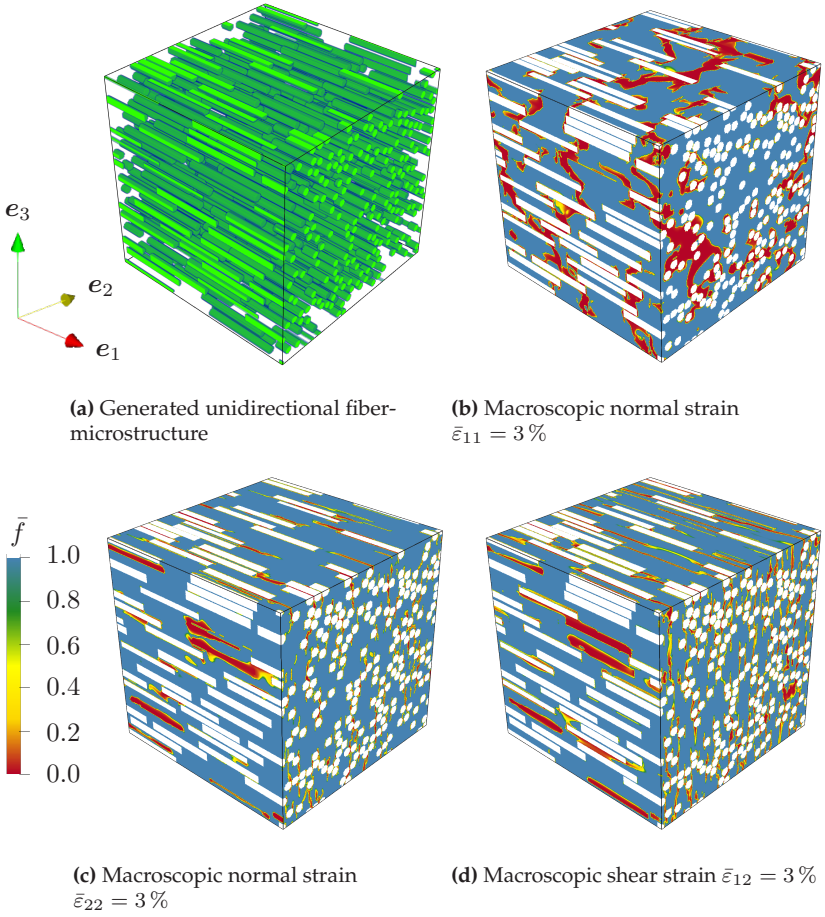
7.4.5 Matrix-failure mechanisms of unidirectional fiber reinforced composites

Last but not least, we investigate the matrix failure of unidirectional fiber-reinforced composites to identify the damage mechanisms predicted by our model. We generate short fiber reinforced microstructures with cubic cell dimensions of $Q_i = 280\mu\mathrm{m}$ by the SAM algorithm (Schneider, 2022; Mehta and Schneider, 2022), prescribing a fiber alignment in $\boldsymbol{e}_1$-direction, a uniform fiber length of $L = 100\,\mu\mathrm{m}$, a fiber diameter of $D = 10\,\mu\mathrm{m}$ and a fiber volume fraction of $\phi = 20\,\%$. According to the resolution study in Section 7.4.4, we resolve the microstructure with the voxel edge-length $h = 1.25\,\mu\mathrm{m}$. A generated microstructure is shown in Figure 7.14(a). The matrix and the fibers are modeled with the isotropic material parameters listed in Table 7.1, and we use the damage parameters $r = 1.00\,\mathrm{MPa}$ and $\dot{d}_{\max} = 4.00\,\mathrm{s}^{-1}$ for the matrix material.

In three loading cases, we investigate the failure mechanisms of the matrix and plot the effective degradation fields in Figures 7.14(b)-7.14(d). For the first and the second loading case, we apply macroscopic normal strains in fiber direction ($\bar{\varepsilon}_{11} = 3\,\%$) and perpendicular to the fiber direction ($\bar{\varepsilon}_{22} = 3\,\%$), respectively. In the last scenario, we load the structure with macroscopic shear strain in fiber direction ($\bar{\varepsilon}_{12} = 3\,\%$). For all scenarios, we apply the load in 80 time steps with a total loading time of $3\,\mathrm{s}$, imposing periodic boundary conditions.

For normal extension in fiber direction, the damage initiates at the fiber ends due to stress concentrations and evolves with increasing applied strain perpendicular to the loading direction. Thus, the loading condition evokes damage peaks at the end of the fibers in the loading direction, see Figure 7.14(b), weakening the load transfer between the matrix and the fibers. In addition, we observe inter-fiber failure in the $\boldsymbol{e}_2$-$\boldsymbol{e}_3$-plane as a result of the dilatation. The random arrangement of the fibers deflects the damage path as the damage grows between the

fiber ends, preventing a strict propagation perpendicular to the loading directions.



(a) Generated unidirectional fiber-microstructure

(b) Macroscopic normal strain $\bar{\varepsilon}_{11} = 3\,\%$

(c) Macroscopic normal strain $\bar{\varepsilon}_{22} = 3\,\%$

(d) Macroscopic shear strain $\bar{\varepsilon}_{12} = 3\,\%$

Figure 7.14: Fiber-reinforced composite with unidirectional fiber arrangement (a) and the distribution of the effective degradation for three different loading conditions (b) - (d). Figure adapted from Figure 14 of Lauff et al. (2026).

Applying the macroscopic normal strain $\bar{\varepsilon}_{22}$ perpendicular to the fiber direction leads to a damage evolution of the matrix in the $\boldsymbol{e}_1$-$\boldsymbol{e}_3$-plane, as shown in Figure 7.14(c), starting along the fiber boundaries. Hence, in contrast to the first loading scenario, the interfacial area between the matrix and the fibers is reduced along the edges of the fibers rather than at the end of the fibers. The effective degradation field associated to the shear loading in fiber direction 7.14(d) reveals similar damage mechanisms as for the normal tension perpendicular to the fiber axis, i.e., damage propagation in the $\boldsymbol{e}_1$-$\boldsymbol{e}_3$-plane. The matrix-failure modes identified in this study are in agreement with previous investigations in the literature (Puck and Schürmann, 2002; Knops and Puck, 2008; Rolland et al., 2016; Hanhan and Sangid, 2021), indicating the validity of the damage prediction for the matrix in fiber-reinforced composites.

7.5 Conclusion

The goal of the work at hand was to complete the agenda of Schwarz et al. (2021): compute the convex envelope of the incremental condensed energy arising from a class of isotropic damage models with rate limitation. These developments were driven by the desire to simulate the stiffness degradation of a material exhibiting strain softening behavior within a component undergoing mechanical loading in a robust and mesh-independent way. To be more precise, our contributions include:

- We identified a condition on the damage-degradation function which permits to compute the convex envelope explicitly: convexity of the reciprocal degradation function. Such a condition is quite natural due to the emergence of the harmonic mean in the degradation pre-factor in front of the undamaged elastic energy. Moreover, the condition is satisfied for the degradation functions considered in this manuscript: the exponential degradation as well as the elementary monomial degradation functions. It might be interesting to investigate other

degradation functions like the ones reported by Wu and Nguyen (2018).

- We computed the convex envelope of the incremental time-discretized energy explicitly. We used a continuum formulation to handle all time steps in the same framework. It turned out that the optimal states arise as convex combinations of the extreme reachable damage states per load step: the undamaged state and the maximum damage reachable in this step. Interestingly, the compliance form of Hooke's elastic energy emerges naturally, which is convex in the strain and the compliance tensor (Görthofer et al., 2022) and was previously used ad-hoc in phenomenological damage models (Magino et al., 2022a;b; 2023). The devised model turns out to be convex in a natural way – which is evident from its formulation(s) in terms of a generalized standard material with convex free energy. However, the space of internal (damage) variables is inherently infinite-dimensional. As the damage-distribution function point of view leads to more ambiguities than necessary, we also introduced another formulation based on measure theory and optimal transportation (Villani, 2009; Santambrogio, 2015), a topic which is well-studied in mathematics but does not appear to be standard in continuum mechanical models.
- Our findings also shed light on the model structure: Whereas classical phenomenological continuum-damage models use damage variables as arguments, the convexified model involves a probability distribution of a damage variable. This finding was already envisioned by Schwarz et al. (2021) in their use of the "emulated RVE". The latter may be imagined as a one-dimensional rod with a distribution of Young's moduli, spread according to the damage distribution under consideration. The "effective" Young's modulus then arises from a harmonic average - a fact which is well-known in micromechanics and thermodynamics, corresponding to the Maxwell construction. Aside from this statics point-of-view, the dynamics of the entire damage

evolution also emerges from the stepwise convexification procedure of the condensed incremental potential. As a result, the convexified local, i.e., gradient-free, damage model is able to reproduce a softening behavior because the localization takes place in "damage space", i.e., in the rod, and not in physical space.

- Aside from the theoretical findings we introduced a full computational procedure to resolve the ensuing mechanical model: we discussed a natural time discretization for equidistant time steps in terms of convex combinations Dirac measures, i.e., *discrete damage distributions*, and provided a Newton-type method which permits to resolve the nonlinear systems arising for each time steps in a robust and efficient manner.
- We provided an analysis of the properties of the resulting damage model. The convexity and the thermodynamical consistency of the model are more or less straightforward: the original (non-convex) damage model was formulated as a GSM, and the convexification procedure retains thermodynamical consistency - both the free energy and the dissipation distance are convex. Moreover, the fact that a convexification process leads to a convex model is not surprising. What is a bit more subtle is the lack of strict convexity of the resulting relaxed model: both the full energy (for the strain *and* the internal variables) and the condensed incremental energy (for the strain tensor only) lack strict convexity, in general. As a result, we cannot conclude uniqueness neither for the evolution of the internal variables nor the attained strain state per load increment. In hindsight, this fact is not surprising due to the linear dissipation distance of the original model and the emergence of the harmonic mean upon convex relaxation. An intriguing question here is whether the lack of strict convexity is a bug or a feature. Maybe the lack of uniqueness reflects the inherent stochasticity of the damage process.

- We wish to stress the consequences of the salient properties of the convexified damage model: For a start, the convexity of the condensed incremental energy permits, together with suitable growth conditions, ensure the existence of minimizers to the associated mechanical boundary-value problems. Thus, no spurious mesh-dependence of the model is observed. In particular, as every local minimizer of a convex objective function is actually a global minimizer, certain pathological situations encountered for non-convex damage models are avoided. Moreover, convexity of the model permits *homogenization* to be simple: Periodic homogenization applies to such convex models, and the emerging homogenized materials involve single-cell formulas only, see Braides (1985) and Müller (1987), avoiding multi-cell homogenization formulas required for non-convex energies. Moreover, other issues observed for non-convex models, like the fact that homogenization and letting the time-step size go to zero do not commute as limiting procedures, see the relevant works (Michel and Suquet, 2022; Hossain et al., 2014; Schneider, 2020b), are not expected to occur. Whether these advantageous properties actually reflect the underlying physics is another matter, however.
- Last but not least we provided pertinent computational examples, showing the performance and robustness of the convexified model and its computational realization, both on material-point level and within a homogenization setting. Due to the salient features of the convexified damage model, it may be used in dedicated upscaling schemes (Köbler et al., 2021; Meyer et al., 2023; Dey et al., 2024) to predict the material degradation including softening effects of components made of microstructured materials.

Apart from the contributions, we also list a number of loose ends and interesting questions to ponder.

- The manuscript at hand was limited to convexifying a *linear-elastic* isotropic damage model without tension-compression anisotropy.

Lifting each of these constraints would be interesting: Dealing with anisotropic damage, incorporating tension-compression asymmetry or extending the framework to inelastic material models like plasticity or viscoelasticity could prove fruitful, in particular when using the obtained model(s) for representing practical materials beyond the theoretical setting of the article at hand.

- There is a number of mathematical questions that might be of interest. We performed relaxation *after* time discretization. Letting the time-step size go to zero might shed further light onto the model. Moreover, it would be interesting to find out whether strict convexity could be introduced into the model. Presumably, this is possible in a variety of ways, and the ramification should be studied. Last but not least, it might be interesting to find out whether rate-independence can be realized in this framework as envisioned by Schwarz et al. (2021).
- From the point of view of computational mechanics it is desirable to study which discretization schemes to use. For a start, we used equidistant time steps only, and monitored discrete damage distributions. Such a naive procedure does not appear optimal, in particular when non-equidistant time steps are used. Moreover, it might be worthwhile to study if fully continuous schemes may be used. Here, a transfer from the optimal transport literature (Solomon, 2018) might be advised.
- The derived convexified model behaves strongly like the model envisioned by Schwarz et al. (2021), which is conceptually much simpler. It might be useful to study the connections more closely, e.g., finding conditions under which both models behave similarly.
- The investigated model (Schwarz et al., 2021) involves the abstract parameters r and $d_{\max}$. It would be desirable to establish the connection to experimentally measurable quantities such as the fracture energy or the critical strain energy density.

- This work was concerned with the mathematical details required to set up a continuum damage model that is local and permits to represent a softening behavior without spurious mesh dependence of the finite-element results. With this focus, less effort was spent on discussing the potential applications of the resulting model, e.g., to damage prediction in polymers, quasi-brittle materials or structural composites.

Chapter 8

Summary and conclusions

8.1 Summary

In this thesis, we contributed to the discipline of full-field multiscale modeling for short and long fiber reinforced polymers. To do so, we presented efficient algorithms to generate representative volume elements for composites reinforced with short and long fibers as well as for hybrid material systems. As the main objectives for the microstructure generation, we desired periodic geometries to decrease the boundary artifacts and a precise realization of the microstructural descriptors, i.e., the fiber volume fraction, the fiber length and orientation distributions as well as the fiber curvature. Furthermore, we discussed a novel class of damage models with strain softening behavior to model the damage degradation of the polymeric matrix. The contributions of each chapter are summarized as follows.

In **Chapter 3**, we introduced the orientation corrected shaking (OCS) method based on the two-step shaking algorithm presented by Li et al. (2022) to generate short fiber reinforced polymers. In particular, we enabled a user-selected cell size and periodicity of the generated microstructures. In addition, we developed a shaking procedure which accounts for the desired fiber orientation tensor of fourth order. In computational studies, the OCS method showed its capabilities to generate representative volume elements even for small unit cell sizes. Com-

paring the effective behavior of generated PA66GF35 microstructures with fiber length distribution to experimental data demonstrated the applicability to industrial materials.

In contrast to short fibers, which may be modeled as straight cylinders, fiber bending is significant when considering long fiber reinforced polymers. To account for the curvilinear fiber description, we discretized a long fiber as a polygonal chain with cylindrical segments in **Chapter 4**. Based on this model assumption, we discussed the fused sequential addition and migration (fSAM) algorithm as an alternative approach to the SAM algorithm for long fibers (Schneider, 2022). Whereas the SAM algorithm satisfies the connectivity constraint between adjacent segments only for convergence, the optimization procedure of the fSAM algorithm is restricted to the configuration space of a polygonal chain, leading to a fused fiber movement. Due to the adapted iteration rule, the fSAM algorithm enables higher fiber volume fractions (up to 32% for an aspect ratio of 150) and larger fiber aspect ratios (up to 2800).

The extension of the fSAM algorithm for hybrid materials, e.g., CoDicoFRP, was discussed in **Chapter 5**. As hybrid material comprise areas with varying microstructural descriptors, we adjusted the formulation of the fSAM algorithm to distinguish between different subcells. In addition, we presented box constraints to restrict the location of a fiber during the optimization procedure to its assigned subcell. The characteristics of the interface between subcells depend on the manufacturing processes and the material combination, and may either be described by interlocking or strict separation. As the subcell interface is mainly controlled by the box constraints, we presented different box-constraint types to tailor the generated microstructures to the considered material system. By applying the extended fSAM algorithm to CoDicoFRP, we studied the influence of the box-constraint type on the effective linear-elastic material behavior and validated the representativity of the generated microstructures with experiments.

In **Chapter 6**, we studied the influence of the fiber curvature on the mechanical properties of long fiber reinforced polymers. To do so, we discussed the deviation from straight curve (DSC) as a novel measure to quantify the averaged curvature of a single fiber. Computed as the trace of the second-order fiber orientation tensor's covariance, the DSC is related to the averaged local curvature, emphasizing its validity as curvature measure. In addition, the DSC exhibits further advantageous properties, namely its boundedness between zero for a straight fiber and $2/3$ for a fiber with an isotropic second-order fiber orientation tensor, the simple computation and the robustness with respect to the discretization of the fibers as polygonal chains. With the DSC at hand, we adapted the objective function of the fSAM algorithm to account for a desired curvature state. As a result, we were enabled to generate microstructures for wide ranges of DSCs and studied the effect of the fiber curvature on the stiffness. The investigation revealed a decrease in stiffness for increasing DSC, where the Young's modulus E_1 degraded by about 10%.

We addressed the damage modeling with strain softening behavior in **Chapter 7**. To derive a convex damage model, we regularized a standard phenomenological damage model with scalar damage variable and damage-rate limitation. The convexification process led to the optimal transport (OT) damage model, describing the internal damage state with one-dimensional damage-distributions. Due to formulation of the original, non-convex damage model as generalized standard model, also the OT damage model is thermodynamically consistent. Furthermore, the convexity of the incremental condensed energy in combination with the damage-rate limitation guarantees mesh-independent results, even for the strain softening regime. At the material point level and within the framework of upscaling schemes, computational studies showed the ramifications of the OT damage model on the mechanical behavior of a polymeric matrix and demonstrated the emergence of representative volume elements for long fiber reinforced polymers.

8.2 Conclusions

This thesis concludes by revisiting the objectives defined at the beginning in Section 1.1 and discussing the extent to which they have been achieved. In addition, possible extensions and alternative approaches for future research are outlined.

According to the defined objectives for the microstructure generation, suitable modeling approaches were chosen for the fibers, i.e., straight cylinders for short fibers and polygonal chains to incorporate the fiber bending of long fibers. The maximum segment length, used as the discretization parameter for the polygonal chains, was found to have only a minor influence on the effective material behavior, provided that the fiber curvature is moderate. Hence, the approximation of continuously curved fibers with polygonal chains is appropriate. To further improve on the modeling approaches, especially for curved fibers, a continuous representation of the fiber curvature might be of interest, e.g., by using B-Splines. However, incorporating such fiber descriptions is currently impractical due to the immense computational effort to measure the required periodic inter-fiber distances.

Furthermore, descriptors to assess the main properties of the microstructure were discussed. Whereas the fiber volume fraction, the fiber length distribution and the fiber orientation tensors were already state of the art, a robust quantity to measure the averaged fiber curvature for long fibers discretized as polygonal chains was lacking. Applying the averaged local curvature seemed to be a natural way to assess the fiber curvature, however, it turned out to be not robust with respect to the discretization of the fibers as polygonal chains. To overcome this limitation, we introduced the DSC, revealing advantageous properties and demonstrating its validity for quantifying the fiber curvature in fiber-reinforced composites.

As the fiber orientation and the fiber curvature distribution are inherently coupled, a completely decoupled consideration is impossible, in general. For example a unidirectional fiber orientation distribution implies that the fiber curvature is zero, which is reflected in the DSC as curvature measure. However, for fiber orientation distributions beyond the unidirectional case, the curvature distribution is no longer completely determined by the orientation distribution. Consequently, varying averaged fiber curvatures may be observed for a fixed fiber orientation distribution.

As a shortcoming of the DSC, it is entirely determined by the fiber orientation tensor of second order for a single fiber, and such a complete coupling does not reflect the actual relation between orientation and curvature distribution. For short and long fiber reinforced polymers, this limitation is negligible as typical microstructures comprise high numbers of fibers. In such cases, the volume-averaged DSC is not strictly coupled to the fiber orientation tensor of second order.

Besides the already mentioned microstructural descriptors, further approaches may be included to assess the microstructural properties even more in detail. For instance, Mehta and Schneider (2024) couple the fiber length and orientation distributions as larger fibers tend to be more oriented. In addition, descriptors for, e.g., the fiber bundling or the microstructural defects, may be incorporated. Addressing the fiber curvature, alternative fiber curvature measures (Hartmann and Liese, 2021; Kumar et al., 2024), e.g., the tortuosity, may be discussed and compared to the DSC, potentially in combination with a continuously curved fiber description.

By including the introduced microstructural descriptors as the desired quantities within the microstructure generation and by ensuring the periodicity of the generated packings, the unit cell size for representativity was minimized, thereby reducing the computational effort for the homogenization. This aspect should not be underestimated since

the computational effort for the homogenization may become critical, especially when non-linear material models such as damage degradation are involved.

An important research objective was the development of efficient microstructure generation in terms of the runtime and the packing limits. The development of the OCS method enabled the generation of microstructures for short fiber reinforced polymers with industrial fiber volume fractions, e.g., for a PA66GF35 with a fiber volume fraction of 19% and a fiber aspect ratio of 33, in reasonable runtime. However, when compared to alternative generation approaches, e.g., the SAM algorithm (Schneider, 2017), the OCS method showed a significantly higher runtime due to its general formulation as a sequential insertion algorithm and the improved shaking scheme to realize the desired orientation distribution precisely. In contrast, the fSAM algorithm demonstrated its capability to outperform cutting-edge generators with respect to the efficiency and the packing limits. The superior performance is attributed to its general formulation as a collective rearrangement algorithm based on a suitable optimization procedure. In particular, the fused fiber movement and the fast implementation should be mentioned here.

Using the developed generation tools, pertinent computational investigations on the linear-elastic mechanical behavior were performed, e.g., by examining the influence of the closure approximations, the interfacial modeling between adjacent subcells or the degree of fiber curvature. In addition, the representativity of the generated microstructures was demonstrated by comparing the effective linear-elastic stiffness with experimental data. Subsequent studies may explore the thermomechanical behavior of the microstructures for non-linear material models and more complex loading conditions. Special attention should be paid to assess whether the applied microstructural descriptors are also sufficient for these cases, or if additional descriptors need to be incorporated to ensure the representativity of the synthetic microstructures.

As the second main research field, this thesis addressed the development of a damage modeling approach with strain softening behavior. The OT damage model is formulated as a phenomenological model in the class of generalized standard materials, reflecting strain softening behavior due to damage and satisfying the thermodynamical consistency. By selecting the damage variables of the OT damage model properly, i.e., the parameter $\dot{d}_{\max}$ to limit the damage rate and the parameter r to determine the onset of inelastic deformation, the damage evolution of various materials with damage softening behavior may be considered. Due to the convex formulation and the damage-rate limitation, the OT damage model prevents localization without non-local regularization techniques. Thus, the material response at a single material point is independent of neighborhood information, and the formulation of the OT damage model works without solving additional partial differential equations.

At the current state, the OT damage model may be applied to materials for which isotropic elastic damage modeling is suitable. To make the model applicable to a broader range of materials, the model formulation may be extended to account for anisotropic damage degradation and inelastic material behavior, e.g., viscoelasticity or plasticity. As many industrial materials show a different damage behavior for tension compared to compression, it may be relevant to account for the tension-compression asymmetry.

Also regarding the mathematical formulation of the OT damage model, further research could be fruitful. At this point, the model requires equidistant time steps, and the number of discrete damage states is directly coupled to the time-step size, i.e., a fine discretization of the damage-distribution demands small step sizes. As these limitations may significantly decrease the efficiency, the OT damage model could be extended for different time-discretization schemes as well as a separated selection of the damage states or even a continuous description of the

damage-distribution. Furthermore, adapting the model for the strict convexity of the condensed incremental energy or a rate-independent formulation might be interesting research tasks. Last but not least, the convex regularization was performed in a time-discretized setting, however, deriving a time-continuous damage model may be useful to understand the model more thoroughly.

To conclude, this thesis addressed fundamental research questions to enhance the prediction of the mechanical behavior of fiber-reinforced polymers. With the developed microstructure generation tools and the OT damage model, the contributions of this thesis substantially improved on the existing approaches to obtain a comprehensive prediction strategy for the mechanical response of short and long fiber reinforced composites.

Appendix A

Separating the first eigenvalue of the computed fiber orientation tensor of second order into two terms[1]

The Appendix A derives Equation (3.27) for computing the shaking parameter $\Delta\varphi$. As starting point, we require that the first eigenvalue of the prescribed and the computed fiber orientation tensor of second order are equal:

$$a_1 \stackrel{!}{=} a_1^{\mathsf{c}}. \tag{A.1}$$

Using Equation (3.22) leads to the equivalent formula

$$\begin{aligned} a_1 \stackrel{!}{=} \int_{-\infty}^{\infty}\int_{-\infty}^{\infty} \Big[& \widetilde{a}_1^{\mathsf{r}}\, p_1\left(\theta_1(\xi_\theta), \varphi_1(\xi_\varphi)\right)^2 \\ & + \widetilde{a}_2^{\mathsf{r}}\, p_1\left(\theta_2(\xi_\theta), \varphi_2(\xi_\varphi)\right)^2 \Big]\; \psi(\xi_\theta)\, \psi(\xi_\varphi)\; \mathrm{d}\xi_\theta\, \mathrm{d}\xi_\varphi, \end{aligned} \tag{A.2}$$

where $p_1\left(\theta_i(\xi_\theta), \varphi_i(\xi_\varphi)\right)$ denotes the first component of the fiber direction. We are interested in the influence of the shaking parameter $\Delta\varphi$ on the fiber orientation tensor of second order. Thus, we need an explicit

[1] This appendix is based on the Appendix of the publication "An orientation corrected shaking method for the microstructure generation of short fiber-reinforced composites with almost planar fiber orientation" (Lauff et al., 2023).

formulation of the shaking procedure for the first component of the fiber direction. Following Equation (3.1) the component is computed as

$$p_1\left(\theta_i(\xi_\theta), \varphi_i(\xi_\varphi)\right) = \sin\left(\theta_i(\xi_\theta)\right) \cos\left(\varphi_i(\xi_\varphi)\right). \tag{A.3}$$

To proceed, we account for the sampling procedure of the angles (3.19) and are led to the expression

$$p_1\left(\theta_i(\xi_\theta), \varphi_i(\xi_\varphi)\right) = \sin\left(\widetilde{\theta}_i + \Delta\theta\,\xi_\theta\right) \cos\left(\widetilde{\varphi}_i + \Delta\varphi\,\xi_\varphi\right). \tag{A.4}$$

With the initial angles (3.20), we obtain the explicit shaking procedure for the x-component of the fiber direction for both initial directions

$$\begin{aligned} p_1\left(\theta_1(\xi_\theta), \varphi_1(\xi_\varphi)\right) &= \sin\left(\frac{\pi}{2} + \Delta\theta\,\xi_\theta\right) \cos\left(\Delta\varphi\,\xi_\varphi\right) \\ p_1\left(\theta_2(\xi_\theta), \varphi_2(\xi_\varphi)\right) &= \sin\left(\frac{\pi}{2} + \Delta\theta\,\xi_\theta\right) \cos\left(\frac{\pi}{2} + \Delta\varphi\,\xi_\varphi\right). \end{aligned} \tag{A.5}$$

To shorten the expressions (A.5), we use the reduction formulas for trigonometrical functions:

$$\begin{aligned} p_1\left(\theta_1(\xi_\theta), \varphi_1(\xi_\varphi)\right) &= \cos\left(\Delta\theta\,\xi_\theta\right) \cos\left(\Delta\varphi\,\xi_\varphi\right) \\ p_1\left(\theta_2(\xi_\theta), \varphi_2(\xi_\varphi)\right) &= -\cos\left(\Delta\theta\,\xi_\theta\right) \sin\left(\Delta\varphi\,\xi_\varphi\right). \end{aligned} \tag{A.6}$$

With this insight at hand, we reformulate Equation (A.2)

$$\begin{aligned} a_1 \overset{!}{=} &\int_{-\infty}^{\infty}\int_{-\infty}^{\infty} \Big[\widetilde{a}_1^{\mathrm{r}} \cos\left(\Delta\theta\,\xi_\theta\right)^2 \cos\left(\Delta\varphi\,\xi_\varphi\right)^2 \\ &+\widetilde{a}_2^{\mathrm{r}} \cos\left(\Delta\theta\,\xi_\theta\right)^2 \sin\left(\Delta\varphi\,\xi_\varphi\right)^2\Big]\ \psi(\xi_\theta)\,\psi(\xi_\varphi)\ \mathrm{d}\xi_\theta\,\mathrm{d}\xi_\varphi \\ = &\int_{-\infty}^{\infty}\int_{-\infty}^{\infty} \cos\left(\Delta\theta\,\xi_\theta\right)^2 \Big[\widetilde{a}_1^{\mathrm{r}} r \cos\left(\Delta\varphi\,\xi_\varphi\right)^2 \\ &+\widetilde{a}_2^{\mathrm{r}} \sin\left(\Delta\varphi\,\xi_\varphi\right)^2\Big]\ \psi(\xi_\theta)\,\psi(\xi_\varphi)\ \mathrm{d}\xi_\theta\,\mathrm{d}\xi_\varphi \end{aligned} \tag{A.7}$$

and uncover that the shaking parameters $\Delta\theta$ and $\Delta\phi$ are considered in two decoupled terms. Hence, the double integral may be separated into

$$\begin{aligned} a_1 \overset{!}{=} \int_{-\infty}^{\infty} \cos\left(\Delta\theta\,\xi_\theta\right)^2 \psi(\xi_\theta)\ \mathrm{d}\xi_\theta \int_{-\infty}^{\infty} \Big[\widetilde{a}_1^{\mathsf{r}} \cos\left(\Delta\varphi\,\xi_\varphi\right)^2 \\ + \widetilde{a}_2^{\mathsf{r}} \sin\left(\Delta\varphi\,\xi_\varphi\right)^2 \Big]\ \psi(\xi_\varphi)\ \mathrm{d}\xi_\varphi. \end{aligned} \tag{A.8}$$

Let us recall Equation (3.24), then we may reformulate the first integral of Equation (A.8)

$$a_1 \overset{!}{=} (1 - a_3) \int_{-\infty}^{\infty} \left[\widetilde{a}_1^{\mathsf{r}} \cos\left(\Delta\varphi\,\xi_\varphi\right)^2 + \widetilde{a}_2^{\mathsf{r}} \sin\left(\Delta\varphi\,\xi_\varphi\right)^2 \right] \psi(\xi_\varphi)\ \mathrm{d}\xi_\varphi, \tag{A.9}$$

leading to Equation (3.27).

Appendix B

Metric of the Riemannian manifold describing a curved fiber[1]

The purpose of this appendix is to provide a streamlined derivation of the natural metric g of the manifold $\mathcal{R}$ (4.19), i.e., Equation (4.23). The manifold $\mathcal{R}$ parametrizes the submanifold $\mathcal{F}$ (4.13) of the Euclidean space $\mathbb{R}^{6\,n}$, whose general elements we will denote as $\mathbf{f}$. More precisely, the coordinate vector $\mathbf{f}$ collects the midpoints $\mathbf{x}^a$ and the directions $\mathbf{p}^a$ of all segments, see Equation (4.12). For the Euclidean space at $\mathbf{f} \in \mathbb{R}^{6\,n}$, the scalar product of a tangent vector $\dot{\mathbf{f}} \in T_{\mathbf{x}}\mathbb{R}^{6\,n} \equiv \mathbb{R}^{6\,n}$ computes as

$$\langle\, \dot{\mathbf{f}}, \dot{\mathbf{f}} \,\rangle_{\mathbb{R}^{6\,n}} = \sum_{a=1}^{n} \left[\|\dot{\mathbf{x}}^a\|^2 + \varepsilon\,(\ell, D)\, \|\dot{\mathbf{p}}^a\|^2 \right], \tag{B.1}$$

where the volume-specific moment of inertia of a spherocylinder $\varepsilon\,(\ell, D)$ (4.24) is responsible for the specific form of the rotational contributions. With the Equation (B.1) at hand, the metric g of the manifold $\mathcal{R}$ is obtained via the pull-back (4.8) of the scalar product in Equation (B.1) onto the tangent space $T_{\mathbf{q}}\mathcal{R}$

$$g_{\mathbf{q}}\,(\dot{\mathbf{q}}, \dot{\mathbf{q}}) = \langle\, \mathrm{d}\mathbf{f}_{\mathbf{q}}\,(\dot{\mathbf{q}})\,, \mathrm{d}\mathbf{f}_{\mathbf{q}}\,(\dot{\mathbf{q}}) \rangle_{\mathbb{R}^{6\,n}}, \quad \mathbf{q} \in \mathcal{R}, \quad \dot{\mathbf{q}} \in T_{\mathbf{q}}\mathcal{R}, \tag{B.2}$$

[1] This appendix is based on the Appendix A of the publication "Generating microstructures of long fiber reinforced composites by the fused sequential addition and migration method" (Lauff et al., 2024).

with the explicit formulation for the differential map $d\mathbf{f}_\mathbf{q}$

$$\begin{aligned} &\mathrm{d}\mathbf{f}_\mathbf{q}\left(\dot{\mathbf{q}}\right) = \left[\left(\mathrm{d}\mathbf{x}_\mathbf{q}^1\left(\dot{\mathbf{q}}\right)\right)^\mathsf{T} \cdots \left(\mathrm{d}\mathbf{x}_\mathbf{q}^n\left(\dot{\mathbf{q}}\right)\right)^\mathsf{T} \quad \left(\mathrm{d}\mathbf{p}_\mathbf{q}^1\left(\dot{\mathbf{q}}\right)\right)^\mathsf{T} \cdots \left(\mathrm{d}\mathbf{p}_\mathbf{q}^n\left(\dot{\mathbf{q}}\right)\right)^\mathsf{T}\right]^\mathsf{T}, \\ &\mathbf{q} \in \mathcal{R}, \quad \dot{\mathbf{q}} \in T_\mathbf{q}\mathcal{R} \end{aligned} \tag{B.3}$$

with

$$\mathrm{d}\mathbf{x}_\mathbf{q}^a\left(\dot{\mathbf{q}}\right) = \hat{\mathbf{Q}}\,\dot{\hat{\mathbf{x}}}^0 + \sum_{b=1}^{a-1} \ell\,\dot{\mathbf{p}}^b + \frac{\ell}{2}\,\dot{\mathbf{p}}^a \quad \text{and} \quad \mathrm{d}\mathbf{p}_\mathbf{q}^a\left(\dot{\mathbf{q}}\right) = \dot{\mathbf{p}}^a, \quad a = 1, \dots n, \tag{B.4}$$

from the tangent space $T_\mathbf{q}\mathcal{R}$ onto the tangent space $T_{\mathbf{f}(\mathbf{q})}\mathcal{F}$. Using the explicit formulation of the differential map $\mathrm{d}\mathbf{f}_\mathbf{q}$ in Equation (B.3) leads to

$$\begin{aligned} g_\mathbf{q}\left(\dot{\mathbf{q}}, \dot{\mathbf{q}}\right) &= \sum_{a=1}^{n} \left[\left\|\mathrm{d}\mathbf{x}^a\left(\dot{\mathbf{q}}\right)\right\|^2 + \varepsilon\left(\ell, D\right) \left\|\,\mathrm{d}\mathbf{p}^a\left(\dot{\mathbf{q}}\right)\right\|^2\right] \\ &= \sum_{a=1}^{n} \left[\left\|\,\hat{\mathbf{Q}}\,\dot{\hat{\mathbf{x}}}^0 + \sum_{b=1}^{a-1} \ell\,\dot{\mathbf{p}}^b + \frac{\ell}{2}\,\dot{\mathbf{p}}^a\right\|^2 + \varepsilon\left(\ell, D\right) \left\|\,\dot{\mathbf{p}}^a\,\right\|^2\right]. \end{aligned} \tag{B.5}$$

Equation (B.5) reveals that the metric of the manifold $\mathcal{R}$ is independent of the location on the manifold $g_\mathbf{q} \equiv g$. We wish to give the metric g in Equation (B.5) in the form of

$$g\left(\dot{\mathbf{q}}, \dot{\mathbf{q}}\right) = \dot{\mathbf{q}}^\mathsf{T}\,\mathbf{G}\,\dot{\mathbf{q}}, \tag{B.6}$$

with the constant metric matrix $\mathbf{G}$. As the metric g is already known, the metric matrix $\mathbf{G}$ may be derived by the relation

$$\mathbf{G} = \frac{1}{2}\frac{\partial^2 g}{\partial\dot{\mathbf{q}}\,\partial\dot{\mathbf{q}}}. \tag{B.7}$$

We compute the first derivative of the halved metric with regard to the normalized starting point

$$\begin{aligned}\frac{1}{2}\frac{\partial g}{\partial \hat{\dot{\mathbf{x}}}^0} &= \sum_{a=1}^{n} \hat{\mathbf{Q}} \left[\hat{\mathbf{Q}}\, \hat{\dot{\mathbf{x}}}^0 + \sum_{b=1}^{a-1} \ell\, \dot{\mathbf{p}}^b + \frac{\ell}{2}\, \dot{\mathbf{p}}^a \right] \\ &= n\, \hat{\mathbf{Q}}^2\, \hat{\dot{\mathbf{x}}}^0 + \sum_{a=1}^{n} \left(n - a + \frac{1}{2} \right) \ell\, \hat{\mathbf{Q}}\, \dot{\mathbf{p}}^a \end{aligned} \tag{B.8}$$

and with regard to the directions

$$\begin{aligned}\frac{1}{2}\frac{\partial g}{\partial \dot{\mathbf{p}}^a} =& \ell \sum_{b=a+1}^{n} \left(\hat{\mathbf{Q}}\, \hat{\dot{\mathbf{x}}}^0 + \sum_{c=1}^{b-1} \ell\, \dot{\mathbf{p}}^c + \frac{\ell}{2} \dot{\mathbf{p}}^b \right) + \frac{\ell}{2} \left(\hat{\mathbf{Q}}\, \hat{\dot{\mathbf{x}}}^0 + \sum_{b=1}^{a-1} \ell\, \dot{\mathbf{p}}^b + \frac{\ell}{2} \dot{\mathbf{p}}^a \right) \\ &+ \varepsilon\left(\ell, D\right)\, \dot{\mathbf{p}}^a \\ =& \left(n - a + \frac{1}{2} \right) \ell\, \hat{\mathbf{Q}}\, \hat{\dot{\mathbf{x}}}^0 + \sum_{b=1}^{a-1} \left(n - a + \frac{1}{2} \right) \ell^2\, \dot{\mathbf{p}}^b \\ &+ \left(\varepsilon\left(\ell, D\right) + \ell^2 \left(n - a + \frac{1}{4} \right) \right) \dot{\mathbf{p}}^a + \sum_{b=a+1}^{n} \left(n - b + \frac{1}{2} \right) \ell^2\, \dot{\mathbf{p}}^b. \end{aligned} \tag{B.9}$$

Hence, the metric matrix attains the form

$$\begin{aligned}\mathbf{G} = &\begin{bmatrix} n\, \hat{\mathbf{Q}}^2 & f_1\, \ell\, \hat{\mathbf{Q}} & f_2\, \ell\, \hat{\mathbf{Q}} & \cdots & f_n\, \ell\, \hat{\mathbf{Q}} \\ & f_{d,1}\, \mathbf{1}_{3\times 3} & f_2\, \ell^2\, \mathbf{1}_{3\times 3} & \cdots & f_n\, \ell^2\, \mathbf{1}_{3\times 3} \\ & & \ddots & & \vdots \\ & & & \ddots & f_n\, \ell^2\, \mathbf{1}_{3\times 3} \\ \text{sym} & & & & f_{d,n}\, \mathbf{1}_{3\times 3} \end{bmatrix} \\ \text{with} \quad & f_a = n - a + \frac{1}{2} \quad \text{and} \quad f_{d,a} = \varepsilon\left(\ell, D\right) + \ell^2 \left(n - a + \frac{1}{4} \right), \end{aligned} \tag{B.10}$$

where the latter equation corresponds to Equation (4.23).

Appendix C

Geodesics on the Riemannian manifold of curved fibers[1]

The goal of this appendix is to derive the equations governing the geodesics of the manifold describing curved fibers $\mathcal{R}$ (4.19). Suppose that we know the coordinate vector at the time points t_1 and t_2 and aim to describe the geodesic curve between these instants. According to Equation (4.4), the geodesic of the manifold $\mathcal{R}$ may be obtained by minimizing the energy functional, parametrizing the midpoints and directions by the coordinate vector $\mathbf{q}(t) \in \mathbb{R}^{n_q}$, see Equation (4.17), under the condition that the vector-valued constraint function $\mathbf{\Phi}_1$ (4.14) vanishes identically

$$\frac{1}{2} \int_0^1 \dot{\mathbf{q}}(t)^\mathsf{T} \, \mathbf{G} \, \dot{\mathbf{q}}(t) \, \mathrm{d}t \longrightarrow \min_{\mathbf{q}(t), \mathbf{\Phi}_1(\mathbf{f}(\mathbf{q}(t)))=\mathbf{0}} \tag{C.1}$$

with the constant metric matrix $\mathbf{G}$ (4.23). The governing equations of the geodesic may be considered as a constrained mechanical system, see Equation (4.5). Then, the geodesic equation is derived by solving Lagrange's equations of the first kind (Hand and Finch, 2008). To shorten the expressions, we will suppress the dependence on the time

[1] This appendix is based on the Appendix B of the publication "Generating microstructures of long fiber reinforced composites by the fused sequential addition and migration method" (Lauff et al., 2024).

of the coordinate vector. For a constrained mechanical system with n holonomic constraints, the equations read

$$\frac{\mathrm{d}}{\mathrm{d}t}\frac{\partial L(\mathbf{q},\dot{\mathbf{q}},t)}{\partial \dot{\mathbf{q}}} - \frac{\partial L(\mathbf{q},\dot{\mathbf{q}},t)}{\partial \mathbf{q}} + \mathbf{R}\left(\mathbf{q},\boldsymbol{\lambda}\right) = \mathbf{0}, \tag{C.2}$$

where $\boldsymbol{\lambda} \equiv \boldsymbol{\lambda}(t)$ refers to the vector of the Lagrangian multipliers and $\mathbf{R}\left(\mathbf{q},\boldsymbol{\lambda}\right)$ corresponds to the constraint forces

$$\mathbf{R}\left(\mathbf{q},\boldsymbol{\lambda}\right) \equiv \left(\frac{\partial \boldsymbol{\Phi}_1\left(\mathbf{f}\left(\mathbf{q}\right)\right)}{\partial \mathbf{q}}\right)^{\mathsf{T}} \boldsymbol{\lambda} \equiv \mathbf{J}\left(\mathbf{q}\right)^{\mathsf{T}} \boldsymbol{\lambda}. \tag{C.3}$$

For the considered polygonal chain, the transposed Jacobian of the constraint vector $\mathbf{J}\left(\mathbf{q}\right)^{\mathsf{T}}$ in Equation (C.3) may be computed explicitly as

$$\mathbf{J}(\mathbf{q}\left(t\right))^{\mathsf{T}} = \begin{bmatrix} \mathbf{0}_{3\times 1} & \mathbf{0}_{3\times 1} & \cdots & \mathbf{0}_{3\times 1} \\ \mathbf{p}^1\left(t\right) & \mathbf{0}_{3\times 1} & \cdots & \mathbf{0}_{3\times 1} \\ \mathbf{0}_{3\times 1} & \mathbf{p}^2\left(t\right) & \cdots & \mathbf{0}_{3\times 1} \\ \vdots & \vdots & \ddots & \vdots \\ \mathbf{0}_{3\times 1} & \mathbf{0} & \cdots & \mathbf{p}^n\left(t\right) \end{bmatrix}. \tag{C.4}$$

As we consider no potential function, the Lagrangian function L in Equation (C.2) equals the kinetic energy and depends only on the first time derivative of the coordinate vector. Hence, Lagrange's equations of the first kind shorten to

$$\frac{\mathrm{d}}{\mathrm{d}t}\frac{\partial E(\dot{\mathbf{q}})}{\partial \dot{\mathbf{q}}} + \mathbf{J}\left(\mathbf{q}\right)^{\mathsf{T}} \boldsymbol{\lambda} = \mathbf{0}, \tag{C.5}$$

where the first term of Equation (C.5) computes as

$$\frac{\mathrm{d}}{\mathrm{d}t}\frac{\partial E(\dot{\mathbf{q}})}{\partial \dot{\mathbf{q}}} \equiv \frac{\mathrm{d}}{\mathrm{d}t}\frac{1}{2}\frac{\partial \dot{\mathbf{q}}^{\mathsf{T}}\,\mathbf{G}\,\dot{\mathbf{q}}}{\partial \dot{\mathbf{q}}} = \mathbf{G}\,\ddot{\mathbf{q}}. \tag{C.6}$$

Accounting for the geometric constraints (4.14) in Equation (C.5) explicitly leads us to the differential algebraic equations for the geodesics of the manifold $\mathcal{R}$ in Equation (4.26)

$$\begin{aligned} \mathbf{G}\,\ddot{\mathbf{q}} + \mathbf{J}\left(\mathbf{q}\right)^{\mathsf{T}}\boldsymbol{\lambda} &= \mathbf{0}, \\ \boldsymbol{\Phi}_1\left(\mathbf{f}\left(\mathbf{q}\right)\right) &= \mathbf{0}. \end{aligned} \tag{C.7}$$

Appendix D

Properties of the deviation from straight curve (DSC)[1]

D.1 A simple representation formula for the DSC

We demonstrate the formula (6.17)

$$K_f = 1 - \|\boldsymbol{A}_f\|^2 \tag{D.1}$$

to hold. We modify Equation (6.13) to obtain

$$\begin{aligned} K_f &= \frac{1}{L}\int_0^L \|\boldsymbol{A}_f\|^2 - 2\,\boldsymbol{A}_f \cdot (\boldsymbol{c}'(s)\otimes\boldsymbol{c}'(s)) + \|\boldsymbol{c}'(s)\otimes\boldsymbol{c}'(s)\|^2\,\mathrm{d}s \\ &= \frac{1}{L}\left(L\|\boldsymbol{A}_f\|^2 - 2\,\boldsymbol{A}_f \cdot \underbrace{\int_0^L \boldsymbol{c}'(s)\otimes\boldsymbol{c}'(s)\,\mathrm{d}s}_{L\,\boldsymbol{A}_f} + \underbrace{\int_0^L \underbrace{\|\boldsymbol{c}'(s)\otimes\boldsymbol{c}'(s)\|^2}_{1}\,\mathrm{d}s}_{L} \right) \\ &= \|\boldsymbol{A}_f\|^2 - 2\,\|\boldsymbol{A}_f\|^2 + 1 \\ &= 1 - \|\boldsymbol{A}_f\|^2. \end{aligned} \tag{D.2}$$

[1] This appendix is based on the Appendix A of the publication "On the influence of the fiber curvature on the stiffness of long fiber reinforced composites" (Lauff et al., 2025a).

D.2 Upper and lower bounds of the DSC

The purpose of this section is to establish the bounds (6.14)

$$0 \leq K_f \leq \frac{2}{3} \tag{D.3}$$

for the DSC. The lower bound is a direct consequence of the definition (6.13). For the upper bound, we use the representation (6.17)

$$K_f = 1 - \|\boldsymbol{A}_f\|^2. \tag{D.4}$$

We insert the fiber orientation tensor of second order in diagonal form (6.6), and find that the DSC may be computed with two of the three eigenvalues, e.g.,

$$K_f = 1 - \left(a_1^2 + a_2^2 + a_3^2\right) = 1 - \left(a_1^2 + a_2^2 + (1 - a_1 - a_2)^2\right). \tag{D.5}$$

The possible values attained by the DSC is determined by the fiber orientation triangle, as shown in Fig. 6.2. It turns out that the DSC takes values in the range

$$0 \leq K_f \leq \frac{2}{3}\,, \tag{D.6}$$

where the parameter is zero only if the fiber is straight and has the value $2/3$ only if the orientation state of the fiber is isotropic.

D.3 Vanishing DSC implies a straight fiber

We would like to establish the validity of the characterization (6.15)

$$K_f = 0 \quad \text{if and only if} \quad \boldsymbol{c}''(s) = \boldsymbol{0} \quad \text{for all} \quad s \in [0, L]. \tag{D.7}$$

As vanishing curvature implies that the fiber is straight, and hence the vanishing of the DSC, we restrict to showing the converse statement. So let us assume that the DSC K_f vanishes. By definition (6.13) and due to the assumed continuity of the second derivative $\boldsymbol{c}''$, the pointwise equation

$$\boldsymbol{A}_f = \boldsymbol{c}'(s) \otimes \boldsymbol{c}'(s) \quad \text{holds for all} \quad s \in [0, L]. \tag{D.8}$$

As the left hand side does not depend on the arc length parameter s, differentiating the latter equation yields

$$\mathbf{0} = \boldsymbol{c}''(s) \otimes \boldsymbol{c}'(s) + \boldsymbol{c}'(s) \otimes \boldsymbol{c}''(s) \quad \text{for all} \quad s \in [0, L]. \tag{D.9}$$

Computing the linear map of the vector $\boldsymbol{c}'(s)$ by the Equation (D.9) yields

$$\mathbf{0} = \underbrace{\boldsymbol{c}'(s) \cdot \boldsymbol{c}'(s)}_{=1}\, \boldsymbol{c}''(s) + \underbrace{\boldsymbol{c}'(s) \cdot \boldsymbol{c}''(s)}_{=0}\, \boldsymbol{c}'(s) \equiv \boldsymbol{c}''(s) \quad \text{for all} \quad s \in [0, L], \tag{D.10}$$

where we used the arc length condition (6.2) which implies that the vectors $\boldsymbol{c}''(s)$ and $\boldsymbol{c}'(s)$ are orthogonal. In particular, the curvature (6.9) vanishes, which was to be shown.

D.4 Lower bound for the average curvature

We intend to justify that the estimate (6.16)

$$K_f \leq 2\,(L\,\bar{\kappa}_f)^2 \tag{D.11}$$

holds. The latter is a direct consequence of the following Poincaré-Wirtinger inequality

$$\int_0^L \|\boldsymbol{T}(s) - \bar{\boldsymbol{T}}\|^2 \,\mathrm{d}s \leq L \left(\int_0^L \|\boldsymbol{T}'(s)\| \,\mathrm{d}s \right)^2, \tag{D.12}$$

valid for a continuously differentiable tensor-valued function $\boldsymbol{T}$ on the interval $[0, L]$ and where we denote by

$$\bar{\boldsymbol{T}} = \frac{1}{L} \int_0^L \boldsymbol{T}(s) \, \mathrm{d}s \tag{D.13}$$

the averaged tensor.
Assuming the validity of the inequality (D.12) for the moment, we apply this estimate to the tensor field

$$\boldsymbol{T}(s) = \boldsymbol{c}'(s) \otimes \boldsymbol{c}'(s), \quad s \in [0, L], \tag{D.14}$$

corresponding to a parametrized fiber (6.1). We notice

$$\bar{\boldsymbol{T}} = \boldsymbol{A}_f, \tag{D.15}$$

$$\int_0^L \|\boldsymbol{T}(s) - \bar{\boldsymbol{T}}\|^2 \, \mathrm{d}s = L \, K_f, \tag{D.16}$$

$$\boldsymbol{T}'(s) = \boldsymbol{c}''(s) \otimes \boldsymbol{c}'(s) + \boldsymbol{c}'(s) \otimes \boldsymbol{c}''(s), \quad s \in [0, L]. \tag{D.17}$$

To proceed, we compute the Frobenius norm of the derivative $\boldsymbol{T}'(s)$ explicitly, and obtain

$$\|\boldsymbol{T}'(s)\|^2 = 2(\|\boldsymbol{c}'(s)\|^2 \|\boldsymbol{c}''(s)\|^2 + (\boldsymbol{c}'(s) \cdot \boldsymbol{c}''(s))^2) \equiv 2 \, \|\boldsymbol{c}''(s)\|^2, \tag{D.18}$$

where we used the normalization condition (6.2) of a curve parametrized by arc length and the subsequent orthogonality of the vectors $\boldsymbol{c}'(s)$ and $\boldsymbol{c}''(s)$. In particular, we might express the integral on the right hand side of the inequality (D.12) in the form

$$\int_0^L \|\boldsymbol{T}'(s)\| \, \mathrm{d}s = \sqrt{2} \int_0^L \|\boldsymbol{c}''(s)\| \, \mathrm{d}s = L \, \sqrt{2} \, \bar{\kappa}_f. \tag{D.19}$$

Collecting these observations, the inequality (D.12) becomes

$$K_f \leq 2\left(L\,\bar{\kappa}_f\right)^2, \tag{D.20}$$

i.e., the desired estimate (D.11).
Thus, it remains to establish the validity of the Poincaré-Wirtinger inequality (D.12)

$$\int_0^L \|\boldsymbol{T}(s)-\bar{\boldsymbol{T}}\|^2\,\mathrm{d}s \leq L\left(\int_0^L \|\boldsymbol{T}'(s)\|\,\mathrm{d}s\right)^2, \tag{D.21}$$

which is a bit non-standard due to the L^2-norm on the left hand side and the $W^{1,1}$-norm on the right hand side.
First, we re-write the term $\boldsymbol{T}(s)-\bar{\boldsymbol{T}}$ as an integral

$$\boldsymbol{T}(s)-\bar{\boldsymbol{T}} = \boldsymbol{T}(s)-\frac{1}{L}\int_0^L \boldsymbol{T}(y)\,\mathrm{d}y = \frac{1}{L}\int_0^L \left[\boldsymbol{T}(s)-\boldsymbol{T}(y)\right]\,\mathrm{d}y. \tag{D.22}$$

In particular, the triangle inequality for integrals implies the estimate

$$\left\|\boldsymbol{T}(s)-\bar{\boldsymbol{T}}\right\| \leq \frac{1}{L}\int_0^L \|\boldsymbol{T}(s)-\boldsymbol{T}(y)\|\,\mathrm{d}y. \tag{D.23}$$

We use the fundamental theorem of calculus to express the difference $\boldsymbol{T}(s)-\boldsymbol{T}(y)$ in the form

$$\boldsymbol{T}(s)-\boldsymbol{T}(y) = \int_y^s \frac{\mathrm{d}}{\mathrm{d}z}\left[\boldsymbol{T}(z)\right]\,\mathrm{d}z = \int_y^s \boldsymbol{T}'(z)\,\mathrm{d}z, \tag{D.24}$$

which implies the estimate

$$\|\boldsymbol{T}(s)-\boldsymbol{T}(y)\| \leq \int_y^s \left\|\boldsymbol{T}'(z)\right\|\,\mathrm{d}z \leq \int_0^L \left\|\boldsymbol{T}'(z)\right\|\,\mathrm{d}z = \|\boldsymbol{T}'\|_{L^1}. \tag{D.25}$$

Inserting this finding into the inequality (D.23) yields the bound

$$\left\|\boldsymbol{T}(s) - \bar{\boldsymbol{T}}\right\| \leq \|\boldsymbol{T}'\|_{L^1} \quad s \in [0, L]. \tag{D.26}$$

Squaring and integrating yields the bound

$$\left\|\boldsymbol{T} - \bar{\boldsymbol{T}}\right\|_{L^2}^2 = \int_0^L \left\|\boldsymbol{T}(s) - \bar{\boldsymbol{T}}\right\|^2 \, \mathrm{d}s \leq L \, \|\boldsymbol{T}'\|_{L^1}^2, \tag{D.27}$$

i.e., the desired inequality (D.12) holds.

Appendix E

The emergence of the harmonic mean[1]

The goal of this section is to provide arguments for the validity of the identity (7.36)

$$\min_{\langle \boldsymbol{\varepsilon} \rangle_{[0,1]} = \bar{\boldsymbol{\varepsilon}}} \left\langle \frac{f(d)}{2}\, \boldsymbol{\varepsilon} \cdot \mathbb{C}\left[\boldsymbol{\varepsilon}\right] \right\rangle_{[0,1]} = \frac{\bar{f}(d)}{2}\, \bar{\boldsymbol{\varepsilon}} \cdot \mathbb{C}\left[\bar{\boldsymbol{\varepsilon}}\right]. \tag{E.1}$$

For this purpose, we re-write the optimization problem on the left-hand side in Lagrangian form

$$\left\langle \frac{f(d)}{2}\, \boldsymbol{\varepsilon} \cdot \mathbb{C}\left[\boldsymbol{\varepsilon}\right] \right\rangle_{[0,1]} + \boldsymbol{\lambda} \cdot \left(\langle \boldsymbol{\varepsilon} \rangle_{[0,1]} - \bar{\boldsymbol{\varepsilon}} \right) \longrightarrow \min_{\bar{\boldsymbol{\varepsilon}}} \max_{\boldsymbol{\lambda}}, \tag{E.2}$$

with a Lagrangian multiplier $\boldsymbol{\lambda} \in \mathrm{Sym}(n)$. The Karush-Kuhn-Tucker (KKT) conditions compute as

$$\begin{aligned} f(d)\, \mathbb{C}\left[\boldsymbol{\varepsilon}\right] + \boldsymbol{\lambda} &= \mathbf{0}, \\ \langle \boldsymbol{\varepsilon} \rangle_{[0,1]} - \bar{\boldsymbol{\varepsilon}} &= \mathbf{0}. \end{aligned} \tag{E.3}$$

[1] This appendix is based on the Appendix A of the publication "Numerically robust local continuum damage models with softening response via convex relaxation" (Lauff et al., 2026).

Solving the first equation explicitly for the strain field $\boldsymbol{\varepsilon}$,

$$\boldsymbol{\varepsilon} = -f(d)^{-1}\mathbb{C}^{-1}\left[\boldsymbol{\lambda}\right], \tag{E.4}$$

averaging yields the equation

$$\langle\boldsymbol{\varepsilon}\rangle_{[0,1]} = -\left\langle f(d)^{-1}\right\rangle_{[0,1]}\mathbb{C}^{-1}\left[\boldsymbol{\lambda}\right]. \tag{E.5}$$

Inserting this insight into the second equation (E.3)

$$\bar{\boldsymbol{\varepsilon}} = -\left\langle f(d)^{-1}\right\rangle_{[0,1]}\mathbb{C}^{-1}\left[\boldsymbol{\lambda}\right] \tag{E.6}$$

provides an explicit expression of the Lagrange multiplier

$$\boldsymbol{\lambda} = -\left\langle f(d)^{-1}\right\rangle_{[0,1]}^{-1}\mathbb{C}\left[\bar{\boldsymbol{\varepsilon}}\right]. \tag{E.7}$$

In particular, we arrive at the following formula for the local strain

$$\boldsymbol{\varepsilon} = f(d)^{-1}\left\langle f(d)^{-1}\right\rangle_{[0,1]}^{-1}\bar{\boldsymbol{\varepsilon}}. \tag{E.8}$$

With this result at hand, the desired identity (E.1) follows readily, as we observe

$$\begin{aligned}\left\langle \frac{f(d)}{2}\,\boldsymbol{\varepsilon}\cdot\mathbb{C}\left[\boldsymbol{\varepsilon}\right]\right\rangle_{[0,1]} &= \left\langle \frac{f(d)}{2}\,\left(f(d)^{-1}\left\langle f(d)^{-1}\right\rangle_{[0,1]}^{-1}\bar{\boldsymbol{\varepsilon}}\right)\cdot\right.\\ &\qquad\left.\mathbb{C}\left[f(d)^{-1}\left\langle f(d)^{-1}\right\rangle_{[0,1]}^{-1}\bar{\boldsymbol{\varepsilon}}\right]\right\rangle_{[0,1]}\\ &= \frac{1}{2}\left\langle f(d)\,f(d)^{-2}\right\rangle_{[0,1]}\left\langle f(d)^{-1}\right\rangle_{[0,1]}^{-2}\bar{\boldsymbol{\varepsilon}}\cdot\mathbb{C}\left[\bar{\boldsymbol{\varepsilon}}\right]\\ &= \frac{1}{2}\left\langle f(d)^{-1}\right\rangle_{[0,1]}^{-1}\bar{\boldsymbol{\varepsilon}}\cdot\mathbb{C}\left[\bar{\boldsymbol{\varepsilon}}\right].\end{aligned} \tag{E.9}$$

Appendix F

Mathematical details for the mixing formula (7.41) [1]

The purpose of this section is to show that the quantities (7.35)

$$\psi^c_{\text{cond}}(\bar{\boldsymbol{\varepsilon}}) = \min\left\{ \bar{f}(d)\,\psi_0(\bar{\boldsymbol{\varepsilon}}) + r\,\left\langle d - d^- \right\rangle_{[0,1]} \,\middle|\, d^- \le d \le d^+ \right\} \tag{F.1}$$

and (7.41)

$$\tilde{\psi}^c_{\text{cond}}(\bar{\boldsymbol{\varepsilon}}) = \min_{\phi_{\text{cost}}:[0,1]\to[0,1]} \left\langle (1-\phi^{\text{mix}}) f\left(d^-\right)^{-1} + \phi^{\text{mix}} f\left(d^+\right)^{-1} \right\rangle^{-1}_{[0,1]} \psi_0(\bar{\boldsymbol{\varepsilon}}) + r\,\left\langle \phi^{\text{mix}}\left(d^+ - d^-\right)\right\rangle_{[0,1]} \tag{F.2}$$

coincide for given piece-wise constant functions $d^{\pm} : [0,1] \to [d, d_{\max})$ which we assume to satisfy the inequalities $d^- \le d^+$ point-wise.
We will follow a sandwich strategy, i.e., we will show that both inequalities

$$\psi^c_{\text{cond}}(\bar{\boldsymbol{\varepsilon}}) \le \tilde{\psi}^c_{\text{cond}}(\bar{\boldsymbol{\varepsilon}}) \quad \text{and} \quad \tilde{\psi}^c_{\text{cond}}(\bar{\boldsymbol{\varepsilon}}) \le \psi^c_{\text{cond}}(\bar{\boldsymbol{\varepsilon}}) \tag{F.3}$$

hold for every strain $\bar{\boldsymbol{\varepsilon}} \in \text{Sym}(n_{\text{dim}})$, leading to the desired equality of the expressions (F.1) and (F.2)
We start with the "simple" case $\psi^c_{\text{cond}}(\bar{\boldsymbol{\varepsilon}}) \le \tilde{\psi}^c_{\text{cond}}(\bar{\boldsymbol{\varepsilon}})$. We assumed that

[1] This appendix is based on the Appendix B of the publication "Numerically robust local continuum damage models with softening response via convex relaxation" (Lauff et al., 2026).

the lower and upper bound functions d^- and d^+ are piece-wise constant, i.e., there is a decomposition of the interval $[0,1]$ into K disjoint intervals I_a $(a = 1, 2, \ldots, K)$ on which the functions d^- and d^+ take constant values $d_a^{\pm}$ $(a = 1, 2, \ldots, K)$. Let $\phi^{\text{mix}} : [0,1] \to [0,1]$ be fixed. We will construct a function $d : [0,1] \to \mathbb{R}_{\geq 0}$ which satisfies the constraints $d^- \leq d \leq d^+$ point-wise, together with the equality

$$\begin{aligned}\bar{f}(d)\,\psi_0(\bar{\boldsymbol{\varepsilon}}) + r\,\left\langle d - d^- \right\rangle_{[0,1]} = \Big\langle (1-\phi^{\text{mix}}) f\left(d^-\right)^{-1} + \phi^{\text{mix}}\, f\left(d^+\right)^{-1} \Big\rangle_{[0,1]}^{-1} \\ \psi_0(\bar{\boldsymbol{\varepsilon}}) + r\,\left\langle \phi^{\text{mix}}\left(d^+ - d^-\right)\right\rangle_{[0,1]}.\end{aligned} \tag{F.4}$$

Thus, as the left-hand side of Equation (F.4) is greater or equal than the minimum, we deduce the estimate

$$\begin{aligned}\psi^c_{\text{cond}}(\bar{\boldsymbol{\varepsilon}}) \leq \Big\langle (1-\phi^{\text{mix}}) f\left(d^-\right)^{-1} + \phi^{\text{mix}}\, f\left(d^+\right)^{-1} \Big\rangle_{[0,1]}^{-1}\ \psi_0(\bar{\boldsymbol{\varepsilon}}) \\ + r\,\left\langle \phi^{\text{mix}}\left(d^+ - d^-\right)\right\rangle_{[0,1]}.\end{aligned} \tag{F.5}$$

Minimizing the right-hand side w.r.t. $\phi^{\text{mix}} : [0,1] \to [0,1]$ then yields the desired inequality $\psi^c_{\text{cond}}(\bar{\boldsymbol{\varepsilon}}) \leq \tilde{\psi}^c_{\text{cond}}(\bar{\boldsymbol{\varepsilon}})$. Thus, for this direction, it remains to construct the function d following the prescribed field ϕ^{mix}. In view of the decomposition $\{I_a\}_{a=1}^K$, we observe

$$\begin{aligned}&\Big\langle (1-\phi^{\text{mix}}) f\left(d^-\right)^{-1} + \phi^{\text{mix}}\, f\left(d^+\right)^{-1} \Big\rangle_{[0,1]} \\ &= \sum_{a=1}^{K} \int_{I_a} (1-\phi^{\text{mix}}(s)) f\left(d_a^-\right)^{-1} + \phi^{\text{mix}}(s)\, f\left(d_a^+\right)^{-1}\,\mathrm{d}s \\ &= \sum_{a=1}^{K} \Big(\left(1-\phi_a^{\text{mix}}\right) f\left(d_a^-\right)^{-1} + \phi_a^{\text{mix}}\, f\left(d_a^+\right)^{-1} \Big) \int_{I_a} \mathrm{d}s\end{aligned} \tag{F.6}$$

with the means

$$\phi_a^{\text{mix}} = \int_{I_a} \phi^{\text{mix}}(s)\,\mathrm{d}s \Big/ \int_{I_a} \mathrm{d}s \in [0,1]. \tag{F.7}$$

Similarly, it holds

$$\left\langle \phi^{\text{mix}} \left(d^+ - d^-\right)\right\rangle_{[0,1]} = \sum_{a=1}^{K} \phi_a^{\text{mix}} \left(d_a^+ - d_a^-\right) \int_{I_a} \mathrm{d}s. \tag{F.8}$$

Then, the function d is constructed as follows: It takes the value d_a^- on the left $(1-\phi_a^{\text{mix}})$-portion of the interval I_a, and is defined to be d_a^+ on the remainder of the interval. Then, it is readily checked that the identities

$$\left\langle f(d)^{-1}\right\rangle_{[0,1]} = \sum_{a=1}^{K} \left(\left(1-\phi_a^{\text{mix}}\right) f\left(d_a^-\right)^{-1} + \phi_a^{\text{mix}} f\left(d_a^+\right)^{-1}\right) \int_{I_a} \mathrm{d}s \tag{F.9}$$

and

$$\left\langle d - d^-\right\rangle_{[0,1]} = \sum_{a=1}^{K} \phi_a^{\text{mix}} \left(d_a^+ - d_a^-\right) \int_{I_a} \mathrm{d}s \tag{F.10}$$

hold. In particular, the identity (F.4) is seen to be true.
The remainder of this section is devoted to establishing the validity of the converse inequality (F.3) $\tilde{\psi}^c_{\text{cond}}(\bar{\boldsymbol{\varepsilon}}) \leq \psi^c_{\text{cond}}(\bar{\boldsymbol{\varepsilon}})$. To proceed, we fix a damage field

$$d : [0,1] \to \mathbb{R}_{\geq 0} \quad \text{which respects the constraints} \quad d^- \leq d \leq d^+. \tag{F.11}$$

We will construct a field $\phi^{\text{mix}} : [0,1] \to [0,1]$, s.t. the inequality

$$\begin{aligned} &\left\langle (1-\phi^{\text{mix}}) f\left(d^-\right)^{-1} + \phi^{\text{mix}} f\left(d^+\right)^{-1}\right\rangle_{[0,1]}^{-1} \psi_0(\bar{\boldsymbol{\varepsilon}}) \\ &+ r \left\langle \phi^{\text{mix}} \left(d^+ - d^-\right)\right\rangle_{[0,1]} \\ &\leq \bar{f}(d)\, \psi_0(\bar{\boldsymbol{\varepsilon}}) + r \left\langle d - d^-\right\rangle_{[0,1]} \end{aligned} \tag{F.12}$$

holds true. Minimizing the left-hand side and using the definition (F.2), we thus obtain the estimate

$$\tilde{\psi}^c_{\text{cond}}(\bar{\boldsymbol{\varepsilon}}) \leq \bar{f}(d)\, \psi_0(\bar{\boldsymbol{\varepsilon}}) + r \left\langle d - d^-\right\rangle_{[0,1]}. \tag{F.13}$$

Then, minimizing with respect to the admissible damage fields, we are led to the desired estimate $\tilde{\psi}^c_{\text{cond}}(\bar{\varepsilon}) \leq \psi^c_{\text{cond}}(\bar{\varepsilon})$.
So, it remains to construct the field ϕ^{mix} and establish the estimate (F.12). Actually, we select the field ϕ^{mix} point-wise, so that the identity

$$d(s) = (1 - \phi^{\text{mix}}(s))\, d^-(s) + \phi^{\text{mix}}(s)\, d^+(s), \quad s \in [0,1], \tag{F.14}$$

is satisfied. Here, we use that the damage field d satisfies the constraints (F.11), s.t. each value may be represented as a convex combination (F.14). Due to the assumed convexity of the function (7.39), we are led to the inequality

$$\begin{aligned} g(d(s)) &\equiv g\left((1 - \phi^{\text{mix}}(s))\, d^-(s) + \phi^{\text{mix}}(s)\, d^+(s)\right) \\ &\leq (1 - \phi^{\text{mix}}(s))\, g\left(d^-(s)\right) + \phi^{\text{mix}}(s)\, g\left(d^+(s)\right). \end{aligned} \tag{F.15}$$

Averaging yields the estimate

$$\langle g(d) \rangle_{[0,1]} \leq \left\langle (1 - \phi^{\text{mix}})\, g(d^-) + \phi^{\text{mix}}\, g(d^+) \right\rangle_{[0,1]}, \tag{F.16}$$

or, rather, by taking inverses

$$\left\langle (1 - \phi^{\text{mix}})\, f\left(d^-\right)^{-1} + \phi^{\text{mix}}\, f\left(d^+\right)^{-1} \right\rangle^{-1}_{[0,1]} \leq \left\langle f(d)^{-1} \right\rangle^{-1}_{[0,1]} \equiv \bar{f}(d), \tag{F.17}$$

As the factor $\psi_0(\bar{\varepsilon})$ is non-negative, we are led to the estimate

$$\left\langle (1 - \phi^{\text{mix}})\, f\left(d^-\right)^{-1} + \phi^{\text{mix}}\, f\left(d^+\right)^{-1} \right\rangle^{-1}_{[0,1]} \psi_0(\bar{\varepsilon}) \leq \bar{f}(d)\, \psi_0(\bar{\varepsilon}). \tag{F.18}$$

Due to the definition (F.14), we notice

$$\begin{aligned} \left\langle d - d^- \right\rangle_{[0,1]} &= \left\langle (1 - \phi^{\text{mix}})\, d^- + \phi^{\text{mix}}\, d^+ - d^- \right\rangle_{[0,1]} \\ &= \left\langle -\phi^{\text{mix}}\, d^- + \phi^{\text{mix}}\, d^+ \right\rangle_{[0,1]} \\ &= \left\langle \phi^{\text{mix}}\, \left(d^+ - d^-\right) \right\rangle_{[0,1]}. \end{aligned} \tag{F.19}$$

In particular, multiplying by the positive factor r, the desired inequality (F.12)

$$\begin{aligned} &\left\langle (1-\phi^{\text{mix}})\, f\left(d^{-}\right)^{-1} + \phi^{\text{mix}}\, f\left(d^{+}\right)^{-1} \right\rangle_{[0,1]}^{-1} \psi_0(\bar{\varepsilon}) \\ &+ r\left\langle \phi^{\text{mix}}\, \left(d^{+} - d^{-}\right) \right\rangle_{[0,1]} \\ &\leq \bar{f}(d)\, \psi_0(\bar{\varepsilon}) + r\left\langle d - d^{-} \right\rangle_{[0,1]} \end{aligned} \tag{F.20}$$

emerges.

Appendix G

Arguments for the convexity properties of the condensed incremental energy [1]

G.1 Two-sided quadratic bounds

The purpose of this Appendix is to provide arguments for the validity of property (1) listed in Section 7.3.3, i.e., the existence of positive constants α_-, α_+ and C_+, s.t. the bounds (7.91)

$$\frac{\alpha_-}{2}\,\boldsymbol{\varepsilon}\cdot\mathbb{C}\,[\boldsymbol{\varepsilon}] \leq \psi_{\text{cond}}(\boldsymbol{\varepsilon}) \leq C_+ + \frac{\alpha_+}{2}\,\boldsymbol{\varepsilon}\cdot\mathbb{C}\,[\boldsymbol{\varepsilon}] \tag{G.1}$$

are valid for all strains $\boldsymbol{\varepsilon} \in \text{Sym}(n_{\text{dim}})$. To do so, we infer the definition of the factors g_j, see Equation (7.66)

$$g_j = f(d_j)^{-1}, \quad j = 0, 1, \ldots, N. \tag{G.2}$$

The considered degradation function f is assumed to be monotonically decreasing and the damage values d_j are increasing (7.62). Thus, by the

[1] This appendix is based on the Appendix C of the publication "Numerically robust local continuum damage models with softening response via convex relaxation" (Lauff et al., 2026).

relation (G.2), the estimates

$$f_0 \geq f_j \geq f_N, \quad j = 0, 1, \ldots, N, \tag{G.3}$$

imply the two-sided bounds

$$g_0 \leq g_j \leq g_N, \quad j = 0, 1, \ldots, N. \tag{G.4}$$

The simplex constraints (7.64)

$$\rho_j \geq 0 \quad (j = 0, 1, \ldots, N) \quad \text{and} \quad \sum_{j=0}^{N} \rho_j = 1 \tag{G.5}$$

imply the estimate

$$g_0 \leq \sum_{j=0}^{N} \rho_j \, g_j \leq g_N. \tag{G.6}$$

Consequently, we obtain the inequalities

$$\frac{1}{2g_N} \boldsymbol{\varepsilon} \cdot \mathbb{C}\,[\boldsymbol{\varepsilon}] \leq \left(\sum_{j=0}^{N} \rho_j \left(\boldsymbol{\Phi}^{\text{mix}} \right) g_j \right)^{-1} \frac{1}{2} \boldsymbol{\varepsilon} \cdot \mathbb{C}\,[\boldsymbol{\varepsilon}] \leq \frac{1}{2g_0} \boldsymbol{\varepsilon} \cdot \mathbb{C}\,[\boldsymbol{\varepsilon}]\,, \tag{G.7}$$
$$\forall\, \boldsymbol{\varepsilon} \in \text{Sym}(n_{\text{dim}}),$$

for the free energy. For the dissipation (7.70)

$$\mathcal{D}(\boldsymbol{\Phi}^{\text{mix}}) = r \sum_{j=0}^{N-1} \rho_j^k \, \phi_j^{\text{mix}} \, \triangle d_j \quad \text{with} \quad \triangle d_j = d_{j+1} - d_j > 0, \tag{G.8}$$

the bounds

$$0 \leq r \sum_{j=0}^{N-1} \rho_j^k \, \phi_j^{\text{mix}} \, \triangle d_j \leq r \sum_{j=0}^{N-1} \rho_j^k \, \triangle d_j \tag{G.9}$$

are immediate in view of the box constraints $\phi_j^{\text{mix}} \in [0,1]$. By definition of the incremental energy (7.90)

$$P\left(\boldsymbol{\varepsilon}, \boldsymbol{\Phi}^{\text{mix}}\right) = \left(\sum_{j=0}^{N} \rho_j \left(\boldsymbol{\Phi}^{\text{mix}}\right) g_j\right)^{-1} \frac{1}{2}\boldsymbol{\varepsilon} \cdot \mathbb{C}[\boldsymbol{\varepsilon}] + r \sum_{j=0}^{N-1} \rho_j^k \, \phi_j^{\text{mix}} \triangle d_j, \tag{G.10}$$

the estimates (G.7) and (G.9) imply the bound

$$\frac{1}{2g_N}\boldsymbol{\varepsilon} \cdot \mathbb{C}[\boldsymbol{\varepsilon}] \leq P\left(\boldsymbol{\varepsilon}, \boldsymbol{\Phi}^{\text{mix}}\right) \leq \frac{1}{2g_0}\boldsymbol{\varepsilon} \cdot \mathbb{C}[\boldsymbol{\varepsilon}] + r \sum_{j=0}^{N-1} \rho_j^k \triangle d_j, \tag{G.11}$$
$$\forall\, \boldsymbol{\varepsilon} \in \text{Sym}(n_{\text{dim}}).$$

As the derived bounds are independent of the variable $\boldsymbol{\Phi}^{\text{mix}}$ to be optimized, minimization w.r.t. $\boldsymbol{\Phi}^{\text{mix}} \in [0,1]^N$ leads to the desired bounds (G.1) with the constants

$$\alpha_- = \frac{1}{g_N}, \quad \alpha_+ = \frac{1}{g_0} \quad \text{and} \quad C_+ = r \sum_{j=0}^{N-1} \rho_j^k \triangle d_j. \tag{G.12}$$

G.2 Convexity of the condensed incremental energy

The purpose of this Appendix is to show that the condensed incremental energy (7.89)

$$\psi_{\text{cond}}(\boldsymbol{\varepsilon}) := \min_{\boldsymbol{\Phi}^{\text{mix}} \in [0,1]^N} P\left(\boldsymbol{\varepsilon}, \boldsymbol{\Phi}^{\text{mix}}\right), \quad \boldsymbol{\varepsilon} \in \text{Sym}(n_{\text{dim}}), \tag{G.13}$$

is a convex function of its argument. This (standard) fact follows directly from the convexity of the function P, see Equation (7.50). We provide the argument for the convenience of the reader.

The condensed incremental energy (G.13) is convex provided the inequality

$$\psi_{\text{cond}}(\lambda\,\boldsymbol{\varepsilon}_1 + (1-\lambda)\,\boldsymbol{\varepsilon}_2) \leq \lambda\,\psi_{\text{cond}}(\boldsymbol{\varepsilon}_1) + (1-\lambda)\,\psi_{\text{cond}}(\boldsymbol{\varepsilon}_2) \tag{G.14}$$

holds for all strains $\boldsymbol{\varepsilon}_1, \boldsymbol{\varepsilon}_2 \in \text{Sym}(n_{\text{dim}})$ and all $\lambda \in [0,1]$. For any two such strains, there are associated states $\boldsymbol{\phi}_1^{\text{mix}}, \boldsymbol{\phi}_2^{\text{mix}} \in [0,1]^N$ realizing the minimum (G.13), i.e., the equations

$$\psi_{\text{cond}}(\boldsymbol{\varepsilon}_i) = P(\boldsymbol{\varepsilon}_i, \boldsymbol{\phi}_i^{\text{mix}}), \quad i = 1, 2, \tag{G.15}$$

are satisfied. By the convexity of the function P, the estimate

$$\begin{aligned} P(\lambda\,\boldsymbol{\varepsilon}_1 + (1-\lambda)\,\boldsymbol{\varepsilon}_2, \lambda\,\boldsymbol{\phi}_1^{\text{mix}} + (1-\lambda)\,\boldsymbol{\phi}_2^{\text{mix}}) \leq \lambda\,P(\boldsymbol{\varepsilon}_1, \boldsymbol{\phi}_1^{\text{mix}}) \\ + (1-\lambda)\,P(\boldsymbol{\varepsilon}_2, \boldsymbol{\phi}_2^{\text{mix}}) \end{aligned} \tag{G.16}$$

holds for all parameters $\lambda \in [0,1]$. By definition (G.13), the left-hand side is not smaller than

$$\begin{aligned} \psi_{\text{cond}}(\lambda\,\boldsymbol{\varepsilon}_1 + (1-\lambda)\,\boldsymbol{\varepsilon}_2) &\equiv \min_{\boldsymbol{\phi}^{\text{mix}} \in [0,1]^N} P\left(\lambda\,\boldsymbol{\varepsilon}_1 + (1-\lambda)\,\boldsymbol{\varepsilon}_2, \boldsymbol{\phi}^{\text{mix}}\right) \\ &\leq P(\lambda\,\boldsymbol{\varepsilon}_1 + (1-\lambda)\,\boldsymbol{\varepsilon}_2, \lambda\,\boldsymbol{\phi}_1^{\text{mix}} + (1-\lambda)\,\boldsymbol{\phi}_2^{\text{mix}}), \end{aligned} \tag{G.17}$$

whereas the right-hand side may be re-written via the expressions (G.15). Thus, we obtain the desired inequality (G.14), finishing the argument.

G.3 Lack of strict convexity of the condensed incremental energy

The goal of this Appendix is to show that the condensed incremental energy (7.89)

$$\psi_{\text{cond}}(\boldsymbol{\varepsilon}) := \min_{\boldsymbol{\Phi}^{\text{mix}} \in [0,1]^N} P\left(\boldsymbol{\varepsilon}, \boldsymbol{\Phi}^{\text{mix}}\right), \quad \boldsymbol{\varepsilon} \in \text{Sym}(n_{\text{dim}}), \tag{G.18}$$

is not strictly convex, in general. For this purpose, we consider the first time step (7.43) only, where the condensed incremental energy (7.90) reduces to the form

$$\begin{aligned} &\psi_{\text{cond}}(\boldsymbol{\varepsilon}) := \min_{\phi^{\text{mix}} \in [0,1]} \frac{\psi_0(\boldsymbol{\varepsilon})}{(1-\phi^{\text{mix}})\, g_0 + \phi^{\text{mix}}\, g_1} + \phi^{\text{mix}}\, r\,(d_1 - d_0), \\ &\boldsymbol{\varepsilon} \in \text{Sym}(n_{\text{dim}}), \end{aligned} \tag{G.19}$$

with the undamaged elastic energy (7.17)

$$\psi_0(\boldsymbol{\varepsilon}) = \frac{1}{2}\, \boldsymbol{\varepsilon} \cdot \mathbb{C}\,[\boldsymbol{\varepsilon}], \quad \boldsymbol{\varepsilon} \in \text{Sym}(n_{\text{dim}}). \tag{G.20}$$

To increase readability, we introduce specific notation for this appendix only, and write

$$d_- \equiv d_0, \quad d_+ \equiv d_1, \quad g_- = g_0, \quad g_+ = g_1. \tag{G.21}$$

Thus, the expression (G.19) becomes

$$\begin{aligned} &\psi_{\text{cond}}(\boldsymbol{\varepsilon}) := \min_{\phi^{\text{mix}} \in [0,1]} \frac{\psi_0(\boldsymbol{\varepsilon})}{(1-\phi^{\text{mix}})\, g_- + \phi^{\text{mix}}\, g_+} + \phi^{\text{mix}}\, r\,(d_+ - d_-), \\ &\boldsymbol{\varepsilon} \in \text{Sym}(n_{\text{dim}}). \end{aligned} \tag{G.22}$$

The problem (G.22) is just a simple one-dimensional optimization problem, and the solution ϕ^{mix} may be computed explicitly:

$$\phi^{\text{mix}} = R_{[0,1]}\left(\frac{\sqrt{\dfrac{g_+ - g_-}{d_+ - d_-}\,\dfrac{\psi_0(\boldsymbol{\varepsilon})}{r}} - g_-}{g_+ - g_-}\right) \tag{G.23}$$

with the clipping function

$$R_{[0,1]} : \mathbb{R} \to [0,1], \quad x \mapsto \max(\min(x,1),0). \tag{G.24}$$

For strains $\boldsymbol{\varepsilon} \in \text{Sym}(n_{\text{dim}})$ with an undamaged elastic energy in the range

$$\psi_0(\boldsymbol{\varepsilon}) \in \left[r\, g_-^2\, \frac{d_+ - d_-}{g_+ - g_-}, r\, g_+^2\, \frac{d_+ - d_-}{g_+ - g_-}\right], \tag{G.25}$$

the associated volume fraction ϕ^{mix} satisfies the equation

$$\psi_0(\boldsymbol{\varepsilon})\, \frac{g_+ - g_-}{((1-\phi^{\text{mix}})\, g_- + \phi^{\text{mix}}\, g_+)^2} = r\,(d_+ - d_-), \tag{G.26}$$

which we may re-write in the form

$$(1-\phi^{\text{mix}})\, g_- + \phi^{\text{mix}}\, g_+ = \sqrt{\frac{\psi_0(\boldsymbol{\varepsilon})}{r}\,\frac{g_+ - g_-}{d_+ - d_-}}. \tag{G.27}$$

Thus, in view of the definition (G.22) and the expressions (G.23) as well as (G.26) for strains in the range (G.25), we are led to the formula

$$\begin{aligned}\psi_{\text{cond}}(\boldsymbol{\varepsilon}) &= \frac{\psi_0(\boldsymbol{\varepsilon})}{\sqrt{\dfrac{\psi_0(\boldsymbol{\varepsilon})}{r}\,\dfrac{g_+ - g_-}{d_+ - d_-}}} + r\,(d_+ - d_-)\,\frac{\sqrt{\dfrac{g_+ - g_-}{d_+ - d_-}\,\dfrac{\psi_0(\boldsymbol{\varepsilon})}{r}} - g_-}{g_+ - g_-} \\ &= 2\sqrt{r\,\frac{d_+ - d_-}{g_+ - g_-}}\,\sqrt{\psi_0(\boldsymbol{\varepsilon})} - r\,g_-\,\frac{d_+ - d_-}{g_+ - g_-},\end{aligned} \tag{G.28}$$

which we may also write in the more abstract form

$$\psi_{\text{cond}}(\boldsymbol{\varepsilon}) = A\,\sqrt{\psi_0(\boldsymbol{\varepsilon})} + B \tag{G.29}$$

for strains $\boldsymbol{\varepsilon} \in \mathrm{Sym}(n_{\text{dim}})$ satisfying the constraints (G.25) with the constants

$$A = 2\sqrt{r\,\frac{d_+ - d_-}{g_+ - g_-}} \quad \text{and} \quad B = -r\,g_-\,\frac{d_+ - d_-}{g_+ - g_-}. \tag{G.30}$$

After these preliminaries, we announce our strategy for showing the lack of strict convexity of the condensed incremental energy (G.22): We pick two different strains $\boldsymbol{\varepsilon}_1$ and $\boldsymbol{\varepsilon}_2$ obeying the constraints (G.25) and show, with the help of the representation formula (G.29), that the condensed incremental energy (G.22) is precisely linear over the interpolated strains

$$\boldsymbol{\varepsilon}(\lambda) = \lambda\,\boldsymbol{\varepsilon}_1 + (1-\lambda)\,\boldsymbol{\varepsilon}_2, \quad \lambda \in [0,1]. \tag{G.31}$$

In case of strict convexity, the values of the condensed incremental energy at interior interpolation points, $\lambda \in (0,1)$, would need to be strictly less than their linear interpolation:

$$\psi_{\text{cond}}(\boldsymbol{\varepsilon}(\lambda)) \overset{!}{<} \lambda\,\psi_{\text{cond}}(\boldsymbol{\varepsilon}_1) + (1-\lambda)\,\psi_{\text{cond}}(\boldsymbol{\varepsilon}_2), \quad 0 < \lambda < 1. \tag{G.32}$$

In particular, as soon as we show the identity

$$\psi_{\text{cond}}(\boldsymbol{\varepsilon}(\lambda)) = \lambda\,\psi_{\text{cond}}(\boldsymbol{\varepsilon}_1) + (1-\lambda)\,\psi_{\text{cond}}(\boldsymbol{\varepsilon}_2), \quad 0 < \lambda < 1, \tag{G.33}$$

strict convexity of the condensed incremental energy is ruled out.
We pick a strain $\boldsymbol{\varepsilon}_1 \in \text{Sym}(n_{\text{dim}})$ with elastic energy

$$\psi_0(\boldsymbol{\varepsilon}_1) = r\,g_-^2\,\frac{d_+ - d_-}{g_+ - g_-}, \tag{G.34}$$

and consider the rescaled strain

$$\boldsymbol{\varepsilon}_2 = M\,\boldsymbol{\varepsilon}_1 \tag{G.35}$$

with a rescaling factor $M > 1$ that we choose in such a way that the equation

$$\psi_0(\boldsymbol{\varepsilon}_2) = r\,g_+^2\,\frac{d_+ - d_-}{g_+ - g_-} \tag{G.36}$$

is satisfied, i.e., we set

$$M = \frac{g_+}{g_-}. \tag{G.37}$$

The strains are chosen to represent the boundary cases for the admissible range (G.25). As the elastic energy (G.20) scales quadratically, we observe

$$\psi_{\text{cond}}(\boldsymbol{\varepsilon}_1) = A\,\sqrt{\psi_0(\boldsymbol{\varepsilon}_1)} + B, \tag{G.38}$$

$$\psi_{\text{cond}}(\boldsymbol{\varepsilon}_2) = A\,M\sqrt{\psi_0(\boldsymbol{\varepsilon}_1)} + B, \tag{G.39}$$

$$\psi_{\text{cond}}(\boldsymbol{\varepsilon}(\lambda)) = A\,[\lambda + (1-\lambda)M]\,\sqrt{\psi_0(\boldsymbol{\varepsilon}_1)} + B, \tag{G.40}$$

where we used the expression

$$\boldsymbol{\varepsilon}(\lambda) = \lambda\,\boldsymbol{\varepsilon}_1 + (1-\lambda)\,\boldsymbol{\varepsilon}_2 = \lambda\,\boldsymbol{\varepsilon}_1 + (1-\lambda)M\,\boldsymbol{\varepsilon}_1 = [\lambda + (1-\lambda)M]\,\boldsymbol{\varepsilon}_1. \tag{G.41}$$

In particular, we observe

$$\begin{aligned}\psi_{\text{cond}}(\boldsymbol{\varepsilon}(\lambda)) &= A\,[\lambda + (1-\lambda)M]\,\sqrt{\psi_0(\boldsymbol{\varepsilon}_1)} + B \\ &= A\,\lambda\,\sqrt{\psi_0(\boldsymbol{\varepsilon}_1)} + (1-\lambda)A\,M\sqrt{\psi_0(\boldsymbol{\varepsilon}_1)} + B \\ &= \lambda\left(A\,\sqrt{\psi_0(\boldsymbol{\varepsilon}_1)} + B\right) + (1-\lambda)\left(A\,M\sqrt{\psi_0(\boldsymbol{\varepsilon}_1)} + B\right) \\ &= \lambda\,\psi_{\text{cond}}(\boldsymbol{\varepsilon}_1) + (1-\lambda)\,\psi_{\text{cond}}(\boldsymbol{\varepsilon}_2),\end{aligned} \tag{G.42}$$

which was to be shown (G.33).

G.4 Existence of minimizers to mechanical mixed boundary-value problems

The purpose of this Appendix is to provide arguments for the validity of property (3) listed in Section 7.3.3, i.e., the existence of a minimizer $\boldsymbol{u} \in H^1_D(\Omega)^{n_{\text{dim}}}$ to the problem (7.95)

$$F(\boldsymbol{u}) := \int_\Omega \psi_{\text{cond}}(\nabla^s(\boldsymbol{u}_0+\boldsymbol{u})) + \boldsymbol{f}\cdot\boldsymbol{u}\;\mathrm{d}V + \int_{\Gamma_N} \boldsymbol{t}\cdot\boldsymbol{u}\;\mathrm{d}A \longrightarrow \min_{\boldsymbol{u}\in H^1_D(\Omega)^{n_{\text{dim}}}}. \tag{G.43}$$

The key properties required for establishing the validity of this statement are the bounds (7.91)

$$c_-\,\|\boldsymbol{\varepsilon}\|^2 \le \psi_{\text{cond}}(\boldsymbol{\varepsilon}) \le C_+ + c_+\,\|\boldsymbol{\varepsilon}\|^2, \quad \boldsymbol{\varepsilon} \in \text{Sym}(n_{\text{dim}}), \tag{G.44}$$

valid with constants $c_\pm$ and C_+ independent of the strain and the convexity of the condensed incremental energy ψ_{cond}. Then, the existence of minimizers for the function F follow from standard arguments, more precisely the direct method in the calculus of variations. Let $(\boldsymbol{u}_k)$ be a minimizing sequence in $H^1_D(\Omega)^{n_{\text{dim}}}$, i.e.,

$$\lim_{k\to\infty} F(\boldsymbol{u}_k) = F^* \equiv \min_{\boldsymbol{u}\in H^1_D(\Omega)^{n_{\text{dim}}}} F(\boldsymbol{u}). \tag{G.45}$$

The lower bound (G.43) implies the inequality

$$\int_\Omega c_- \|\nabla^s(\boldsymbol{u}_0+\boldsymbol{u})\|^2 + \boldsymbol{f}\cdot\boldsymbol{u}\,\mathrm{d}V + \int_{\Gamma_N} \boldsymbol{t}\cdot\boldsymbol{u}\,\mathrm{d}A \le F(\boldsymbol{u}), \quad \boldsymbol{u}\in H^1_D(\Omega)^{n_{\mathrm{dim}}}, \tag{G.46}$$

or, put differently

$$\|\nabla^s(\boldsymbol{u}_0+\boldsymbol{u})\|^2_{H^1_D(\Omega)^{n_{\mathrm{dim}}}} \le C\left[F(\boldsymbol{u}) + \left(\|\boldsymbol{f}\|_{H_D^{-1}(\Omega)^{n_{\mathrm{dim}}}} + \|\boldsymbol{t}\|_{H_D^{-\frac{1}{2}}(\Gamma_N)^{n_{\mathrm{dim}}}}\right) \|\nabla^s(\boldsymbol{u}_0+\boldsymbol{u})\|_{H^1_D(\Omega)^{n_{\mathrm{dim}}}}\right] \tag{G.47}$$

for some constant C independent of $\boldsymbol{u}\in H^1_D(\Omega)^{n_{\mathrm{dim}}}$. As a consequence of the definition (G.45), the sequence $(\boldsymbol{u}_k)$ is uniformly bounded in $H^1_D(\Omega)^{n_{\mathrm{dim}}}$. By the weak compactness of bounded sets in Hilbert spaces, there is a limit $\boldsymbol{u}^*\in H^1_D(\Omega)^{n_{\mathrm{dim}}}$, s.t., possibly up to selecting a subsequence, the sequence $(\boldsymbol{u}_k)$ converges weakly to $\boldsymbol{u}^*$, i.e.,

$$\boldsymbol{u}_k \to \boldsymbol{u}^* \text{ strongly in } L^2(\Omega)^{n_{\mathrm{dim}}}, \tag{G.48}$$

$$\nabla\boldsymbol{u}_k \rightharpoonup \nabla\boldsymbol{u}^* \text{ weakly in } L^2(\Omega)^{n_{\mathrm{dim}}\times n_{\mathrm{dim}}}. \tag{G.49}$$

As integral functionals with convex integrands satisfying the upper bound (G.43) are weakly lower semicontinuous in L^2, see, e.g., Dacorogna (1982), we deduce

$$F(\boldsymbol{u}^*) \le \liminf_{k\to\infty} F(\boldsymbol{u}) \equiv F^* \equiv \min_{\boldsymbol{u}\in H^1_D(\Omega)^{n_{\mathrm{dim}}}} F(\boldsymbol{u}) \tag{G.50}$$

where we used the construction (G.45). In particular, $\boldsymbol{u}^*\in H^1_D(\Omega)^{n_{\mathrm{dim}}}$ represents the sought minimizer.

Bibliography

Abu Al-Rub, R. K., Voyiadjis, G. Z., 2009. Gradient-enhanced Coupled Plasticity-anisotropic Damage Model for Concrete Fracture: Computational Aspects and Applications. International Journal of Damage Mechanics 18 (2), 115–154.

Abu-Farsakh, G., Asfa, A., 2020. A unified damage model for fibrous composite laminae subject to in-plane stress-state and having multi material-nonlinearity. International Journal of Damage Mechanics 29 (9), 1329–1344.

Advani, S. G., Tucker III, C. L., 1987. The Use of Tensors to Describe and Predict Fiber Orientation in Short Fiber Composites. Journal of Rheology 31 (8), 751–784.

Advani, S. G., Tucker III, C. L., 1990. A numerical simulation of short fiber orientation in compression molding. Polymer Composites 11 (3), 164–173.

Allen, M. P., Tildesley, D. J., 2017. Computer simulation of liquids, 2nd Edition. Oxford University Press, Oxford.

Allix, O., 2013. The bounded rate concept: A framework to deal with objective failure predictions in dynamic within a local constitutive model. International Journal of Damage Mechanics 22 (6), 808–828.

Altech®, 2020. Technical Datasheet ALTECH PA6 A 1000/677.

Angeles, J., Lee, S., 1989. The modelling of holonomic mechanical systems using a natural orthogonal complement. Transactions of the Canadian Society for Mechanical Engineering 13 (4), 81–89.

Araújo, P. V., 2024. Differential geometry. Springer Nature, Cham.

Bahmani, A., Li, G., Willett, T. L., Montesano, J., 2019. Three-dimensional micromechanical assessment of bio-inspired composites with non-uniformly dispersed inclusions. Composite Structures 212, 484–499.

Bahmani, A., Nooraie, R. Y., Willett, T. L., Montesano, J., 2023. A sequential mobile packing algorithm for micromechanical assessment of heterogeneous materials. Composites Science and Technology 237, 110008.

Balzani, D., Köhler, M., Neumeier, T., Peter, M. A., Peterseim, D., 2024. Multidimensional rank-one convexification of incremental damage models at finite strains. Computational Mechanics 73 (1), 27–47.

Balzani, D., Ortiz, M., 2012. Relaxed incremental variational formulation for damage at large strains with application to fiber-reinforced materials and materials with truss-like microstructures. International Journal for Numerical Methods in Engineering 92 (6), 551–570.

Bauer, J. K., Böhlke, T., 2022a. On the dependence of orientation averaging mean field homogenization on planar fourth-order fiber orientation tensors. Mechanics of Materials 170, 104307.

Bauer, J. K., Böhlke, T., 2022b. Variety of fiber orientation tensors. Mathematics and Mechanics of Solids 27 (7), 1185–1211.

Bauer, J. K., Böhlke, T., 2023. Fiber orientation distributions based on planar fiber orientation tensors of fourth order. Mathematics and Mechanics of Solids 28 (3), 773–794.

Bauer, J. K., Schneider, M., Böhlke, T., 2023. On the Phase Space of Fourth-Order Fiber-Orientation Tensors. Journal of Elasticity 153 (2), 161–184.

Bay, R. S., Tucker III, C. L., 1992a. Fiber orientation in simple injection moldings. Part I: Theory and numerical methods. Polymer Composites 13 (4), 317–331.

Bay, R. S., Tucker III, C. L., 1992b. Fiber orientation in simple injection moldings. Part II: Experimental results. Polymer Composites 13 (4), 332–341.

Bažant, Z. P., Jirásek, M., 2002. Nonlocal Integral Formulations of Plasticity and Damage: Survey of Progress. Journal of Engineering Mechanics 128 (11), 1119–1149.

Bernasconi, A., Cosmi, F., Dreossi, D., 2008. Local anisotropy analysis of injection moulded fibre reinforced polymer composites. Composites Science and Technology 68 (12), 2574–2581.

Bernasconi, A., Cosmi, F., Hine, P. J., 2012. Analysis of fibre orientation distribution in short fibre reinforced polymers: A comparison between optical and tomographic methods. Composites Science and Technology 72 (16), 2002–2008.

Bertram, A., 2021. Elasticity and Plasticity of Large Deformations: Including Gradient Materials. Springer International Publishing, Cham.

Betsch, P., 2005. The discrete null space method for the energy consistent integration of constrained mechanical systems: Part I: Holonomic constraints. Computer Methods in Applied Mechanics and Engineering 194 (50-52), 5159–5190.

Biot, M. A., 1965. Mechanics of Incremental Deformations. Wiley, New York.

Blarr, J., Sabiston, T., Krauß, C., Bauer, J. K., Liebig, W. V., Inal, K., Weidenmann, K. A., 2023. Implementation and comparison of algebraic and machine learning based tensor interpolation methods applied to fiber orientation tensor fields obtained from CT images. Computational Materials Science 228, 112286.

Böhlke, T., Brüggemann, C., 2001. Graphical representation of the generalized Hooke's law. Technische Mechanik 21 (2), 145–158.

Böhlke, T., Henning, F., Hrymak, A., Kärger, L., Weidenmann, K. A., Wood, J. T., 2019. Continuous–Discontinuous Fiber-Reinforced Polymers: An Integrated Engineering Approach. Carl Hanser Verlag, München.

Böhm, H. J., Eckschlager, A., Han, W., 2002. Multi-inclusion unit cell models for metal matrix composites with randomly oriented discontinuous reinforcements. Computational Materials Science 25 (1-2), 42–53.

Bondy, M., Pinter, P., Altenhof, W., 2017. Experimental characterization and modelling of the elastic properties of direct compounded compression molded carbon fibre/polyamide 6 long fibre thermoplastic. Materials & Design 122, 184–196.

Bourgogne, Q. C. P., 2024. Influence of fibre curvature and orientation on the mechanical properties of injected irregular short hemp fibres reinforced polypropylene. Journal of Thermoplastic Composite Materials 37 (9), 2963–2986.

Bourgogne, Q. C. P., Bouchart, V., Chevrier, P., Dattoli, E., 2021. Numerical investigation of the fiber/matrix inter-phase damage of a PPS composite considering temperature and cooling liquid ageing. SN Applied Sciences 3 (1), 132.

Boyd, S. P., Vandenberghe, L., 2009. Convex optimization, 7th Edition. Cambridge University Press, Cambridge.

Braides, A., 1985. Homogenization of some almost periodic coercive functional. Rendiconti della Accademia Nazionale delle Scienze Detta Dei XL 103, 313–322.

Brepols, T., Wulfinghoff, S., Reese, S., 2017. Gradient-extended two-surface damage-plasticity: Micromorphic formulation and numerical aspects. International Journal of Plasticity 97, 64–106.

Breuer, K., Spickenheuer, A., Stommel, M., 2021. Statistical Analysis of Mechanical Stressing in Short Fiber Reinforced Composites by Means of Statistical and Representative Volume Elements. Fibers 9 (5), 32.

Breuer, K., Stommel, M., 2019. RVE modelling of short fiber reinforced thermoplastics with discrete fiber orientation and fiber length distribution. SN Applied Sciences 2 (91).

Breuer, K., Stommel, M., Korte, W., 2019. Analysis and Evaluation of Fiber Orientation Reconstruction Methods. Journal of Composites Science 3 (3), 67.

Brisard, S., Dormieux, L., 2012. Combining Galerkin approximation techniques with the principle of Hashin and Shtrikman to derive a new FFT-based numerical method for the homogenization of composites. Computer Methods in Applied Mechanics and Engineering 217–220, 197–212.

Brünig, M., Michalski, A., 2017. A stress-state-dependent continuum damage model for concrete based on irreversible thermodynamics. International Journal of Plasticity 90, 31–43.

Brünig, M., Ricci, S., 2005. Nonlocal continuum theory of anisotropically damaged metals. International Journal of Plasticity 21 (7), 1346–1382.

Carathéodory, C., 1911. Über den Variabilitätsbereich der Fourier'schen Konstanten von positiven harmonischen Funktionen. Rendiconti del Circolo Matematico di Palermo 32 (1), 193–217.

Carstensen, C., Hackl, K., Mielke, A., 2002. Non–convex potentials and microstructures in finite–strain plasticity. Proceedings of the Royal Society of London. Series A: Mathematical, Physical and Engineering Sciences 458 (2018), 299–317.

Cender, T. A., Simacek, P., Gillespie, J. W., Advani, S. G., 2024. Microstructural evolution of highly aligned discontinuous fiber composites during longitudinal extension in forming. Composites Science and Technology 254, 110649.

Chaboche, J.-L., 1981. Continuous damage mechanics – A tool to describe phenomena before crack initiation. Nuclear Engineering and Design 64 (2), 233–247.

Chaboche, J.-L., 1988. Continuum Damage Mechanics: Part I – General Concepts. Journal of Applied Mechanics 55 (1), 59–64.

Chaboche, J.-L., 1993. Development of Continuum Damage Mechanics for Elastic Solids Sustaining Anisotropic and Unilateral Damage. International Journal of Damage Mechanics 2 (4), 311–329.

Chaubal, C. V., Leal, L. G., 1998. A closure approximation for liquid-crystalline polymer models based on parametric density estimation. Journal of Rheology 42 (1), 177–201.

Chen, L., Gu, B., Zhou, J., Tao, J., 2019. Study of the Effectiveness of the RVEs for Random Short Fiber Reinforced Elastomer Composites. Fibers and Polymers 20 (7), 1467–1479.

Chow, C. L., Wang, J., 1987. An anisotropic theory of elasticity for continuum damage mechanics. International Journal of Fracture 33 (1), 3–16.

Christ, N., Scheuring, B. M., Schelleis, C., Liebig, W. V., Montesano, J., Weidenmann, K. A., Hohe, J., 2024. Characterization and Simulation of the Interface between a Continuous and Discontinuous Carbon Fiber Reinforced Thermoplastic by Using the Climbing Drum Peel Test Considering Humidity. Polymers 16 (7), 976.

Cintra, J. S., Tucker III, C. L., 1995. Orthotropic closure approximations for flow-induced fiber orientation. Journal of Rheology 39 (6), 1095–1122.

Coleman, B. D., Noll, W., 1963. The thermodynamics of elastic materials with heat conduction and viscosity. Archive for Rational Mechanics and Analysis 13 (1), 167–178.

Corbridge, D. M., Harper, L. T., De Focatiis, D. S. A., Warrior, N. A., 2017. Compression moulding of composites with hybrid fibre architectures. Composites Part A: Applied Science and Manufacturing 95, 87–99.

Cowin, S. C., 1985. The relationship between the elasticity tensor and the fabric tensor. Mechanics of Materials 4 (2), 137–147.

Dacorogna, B., 1982. Quasiconvexity and relaxation of nonconvex problems in the calculus of variations. Journal of Functional Analysis 46 (1), 102–118.

Dacorogna, B., 2008. Direct Methods in the Calculus of Variations, 2nd Edition. No. 78 in Applied Mathematical Sciences. Springer Science+Business Media, Luxemburg.

Dai, T., Wei, Y., Tao, C., Huang, J., 2023. Mechanical model of stiffness coefficients prediction of curved fiber reinforced composites considering fiber distribution and aggregation. Composite Structures 321, 117277.

De Borst, R., Sluys, L. J., Muhlhaus, H.-B., Pamin, J., 1993. Fundamental issues in finite element analyses of localization of deformation. Engineering Computations 10 (2), 99–121.

De Paiva, R. F., Bisiaux, M., Lynch, J., Rosenberg, E., 1996. High resolution x-ray tomography in an electron microprobe. Review of Scientific Instruments 67 (6), 2251–2256.

Deiters, U. K., 2013. Efficient Coding of the Minimum Image Convention. Zeitschrift für Physikalische Chemie 227 (2-3), 345–352.

Dey, A. P., Welschinger, F., Schneider, M., Köbler, J., Böhlke, T., 2024. On the effectiveness of deep material networks for the multi-scale virtual characterization of short fiber-reinforced thermoplastics under highly nonlinear load cases. Archive of Applied Mechanics 94 (5), 1177–1202.

Dimitrijevic, B. J., Hackl, K., 2011. A regularization framework for damage-plasticity models via gradient enhancement of the free energy. International Journal for Numerical Methods in Biomedical Engineering 27 (8), 1199–1210.

Dirrenberger, J., Forest, S., Jeulin, D., 2014. Towards gigantic RVE sizes for 3D stochastic fibrous networks. International Journal of Solids and Structures 51 (2), 359–376.

Do Carmo, M. P., 1992. Riemannian Geometry. Birkhäuser, Basel.

Doghri, I., Brassart, L., Adam, L., Gérard, J.-S., 2011. A second-moment incremental formulation for the mean-field homogenization of elasto-plastic composites. International Journal of Plasticity 27 (3), 352–371.

DOMO, 2025. Technical Datasheet TECHNYL® LITE C130 C60.

DOW® Chemical Company, 2003. C711–70RNA polypropylene resin. Product information.

Dray, D., Gilormini, P., Régnier, G., 2007. Comparison of several closure approximations for evaluating the thermoelastic properties of an injection molded short-fiber composite. Composites Science and Technology 67 (7-8), 1601–1610.

Drugan, W. J., Willis, J. R., 1996. A micromechanics-based nonlocal constitutive equation and estimates of representative volume element size for elastic composites. Journal of the Mechanics and Physics of Solids 44 (4), 497–524.

Dubé, J.-F., Pijaudier-Cabot, G., Borderie, C. L., 1996. Rate Dependent Damage Model for Concrete in Dynamics. Journal of Engineering Mechanics 122 (10), 939–947.

Duschlbauer, D., Böhm, H. J., Pettermann, H. E., 2006. Computational Simulation of Composites Reinforced by Planar Random Fibers: Homogenization and Localization by Unit Cell and Mean Field Approaches. Journal of Composite Materials 40 (24), 2217–2234.

Elmasry, A., Azoti, W., El-Safty, S. A., Elmarakbi, A., 2023. A comparative review of multiscale models for effective properties of nano- and micro-composites. Progress in Materials Science 132, 101022.

Ernesti, F., Schneider, M., 2021. A fast Fourier transform based method for computing the effective crack energy of a heterogeneous material on a combinatorially consistent grid. International Journal for Numerical Methods in Engineering 122 (21), 6283–6307.

Ernesti, F., Schneider, M., 2022. Computing the effective crack energy of heterogeneous and anisotropic microstructures via anisotropic minimal surfaces. Computational Mechanics 69 (1), 45–57.

Ernesti, F., Schneider, M., 2023. Accounting for weak interfaces in computing the effective crack energy of heterogeneous materials using the composite voxel technique. Archive of Applied Mechanics 93 (10), 3983–4008.

Evans, K. E., Gibson, A. G., 1986. Prediction of the maximum packing fraction achievable in randomly oriented short-fibre composites. Composites Science and Technology 25 (2), 149–162.

Feder, J., 1980. Random sequential adsorption. Journal of Theoretical Biology 87 (2), 237–254.

Feyel, F., 1999. Multiscale FE2 elastoviscoplastic analysis of composite structures. Computational Materials Science 16 (1-4), 344–354.

Feyel, F., 2003. A multilevel finite element method (FE2) to describe the response of highly non-linear structures using generalized continua. Computer Methods in Applied Mechanics and Engineering 192 (28-30), 3233–3244.

Feyel, F., Chaboche, J.-L., 2000. FE2 multiscale approach for modelling the elastoviscoplastic behaviour of long fibre SiC/Ti composite materials. Computer Methods in Applied Mechanics and Engineering 183 (3-4), 309–330.

Fiedler, B., Holst, S., Hobbiebrunken, T., Hojo, M., Schulte, K., 2004. Modelling of the Initial Failure of CFRP Structures by Partial Discretisation: A micro / Macro-Mechanical Approach of First Ply Failure. Advanced Composites Letters 13 (5), 219–226.

Fish, J., Wagner, G. J., Keten, S., 2021. Mesoscopic and multiscale modelling in materials. Nature Materials 20 (6), 774–786.

Fitoussi, J., Bourgeois, N., Guo, G., Baptiste, D., 1996. Prediction of the anisotropic damaged behavior of composite materials: introduction of multilocal failure criteria in a micro-macro relationship. Computational Materials Science 5 (1-3), 87–100.

Fliegener, S., Luke, M., Gumbsch, P., 2014. 3D microstructure modeling of long fiber reinforced thermoplastics. Composites Science and Technology 104, 136–145.

Folgar, F., Tucker III, C. L., 1984. Orientation Behavior of Fibers in Concentrated Suspensions. Journal of Reinforced Plastics and Composites 3 (2), 98–119.

Fonseca, I., Kinderlehrer, D., Pedregal, P., 1994. Energy functional depending on elastic strain and chemical composition. Calculus of Variations and Partial Differential Equations 2 (3), 283–313.

Forest, S., Lorentz, E., 2004. Localization phenomena and regularization methods. In: Local approach to fracture. École des Mines de Paris, Paris, pp. 311–371.

Francfort, G. A., Garroni, A., 2006. A Variational View of Partial Brittle Damage Evolution. Archive for Rational Mechanics and Analysis 182 (1), 125–152.

Francfort, G. A., Marigo, J.-J., 1993. Stable damage evolution in a brittle continuous medium. Europian Journal of Mechanics A/Solids 12 (2), 149–189.

Friedrich, H. E. (Ed.), 2017. Leichtbau in der Fahrzeugtechnik, 2nd Edition. Springer Vieweg, Wiesbaden.

Fu, S.-Y., Yue, C.-Y., Hu, X., Mai, Y.-W., 1999. Effects of fiber length and orientation distributions on the mechanical properties of short-fiber-reinforced polymers. A review. Materials Science Research International 5 (2), 74–83.

Fuchs, E., Field, F., Roth, R., Kirchain, R., 2008. Strategic materials selection in the automobile body: Economic opportunities for polymer composite design. Composites Science and Technology 68 (9), 1989–2002.

García, A. G., 2015. Random packings via mechanical contraction. Universiteit Utrecht, Utrecht.

Garesci, F., Fliegener, S., 2013. Young's modulus prediction of long fiber reinforced thermoplastics. Composites Science and Technology 85, 142–147.

Germain, P., Nguyen, Q. S., Suquet, P., 1983. Continuum Thermodynamics. Journal of Applied Mechanics 50 (4b), 1010–1020.

Gitman, I. M., Askes, H., Sluys, L. J., 2007. Representative volume: Existence and size determination. Engineering Fracture Mechanics 74 (16), 2518–2534.

Gloria, A., Otto, F., 2011. An optimal variance estimate in stochastic homogenization of discrete elliptic equations. The Annals of Probability 39 (3), 779–856.

Gonzalez, O., 1996. Time integration and discrete Hamiltonian systems. Journal of Nonlinear Science 6 (5), 449–467.

Gonzalez, O., 1999. Mechanical systems subject to holonomic constraints: Differential–algebraic formulations and conservative integration. Physica D: Nonlinear Phenomena 132 (1-2), 165–174.

Goodman, A. W., Goodman, G., 1969. Generalizations of the Theorems of Pappus. The American Mathematical Monthly 76 (4), 355–366.

Görthofer, J., Meyer, N., Pallicity, T. D., Schöttl, L., Trauth, A., Schemmann, M., Hohberg, M., Pinter, P., Elsner, P., Henning, F., Hrymak, A., Seelig, T., Weidenmann, K. A., Kärger, L., Böhlke, T., 2019. Virtual process chain of sheet molding compound: Development, validation and perspectives. Composites Part B: Engineering 169, 133–147.

Görthofer, J., Schneider, M., Hrymak, A., Böhlke, T., 2022. A convex anisotropic damage model based on the compliance tensor. International Journal of Damage Mechanics 31 (1), 43–86.

Görthofer, J., Schneider, M., Ospald, F., Hrymak, A., Böhlke, T., 2020. Computational homogenization of sheet molding compound composites based on high fidelity representative volume elements. Computational Materials Science 174, 109456.

Gross, D., Seelig, T., 2018. Fracture Mechanics: With an Introduction to Micromechanics. Mechanical Engineering Series. Springer International Publishing, Cham.

Guo, G., Fitoussi, J., Baptiste, D., Sicot, N., Wolff, C., 1997. Modelling of Damage Behaviour of a Short-Fiber Reinforced Composite Structure by the Finite Element Analysis Using a Micro-Macro Law. International Journal of Damage Mechanics 6 (3), 278–299.

Halphen, B., Nguyen, Q. S., 1975. Sur les matériaux standard généralisés. Journal de Mécanique 14 (1), 39–63.

Hammersley, J. M., Handscomb, D. C., 1964. Monte Carlo Methods. Chapman & Hall, London.

Hand, L. N., Finch, J. D., 2008. Analytical mechanics, 7th Edition. Cambridge University Press, Cambridge.

Hanhan, I., Sangid, M. D., 2021. Damage propagation in short fiber thermoplastic composites analyzed through coupled 3D experiments and simulations. Composites Part B: Engineering 218, 108931.

Hansen, N. R., Schreyer, H. L., 1994. A thermodynamically consistent framework for theories of elastoplasticity coupled with damage. International Journal of Solids and Structures 31 (3), 359–389.

Hartmann, S., Liese, T., 2021. Measures describing curvilinear short fiber distributions. Archive of Applied Mechanics 91 (2), 673–685.

Haupt, P., 2002. Continuum Mechanics and Theory of Materials. Advanced Texts in Physics. Springer, Berlin, Heidelberg.

Hessman, P. A., Riedel, T. A., Welschinger, F., Hornberger, K., Böhlke, T., 2019. Microstructural analysis of short glass fiber reinforced thermoplastics based on x-ray micro-computed tomography. Composites Science and Technology 183, 107752.

Hessman, P. A., Welschinger, F., Hornberger, K., Böhlke, T., 2021. On mean field homogenization schemes for short fiber reinforced composites: Unified formulation, application and benchmark. International Journal of Solids and Structures 230–231, 111141.

Hill, R., 1963. Elastic properties of reinforced solids: Some theoretical principles. Journal of the Mechanics and Physics of Solids 11 (5), 357–372.

Hill, R., 1968. On constitutive inequalities for simple materials—I. Journal of the Mechanics and Physics of Solids 16 (4), 229–242.

Hossain, M., Hsueh, C.-J., Bourdin, B., Bhattacharya, K., 2014. Effective toughness of heterogeneous media. Journal of the Mechanics and Physics of Solids 71, 15–32.

Iorga, L., Pan, Y., Pelegri, A. A., 2008. Numerical characterization of material elastic properties for random fiber composites. Journal of Mechanics of Materials and Structures 3 (7), 1279–1298.

Ito, K., 2008. Lagrange multiplier approach to variational problems and applications. No. 15 in Advances in Design and Control. Society for Industrial and Applied Mathematics (SIAM), Philadelphia.

Jeulin, D., 2016. Power Laws Variance Scaling of Boolean Random Varieties. Methodology and Computing in Applied Probability 18 (4), 1065–1079.

Ju, J. W., Wu, Y., 2016. Stochastic micromechanical damage modeling of progressive fiber breakage for longitudinal fiber-reinforced composites. International Journal of Damage Mechanics 25 (2), 203–227.

Kachanov, L. M., 1999. Rupture Time Under Creep Conditions. International Journal of Fracture 97 (1-4), 11–18.

Kanatani, K.-I., 1984. Distribution of directional data and fabric tensors. International Journal of Engineering Science 22 (2), 149–164.

Kanit, T., Forest, S., Galliet, I., Mounoury, V., Jeulin, D., 2003. Determination of the size of the representative volume element for random composites: statistical and numerical approach. International Journal of Solids and Structures 40 (13-14), 3647–3679.

Kantorovich, L. V., 2006. On the Translocation of Masses. Journal of Mathematical Sciences 133 (4), 1381–1382.

Karl, T., Gatti, D., Frohnapfel, B., Böhlke, T., 2021. Asymptotic fiber orientation states of the quadratically closed Folgar–Tucker equation and a subsequent closure improvement. Journal of Rheology 65 (5), 999–1022.

Karl, T., Schneider, M., Böhlke, T., 2023. On fully symmetric implicit closure approximations for fiber orientation tensors. Journal of Non-Newtonian Fluid Mechanics 318, 105049.

Kehrer, L., Keursten, J., Hirschberg, V., Böhlke, T., 2023. Dynamic mechanical analysis of PA 6 under hydrothermal influences and viscoelastic material modeling. Journal of Thermoplastic Composite Materials 36 (11), 4630–4664.

Kennedy, P., Zheng, R., 2013. Flow analysis of injection molds, 2nd Edition. Carl Hanser Verlag, München.

Knops, M., Puck, A., 2008. Analysis of failure in fiber polymer laminates: the theory of Alfred Puck. Springer, Berlin.

Köbler, J., Magino, N., Andrä, H., Welschinger, F., Müller, R., Schneider, M., 2021. A computational multi-scale model for the stiffness degradation of short-fiber reinforced plastics subjected to fatigue loading. Computer Methods in Applied Mechanics and Engineering 373, 113522.

Kochmann, J., Wulfinghoff, S., Reese, S., Mianroodi, J. R., Svendsen, B., 2016. Two-scale FE–FFT- and phase-field-based computational modeling of bulk microstructural evolution and macroscopic material behavior. Computer Methods in Applied Mechanics and Engineering 305, 89–110.

Köhler, M., Balzani, D., 2023. Evolving microstructures in relaxed continuum damage mechanics for the modeling of strain softening. Journal of the Mechanics and Physics of Solids 173, 105199.

Köhler, M., Neumeier, T., Peter, M. A., Peterseim, D., Balzani, D., 2024. Hierarchical rank-one sequence convexification for the relaxation of variational problems with microstructures. Computer Methods in Applied Mechanics and Engineering 432, 117321.

Kozlov, S. M., 1979. Averaging of differential operators with almost periodic rapidly oscillating coefficients. Mathematics of the USSR-Sbornik 35 (4), 481–498.

Krajcinovic, D., 1989. Damage mechanics. Mechanics of Materials 8 (2-3), 117–197.

Krause, M., Hausherr, J. M., Burgeth, B., Herrmann, C., Krenkel, W., 2010. Determination of the fibre orientation in composites using the structure tensor and local X-ray transform. Journal of Materials Science 45 (4), 888–896.

Krause, W., Henning, F., Tröster, S., Geiger, O., Eyerer, P., 2003. LFT-D - A Process Technology for Large Scale Production of Fiber Reinforced Thermoplastic Components. Journal of Thermoplastic Composite Materials 16 (4), 289–302.

Kugler, S. K., Kech, A., Cruz, C., Osswald, T., 2020. Fiber Orientation Predictions—A Review of Existing Models. Journal of Composites Science 4 (2), 69.

Kuhn, C., Walter, I., Taeger, O., Osswald, T. A., 2017. Experimental and Numerical Analysis of Fiber Matrix Separation during Compression Molding of Long Fiber Reinforced Thermoplastics. Journal of Composites Science 1 (1), 1–16.

Kumar, A., DasGupta, A., Jain, A., 2024. Microstructure generation algorithm and micromechanics of curved fiber composites with random waviness. International Journal of Solids and Structures 289, 112625.

Lahellec, N., Suquet, P., 2007. On the effective behavior of nonlinear inelastic composites: I. Incremental variational principles. Journal of the Mechanics and Physics of Solids 55 (9), 1932–1963.

Lauff, C., Krause, M., Schneider, M., Böhlke, T., 2025a. On the Influence of the Fiber Curvature on the Stiffness of Long Fiber Reinforced Composites. International Journal for Numerical Methods in Engineering 126 (15), e70094.

Lauff, C., Schneider, M., Böhlke, T., 2025b. Microstructure generation of long fiber reinforced hybrid composites using the fused sequential addition and migration method. Journal of Thermoplastic Composite Materials 38 (8), 2855–2893.

Lauff, C., Schneider, M., Böhlke, T., 2026. Numerically robust local continuum damage models with softening response via convex relaxation. Computer Methods in Applied Mechanics and Engineering 452, 118759.

Lauff, C., Schneider, M., Montesano, J., Böhlke, T., 2023. An orientation corrected shaking method for the microstructure generation of short fiber-reinforced composites with almost planar fiber orientation. Composite Structures 322, 117352.

Lauff, C., Schneider, M., Montesano, J., Böhlke, T., 2024. Generating microstructures of long fiber reinforced composites by the fused sequential addition and migration method. International Journal for Numerical Methods in Engineering 125 (22), e7573.

Le Dret, H., Raoult, A., 2000. Variational Convergence for Nonlinear Shell Models with Directors and Related Semicontinuity and Relaxation Results. Archive for Rational Mechanics and Analysis 154 (2), 101–134.

Lemaitre, J., 1985. A Continuous Damage Mechanics Model for Ductile Fracture. Journal of Engineering Materials and Technology 107 (1), 83–89.

Lemaitre, J., 1986. Local approach of fracture. Engineering Fracture Mechanics 25 (5-6), 523–537.

Lemaitre, J., 1996. A Course on Damage Mechanics, 2nd Edition. Springer, Berlin.

Li, G., Tang, C.-A., 2015. A statistical meso-damage mechanical method for modeling trans-scale progressive failure process of rock. International Journal of Rock Mechanics and Mining Sciences 74, 133–150.

Li, W.-S., Wu, J.-Y., 2018. A consistent and efficient localized damage model for concrete. International Journal of Damage Mechanics 27 (4), 541–567.

Li, X., Qu, X., Qi, C., Shao, Z., 2020. An analytical model of multi-stress drops triggered by localized microcrack damage in brittle rocks during progressive failure. International Journal of Damage Mechanics 29 (9), 1345–1360.

Li, Z., Liu, Z., Xue, Y., Zhu, P., 2022. A novel algorithm for significantly increasing the fiber volume fraction in the reconstruction model with large fiber aspect ratio. Journal of Industrial Textiles 51 (1), 506–530.

Liu, D., He, M., Cai, M., 2018. A damage model for modeling the complete stress–strain relations of brittle rocks under uniaxial compression. International Journal of Damage Mechanics 27 (7), 1000–1019.

Liu, I.-S., 2002. Continuum mechanics. Advanced texts in physics. Springer, Berlin, Heidelberg.

Liu, W. K., Hao, S., Belytschko, T., Li, S., Chang, C. T., 1999. Multiple scale meshfree methods for damage fracture and localization. Computational Materials Science 16 (1-4), 197–205.

Liu, Y., Sun, B., Guo, T., Li, Z., 2025. Multiscale damage analysis of engineering structures from material level to structural level: a systematic review. International Journal of Structural Integrity 16 (2), 275–310.

Lorentz, E., Andrieux, S., 2003. Analysis of non-local models through energetic formulations. International Journal of Solids and Structures 40 (12), 2905–2936.

Magino, N., Köbler, J., Andrä, H., Welschinger, F., Müller, R., Schneider, M., 2022a. A multiscale high-cycle fatigue-damage model for the stiffness degradation of fiber-reinforced materials based on a mixed variational framework. Computer Methods in Applied Mechanics and Engineering 388, 114198.

Magino, N., Köbler, J., Andrä, H., Welschinger, F., Müller, R., Schneider, M., 2022b. A space-time upscaling technique for modeling high-cycle fatigue-damage of short-fiber reinforced composites. Composites Science and Technology 222, 109340.

Magino, N., Köbler, J., Andrä, H., Welschinger, F., Müller, R., Schneider, M., 2023. Accounting for viscoelastic effects in a multiscale fatigue model for the degradation of the dynamic stiffness of short-fiber reinforced thermoplastics. Computational Mechanics 71 (3), 493–515.

Marsden, J. E., Hughes, T. J. R., 2012. Mathematical Foundations of Elasticity. Dover Civil and Mechanical Engineering. Dover Publications, Newburyport.

Matouš, K., Geers, M. G. D., Kouznetsova, V. G., Gillman, A., 2017. A review of predictive nonlinear theories for multiscale modeling of heterogeneous materials. Journal of Computational Physics 330, 192–220.

Mehta, A., Schneider, M., 2022. A sequential addition and migration method for generating microstructures of short fibers with prescribed length distribution. Computational Mechanics 70 (4), 829–851.

Mehta, A., Schneider, M., 2024. A maximum-entropy length-orientation closure for short-fiber reinforced composites. Computational Mechanics 74 (3), 615–640.

Melchior, J., Köhler, M., Balzani, D., 2026. Variationally consistent microstructure evolution and microsphere-based reconvexification for damage with application to arterial tissues. Mechanics of Materials 212, 105495.

Menzel, A., 2020. Continuum Damage Mechanics – Modelling and Simulation. In: Constitutive Modelling of Solid Continua. Vol. 262. Springer International Publishing, Cham, pp. 231–256.

Meyer, C., 2000. Matrix Analysis and Applied Linear Algebra Book with Solutions. Society for Industrial and Applied Mathematics (SIAM), Philadelphia.

Meyer, N., Gajek, S., Görthofer, J., Hrymak, A., Kärger, L., Henning, F., Schneider, M., Böhlke, T., 2023. A probabilistic virtual process chain to quantify process-induced uncertainties in Sheet Molding Compounds. Composites Part B: Engineering 249, 110380.

Meyer, N., Schöttl, L., Bretz, L., Hrymak, A. N., Kärger, L., 2020. Direct Bundle Simulation approach for the compression molding process of Sheet Molding Compound. Composites Part A: Applied Science and Manufacturing 132, 105809.

Michel, J.-C., Suquet, P., 2022. Merits and limits of a variational definition of the effective toughness of heterogeneous materials. Journal of the Mechanics and Physics of Solids 164, 104889.

Miehe, C., 2002. Strain-driven homogenization of inelastic microstructures and composites based on an incremental variational formulation. International Journal for Numerical Methods in Engineering 55 (11), 1285–1322.

Mielke, A., Roubíček, T., 2015. Rate-Independent Systems: Theory and Application. Vol. 193 of Applied Mathematical Sciences. Springer New York, New York, NY.

Mittelstedt, C., 2025. Engineering mechanics 3: dynamics. Springer, Berlin.

Montgomery-Smith, S., He, W., Jack, D. A., Smith, D. E., 2011a. Exact tensor closures for the three-dimensional Jeffery's equation. Journal of Fluid Mechanics 680, 321–335.

Montgomery-Smith, S., Jack, D. A., Smith, D. E., 2011b. The Fast Exact Closure for Jeffery's equation with diffusion. Journal of Non-Newtonian Fluid Mechanics 166 (7-8), 343–353.

Morrey, C. B., 1952. Quasi-convexity and the lower semicontinuity of multiple integrals. Pacific Journal of Mathematics 2 (1), 25–53.

Moulinec, H., Suquet, P., 1994. A fast numerical method for computing the linear and nonlinear mechanical properties of composites. Comptes Rendus de l'Académie des Sciences. Série II 318 (11), 1417–1423.

Moulinec, H., Suquet, P., 1998. A numerical method for computing the overall response of nonlinear composites with complex microstructure. Computer Methods in Applied Mechanics and Engineering 157 (1-2), 69–94.

Müller, S., 1987. Homogenization of nonconvex integral functionals and cellular elastic materials. Archive for Rational Mechanics and Analysis 99 (3), 189–212.

Müller, V., Böhlke, T., 2016. Prediction of effective elastic properties of fiber reinforced composites using fiber orientation tensors. Composites Science and Technology 130, 36–45.

Müller, V., Kabel, M., Andrä, H., Böhlke, T., 2015. Homogenization of linear elastic properties of short-fiber reinforced composites – A comparison of mean field and voxel-based methods. International Journal of Solids and Structures 67–68, 56–70.

Murakami, S., 1988. Mechanical Modeling of Material Damage. Journal of Applied Mechanics 55 (2), 280–286.

Murakami, S., 2012. Continuum Damage Mechanics. Vol. 185 of Solid Mechanics and Its Applications. Springer Netherlands, Dordrecht.

Naghipour, P., Bartsch, M., Chernova, L., Hausmann, J., Voggenreiter, H., 2010. Effect of fiber angle orientation and stacking sequence on mixed mode fracture toughness of carbon fiber reinforced plastics: Numerical and experimental investigations. Materials Science and Engineering: A 527 (3), 509–517.

Navidtehrani, Y., Betegón, C., Martínez-Pañeda, E., 2021. A simple and robust Abaqus implementation of the phase field fracture method. Applications in Engineering Science 6, 100050.

Needleman, A., 1988. Material rate dependence and mesh sensitivity in localization problems. Computer Methods in Applied Mechanics and Engineering 67 (1), 69–85.

Nguyen, B. N., Bapanapalli, S. K., Holbery, J. D., Smith, M. T., Kunc, V., Frame, J., B., Phelps, J. H., Tucker III, C. L., 2008. Fiber Length and Orientation in Long-Fiber Injection-Molded Thermoplastics — Part I: Modeling of Microstructure and Elastic Properties. Journal of Composite Materials 42 (10), 1003–1029.

Nguyen, Q. S., 2000. Stability and Nonlinear Solid Mechanics. Wiley, New York.

Nocedal, N., Wright, J. W., 2006. Numerical Optimization. Springer Series in Operations Research and Financial Engineering. Springer Science+Business Media, Luxemburg.

Olsen-Kettle, L., 2018a. Quantifying the orthotropic damage tensor for composites undergoing damage-induced anisotropy using ultrasonic investigations. Composite Structures 204, 701–711.

Olsen-Kettle, L., 2018b. Using ultrasonic investigations to develop anisotropic damage models for initially transverse isotropic materials undergoing damage to remain transverse isotropic. International Journal of Solids and Structures 138, 155–165.

Onodera, S., Okabe, T., 2020. Analytical model for determining effective stiffness and mechanical behavior of polymer matrix composite laminates using continuum damage mechanics. International Journal of Damage Mechanics 29 (10), 1512–1542.

Ortiz, M., Stainier, L., 1999. The variational formulation of viscoplastic constitutive updates. Computer Methods in Applied Mechanics and Engineering 171 (3-4), 419–444.

Pan, Y., Iorga, L., Pelegri, A. A., 2008. Analysis of 3D random chopped fiber reinforced composites using FEM and random sequential adsorption. Computational Materials Science 43 (3), 450–461.

Papanicolaou, G. C., Varadhan, S. R. S., 1981. Boundary value problems with rapidly oscillating random coefficients. In: Random fields, Vol. I, II (Esztergom, 1979). Vol. 27 of Colloq. Math. Soc. János Bolyai. North-Holland Publishing Company, Amsterdam-New York, pp. 835–873.

Papenfuß, C., 2020. Continuum Thermodynamics and Constitutive Theory. Springer International Publishing, Cham.

Papoulis, A., Pillai, S. U., 2002. Probability, random variables, and stochastic processes, 4th Edition. McGraw-Hill, Boston.

Peerlings, R. H. J., De Borst, R., Brekelmans, W. A. M., De Vree, J. H. P., 1996. Gradient Enhanced Damage for Quasi-Brittle Materials. International Journal for Numerical Methods in Engineering 39 (19), 3391–3403.

Petersen, P., 2016. Riemannian Geometry. Vol. 171 of Graduate Texts in Mathematics. Springer International Publishing, Cham.

Pijaudier-Cabot, G., Bažant, Z. P., 1987. Nonlocal Damage Theory. Journal of Engineering Mechanics 113 (10), 1512–1533.

Pinkall, U., Gross, O., 2024. Differential Geometry: From Elastic Curves to Willmore Surfaces. Compact Textbooks in Mathematics Series. Springer International Publishing, Cham.

Pinter, P., Dietrich, S., Bertram, B., Kehrer, L., Elsner, P., Weidenmann, K. A., 2018. Comparison and error estimation of 3D fibre orientation analysis of computed tomography image data for fibre reinforced composites. NDT & E International 95, 26–35.

Pournin, L., Weber, M., Tsukahara, M., Ferrez, J.-A., Ramaioli, M., Liebling, T. M., 2005. Three-dimensional distinct element simulation of spherocylinder crystallization. Granular Matter 7 (2-3), 119–126.

PPG Fiber Glass, 2013. Data Sheet - TufRov® 4575.

Puck, A., Schürmann, H., 2002. Failure analysis of FRP laminates by means of physically based phenomenological models. Composites Science and Technology 62 (12-13), 1633–1662.

Qi, L., Sun, J., 1993. A nonsmooth version of Newton's method. Mathematical Programming 58 (1-3), 353–367.

Rabotnov, Y. N., 1963. On the Equation of State of Creep. Proceedings of the Institution of Mechanical Engineers, Conference Proceedings 178 (1), 2–117.

Riaño, L., Joliff, Y., 2019. An Abaqus™ plug-in for the geometry generation of Representative Volume Elements with randomly distributed fibers and interphases. Composite Structures 209, 644–651.

Robinson, S. M., 1994. Newton's method for a class of nonsmooth functions. Set-Valued Analysis 2 (1-2), 291–305.

Rockafellar, R. T., 1970. Convex Analysis. Princeton University Press, Princeton.

Rolland, H., Saintier, N., Robert, G., 2016. Damage mechanisms in short glass fibre reinforced thermoplastic during in situ microtomography tensile tests. Composites Part B: Engineering 90, 365–377.

Sab, K., Nedjar, B., 2005. Periodization of random media and representative volume element size for linear composites. Comptes Rendus. Mécanique 333 (2), 187–195.

Santambrogio, F., 2015. Optimal Transport for Applied Mathematicians: Calculus of Variations, PDEs, and Modeling. Progress in Nonlinear Differential Equations and Their Applications. Springer International Publishing, Cham.

Schelleis, C., Scheuring, B. M., Liebig, W. V., Hrymak, A. N., Henning, F., 2023. Approaching Polycarbonate as an LFT-D Material: Processing and Mechanical Properties. Polymers 15 (9), 2041.

Scheuring, B. M., Christ, N., Blarr, J., Liebig, W. V., Hohe, J., Montesano, J., Weidenmann, K. A., 2024. Experimental and homogenized orientation-dependent properties of hybrid long fiber-reinforced thermoplastics. International Journal of Mechanical Sciences 280, 109470.

Schmidt, T., Balzani, D., 2016. Relaxed incremental variational approach for the modeling of damage-induced stress hysteresis in arterial walls. Journal of the Mechanical Behavior of Biomedical Materials 58, 149–162.

Schneider, M., 2015. Convergence of FFT-based homogenization for strongly heterogeneous media. Mathematical Methods in the Applied Sciences 38 (13), 2761–2778.

Schneider, M., 2017. The sequential addition and migration method to generate representative volume elements for the homogenization of short fiber reinforced plastics. Computational Mechanics 59 (2), 247–263.

Schneider, M., 2019. On the Barzilai-Borwein basic scheme in FFT-based computational homogenization. International Journal for Numerical Methods in Engineering 118 (8), 482–494.

Schneider, M., 2020a. A dynamical view of nonlinear conjugate gradient methods with applications to FFT-based computational micromechanics. Computational Mechanics 66 (1), 239–257.

Schneider, M., 2020b. An FFT-based method for computing weighted minimal surfaces in microstructures with applications to the computational homogenization of brittle fracture. International Journal for Numerical Methods in Engineering 121 (7), 1367–1387.

Schneider, M., 2021. A review of nonlinear FFT-based computational homogenization methods. Acta Mechanica 232 (6), 2051–2100.

Schneider, M., 2022. An algorithm for generating microstructures of fiber-reinforced composites with long fibers. International Journal for Numerical Methods in Engineering 123 (24), 6197–6219.

Schneider, M., Josien, M., Otto, F., 2022. Representative volume elements for matrix-inclusion composites - a computational study on the effects of an improper treatment of particles intersecting the boundary and the benefits of periodizing the ensemble. Journal of the Mechanics and Physics of Solids 158, 104652.

Schneider, M., Ospald, F., Kabel, M., 2016. Computational homogenization of elasticity on a staggered grid. International Journal for Numerical Methods in Engineering 105 (9), 693–720.

Schneider, M., Wicht, D., Böhlke, T., 2019. On polarization-based schemes for the FFT-based computational homogenization of inelastic materials. Computational Mechanics 64 (4), 1073–1095.

Schwarz, S., Junker, P., Hackl, K., 2021. Variational regularization of damage models based on the emulated RVE. Continuum Mechanics and Thermodynamics 33 (1), 69–95.

Senior, A. B., Osswald, T., 2020. Measuring Fiber Length in the Core and Shell Regions of Injection Molded Long Fiber-Reinforced Thermoplastic Plaques. Journal of Composites Science 4 (3), 104.

Seth, B. R., 1961. Generalized strain measure with applications to physical problems. Tech. rep., Wisconsin University - Madison Mathematics Research Center.

Shen, H., Nutt, S., Hull, D., 2004. Direct observation and measurement of fiber architecture in short fiber-polymer composite foam through micro-CT imaging. Composites Science and Technology 64 (13-14), 2113–2120.

Simo, J. C., Ju, J. W., 1987. Strain- and stress-based continuum damage models – I. Formulation. International Journal of Solids and Structures 23 (7), 821–840.

Sluys, L. J., De Borst, R., 1992. Wave propagation and localization in a rate-dependent cracked medium – model formulation and one-dimensional examples. International Journal of Solids and Structures 29 (23), 2945–2958.

Sobol, I. M., 1967. On the distribution of points in a cube and the approximate evaluation of integrals. USSR Computational Mathematics and Mathematical Physics 7 (4), 86–112.

Sobol, I. M., 1976. Uniformly distributed sequences with an additional uniform property. USSR Computational Mathematics and Mathematical Physics 16 (5), 236–242.

Solomon, J., 2018. Optimal transport on discrete domains. AMS Short Course on Discrete Differential Geometry 3, 1–38.

Song, Y., Yeon, J., Voyiadjis, G. Z., 2024. Theoretical and numerical modeling of the effect of damage and dynamic strain aging on the plastic response of C45 steel alloys. International Journal of Damage Mechanics 34 (5), 736–755.

Spahn, J., Andrä, H., Kabel, M., Müller, R., 2014. A multiscale approach for modeling progressive damage of composite materials using fast Fourier transforms. Computer Methods in Applied Mechanics and Engineering 268, 871–883.

Tian, W., Chao, X., Fu, M. W., Qi, L., 2021. An advanced method for efficiently generating composite RVEs with specified particle orientation. Composites Science and Technology 205, 108647.

Tian, W., Qi, L., Zhou, J., Liang, J., Ma, Y., 2015. Representative volume element for composites reinforced by spatially randomly distributed discontinuous fibers and its applications. Composite Structures 131, 366–373.

Tojaga, V., Prapavesis, A., Faleskog, J., Gasser, T. C., Van Vuure, A. W., Östlund, S., 2023. Continuum damage micromechanics description of the compressive failure mechanisms in sustainable biocomposites and experimental validation. Journal of the Mechanics and Physics of Solids 171, 105138.

Toll, S., 1998. Packing mechanics of fiber reinforcements. Polymer Engineering & Science 38 (8), 1337–1350.

Tschoegl, N. W., Knauss, W. G., Emri, I., 2002. Poisson's Ratio in Linear Viscoelasticity – A Critical Review. Mechanics of Time-Dependent Materials 6 (1), 3–51.

Vega, C., Lago, S., 1994. A fast algorithm to evaluate the shortest distance between rods. Computers & Chemistry 18 (1), 55–59.

Verlet, L., 1967. Computer "Experiments" on Classical Fluids. I. Thermodynamical Properties of Lennard-Jones Molecules. Physical Review 159 (1), 98–103.

Villani, C., 2009. Optimal Transport. Vol. 338 of Grundlehren der mathematischen Wissenschaften. Springer, Berlin, Heidelberg.

Voyiadjis, G. Z., Kattan, P. I., 2006. Advances in Damage Mechanics: Metals and Metal Matrix Composites with an Introduction to Fabric Tensors, 2nd Edition. Elsevier Science, Burlington.

Voyiadjis, G. Z., Kattan, P. I., 2009. A Comparative Study of Damage Variables in Continuum Damage Mechanics. International Journal of Damage Mechanics 18 (4), 315–340.

Weibull, W., 1951. A Statistical Distribution Function of Wide Applicability. Journal of Applied Mechanics 18 (3), 293–297.

Weigel, N., Dinkler, D., Kröplin, B. H., 2001. Micromechanically based continuum damage mechanics material laws for fiber-reinforced ceramics. Computers & Structures 79 (22-25), 2277–2286.

Wicht, D., Schneider, M., Böhlke, T., 2020. On Quasi-Newton methods in fast Fourier transform-based micromechanics. International Journal for Numerical Methods in Engineering 121 (8), 1665–1694.

Widom, B., 1966. Random Sequential Addition of Hard Spheres to a Volume. The Journal of Chemical Physics 44 (10), 3888–3894.

Williams, S. R., Philipse, A. P., 2003. Random packings of spheres and spherocylinders simulated by mechanical contraction. Physical Review E 67 (5), 051301.

Willot, F., 2017. Mean covariogram of cylinders and applications to Boolean random sets. Journal of Contemporary Mathematical Analysis (Armenian Academy of Sciences) 52 (6), 305–315.

Wirjadi, O., Schladitz, K., Easwaran, P., Ohser, J., 2016. Estimating fibre direction distributions of reinforced composites from tomographic images. Image Analysis & Stereology 35 (3), 167–179.

Wriggers, P., Moftah, S., 2006. Mesoscale models for concrete: Homogenisation and damage behaviour. Finite Elements in Analysis and Design 42 (7), 623–636.

Wu, J.-Y., Nguyen, V. P., 2018. A length scale insensitive phase-field damage model for brittle fracture. Journal of the Mechanics and Physics of Solids 119, 20–42.

Wu, Y., Ju, J. W., 2017. Elastoplastic damage micromechanics for continuous fiber-reinforced ductile matrix composites with progressive fiber breakage. International Journal of Damage Mechanics 26 (1), 4–28.

Yan, H., Jin, H., Yao, R., 2020. Prediction of the damage and fracture of cast steel containing pores. International Journal of Damage Mechanics 29 (1), 166–183.

Yarlagadda, S., Deitzel, J., Heider, D., Tierney, J., Gillespie Jr., J., 2019. Tailorable Universal Feedstock for Forming (TUFF): Overview and Performance. In: International SAMPE Technical Conference 2019. SAMPE, Charlotte, NC, USA.

Zeman, J., Vondřejc, J., Novák, J., Marek, I., 2010. Accelerating a FFT-based solver for numerical homogenization of periodic media by conjugate gradients. Journal of Computational Physics 229 (21), 8065–8071.

Zhang, H., Yang, D., Sheng, Y., 2018. Performance-driven 3D printing of continuous curved carbon fibre reinforced polymer composites: A preliminary numerical study. Composites Part B: Engineering 151, 256–264.

Zhu, W. C., Tang, C. A., 2004. Micromechanical Model for Simulating the Fracture Process of Rock. Rock Mechanics and Rock Engineering 37 (1), 25–56.

ZOLTEK Corporation, 2019. Technical Datasheet ZOLTEK™ PX35 Vinyl Ester Compatible Tow.

Schriftenreihe Kontinuumsmechanik im Maschinenbau
Karlsruher Institut für Technologie (KIT)
(ISSN 2192-693X)

Band 1 Felix Fritzen
Microstructural modeling and computational homogenization of the physically linear and nonlinear constitutive behavior of micro-heterogeneous materials.
ISBN 978-3-86644-699-1

Band 2 Rumena Tsotsova
Texturbasierte Modellierung anisotroper Fließpotentiale.
ISBN 978-3-86644-764-6

Band 3 Johannes Wippler
Micromechanical finite element simulations of crack propagation in silicon nitride.
ISBN 978-3-86644-818-6

Band 4 Katja Jöchen
Homogenization of the linear and non-linear mechanical behavior of polycrystals.
ISBN 978-3-86644-971-8

Band 5 Stephan Wulfinghoff
Numerically Efficient Gradient Crystal Plasticity with a Grain Boundary Yield Criterion and Dislocation-based Work-Hardening.
ISBN 978-3-7315-0245-6

Band 6 Viktor Müller
Micromechanical modeling of short-fiber reinforced composites.
ISBN 978-3-7315-0454-2

Die Bände sind unter www.ksp.kit.edu als PDF frei verfügbar oder als Druckausgabe bestellbar.

Band 7 Florian Rieger
Work-hardening of dual-phase steel.
ISBN 978-3-7315-0513-6

Band 8 Vedran Glavas
Micromechanical Modeling and Simulation of Forming Processes.
ISBN 978-3-7315-0602-7

Band 9 Eric Bayerschen
Single-crystal gradient plasticity with an accumulated plastic slip: Theory and applications.
ISBN 978-3-7315-0606-5

Band 10 Bartholomäus Brylka
Charakterisierung und Modellierung der Steifigkeit von langfaserverstärktem Polypropylen.
ISBN 978-3-7315-0680-5

Band 11 Rudolf Neumann
Two-Scale Thermomechanical Simulation of Hot Stamping.
ISBN 978-3-7315-0714-7

Band 12 Mauricio Lobos Fernández
Homogenization and materials design of mechanical properties of textured materials based on zeroth-, first- and second-order bounds of linear behavior.
ISBN 978-3-7315-0770-3

Band 13 Malte Schemmann
Biaxial Characterization and Mean-field Based Damage Modeling of Sheet Molding Compound Composites.
ISBN 978-3-7315-0818-2

Band 14 Jürgen Albiez
Finite element simulation of dislocation based plasticity and diffusion in multiphase materials at high temperature.
ISBN 978-3-7315-0918-9

Die Bände sind unter www.ksp.kit.edu als PDF frei verfügbar oder als Druckausgabe bestellbar.

Band 15 Maria Loredana Kehrer
Thermomechanical Mean-Field Modeling and Experimental Characterization of Long Fiber-Reinforced Sheet Molding Compound Composites.
ISBN 978-3-7315-0924-0

Band 16 Peter Hölz
A dynamic and statistical analysis of the temperature- and fatigue behavior of a race power unit – The effect of different thermodynamic states.
ISBN 978-3-7315-0988-2

Band 17 Andreas Prahs
A Gradient Crystal Plasticity Theory Based on an Extended Energy Balance.
ISBN 978-3-7315-1025-3

Band 18 Johannes Ruck
Modeling martensitic phase transformation in dual phase steels based on a sharp interface theory.
ISBN 978-3-7315-1072-7

Band 19 Hannes Erdle
Modeling of Dislocation - Grain Boundary Interactions in Gradient Crystal Plasticity Theories.
ISBN 978-3-7315-1196-0

Band 20 Johannes Görthofer
Microstructure generation and micromechanical modeling of sheet molding compound composites.
ISBN 978-3-7315-1205-9

Band 21 Daniel Wicht
Efficient fast Fourier transform-based solvers for computing the thermomechanical behavior of applied materials.
ISBN 978-3-7315-1220-2

Band 22 Juliane Lang
Thermomechanical Modeling and Experimental Characterization of Sheet Molding Compound Composites.
ISBN 978-3-7315-1232-5

Die Bände sind unter www.ksp.kit.edu als PDF frei verfügbar oder als Druckausgabe bestellbar.

Band 23 Julian Karl Bauer
Fiber Orientation Tensors and Mean Field Homogenization: Application to Sheet Molding Compound.
ISBN 978-3-7315-1262-2

Band 24 Sebastian Gajek
Deep material networks for efficient scale-bridging in thermomechanical simulations of solids.
ISBN 978-3-7315-1278-3

Band 25 Jannick Kuhn
Microstructure modeling and crystal plasticity parameter identification for predicting the cyclic mechanical behavior of polycrystalline metals.
ISBN 978-3-7315-1272-1

Band 26 Felix Ernesti
A computational multi-scale approach for brittle materials.
ISBN 978-3-7315-1285-1

Band 27 Patrick Arthur Hessman
On multi-scale modeling of fatigue in short glass fiber reinforced thermoplastics.
ISBN 978-3-7315-1398-8

Band 28 Benedikt Sterr
Machine learning aided multiscale mechanics of fiber suspensions.
ISBN 978-3-7315-11421-3

Band 29 Maximilian Krause
Local Stresses and Strains in Polycrystals.
ISBN 978-3-7315-1411-4

Band 30 Johannes Keursten
Thermoviscoelastic Modeling of Thermoplastic Polymers.
ISBN 978-3-7315-1422-0

Band 31 Alexander Dyck
Chemo-Mechanically Coupled Models in Continuum Thermodynamics.
ISBN 978-3-7315-1425-1

Band 32 Tobias Karl
Micromechanical Modeling of Short-Fiber Orientation Dynamics.
ISBN 978-3-7315-1431-2

Band 33 Celine Lauff
Multiscale simulation of fiber-reinforced thermoplastics accounting for damage.
ISBN 978-3-7315-1486-2

This work contributes to the field of computational multiscale modeling for fiber-reinforced polymers. More specifically, efficient algorithms for the generation of periodic microstructures for short and long fiber reinforced polymers as well as hybrid material systems are presented. To ensure the representativity of the synthetic microstructures, the main descriptors of the microstructure are taken into account, i.e., the fiber volume fraction, the fiber length and orientation distributions as well as the fiber curvature. The generation tools are applied to industrial material systems and the linear-elastic material behavior is validated with experimental data. Due to the precise realization of the microstructural descriptors and the periodicity of the geometries, the necessary unit cell size for representativity is minimized.

In addition, a novel class of linear-elastic isotropic damage models with damage softening behavior is developed. To do so, convex regularization techniques are applied to a classical isotropic damage model with damage rate limitation. The convexity of the resulting condensed incremental energy ensures mesh-independent results even for damage softening. In computational studies, the performance of the developed algorithm and the mechanical implications of the novel class of damage models are studied. By applying the damage models to the matrix material of fiber-reinforced polymers, the existence of representative volume elements is demonstrated - indispensable for computational homogenization.

ISSN 2192-693X
ISBN 978-3-7315-1486-2

Gedruckt auf FSC-zertifiziertem Papier

